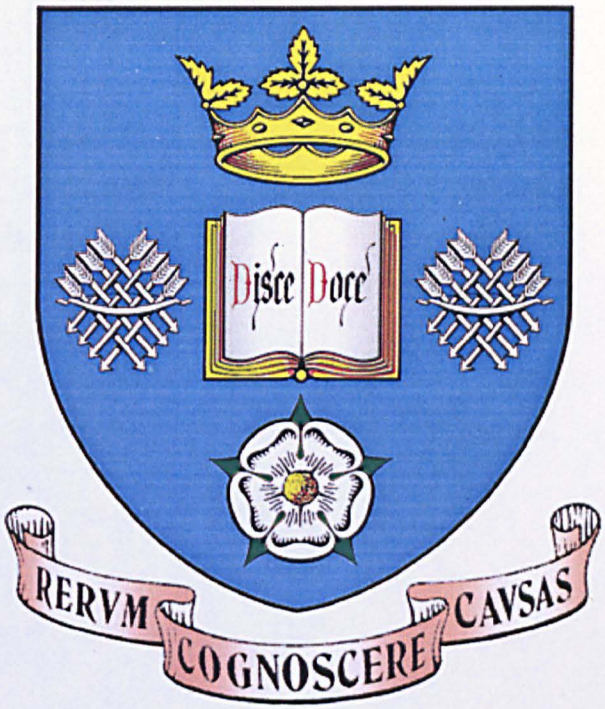

Modelling, Analysis and Design of LCLC Resonant Power Converters

Yong-Ann Ang

A thesis submitted for the degree of Ph.D., in the
Department of Electronic and Electrical Engineering,
The University of Sheffield.

April 2005

Summary

The thesis investigates the modelling, analysis, design and control of 4^{th}-order LCLC resonant power converters. Both voltage-output and current-output variants, are considered. Key research outcomes are the derivation of new frequency- and time-domain models of the converters, based on normalised component ratios, and including the effects that parasitic elements have on circuit behaviour, and a detailed account of multi-resonant characteristics; extensions to the use of cyclic-mode modelling methods for application to LCLC converters, to provide rapid steady-state analysis, thereby facilitating the use of the derived methodologies as part of an interactive design tool; the formulation of analytical methods to predict the electrical stresses on tank components—an important consideration when designing resonant converters, as they are often higher than for hard-switched converter counterparts; the characterisation of both continuous and discontinuous modes of operation and the boundary conditions that separate them; and a substantial treatment of the modelling, analysis and design of LCLC converters that can provide multiple regulated outputs by the integrated control of both excitation frequency and pulse-width-modulation.

The proposed methodologies are employed, for validation purposes, in the realisation of two proof-of-concept demonstrator converters. The first, to satisfy the requirements for delivering 65V (rms) to an electrode-less, 8W, fluorescent lamp, to improve energy efficiency and lifetime, and operating at a nominal frequency of 2.65 MHz, is used to demonstrate capacitively-coupled operation through the lamp tube, thereby mitigating the normally detrimental effects of excitation via the electrodes. The second prototype considers the realization of an LCLC resonant power supply that can provide multiple regulated outputs without the need for post-regulation circuitry. The two outputs of the supply are independently, closed-loop regulated, to provide asymmetrical output voltage distributions, using a combination of frequency- and duty-control. Although, an analysis of the supply shows that the behaviour is extremely complex, due, in particular, to the highly non-linear interaction between the multiple outputs and parasitic inductances, and rectifier, an analysis to provide optimum performance characteristics, is proposed. Moreover, a PIC/FPGA-based digital controller is developed that allows control of the transient performance of both outputs under start-up and steady-state conditions.

The work presented in the thesis has been disseminated by publications at international conferences and in learned society journals, details of which are given below.

Y. Ang, M. P. Foster, H. I. Sewell, C. M. Bingham and D. A. Stone, "Stress analysis of 4th-order LLCC resonant converters", *IEE Electronics Letters*, **38**, pp. 1585-1586, 2002.

Y. Ang, M. P. Foster, C. M. Bingham, D. A. Stone, H. I. Sewell and D. Howe, "Analysis of 4th-order LCLC Resonant Power Converters", *IEE Proc. Electric Power Applications*, **151**, pp. 169-181, 2004.

Y. Ang, D. A. Stone, C. M. Bingham and M. P. Foster, "Analysis & Design of High-Frequency LCLC Resonant Converters for Electrode-Less Fluorescent Lamp Ballasts", in *2nd IEE International Conference on Power Electronics, Machines and Drives*, Edinburgh, 2004, pp. 137-142.

Y. Ang, C. M. Bingham, M. P. Foster, D. A. Stone and D. Howe, "Design Orientated Analysis of 4th-Order LCLC Converters with Capacitive Output Filter", *IEE Proc. Electric Power Applications*, **152**, pp. 310-322, 2005.

Acknowledgements

Firstly, I would like to express my appreciation to Dr. Chris Bingham for the support and guidance throughout this work. I am deeply indebted to you for your enthusiasm, encouragement and advice. Thank you for providing me with financial support and a cosy and friendly environment to carry out my research. Many thanks go to Dr. David Stone; I am always amazed with your sharp sense toward scientific problems. You are a good scientist and great teacher whom I always admire. I have learned a lot from you. Thank you.

I would like to thank Dr. Martin Paul Foster, for the discussions we've had, from which I have greatly benefited. As a colleague, you are knowledgeable and helpful. Your passion towards research and scientific insights are much admired, which I have taken as an example.

I take this opportunity to thank all members of EMD research group, who have provided a stimulating and friendly environment to carry out my research work.

Finally, I would like to extend my appreciation to Sin Yee, my family and all my close friends for their love, encouragement and support especially time when I have become lost in my PhD life.

Table of Contents

Nomenclature

Variable	Description	
C_e	Extended FMA equivalent circuit capacitance	(F)
C_{eq}	L_p-C_p combined frequency-dependent capacitance	(F)
C_f	Output filter capacitance	(F)
C_n	Resonant capacitance ratio	
C_{neff}	Voltage-output converter effective resonant capacitance ratio	
C_p	Parallel resonant capacitance	(F)
C_{p1}	High-side parallel resonant capacitance	(F)
C_{p2}	Low-side parallel resonant capacitance	(F)
C_s	Series resonant capacitance	(F)
C_T	Parasitic capacitance	(F)
c_{tot}	L_p-C_e combined frequency-dependent capacitance	(F)
f_{crit}	Minimum frequency to achieve ZVS under asymmetrical V_{in} excitation	(Hz)
f_{oeff}	Voltage-output converter effective resonant frequency	(Hz)
f_s	Switching frequency	(Hz)
i_{Cp}	Current through parallel resonant capacitor	(A)
i_{in}	Time-varying input current to resonant tank	(A)
i_L	Link current from resonant tank	(A)
$\hat{i}_{in}$	Peak input current to resonant circuit	(A)
i_{Lp}	Current through parallel resonant inductor	(A)
$\hat{i}_{Lp}$	Peak current through parallel resonant inductor	(A)
i_{Ls}	Current through series resonant inductor	(A)
$\hat{i}_{Ls}$	Peak current through series resonant inductor	(A)
i_{out}	DC output current	(A)
i_R	Input current to bridge rectifier	(A)
L_{eq}	Equivalent inductance to account for C_T, L_T	(H)

L_f	Output filter inductance	(H)
L_{lp}	Transformer primary leakage inductance	(H)
L_{ls}	Transformer output winding series inductance	(H)
L_m	Transformer's magnetising inductance	(H)
L_n	Resonant inductance ratio	
L_p	Parallel resonant inductance	(H)
L_s	Series resonant inductance	(H)
L_T	Inductance	(H)
M_{vcr}	Designated voltage gain	
N	Transformer secondary-to-primary turns ratio	
p_{out}	Output power rating	(W)
Q_{op1}	Series resonant tank load quality factor	
Q_{op2}	Parallel resonant tank load quality factor	
Q_o	Effective load quality factor	
Q_{oeff}	Voltage-output converter effective load quality factor	
$\Re_{Cp\_clamp}$	Equivalent resistor for modelling capacitor voltage clamping	(Ω)
r_{ds}	MOSFET turn-on resistance	(Ω)
$\Re_e$	Equivalent circuit resistor	(Ω)
R_{eq}	FMA equivalent circuit resistor	(Ω)
R_i	Resonant inverter load	(Ω)
R_L	Load resistance	(Ω)
R_{lamp}	Equivalent lamp resistance	(Ω)
R_{tot}	Sum of parasitic resistances, r_{ds}, r_{ls}, r_{cs}	(Ω)
v_b	Output voltage plus diode voltage drop	(V)
v_{Cf}	Voltage across output filter capacitor	(V)
v_{Cp}	Voltage across parallel resonant capacitor	(V)
v_{Cs}	Voltage across series resonant capacitor	(V)
v_{Cp_charge}	Time-domain capacitor charging voltage waveform	(V)
v_{Cp_clamp}	Time-domain capacitor clamping voltage	(V)
$\hat{V}_{Cp}$	Peak voltage across parallel resonant capacitor	(V)
$\hat{V}_{Cs}$	Peak voltage across series resonant capacitor	(V)
v_{DC}	DC supply voltage	(V)

v_{diode}	Rectifier diode on-state volt-drop	(V)
$v_{i(1)}$	Fundamental component of input voltage	(V)
V_{in}	Input excitation voltage	(V)
V_{out}	DC output voltage	(V)
v_R	Bridge rectifier input voltage	(V)
$\overline{\omega}_{eff}$	Effective resonant to series resonant frequency ratio	
ω_n	Normalised frequency	
ω_o	Angular series resonant frequency	($rads^{-1}$)
ω_o'	Second effective resonant frequency	($rads^{-1}$)
ω_{op1}	Angular resonant frequencies of the series resonant tank component	($rads^{-1}$)
ω_{op2}	Angular resonant frequencies of the parallel resonant tank component	($rads^{-1}$)
ω_{oeff}	Voltage-output converter effective resonant frequency	($rads^{-1}$)
ω_s	Angular switching frequency	($rads^{-1}$)
$\omega_{s\,min}$	Minimum angular frequency for CCM	($rads^{-1}$)
Z_{in}	Input impedance of resonant circuit	(Ω)
Z_o	Characteristic impedance	
Z_{oeff}	Voltage-output converter effective characteristic impedance	
α_i	Phase difference between the i_L and v_{Cp}	(rad)
β_{in}	Phase angle between $v_{i(1)}$ and i_{Ls}	(rad)
$\Delta\beta_{in}$	Phase angle between V_{in} and i_{Ls}	(rad)
γ_c	Phase difference between the fundament of the input voltage and v_{Cp}	(rad)
λ_τ	Ratio of the effective resonant frequency and the series resonant frequency	
ϕ_c	Rectifier non-conduction angle	(rad)
$\phi_{vi(1)}$	Phase angle of $v_{i(1)}$	(rad)
δ_{cond}	Parallel capacitor non-conduction phase angle	(rad)

CHAPTER 1

Introduction

With the increased power capability, improved control and reduced cost of modern power semiconductor devices, designers of electronic equipment, computers and electronic instrumentation are increasingly demanding higher energy-density and efficient power sources to supply their equipment, Fig. 1.1. Power supply technologies can be divided into two distinct groups; linear regulators and switched-mode power conversion techniques. Over recent decades, a substantial movement from simpler linear regulators, to high frequency pulse-width modulated (PWM) converters with similar power handling capabilities, but with a reduction of overall size and weight, has emerged. Theoretically, at least, using ideal component characteristics, switched-mode power conversion offers the possibility of loss-less power transfer, with duty-cycle or frequency control of an idealised switching element controlling the flow of energy to achieve regulation.

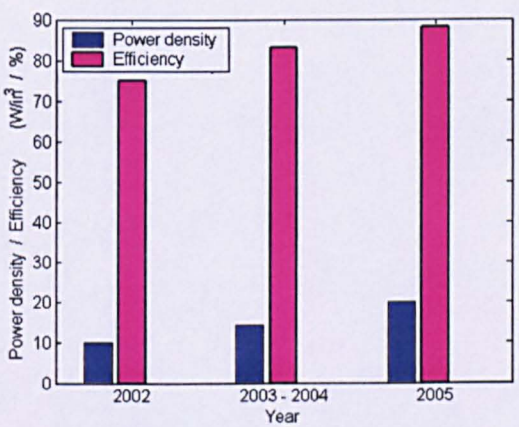

Figure 1.1 Recent trends in power supply technology

To date, most commercial switch-mode power supplies on the market operate in the frequency range 10 kHz to 50 kHz [A1], and are found in many commercial products and white-goods viz. computers, television receivers, battery chargers etc. For domestic applications, switching frequencies in excess of 20 kHz are usually employed to reduce the impact of acoustic noise emissions. However, the trend towards miniaturisation of electronic systems [A2], particularly for communication and entertainment products, and the emergence of enhanced power switch technologies, is leading to the use of switching frequencies in the range of 100's kHz to several MHz, Fig. 1.2 [A3].

During their infancy, switched-mode converters employed Bipolar Junction Transistors (BJTs), which had, by then, been optimized for low power transfer, as a result of requirements to develop digital logic circuits, but have been subsequently realized for higher voltage/current applications. However, the introduction of power Metal Oxide Semiconductor Field Effect Transistors (MOSFETs), during the 1970/80s [A4], provided the power electronics industry with a device capable of much greater switching speeds and lower power dissipation. Nevertheless, whilst significant advances have been made, MOSFETs remain limited by achievable voltage ratings and greater fabrication cost.

The Insulated Gate Bipolar Transistor (IGBT) combines the low-power drive advantages of the MOSFET with the low conduction losses and high blocking-voltage characteristics of the BJT, thereby making it very suitable for high power, high voltage systems. However, since current transport is by the same process as the BJT, the maximum switching speed is much lower than can be achieved by MOSFETs, and is therefore currently limited to applications requiring switching speeds of typically <50kHz.

The MOS-controlled Thyristor (MCT) is a relatively new device to the commercial market. The MCT combines the properties of a Gate-Turn-Off Thyristor, including low on-state voltage drop at high current, with the advantage of being a voltage-controlled device like the IGBT and MOSFET. A comparison between MCTs and IGBTs of similar ratings show that the MCTs have smaller on-state voltages and are now available in voltage ratings up to 1500V, at a few hundred amperes. Nevertheless, the MCT remains a relatively new technology, albeit in a state of rapid development, and significant improvements in the device capabilities are anticipated in the next few years. A summary of the capabilities of recent power devices is shown in Fig. 1.2 [A5].

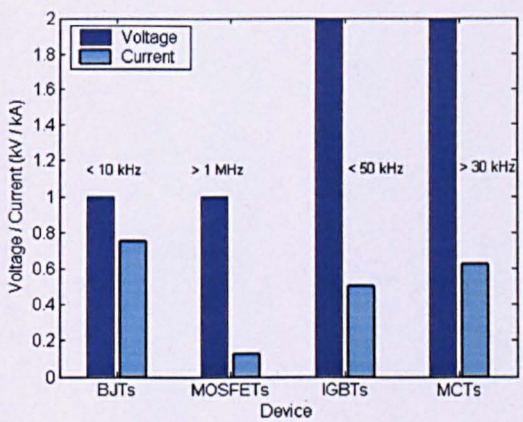

Figure 1.2 Power semiconductor device capabilities.

Although the use of higher switching frequencies allows smaller reactive components to be employed in designs, in-turn leading to systems with lower volume envelope and reduced cost, the resulting supplies are often more susceptible to the effects of parasitic capacitance and leakage inductance, higher peak current stress, and higher switching losses. In conventional PWM converters, such effects manifest themselves as high-frequency ringing and large current spikes that are generated by the rapid charging and discharging of device capacitances, and unwanted electromagnetic interference (EMI).

As a consequence, with ever-stringent regulations regarding supply quality and EMI, as well as the techno-economic benefits afforded by the use of high power-factor loads, the merits of resonant power converters, particularly those which employ high-order tank circuits, are now attracting increased attention. This is most apparent in market sectors such as compact fluorescent lamp ballasts [A6], plasma televisions [A7], x-ray generators [A8, A9], electric vehicle inductive battery chargers [A10] and electric welding [A11] (Fig. 1.3), for instance.

(a) (b) (c)

Figure 1.3 Possible applications for resonant power converter: a) Plasma display panel, b) Fluorescent lamp electronic ballast, and c) X-ray medical system.

The input switching devices of resonant converters, as opposed to hard-switched counterparts, can be configured to operate in either 'zero current' (ZCS) or 'zero voltage' (ZVS) switching modes [A12], thereby greatly reducing levels of electrical stresses on devices (see Fig. 1.4) and minimizing switching losses. Another advantage is the reduction of EMI normally associated with applying high-bandwidth switching transients to internal capacitances of devices. Converters designed to exhibit ZVS, for instance, do not generate this type of EMI [A13]. Furthermore, the sine-wave characteristics of resonant tank voltages and currents reduce the generation of high frequency harmonics.

Although many variants of resonant converter have emerged, they can be broadly categorized into those employing series-resonant or parallel-resonant tank networks [A14-A17]. Generally, the resonant tank is switched above the resonant frequency, thereby imparting ZVS to minimize turn-on losses—variable frequency control being used for regulating the output voltage. However, a disadvantage with this method is that the transfer characteristic is non-linear and generally changes with load.

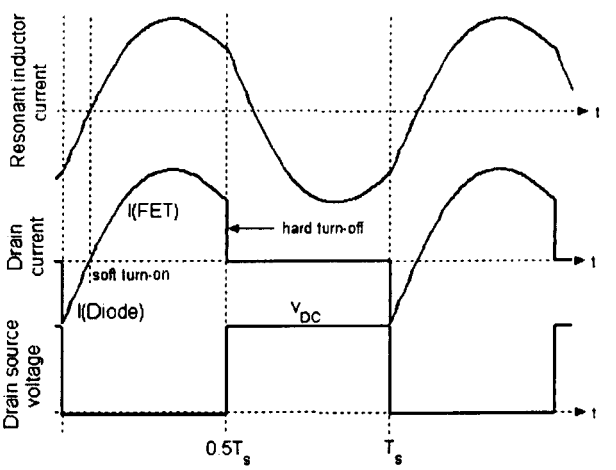

Figure 1.4 Switch current and voltage waveforms when a resonant converter is operated using ZVS.

Higher-order resonant converters are constructed from tank networks typically employing three or four reactive components, contained in two resonant branches (a series branch and a parallel branch), and, by appropriate selection of component values, it is possible to obtain converters with the combined advantages of both the series- and parallel-tank variants.

It has previously been reported that 36 × 3rd-order and 182 × 4th-order resonant converter topologies have been identified, consisting of three or more energy storage elements, respectively, [A18, A19], not all of which are practically useful. To date, few converter topologies have been fully analyzed with experimental verification—with the most common being the LCC series-parallel converter [A20-A25] which features desirable properties of both series- and parallel-converter counterparts. The CLL counterpart, which is more complex to analyze, has also been considered in [A26-A29].

In addition to improving the specific characteristics of converters employing 2nd-order tank circuits, high-order converters are also able to usefully 'absorb' circuit parasitic elements, as designed

components—an important feature for switching frequencies in the 100'skHz/MHz range. By contrast, parasitic effects stemming from semiconductor junction capacitances, transformer leakage and magnetizing inductance, winding stray capacitance and rectifier diode internal capacitance, are the primary reasons hindering the operation of 'hard switched' converter counterparts, at such frequencies.

1.1. Review of Modelling and Analysis Methodologies

Whilst resonant power conversion has significant potential to supply the future needs of equipment manufacturers, their widespread adoption remains impeded by the higher electrical stresses to which individual electronic components are exposed, and a lack of suitable design methodologies that can provide accurate and rapid predictions of circuit behaviour at the design stage; particularly those that consider the significant effects that parasitic resistances, capacitances and inductances have on resonant tank behaviour.

The properties of the series [A14, A30], parallel [A15], and other 3rd-order resonant converter topologies [A31-A33] have been traditionally explored using the Fundamental Mode Approximation (FMA), and a systematic design guide has been previously reported for a resonant converter employing a 4th-order LCLC tank using a more complex form of AC analysis [A34]. Harmonics of the switching frequency are neglected, and tank waveforms are assumed to be purely sinusoid, thereby facilitating the generation of simple equivalent circuits to be obtained to describe the behaviour of the resonant tank, rectifier, and output filter.

A consequence of using FMA, is that the dc-input voltage to output-voltage conversion ratio, during continuous conduction mode operation, is approximately given by the ac-transfer function of the tank circuit, an example being shown in Fig. 1.5. The tank is loaded by an 'effective' output resistance that models the interaction between rectifier/output filter networks. It is thereby relatively straightforward to determine how the arrangement of tank components, and their values, affects converter behaviour. This intuitive approach is shown to be sufficiently accurate to model converter operation in continuous conduction mode with a high quality factor, Q, but becomes very inaccurate when the tank is operated at low Q-factors or when operating in the region of discontinuous conduction mode conditions, and when parasitic components have significant influence on current/voltage wave-shapes.

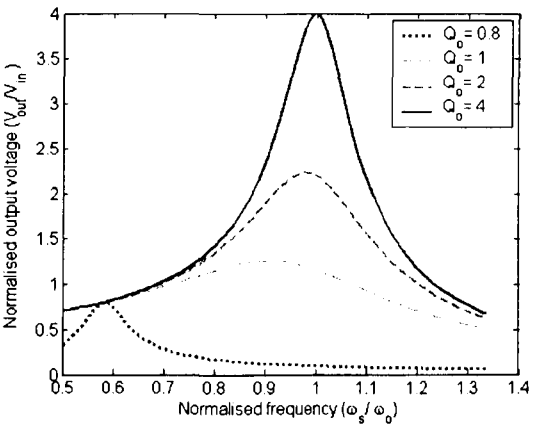

Figure 1.5 Example voltage gain curve of an LCC resonant converter.

This is particularly apparent for converters based on LCLC structures, including the LCC counterpart, when a capacitive output filter is employed, and the combined clamping action of the parallel resonant capacitor and bridge rectifier creates voltage/current waveforms that are neither sinusoidal nor square-wave (Fig. 1.6). To date, the most accurate frequency-domain methodology for analysing such converters is by recourse to Rectifier–Compensated FMA (RCFMA) [A31], where, in addition to the use of an 'equivalent resistor' to model the effects of the rectifier and output filter (as in classical FMA), other components, specifically an additional 'equivalent capacitor', is also used to improve accuracy.

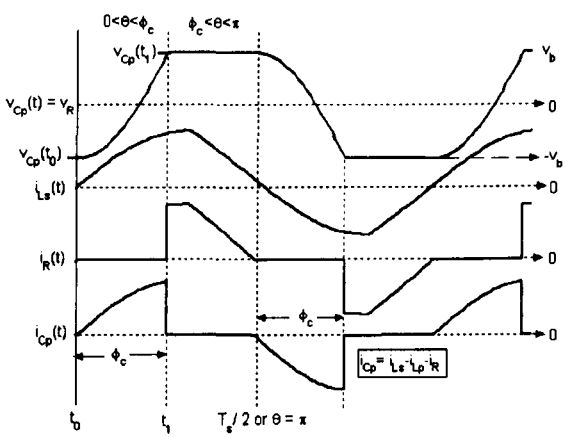

Figure 1.6 Example voltage and current waveforms of the voltage-output converter.

RCFMA allows the underlying attributes of FMA to be applied to the more complex voltage-output converter variants whilst still allowing rapid analysis by virtue of employing the fundamental mode principle. The method has been demonstrated to combine low computational overhead with significantly enhanced prediction accuracy with respect to classical FMA techniques. Other

publications from Forsyth [A25], Ivensky *et al.* [A23], and Sewell *et al.* [A36] have directly addressed the analysis of LCC resonant converters using such 'describing function' methods, all providing incremental modifications to enhance the model of the non-linear interaction between the third-order LCC resonant tank and rectifier/output filter. Herein, the underlying principles are further extended to accommodate their use for the analysis of 4^{th}-order LCLC converters.

Although exact time-domain analysis of the resonant converters is more complex than when employing FMA principles, such approaches are necessary to obtain a complete understanding of converter behaviour when the 'sinusoidal approximation' does not hold. In such cases, the dynamics are more readily described by time-domain state-variable differential equations, of the form given in (1.1),

$$\begin{aligned} \dot{\mathrm{x}}(t) &= \mathbf{A}\mathrm{x}(t) + \mathbf{B}\mathrm{u}(t) \\ \mathrm{y}(t) &= \mathbf{C}\mathrm{x}(t) + \mathbf{D}\mathrm{u}(t) \end{aligned} \tag{1.1}$$

where **A** is the state matrix, **B** is the input matrix, **C** is the output matrix, **D** is the direct transmission matrix, $\mathrm{x}(t)$ is the state vector, $\mathrm{u}(t)$ is the input vector, and $\mathrm{y}(t)$ is the output vector. The state-variable representation allows the 'internal behaviour' of the system to be determined, and hence, the states of the system to be represented as a trajectory in n-dimensional state-space ('n' being the number of states).

Candidate transient response equation-based modelling environments have been previously reported, most notably for simulating the control of Quasi-resonant converters [A37, A38] using MATLAB®/SIMULINK. In such cases, the state-variables, as well as models of the passive and active switches, are derived, with less computational overhead being required when compared to component based simulation packages, such as SPICE. Once the composite non-linear state-variable model is developed, the transient behaviour of the converter can be accurately predicted.

To reduce complexity, state-space averaging techniques have been widely investigated to estimate the mean contribution of the converter voltages and currents [A39, A40, and A42], to the output voltage, and rely on the derivation of a number of state matrices, each corresponding to a distinct switching mode of the converter, which are then combined into a weighted (as a function of mode duty) averaged model. Perturbing and linearizing the resulting large signal model about the operating point subsequently allows the production of a small-signal dynamic model. Such methods therefore provide a valuable means of analysing both the dc- and ac-behaviour of power converters. However, the results are only valid if the averaging is applied over a switching interval (T_s) that is small compared to

the converter's natural response time—the 'linear ripple assumption'. Unfortunately, operation of resonant converters is different from that of hard-switched PWM converters, which have high-frequency energy storage elements whose natural response time is typically shorter than the switching time, T_s [A42], thereby rendering classical state-space averaging techniques inapplicable in such cases.

Other modelling approaches capable of producing basic, yet accurate, closed-form dynamic solutions suitable for describing the behaviour of resonant converters, have been reported, particularly to describe the many continuous and discontinuous conduction modes of the classical series-resonant converter [A43], as well as for the parallel-resonant [A16, A17, A44, A45], and some high-order resonant converter topologies [A46-A48]. One technique reduces the complicated tank waveforms to a set of geometric relationships, an example being shown in Fig. 1.7 [A46]. When appropriately normalised, the underlying tank waveforms are described by segments of arcs and lines in the state-plane. Determining the steady-state characteristics then consists of piecing together the appropriate segments, and solving. Equally important has been another averaging concept, in which the dc- and low-frequency ac-components of the converter waveforms, are obtained, while neglecting high frequency switching harmonics, thereby significantly simplifying the analysis. The use of circuit averaging, in this instance, is justified, since the switching harmonics are usually negligibly small at the load due to sufficient low-pass filtering being incorporated into a well-designed resonant converter.

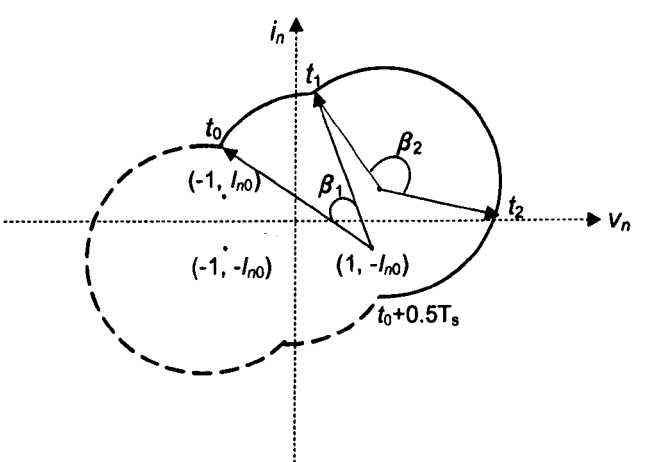

Figure 1.7 Typical steady-state state-plane trajectory of a parallel resonant converter [A46].

Although state-plane analysis approaches have been successfully applied to analyze 2nd and 3rd-order converters, systems based on 4thorder tank circuits, with nonlinear output current or voltage sources, become difficult to solve using conventional approaches. This is due to the fact that dynamics of the higher-order system are tightly coupled, thereby allowing the steady-state behaviour of the converter's

operation to be portrayed independently on 2× 2-dimensional state-planes. The required interpolation between the two design charts leads to a complex optimisation procedure. Due to its complexity (as will be shown) the voltage-output variant of 4^{th}-order resonant converter has yet to be investigated using this approach.

1.2. Outline of Thesis

The thesis is divided into nine chapters, organized as follows. Chapter 2 presents the derivation and application of state-variable models for topologies of resonant converter with higher-order tank circuits. From basic network theory, the resulting state-variable equations partition the converter dynamics into fast- and slow-subsystems, to be used as a basis for proposed analysis techniques that are derived in later chapters. Both voltage- and current-output converter variants, are considered.

Chapter 3 introduces frequency-domain analysis procedures for the 4^{th}-order current-output LCLC converter when operating in continuous conduction mode, with a high-Q response. Harmonics of the input excitation voltage are assumed to be sufficiently filtered by the tank so as to allow the tank waveforms to be considered purely sinusoidal, thereby allowing basic equivalent circuits to be derived for the resonant inverter and rectifier/output filter of the converter, which can be combined and solved using standard ac-analysis. However, when operating conditions are such that the 'sinusoidal waveform' approximation leads to inaccurate results, as in the case during discontinuous conduction modes of operation, for instance, the use of Fundamental Mode Approximation (FMA) techniques are shown to be inappropriate.

Chapter 4 therefore develops an alternative analysis methodology for this topology of converter, based on the *cyclic-mode* principle. It is shown that the proposed technique provides a mechanism for rapidly determining the steady-state characteristics of the converter, and, importantly, provides a route for analytically predicting the voltage and current stresses on the electrical components. Chapter 5 then provides a case-study that applies the techniques for the realization of an LCLC resonant inverter to meet the requirements for delivering 65V (rms) to a novel, prototype, electrode-less, 8W, fluorescent lamp. Improved energy efficiency and lifetime of the fluorescent lamp, beyond that normally obtainable by excitation by a 50/60Hz domestic supply, is demonstrated by capacitively-coupling the output of the LCLC inverter to the fluorescent tube, and using excitation frequencies in the MHz range.

Chapter 6 develops enhancements to classical FMA analysis techniques, and gives refinement procedures that further improve analysis accuracy. Moreover, the resulting equations lead to the derivation of four new design/synthesis procedures for the realisation LCLC converters that are subsequently used for the design of voltage-output converters. The analysis technique is then used to obtain the switching transition times of the converter. From the knowledge of the mode transition times, cyclic-averaging analysis is employed to facilitate high-speed, steady-state analysis.

Finally, Chapter 8 extends results from the previous chapters to the analysis and design of resonant converters to provide multiple regulated outputs. In particular, the characteristics of a dual-load LCLC voltage-output resonant converter, is explored for the first time. Two state-variable models are derived, one of which incorporates the effects of transformer leakage to improve prediction accuracy. It is shown that the two outputs of the converter can be independently regulated to provide asymmetrical output voltage distributions using a combination of frequency and duty control. A comparison of measurements from a prototype converter, capable of delivering 5V and 3.3V, suitable for a standard electronic supply, with those from the derived state-variable models, and SPICE simulations, shows that the underlying equations provide accurate predictions of output voltage under steady state conditions. Moreover, a digital feedback control scheme is realised that allows control of the transient performance of both outputs under start-up conditions, and regulation at steady-state.

References

[A1] R. P. Severns and G. E. Bloom (1st ed.), *Modern DC-to-DC Switch Mode Power Converter Circuits*, New York: Van Nostrand Reinhold Co., 1985.

[A2] A. Offner, "Trends in the power supply industry", 2003.

[A3] IBM Corporation, *1999 IBM Power Technology Symposium, Theme: DC/DC Conversion*, Research Triangle Park, NC, 1999.

[A4] K. H. Billings (2nd ed.), *Switchmode Power Supply Handbook*, New York: McGraw-Hill, 1999.

[A5] N. Mohan, T. M. Undeland and W. P. Robbins (3rd Ed.), *Power Electronics*, USA: John Wiley and Son, 2003.

[A6] S. Glozman and S. Ben-Yaakov, "Dynamic interaction of high frequency electronic ballasts and fluorescent lamps", in *IEEE Power Electronics Specialists Conference Proc.*, 2000, pp. 1363-1368.

[A7] www.sv.philips.com/newtech/flattv.html

[A8] L. Zhao, D. Peng and J. Wyk, "Analysis and Design of LCLC Resonant Converter Suitable for X-ray Generator Power Supply", in *1st IEE International Conference on Power Electronics, Machines and Drives*, 2002, pp. 360-365.

[A9] G. Dolan, D. Grafham and J. Saiz, "48kW Resonant Converter for X-Ray Machines Uses High Speed Power Modules with Integral Liquid Cooling", in *PCIM Europe*, 1999.

[A10] R. Laouamer, J. P. Ferrieux and H. Benqassmi, "A Comparison of Resonant Converter Topologies with Three and Four Energy Storage Elements for Automotive Inductive Charging Application", *Electric Machines and Power Systems*, **27**, pp. 221-235, 1999.

[A11] J. A. Ferreira, "A Series Resonant Converter for Arc-Striking Applications", *IEEE Trans. on Industrial Electronics*, **45**, pp. 585-595, 1998.

[A12] R. L. Steigerwald, "A Comparison of Half-Bridge Resonant Converter Topologies", *IEEE Trans. on Power Electronics*, **3**, pp. 174-182, 1988.

[A13] M. Jovanovics, "Resonant, quasi-resonant, multi-resonant and soft-switching techniques—merits and limitations", *International Journal of Electronics*, **77**, pp. 537-554, 1994.

[A14] M. K. Kazimierzuk and S. Wang, "Frequency-domain analysis of series resonant converter for continuous conduction mode", *IEEE Trans. on Power Electronics*, **7**, pp. 270-279, 1992.

[A15] M. K. Kazimierzuk, W. Szaraniec and S. Wang, "Analysis and design of parallel resonant converter at high Q_L", *IEEE Trans. on Aerospace and Electronics Systems*, **28**, pp. 35-49, 1992.

[A16] K. Siri, I. Batarseh and C. Q. Lee, "Frequency response for the conventional parallel resonant converter based on the state-plane diagram," *IEEE Trans. on Circuits and Systems*, **40**, pp. 33-42, 1993.

[A17] R. Liu, I. Batarseh and C. Q. Lee, "Comparison of Capacitively and Inductively Coupled parallel Resonant Converters", *IEEE Trans. on Power Electronics*, **8**, pp. 445-452, 1993.

[A18] R. P. Severns, "Topologies for Three-Elements Resonant Converters", *IEEE Trans. on Power Electronics*, **7**, pp. 89-96, 1992.

[A19] I. Batarseh, "Resonant Converter Topologies with Three and Four Energy Storage Elements", *IEEE Trans. on Power Electronics*, **9**, pp. 64-73, 1994.

[A20] A. K. S. Bhat and S. B. Dewan, "Analysis and design of a high frequency resonant converter using LCC-type commutation", *IEEE Trans. on Power Electronics*, **2**, pp. 291-300, 1987.

[A21] I. Batarseh, R. Liu, C. Q. Lee and A. K. Upadgyay, "Theoretical and experimental studies of LCC-type parallel resonant converter", *IEEE Trans. on Power Electronics*, **5**, pp. 140-150, 1990.

[A22] A. J. Forsyth, G. A. Ward and S. V. Mollov, "Extended Fundamental Frequency Analysis of LCC Resonant Converter", *IEEE Trans. on Power Electronics*, **18**, pp. 1286-1292, 2003.

[A23] G. Ivensky; A. Kats; S. Yaakov, "An RC Load Model of Parallel and Series-Parallel Resonant DC-DC Converters with Capacitive Output Filter", *IEEE Trans. on Power Electronics*, **14**, pp. 515-521, 1999.

[A24] M. P. Foster, H. I. Sewell, C. M. Bingham, D. A. Stone, D. Hente and D. Howe, "High Speed Analysis of Resonant Power Converters", *IEE Proc. Electric Power Applications*, **150**, pp. 62-70, 2003.

[A25] A. J. Forsyth and S. V. Mollov, "Simple equivalent circuit for the series-loaded resonant converter with voltage boosting capacitor", *IEE Proc. Electric Power Applications*, **145**, pp.301-306, 1998.

[A26] G. Raju and S. Doradla, "An LCLC resonant converter with PWM control analysis, simulation and implementation", *IEEE Trans. on Power Electronics*, **10**, pp. 164-174, 1995.

[A27] G. Raju and S. Doradla, "A novel LCLC resonant converter with PWM control analysis, simulation and implementation", in *9th Annual IEEE Applied Power Electronics Conference Rec.*, 1994, pp. 998-1004.

[A28] B. Yang, R. Chen and F. C. Lee, "Integrated magnetic for LLC Resonant Converter", in *17th Annual IEEE Applied Power Electronics Conference Proc.*, 2002, pp. 346-351.

[A29] B. Yang, F. C. Lee and m. Concannon, "Over Current Protection Methods for LLC Resonant Converter", in *18th Annual IEEE Applied Power Electronics Conference Proc.*, 2003, pp. 605-609.

[A30] H. Jiang, G. Maggetto and P. Lataire, "Steady-State Analysis of the Series Resonant DC-DC Converter in Conjunction with Loosely Coupled Transformer—above Resonance Operation", *IEEE Trans. on Power Electronics*, **14**, pp. 469-477, 1999.

[A31] O. P. Mandhana, "Computer aided analysis and design of load commutated resonant converter", in *27th Annual IEEE Power Electronics Specialists Conference Rec.*, 1996, pp. 279-285.

[A32] A. K. S. Bhat, "A Unified Approach for the Steady-State Analysis of Resonant Converters", *IEEE Trans. on Industrial Electronics*, **38**, pp. 251-259, 1991.

[A33] A. K. S. Bhat, "Analysis and Design of LCL-Type Series Resonant Converter", *IEEE Trans. on Industrial Electronics*, **41**, pp. 118-124, 1994.

[A34] H. M. Suryawanshi and S. G. Tarnekar, "Modified LCLC-type series resonant converter with improved performance,' *IEE Proc. Electric Power Applications*, **143**, pp. 354-360, 1996.

[A35] J. G. Hayes; M. G. Egan, "Rectifier-Compensated Fundamental Mode Approximation Analysis of the Series Parallel LCLC Family of Resonant converters with Capacitive Output Filter and Voltage-Source load", in *30th IEEE Power Electronics Specialist Conference Rec.*, 1999, pp. 1030-1036.

[A36] H. I. Sewell, M. P. Foster, C. M. Bingham, D. A. Stone, D. Hente and D. Howe, "Analysis of voltage output LCC resonant converters, including boost mode operation", *IEE Proc. Electric Power Applications*, **150**, pp.673-679, 2003.

[A37] B. Baha, "Modelling of resonant switched-mode converters using SIMULINK", *IEE Proc. Electric Power Application*, **145**, pp. 159-163, 1998.

[A38] L. K. Wong, F. H. Leung and P. K. S. Tam, "A Simple Large-Signal Non-linear Modelling Approach for Fast Simulation of Zero-Current-Switch Quasi-Resonant Converters", *IEEE Trans. on Power Electronics*, **12**, pp.437-442, 1997.

[A39] R. D. Middlebrook, "Small-signal modeling of pulse-width modulated switched-mode power converters", *IEEE Proceedings*, **76**, pp. 343-354, 1988.

[A40] J. Mahdavi, A. Emaadi, M. Bellar and M. Ehsani, "Analysis of power electronic converters using the generalized state-space averaging approach", *IEEE Trans. on Circuits and Systems I: Fundamental Theory and Applications*, **44**, pp. 767-770, 1997.

[A41] A. F. Witulski and R. W. Erickson, "Extension of state-space averaging to resonant switches and beyond", *IEEE Trans. on Power Electronics*, **5**, pp. 98-109, 1990.

[A42] J. Xu and C. Q. Lee, "A unified averaging technique for the modeling of quasi-resonant converters", *IEEE Trans. on Power Electronics*, **13**, pp. 556-563, 1998.

[A43] H. Kojori, S. B. Dewan and J. D. Lavers, "Steady-state analysis and design optimization of an inductor-transformer resonant DC-DC converter", *IEEE Trans. on Industrial Applications*, **27**, pp. 515-522, 1991.

[A44] F. Tsai and F. C. Lee, "State-plane analysis of a constant-frequency clamped-mode parallel-resonant converter", *IEEE Trans. on Power Electronics*, **3**, pp. 364-378, 1988.

[A45] I. Batarseh, "State-plane approach for analysis of half-bridge parallel resonant converters", *IEE Proc. Circuits Devices System*, **142**, pp. 200-2004, 1995.

[A46] I. Batarseh and C. Q. Lee, "State-plane analysis of high order parallel resonant converters", in *34th Midwest Symposium on Circuits and Systems Proc.*, 1991, pp. 939-942.

[A47] I. Batarseh, "Steady-State Analysis of the Parallel Resonant Converter with LLCC-Type Commutation Network", *IEEE Trans. on Power Electronics*, **6**, pp. 525-537, 1991.

[A48] J. Cheng and A. F. Witulski, "Analytic solutions for LLCC parallel resonant converter simplify use of two and three-element converters", *IEEE Trans. on Power Electronics*, **13**, pp. 235-243, 1998.

CHAPTER 2

State Variable Modelling of Resonant Converters

Simulation studies are a powerful supplement to conventional design methodologies to establish transient behavioural characteristics and sensitivities prior to finalising circuit designs. Classically, component-based simulation packages such as SPICE and SABER are often used to obtain large-signal dynamic characteristics of power electronic converters. However, there remains a need for equation-based simulation models as a result of the prohibitive execution times normally associated with component-based simulator kernels.

Candidate transient response equation-based modelling environments have been explored, most notably for simulating feedback control of Fly-back Quasi-resonant converters [B1] in MATHWORK®/SIMULINK. In this case, equations for the state-variables, as well as models of the passive and active switches, are derived, and with less computational overhead being required compared to SPICE. Averaging techniques are used with Fundamental Mode Approximation (FMA) to model the time-dependant voltages and currents in the resonant circuit, as behavioural dependant sources. Although an average model of the resonant converter is constructed, the core feature when deriving the model solution still requires circuit simulators capable of handling behavioural dependant sources, namely SPICE-type simulators.

Another modelling approach for the single-ended quasi resonant Converter, is proposed in [B2], based on basic analytical techniques from inductor currents and capacitor voltages. Non-linear differential equation models are used to accurately predict the transient behaviour of the targeted converter.

The objective of this chapter is to present the application of equation-based modelling techniques for the rapid analysis of higher-order resonant converters. The half-bridge 4^{th}-order converter, with a LCLC resonant tank configuration, as shown in Fig. 2.1, is specifically considered, with full-bridge rectification, and both inductor-capacitor (current-output) and capacitor-type (voltage-output) output filter configurations.

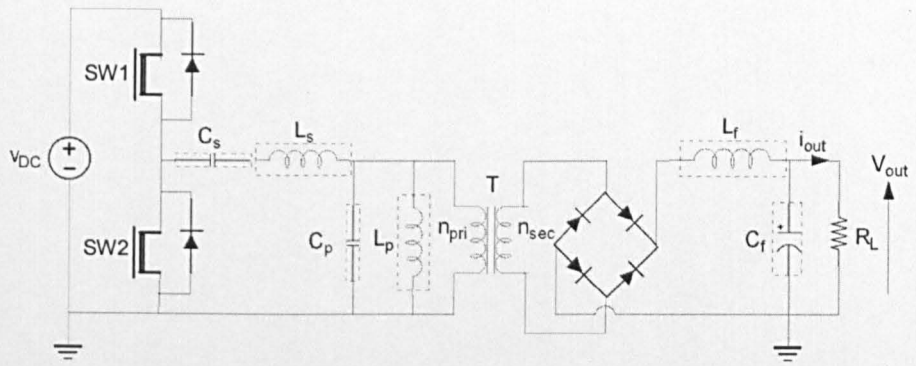

Figure 2.1 Circuit diagram of a 4th-order LCLC resonant converter (optional filter inductor L_f).

To derive appropriate models, the converter dynamics are first partitioned into fast- and slow-subsystems, for convenience. The fast sub-system represents the behaviour of the resonant tank and power switches, and the 'slow' sub-system, the output filter and load [B3]. Although the rectifier is excluded, the interaction between the fast- and slow-subsystems is described by a set of coupling equations describing the rectifier's non-linear contribution to the dynamics.

Here, models of inductive-output converters under both continuous (CCM) and discontinuous modes (DCM) of operation, are derived, during light- and heavy-loadings. The accuracy of the models is verified against cycle-to-cycle SPICE simulations and practical measurements from a prototype converter. Moreover, the resulting models provide the basis for 'cyclic-averaging' techniques to be employed to facilitate steady state behavioural analysis of resonant converters, described in later chapters.

2.1. State-variable Modelling of the Current-output Resonant Converter

Figure 2.2(a) shows a 4th-order LCLC current-output resonant power converter with idealised reactive components and associated parasitic resistances. The filter inductor L_f is often used in high-power converters, and those that require a low output current ripple, and facilitates a reduction in the size of the output filter capacitor. In high voltage converters, such as those for TV or monitor CRTs, the parallel resonant components, L_p and C_p, can be designed to be the magnetising inductance and parasitic capacitance of a step-up transformer (not shown in Fig. 2.2(a) for clarity), whilst the series resonant component, L_s, takes advantage of the transformer leakage inductance.

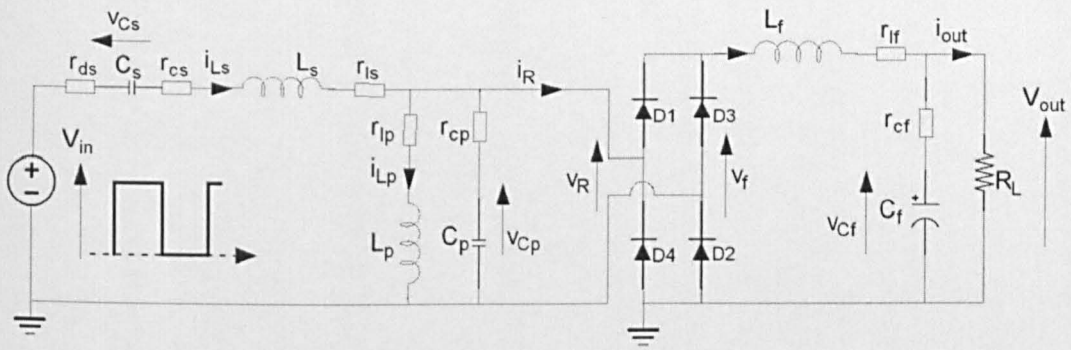

(a)

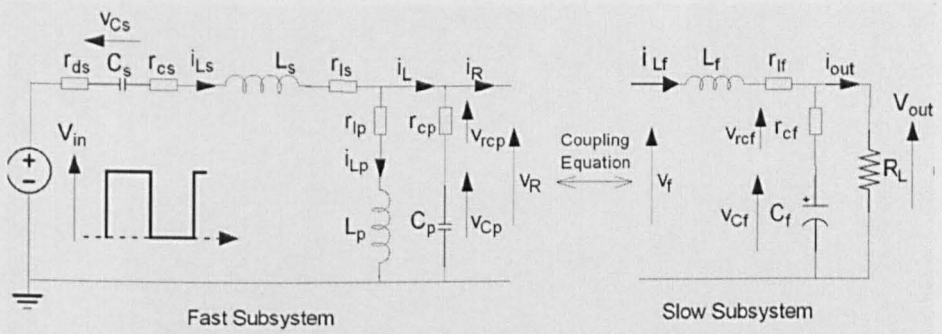

(b)

Figure 2.2 LCLC resonant converter (a) Current output variant including parasitic resistances (b) Fast- and slow-subsystems.

As previously stated, a state-variable model of the converter is derived by partitioning the dynamics into fast and slow-subsystems, as shown in Fig. 2.2(b) with coupling equations describing their interaction.

The fast sub-system describes the dynamics of the resonant tank and power switches, viz.:

$$\begin{aligned}
\frac{dv_{Cp}}{dt} &= \frac{i_{Ls} - i_{Lp} - i_R}{C_p} \\
\frac{dv_{Cs}}{dt} &= \frac{i_{Ls}}{C_s} \\
\frac{di_{Lp}}{dt} &= \frac{v_{Cp}}{L_p} \\
\frac{di_{Ls}}{dt} &= \frac{V_{in} - v_{Cs} - v_{Cp} - i_{Ls}(r_{ds} + r_{cp} + r_{cs} + r_{ls}) + r_{cp} i_{Lp} + r_{cp} i_R}{L_s}
\end{aligned} \tag{2-1}$$

Noting that the voltage across the parallel resonant inductor, L_p is assumed to be identical to voltage v_{Cp} throughout the analysis. The dynamics of the output filter, i.e. the slow sub-system, are dependent on the presence, or otherwise, of filter inductor L_f. When L_f is included, the output voltage, V_{out} = (v_{Cf}+v_{rcf}), and the dynamics of the inductor current and filter capacitor voltage, are given by (2-2):

$$\begin{aligned}
\frac{dv_{Cf}}{dt} &= \frac{-v_{Cf}}{C_f(R_L + r_{cf})} + \frac{i_{Lf} R_L}{C_f(R_L + r_{cf})} \\
\frac{di_{Lf}}{dt} &= -v_{Cf} \frac{R_L}{L_f(R_L + r_{cf})} - i_{Lf}\left[\frac{r_{lf}(R_L + r_{cf}) + R_L r_{cf}}{L_f(R_L + r_{cf})}\right] + \frac{v_f}{L_f}
\end{aligned} \tag{2-2}$$

Under light- and moderate-loading, the coupling equations governing the action of the rectifier can be derived by considering the voltage across the input and output of the rectifier, and assuming that the two-pole low-pass output filter is sufficient so as to assume that ripple components are small compared to the dc output voltage component. In this case:

$$\begin{aligned}
i_R &= i_{Lf}\,\mathrm{sgn}(v_{Cp}) \\
v_f &= |v_R| - 2v_{diode}
\end{aligned} \tag{2-3}$$

where $v_R = v_{Cp} + r_{cp}(i_{Ls} - i_{Lp} - i_R)$ and v_{diode} is the rectifier diode on-state voltage.

A complete state-variable model for continuous conduction mode operation is therefore:

$$\begin{bmatrix} \dot{v}_{Cp} \\ \dot{v}_{Cs} \\ \dot{i}_{Lp} \\ \dot{i}_{Ls} \\ \dot{v}_{Cf} \\ \dot{i}_{Lf} \end{bmatrix} = \begin{bmatrix} 0 & 0 & -\frac{1}{C_p} & \frac{1}{C_p} & 0 & 0 \\ 0 & 0 & 0 & \frac{1}{C_s} & 0 & 0 \\ \frac{1}{L_p} & 0 & 0 & 0 & 0 & 0 \\ -\frac{1}{L_s} & -\frac{1}{L_s} & \frac{r_{cp}}{L_s} & -\frac{r_{ds}+r_{cs}+r_{ls}+r_{cp}}{L_s} & 0 & 0 \\ 0 & 0 & 0 & 0 & -\frac{1}{C_f(R_L+r_{cf})} & \frac{R_L}{C_f(R_L+r_{cf})} \\ 0 & 0 & 0 & 0 & -\frac{R_L}{L_f(R_L+r_{cf})} & -\frac{r_{lf}(R_L+r_{cf})+R_L r_{cf}}{L_f(R_L+r_{cf})} \end{bmatrix} \begin{bmatrix} v_{Cp} \\ v_{Cs} \\ i_{Lp} \\ i_{Ls} \\ v_{Cf} \\ i_{Lf} \end{bmatrix} + \begin{bmatrix} -\frac{i_R}{C_p} \\ 0 \\ 0 \\ \frac{V_{in}}{L_s}+\frac{r_{cp}i_R}{L_s} \\ 0 \\ \frac{v_f}{L_f} \end{bmatrix} \tag{2-4a}$$

with the output voltage being given by,

$$V_{out} = \frac{R_L r_{cf}}{R_L + r_{cf}} \times i_{Lf} + \frac{R_L}{R_L + r_{cf}} \times v_{Cf} \tag{2-4b}$$

The non-linear model obtained for the current-output converter is readily employed in MATLAB for analysis and design of both the open- and closed-loop configurations.

Figure 2.3 shows a Simulink model of a current-output resonant converter driven by an equivalent square-wave voltage source, V_{in}. The 'dead-zone' and 'absolute value' blocks are used to model the coupling equation relating the fast- and slow-subsystems. The dead-zone is assigned with a 'start' and 'end' value of $2v_{diode}$ to offset the rectifier input voltage, v_R, by the on-state rectifier voltage; meanwhile the output from the dead-zone block is the equivalent of the bridge rectifier output voltage, v_f.

To investigate the accuracy of the proposed state-variable model for predicting the steady-state output voltage, a prototype 4th-order current-output converter, Fig. 2.4, has been commissioned with the component values given in Table 2.1. Load resistors of R_L = 2.5Ω and 5Ω are applied. Boundary conditions between CCM and DCM are reserved until Chapter 4.

Table 2.1 Current-output converter model parameters.

Parameters	Values
DC link input voltage, v_{DC} (V)	20
Series resonant inductance, L_s (μH)	2.7
Stray capacitance of series inductance, C_{T1} (pF)	12
Series resonant capacitance, C_s (μF)	2
Parallel resonant inductance, L_p (μH)	5.4
Stray capacitance of parallel inductance, C_{T2} (pF)	21.6
Parallel resonant capacitance, C_p (μF)	1
Output filter inductance, L_f (mH)	1
Output filter capacitance, C_f (μF)	10

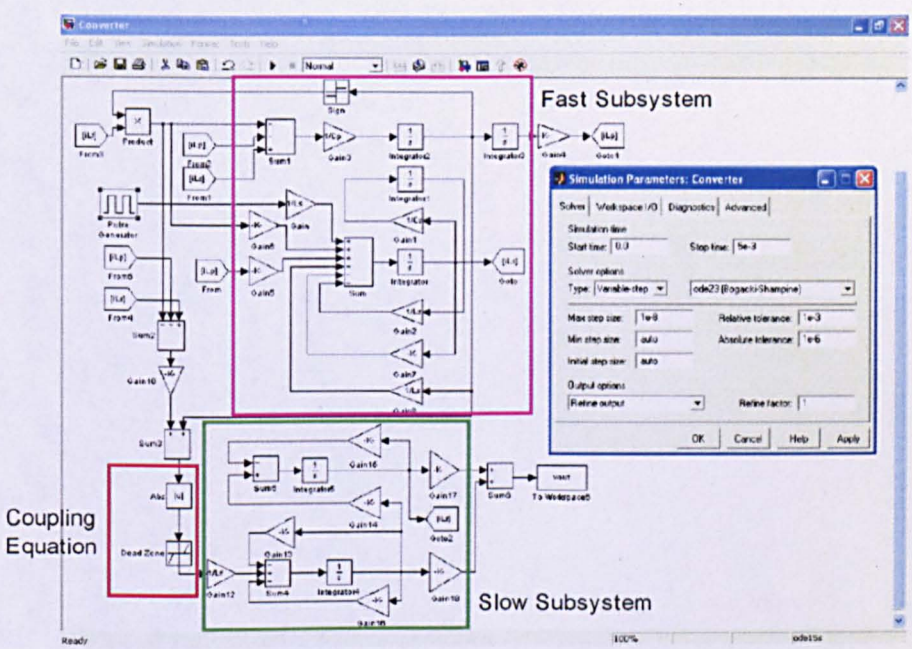

Figure 2.3 MathWorks® Simulink model of the current-output converter.

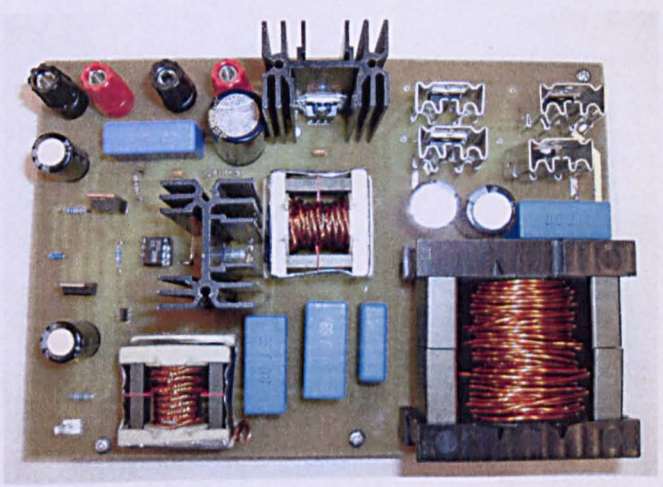

Figure 2.4 The experimental current-output LCLC converter.

Figure 2.5 shows simulated steady-state operating waveforms from the state-variable model, whilst Fig. 2.6 compares the measured output voltage of the converter with that predicted from the proposed model, over a range of operating frequencies. A discrepancy in the frequency response, is evident, and is indicative of a shift in the resonant frequency—a common feature of this converter topology, in which the resonant frequency is highly sensitive to variations in resonant component values.

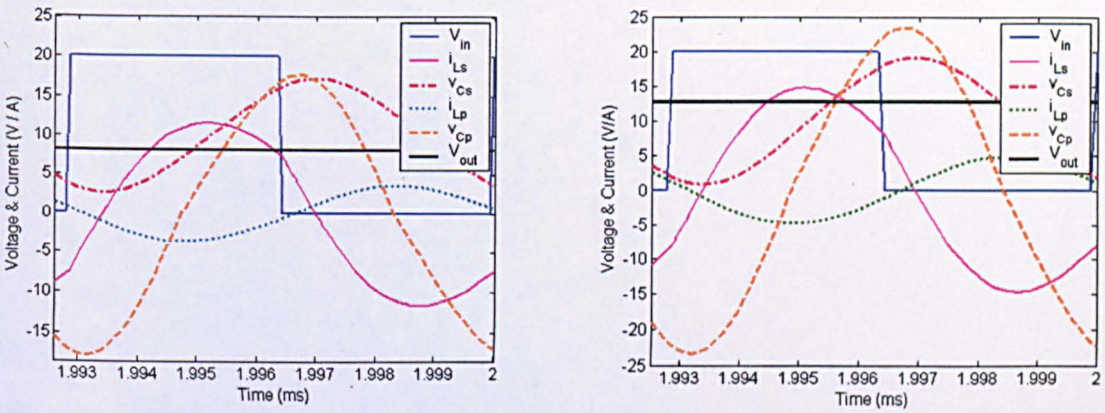

(a) (b)

Figure 2.5 Simulated waveforms of the modelled current-output converter (a) R_L=2.5Ω and (b) R_L=5Ω.

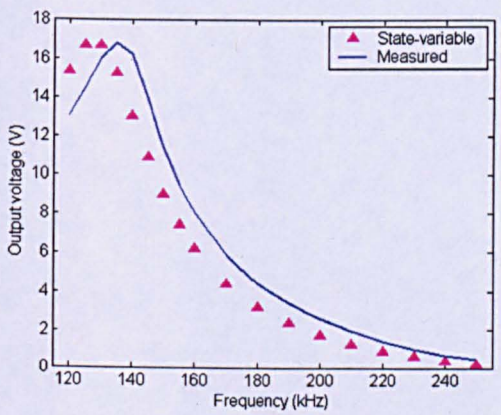

(a)

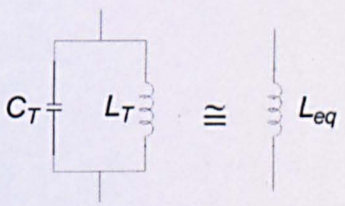

(b)

Figure 2.6 Simulation results neglecting the effects of inter-winding capacitance (a) Output voltage and (b) Equivalent circuit of resonant inductor with inter-winding capacitance

Although values of resonant capacitances C_s and C_p can be assumed to be within standard component tolerances, the inter-turn capacitance of resonant inductors, L_s and L_p, must also be accommodated. One method of accomplishing this is to define inductors L_s and L_p as frequency-dependent components that incorporate the effects of inter-winding capacitance, C_T, as illustrated in Fig. 2.6(b). A frequency response analysis of the series resonant inductor, using a network analyser, indicates that the

transformer self-capacitance, is ≈21.6pF, at resonance. The equivalent inductance, L_{eq} is obtained from the equivalent impedance of the associated parallel branch i.e.:

$$Z_{eq} = \frac{j\omega_s L_T}{1-\omega_s{}^2 L_T C_T} = j\omega_s L_{eq}$$
$$L_{eq} = \frac{L_T}{1-\omega_s{}^2 L_T C_T} \tag{2-5}$$

When the modified values of inductance are used in the model, the results shown in Fig. 2.7(a) and (b), are obtained, when the converter is operated under the two specified load conditions. A comparison with results from SPICE simulations confirms that the accuracy of the state-variable model is comparable.

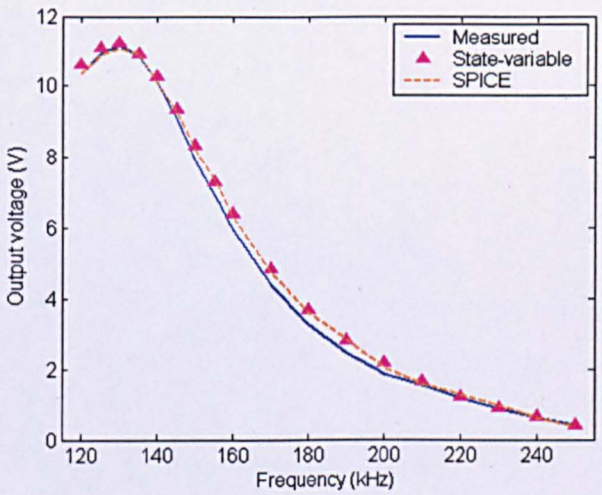

(a)

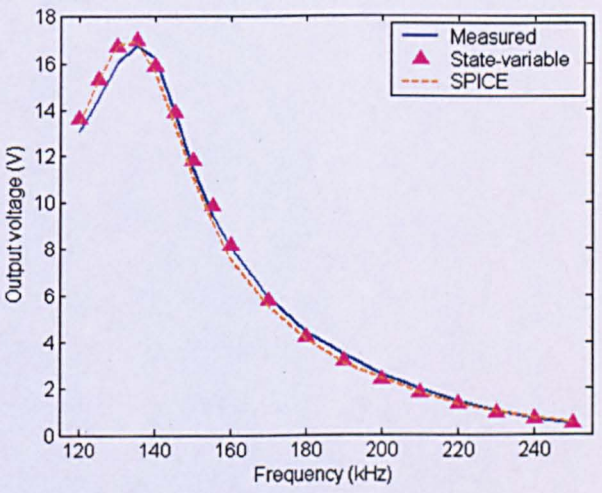

(b)

Figure 2.7 Output voltage of 4th-order current-output converter: (a) R_L=2.5Ω; (b) R_L= 5Ω.

2.1.1. State-Variable Modelling of Current-output Converter in Discontinuous Conduction Mode

Discontinuous conduction mode occurs during operation of the current-output resonant converter when it is subject to heavy loading conditions [B4]. During discontinuous conduction, all four bridge rectifier diodes, D1-D4, as shown in Fig. 2.8(a), are forward biased and the parallel resonant tank capacitor remains at zero volts i.e. $v_{Cp} = 0$. Such modes occur both above and below the resonant frequency. Operation of the converter during discontinuous conduction mode operation, is therefore now addressed, and the state variable equations describing the resulting behaviour, derived.

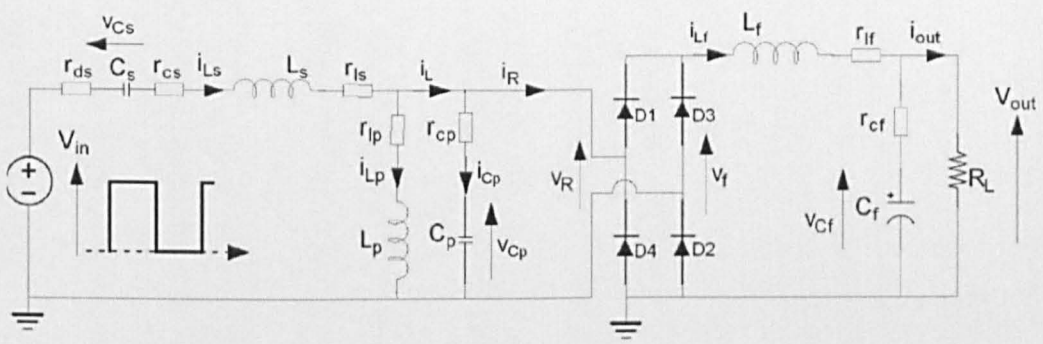

(a)

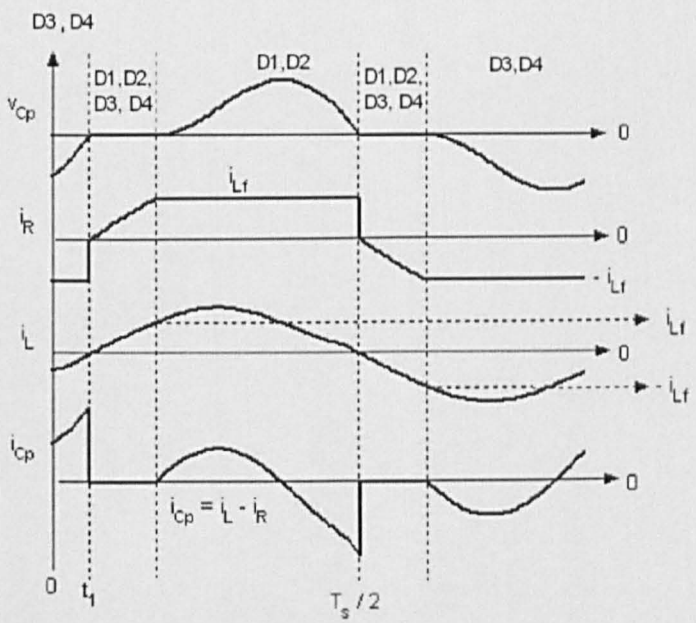

(b)

Figure 2.8 Current-output resonant converter discontinuous conduction mode operation at heavy load (a) simplified circuit (b) Resonant tank waveforms.

Figure 2.8(b) shows typical waveforms of the resonant tank inductor current, i_L, parallel resonant capacitor voltage, v_{Cp}, parallel capacitor current, i_{Cp}, and rectifier diode current, i_R, during discontinuous conduction operation. During the interval $0 \le t \le t_1$, the parallel resonant capacitor voltage, v_{Cp}, is negative, hence, rectifier diodes D3 and D4 conduct. At the end of this period, v_{Cp} increases toward zero and the capacitor current, i_{Cp}, is positive and rises to $i_{Cp} = i_L + i_{Lf}$. At $t = t_1$, the capacitor voltage v_{Cp} approaches zero, and D_3 and D_4 are reversed biased, and D1 and D2 begin conducting. The capacitor current is now given by $i_{Cp} = i_L - i_{Lf}$.

However, during heavy loading, the resonant tank inductor current is less than the output-filter current i_{Lf}, implying that the capacitor voltage should decrease after the diodes commutate. However, since diode commutation does not occur until v_{Cp} becomes positive, the residual current from the output filter/load, i_{Lf}, must circulate through the rectifier until i_L rises to the level of i_{Lf}; therefore, the rectifier input current at this stage is $i_R = i_L$. Whilst the difference between i_L and i_{Lf} is essentially the current that flows into parallel capacitor C_p, according to (2-3), in fact, no current actually flows into C_p during this interval. A new state of discontinuous conduction occurs in which all four rectifier diodes D1 to D4 are forward biased.

Since this mode is only active when current circulates through the bridge rectifier, at the beginning of a period where $|i_R| = i_L$, it complicates the state variable model, making it necessary to switch between two modes of operation, namely:

i) Normal conduction: $|v_{Cp}| > 0$ and $|i_R| = i_{Lf}$, hence the rectifier operates as a normal.

ii) Discontinuous conduction mode (DCM): $|v_{Cp}| = 0$ and $|i_R| < i_{Lf}$, hence the rectifier and output filter are essentially decoupled from the resonant tank circuit.

To produce an accurate result, the natural commutation between the two modes needs to occur at times that are precisely determined. The DCM is entered as the capacitor voltage v_{Cp} reaches 0V, which, in turn, only happens when $|i_L| < i_{Lf}$. During this mode, voltage v_{Cp} will always equal 0V, and the boundary time for when normal conduction resumes, is taken as the instant when the condition $|i_R| = i_{Lf}$ is reached.

The previously derived coupling equation model therefore has to be modified, and augmented with an additional SR flip-flop, as shown in Fig. 2.9, to ensure that the rectifier commutates correctly and to force v_{cp} to zero during clamping.

$$v_{Cp} = 0 \rightarrow i_R = \begin{cases} i_{Lf}\,\mathrm{sgn}(v_{Cp}) & \text{for} \quad |i_L| \geq i_{Lf} \\ i_L & \text{for} \quad |i_L| < i_{Lf} \end{cases} \tag{2-6}$$

Figure 2.10 shows waveforms obtained from the modified state-variable model, simulated to steady-state, after incorporating the refined coupling equation relating the fast- and slow-subsystems. The converter (see Table 1) is simulated with R_L=0.5 Ω and 0.1Ω to provide heavy-loading and near short-circuit operating conditions, respectively.

From Fig. 2.10(b) to (d), the occurrence of discontinuous conduction mode is apparent at all frequencies, slightly above resonant frequency, or at very high switching frequencies away from resonance under very heavy loading. A comparison of output voltage from the proposed model, and results obtained from SPICE simulations when subjected to the two heavy load conditions, is shown in Fig. 2.11. Again, a good correlation between SPICE and the state variable model is clearly evident.

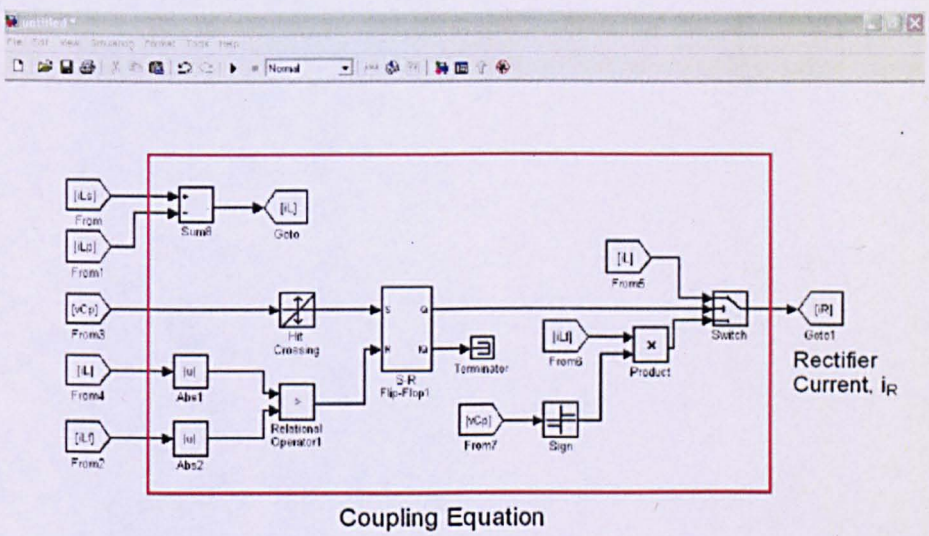

Figure 2.9 Augmented coupling equation including SR flip-flop.

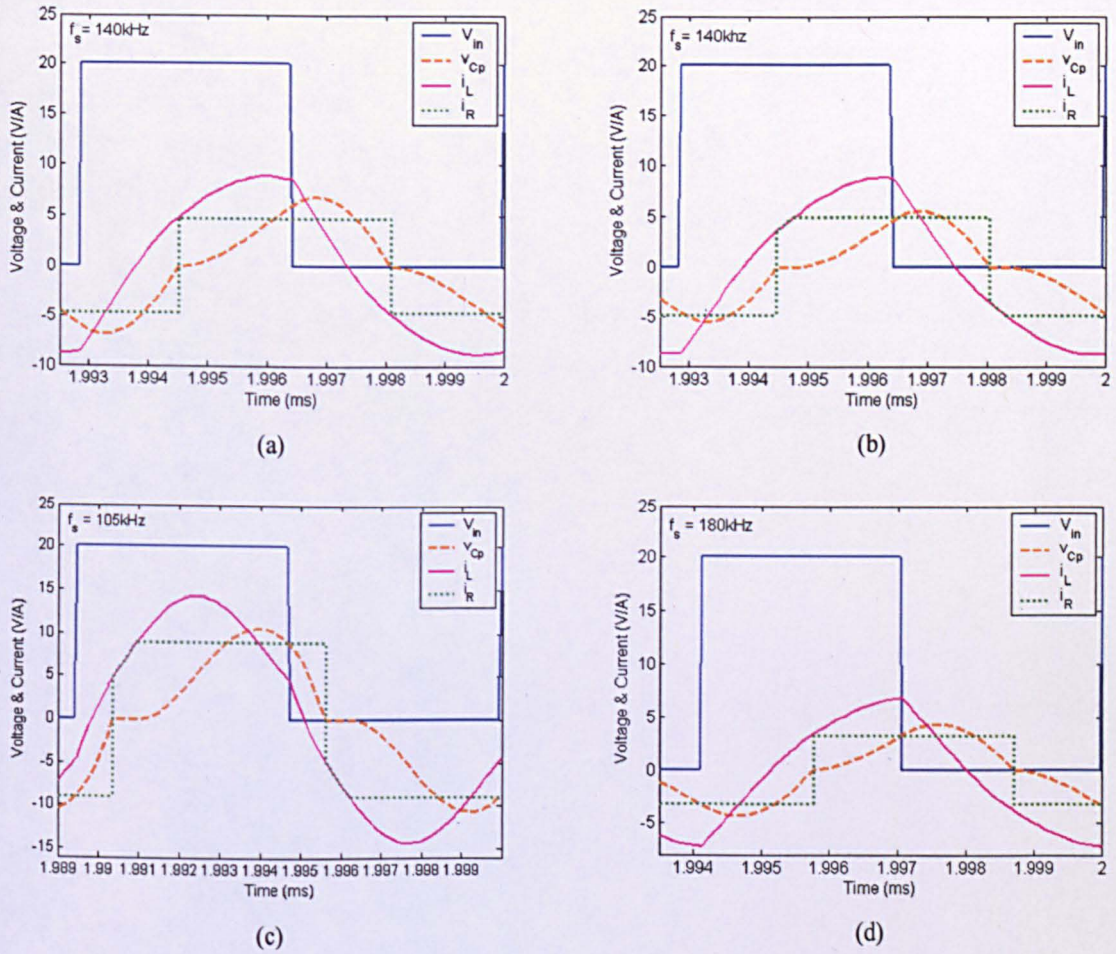

Figure 2.10 Voltage and current waveforms of a current-output converter at (a) heavy load (R_L=0.5Ω) at 140 kHz, (b) near short-circuit condition (R_L=0.1Ω) at 140 kHz, (c) R_L=0.1Ω at 105 kHz, and (d) R_L=0.1Ω at 180 kHz.

Figure 2.12 shows the maximum current through L_s obtained during steady-state operation. An observation from Fig. 2.12 is that the power switches are exposed to progressively lower current stresses as the loading changes from light load R_L=2.5Ω to moderate load R_L=0.5Ω conditions. If the resonant converter is heavily loaded, the tank sees a near short-circuit at the output, and the resonant components essentially only consists of the series inductor L_s and series capacitor C_s.

The maximum current stresses seen by the power devices when approaching resonance under these conditions can be greater than that seen in cases of lighter loadings, namely R_L = 0.5 or 2.5Ω. However, since the operating frequency is far away from the series resonant frequency, the peak current is limited by the reactive impedance of the tank.

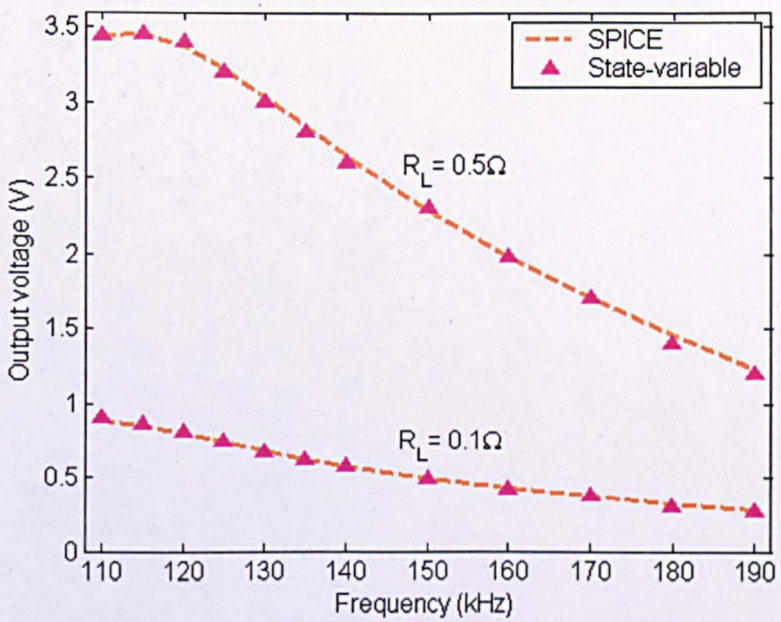

Figure 2.11 Comparison of output voltage as a function of switching frequency from the state-variable model and SPICE.

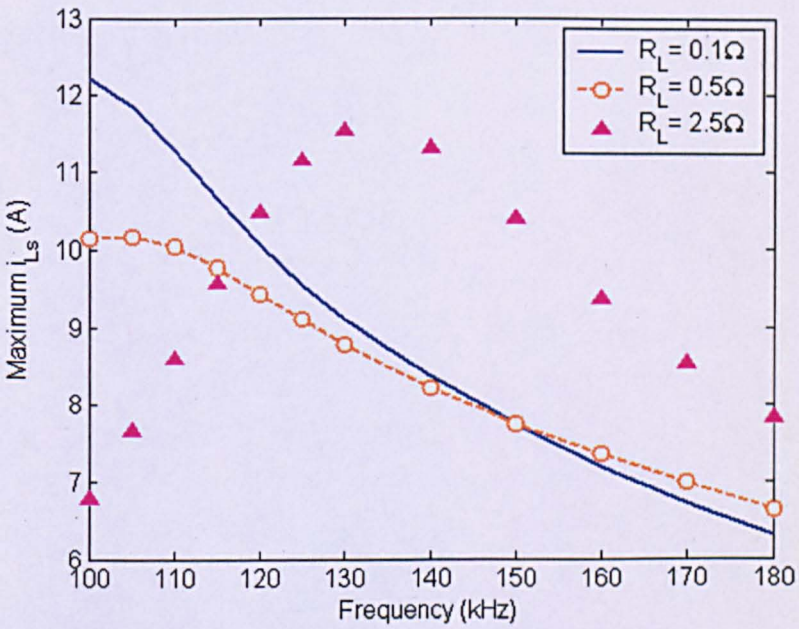

Figure 2.12 Simulated maximum input current of the converter.

2.2. State-Variable Modelling of the Voltage-Output Converter

A similar approach for the voltage-output 4th-order resonant converter, is now proposed, through which, a converter model is derived using simple analytical techniques. The result is a non-linear model that can be readily used by analytical tools, such as MATLAB, for the purpose of analysis and simulation. Omitting the output filter inductor, L_f, however significantly complicates the model of the converter, Fig. 2.13(a), since, for a specific time interval within the switching cycle, the rectifier current ceases conduction and the resonant network is effectively decoupled from the output. Nevertheless, the converter can be analysed using a similar procedure to that presented previously, by partitioning into fast- and slow- subsystems (see Fig. 2.13(b)), and determining coupling equations to describe their dynamic interaction.

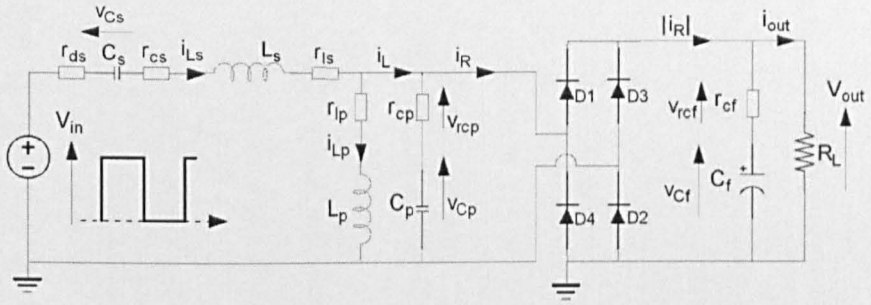

(a)

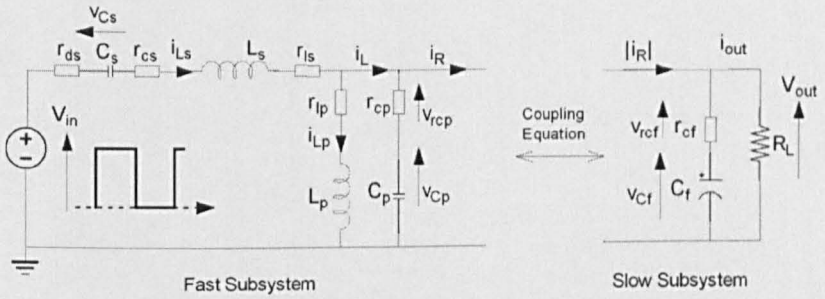

(b)

Figure 2.13 4th-order voltage-output resonant converter (a) Simplified circuit (b) Fast and slow subsystems.

The fast sub-system described the dynamics of the resonant tank and power switches is described by:

$$\frac{dv_{Cp}}{dt} = \frac{i_{Ls} - i_{Lp} - i_R}{C_p} \qquad \frac{dv_{Cs}}{dt} = \frac{i_{Ls}}{C_s}$$

$$\frac{di_{Lp}}{dt} = \frac{v_{Cp}}{L_p} \tag{2-7}$$

$$\frac{di_{Ls}}{dt} = \frac{V_{in} - v_{Cs} - v_{Cp} - i_{Ls}(r_{ds} + r_{cp} + r_{cs} + r_{ls}) + r_{cp} i_{Lp} + r_{cp} i_R}{L_s}$$

As discussed, during periods of discontinuous conduction, when the output filter is dynamically decoupled from the resonant tank circuit [B3], the voltage across the output filter capacitor is given by,

$$\frac{dv_{Cf}}{dt} = \frac{R_L}{C_f(R_L + r_{cf})}|i_R| - \frac{v_{Cf}}{C_f(R_L + r_{cf})} \tag{2-8}$$

and, by assuming that the current which flows into the parallel resonant capacitor, C_p, is small compared to that which flows through L_s and L_p, the voltage at the rectifier is dependent on the direction of the link-current flowing from the resonant tank circuit ($i_L = i_{Ls} - i_{Lp}$). The relevant coupling term is, therefore, obtained by equating voltages at either side of the rectifier, i.e.:

$$v_{Cp} + v_{rcp} = \text{sgn}(i_L)(V_{out} + 2v_{diode}) = \text{sgn}(i_L)(v_{Cf} + v_{rcf} + 2v_{diode}) \tag{2-9}$$

Neglecting parasitic resistances, and assuming a constant rectifier-diode voltage, the derivative of (2-9) simplifies to:

$$\frac{dv_{Cp}}{dt} = \text{sgn}(i_L)\left(\frac{dv_{Cf}}{dt}\right) \tag{2-10}$$

Finally, the rectifier current, i_R, is found by substituting (2-7) and (2-8) into (2-10),

$$i_R = \frac{C_f}{\text{sgn}(i_L)C_p + C_f} i_L + \text{sgn}(i_L)\frac{C_p}{\text{sgn}(i_L)C_p + C_f}\frac{v_{Cf}}{R_L} \tag{2-11}$$

This leads to the coupling equation;

$$i_R = \begin{cases} \dfrac{C_f}{\text{sgn}(i_L)C_p + C_f} i_L + \text{sgn}(i_L)\dfrac{C_p}{\text{sgn}(i_L)C_p + C_f}\dfrac{v_{Cf}}{R_L} & \text{for } |v_{Cp}| \geq V_{out} + 2v_{diode} \\ 0 & \text{for } |v_{Cp}| < V_{out} + 2v_{diode} \end{cases} \tag{2-12}$$

The state-variable model for voltage-output converter is therefore given by,

$$\begin{bmatrix} \dot{v}_{Cp} \\ \dot{v}_{Cs} \\ \dot{i}_{Lp} \\ \dot{i}_{Ls} \\ \dot{v}_{Cf} \end{bmatrix} = \begin{bmatrix} 0 & 0 & -\frac{1}{C_p} & \frac{1}{C_p} & 0 \\ 0 & 0 & 0 & \frac{1}{C_s} & 0 \\ \frac{1}{L_p} & 0 & 0 & 0 & 0 \\ -\frac{1}{L_s} & -\frac{1}{L_s} & \frac{r_{cp}}{L_s} & -\frac{r_{ds} + r_{cp} + r_{cs} + r_{ls}}{L_s} & 0 \\ 0 & 0 & 0 & 0 & -\frac{1}{C_f(R_L + r_{cf})} \end{bmatrix} \begin{bmatrix} v_{Cp} \\ v_{Cs} \\ i_{Lp} \\ i_{Ls} \\ v_{Cf} \end{bmatrix} + \begin{bmatrix} -\frac{i_R}{C_p} \\ 0 \\ 0 \\ \frac{V_{in}}{L_s} + \frac{r_{cp} i_R}{L_s} \\ \frac{|i_R| R_L}{C_f(R_L + r_{cf})} \end{bmatrix} \tag{2-13}$$

To demonstrate the accuracy of the proposed model, a prototype 4th-order LCLC voltage-output converter (see Fig. 2.14) has been commissioned with the component parameters given in Table 2.2. Figure 2.15 shows a screenshot of a Simulink model implementing the state-equations, driven by an equivalent square wave voltage source V_{in}. The 'zero-crossing' function and 'S-R flip-flop' blocks are included to ensure correct commutation of the rectifier current when i_R falls to zero (2-12) and to force $v_{Cp} = V_{out} + 2V_{diode}$ during the clamping period.

Table 2.2 Voltage-output converter model parameters.

Parameters	Values
DC link input voltage, v_{DC} (V)	30
Series resonant inductance, L_s (μH)	12.6
Series resonant capacitance, C_s (μF)	0.737
Parallel resonant inductance, L_p (μH)	25
Parallel resonant capacitance, C_p (μF)	0.141
Output filter capacitance, C_f (μF)	100
Output load Resistance, R_L (Ω)	5, 10
Nominal angular resonant frequency, ω_o (rads^{-1})	$2\pi \times 90 \times 10^3$

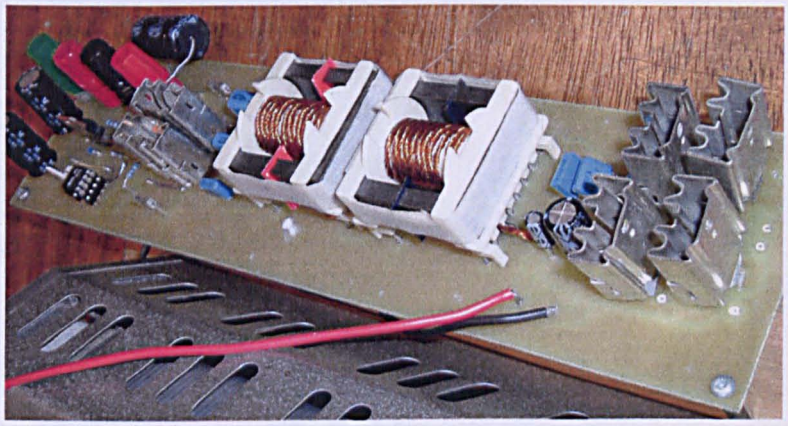

Figure 2.14 Experimental setup for voltage-output 4th-order resonant converter.

Figure 2.16 shows example steady-state waveforms from the state-variable model for two load conditions. For completeness, Fig. 2.17 also provides a comparison of measurements of output voltage from the experimental converter, with those predicted from the proposed state-variable model (including the 'equivalent' series and parallel resonant inductances) and SPICE simulations, for various-operating frequencies. Again, the level of agreement is seen to be excellent.

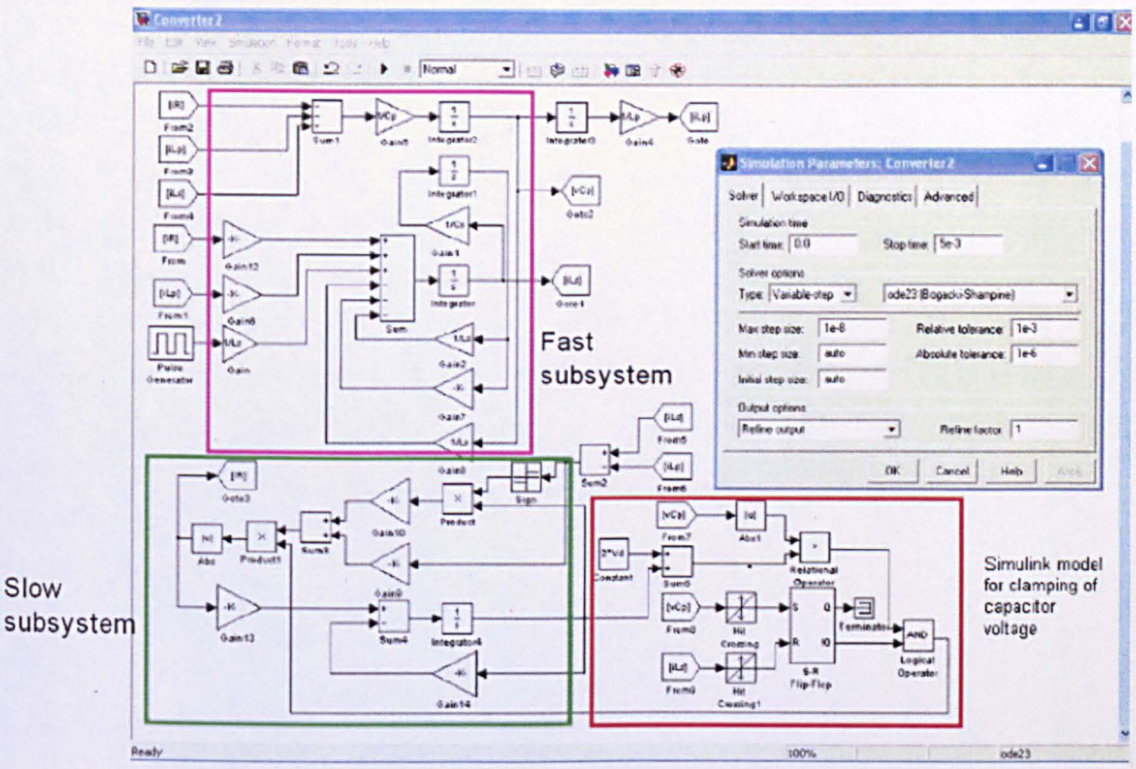

Figure 2.15 SIMULINK model of a 4th-order voltage-output resonant converter.

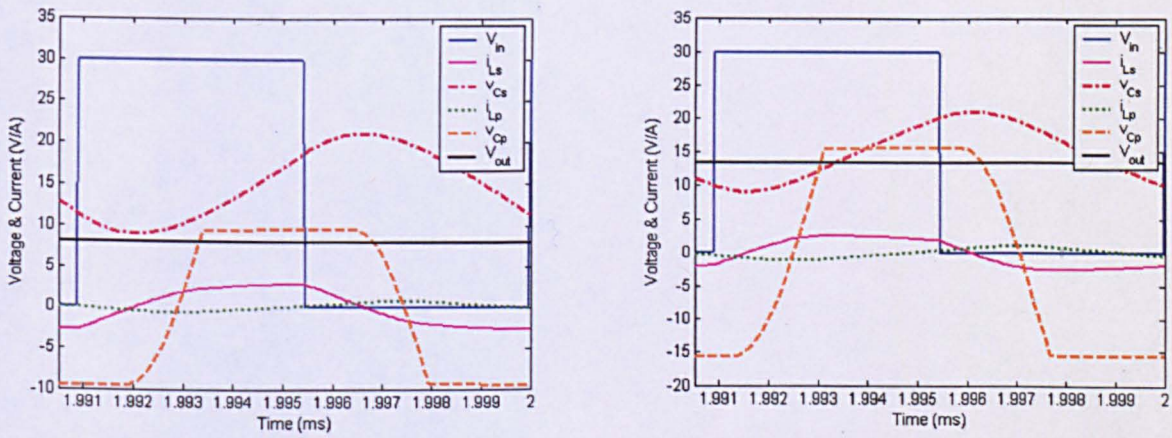

(a) (b)

Figure 2.16 Simulated waveforms of a voltage-output resonant converter operating at 110 kHz: (a) R_L=5Ω and (b) R_L=10Ω.

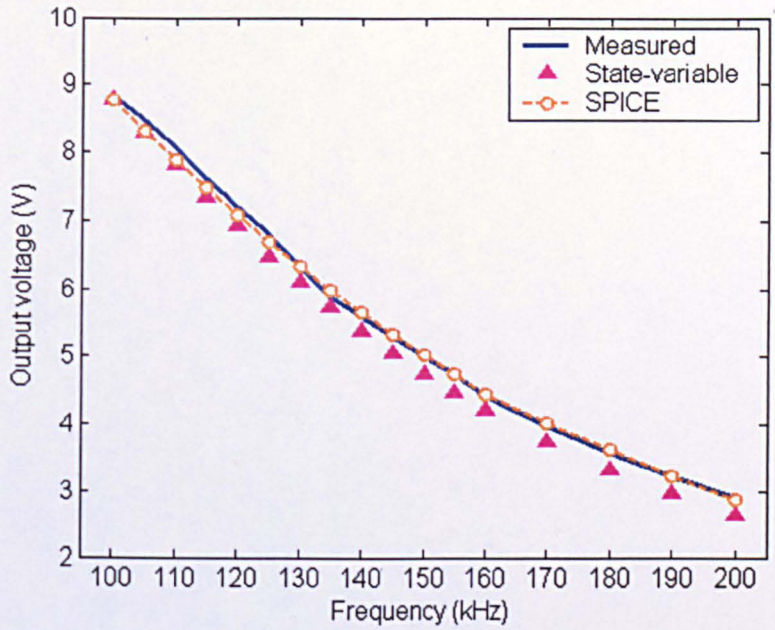

(a)

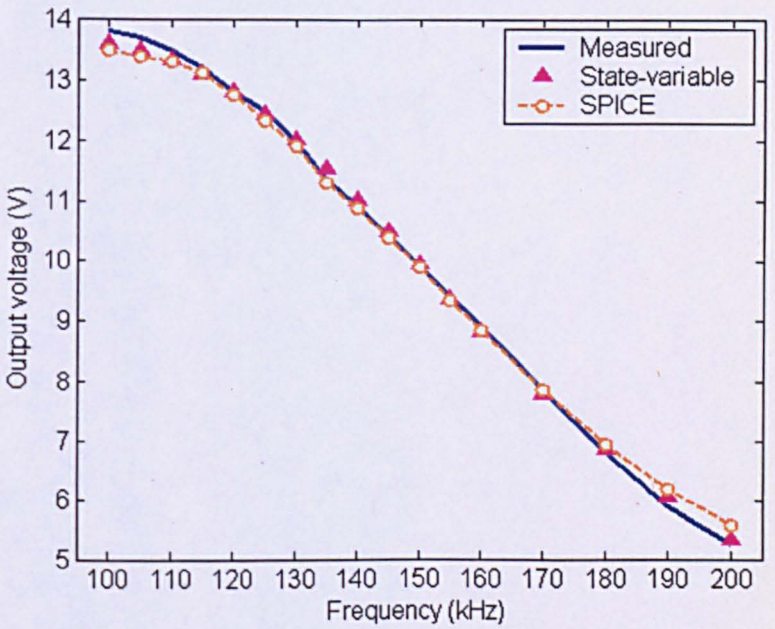

(b)

Figure 2.17 Comparison of output voltage of the prototype converter from the state-variable model and SPICE simulations: (a) R_L=5Ω; (b) R_L=10Ω.

2.3. Summary

State-variable models of current- and voltage-output variants of 4th-order LCLC resonant converter, have been derived, with derivation details for dynamically modelling the rectifier and output filter under heavy load conditions, being given. Prototype converters have been commissioned to investigate the accuracy of the resulting models, which are proven to be commensurate with results from SPICE models, whilst requiring lower execution times. Specifically, for the results presented, the state variable models typically take 1/10th of the time to simulate to steady state, compared to equivalent SPICE models. The resulting models form the basis of investigations presented in Chapters 4 and 7, where cyclic averaging is developed as a means of rapidly obtaining steady-state analysis solutions for the converters variants.

References

[B1] B. Baha, "Modelling of resonant switched-mode converters using SIMULINK", *IEE Proc. Electric Power Application*, **145**, pp. 159-163, 1998.

[B2] L. K. Wong, F. H. Leung and P. K. S. Tam, "A Simple Large-Signal Non-linear Modelling Approach for Fast Simulation of Zero-Current-Switch Quasi-Resonant Converters", *IEEE Trans. on Power Electronics*, **12**, pp.437-442, 1997.

[B3] Y. Ang, M. P. Foster, C. M. Bingham, D. A. Stone, H. I. Sewell and D. Howe, "Analysis of 4th-order LCLC Resonant Power Converters", *IEE Proc. Electric Power Applications*, **151**, pp. 169-181, 2004.

[B4] N. Mohan, T. M. Undeland and W. P. Robbins (3rd Ed.), *Power Electronics*, USA: John Wiley and Son, 2003.

CHAPTER 3

Frequency Domain Modelling of LCLC Current-Output Resonant Converters

Frequency domain analysis techniques, and variants thereof, are often preferred tools when the protracted simulation times associated with traditional circuit simulators are considered too lengthy. When designing a resonant converter with a high-load quality factor (Q), higher harmonics of the input can be considered to be sufficiently filtered so they present a negligible contribution to the output, thereby allowing equivalent sinusoidal voltage and current sources to appear at the input to the tank, and permit the use of Fundamental Mode Approximation (FMA) to be employed to predict the steady-state behaviour of the converter. Based on FMA, an input-output transfer function is derived that enables classical ac-analysis to be applied to analyse the frequency response of the converter. Predictions of output voltage and, importantly, estimates of voltage and current stresses on resonant components, are also shown to be readily obtainable.

Key features of this chapter are the derivation of frequency domain analysis techniques that rely on ratios of primary reactive components, rather than specific parameter values, and an analysis of previously unreported regions of LCLC resonant converter operation that is shown to provide multi-resonant behaviour.

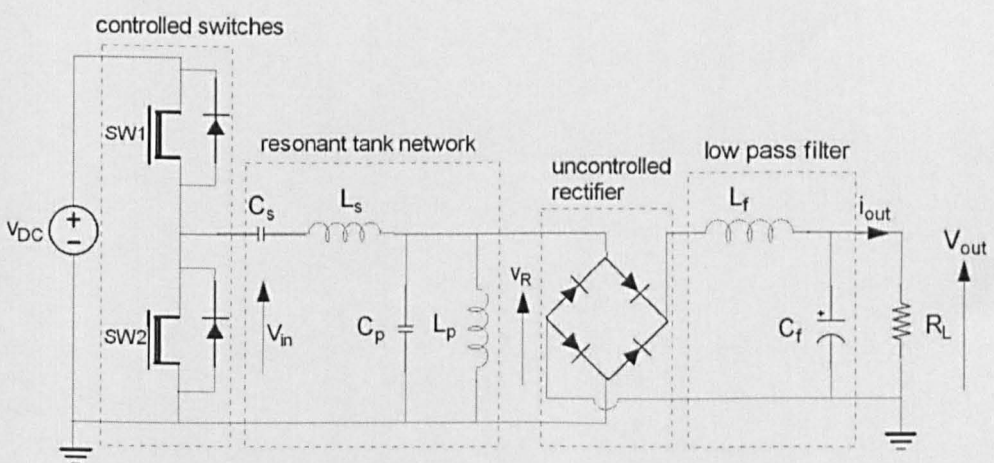

Figure 3.1 4th-order LCLC current-output resonant converter.

3.1. Effective Resonant Frequency of LCLC Resonant Circuit

The resonant frequency of the parallel resonance network L_p-C_p, ($\omega_{op2} = \sqrt{1/L_p C_p}$), is designed to be below the effective resonant frequency of the overall circuit. During nominal operation above, ω_{op2}, therefore, the capacitor reactance, X_{Cp}, is greater than the inductor reactance, X_{Lp}, and the parallel branch components appear capacitive, as shown in Fig. 3.2(a).

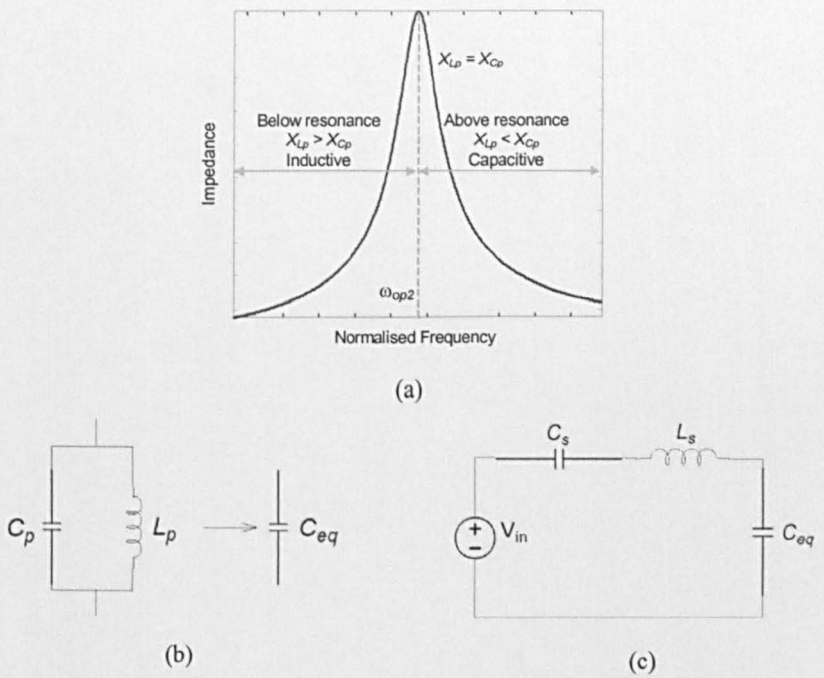

Figure 3.2 Parallel combination of C_p and L_p: (a) Impedance curve of parallel LC network; (b) Equivalent frequency dependant capacitance, C_{eq} and (c) Resulting equivalent 3rd-order resonant circuit.

To calculate the effective resonant frequency of the complete tank, the combined action of the parallel inductor and capacitor can be modelled as an equivalent frequency-dependant capacitance, C_{eq}, as shown in Fig. 3.2(b), with a value given by:

$$C_{eq} = \frac{\omega^2 C_p L_p - 1}{\omega^2 L_p} \tag{3-1}$$

The undamped effective resonant frequency of the resulting equivalent 3rd-order network (see Fig. 3.2(c)) is then given by [C1, C2]:

$$\omega_o = \sqrt{\frac{C_s + C_{eq}}{L_s C_s C_{eq}}} \tag{3-2}$$

Substituting for equivalent parallel branch capacitance, C_{eq} yields:

$$\omega_o = \sqrt{C_s + \frac{(\omega_o{}^2 C_p L_p - 1)}{\omega_o{}^2 L_p} \times \frac{\omega_o{}^2 L_p}{L_s C_s (\omega_o{}^2 C_p L_p - 1)}} \tag{3-3}$$

By rearranging (3-3), the undamped resonant frequency of the tank, ω_o, is obtained from the solution of (3-4),

$$(C_s L_s C_p L_p)\omega_o{}^4 - (C_s L_s + C_s L_p + C_p L_p)\omega_o{}^2 + 1 = 0 \tag{3-4}$$

giving:

$$\omega_o = \left[\frac{C_s L_s + C_s L_p + C_p L_p + \sqrt{(C_s L_s + C_s L_p + C_p L_p)^2 - 4 C_s L_s C_p L_p}}{2 C_s L_s C_p L_p} \right]^{\frac{1}{2}} \tag{3-5}$$

Consideration of the tank shows that the load quality factor of the series resonant components, Q_{op1}, and angular resonant frequencies of the series (ω_{op1}) and parallel (ω_{op2}) resonant tank components, are given, respectively, by (note: C_p, and L_p are normally the inter-winding capacitance and magnetizing inductance of an isolation transformer, by design):

$$\begin{aligned} Q_{op1} &= \frac{R_{eq}}{\omega_{op1} L_s} = \omega_{op1} C_s R_{eq} \\ \omega_{op1} &= \frac{1}{\sqrt{L_s C_s}} \\ \omega_{op2} &= \frac{1}{\sqrt{L_p C_p}} \end{aligned} \tag{3-6}$$

where R_{eq} is given by the output load resistance of the equivalent circuit. For design purposes, it is convenient to re-express (3-3) in terms of the ratio of resonant tank capacitances, $C_n = C_p / C_s$ and the ratio of resonant tank inductances $L_n = L_s / L_p$, as follows:

$$\omega_o{}^2 = \frac{\frac{\omega_o{}^2 C_s L_s}{L_n} + \frac{\omega_o{}^2 C_s L_s C_n}{L_n} - 1}{C_s L_s \left(\frac{\omega_o{}^2 C_s L_s C_n}{L_n} - 1 \right)} \tag{3-7}$$

which, after rearrangement, can be solved for ω_o from:

$$\frac{C_n \omega_o{}^4}{L_n} \left(\frac{1}{\omega_{op1}} \right)^4 - \omega_o{}^2 \left(1 + \frac{1}{L_n} + \frac{C_n}{L_n} \right) \left(\frac{1}{\omega_{op1}} \right)^2 + 1 = 0 \tag{3-8}$$

The significance of (3-8) is that it provides a means of calculating the resonant frequency of the series resonant tank components, ω_{op1}, as a function of effective resonant frequency ω_o, i.e.

$$\omega_{op1} = \left[\frac{\omega_o^2 \left(1 + \frac{1}{L_n} + \frac{C_n}{L_n}\right)}{2\left(\frac{C_n}{L_n}\right)\omega_o^4} + \sqrt{\frac{\omega_o^4 \left(1 + \frac{1}{L_n} + \frac{C_n}{L_n}\right)^2 - 4\left(\frac{C_n}{L_n}\right)\omega_o^4}{4\left(\frac{C_n}{L_n}\right)^2 \omega_o^8}} \right]^{-\frac{1}{2}} \tag{3-9}$$

Moreover, design values for L_s and C_s can be obtained from the ratio of ω_o and ω_{op1}. In particular, re-arranging (3-9) provides,

$$\left(\frac{\omega_o}{\omega_{op1}}\right)^2 = \frac{L_n}{2C_n} \times \left(1 + \frac{1}{L_n} + \frac{C_n}{L_n} + \sqrt{\left(1 + \frac{1}{L_n} + \frac{C_n}{L_n}\right)^2 - \frac{4C_n}{L_n}}\right) \tag{3-10}$$

The solution of (3-10) also shows that two resonant frequencies are present, thereby demonstrating that the converter essentially constitutes a multi-resonant system. The second effective resonant frequency, ω_o' can be solved from (3-10),

$$\left(\frac{\omega_o'}{\omega_{op1}}\right)^2 = \frac{\left(1 + \frac{1}{L_n} + \frac{C_n}{L_n}\right) - \sqrt{\left(1 + \frac{1}{L_n} + \frac{C_n}{L_n}\right)^2 - \frac{4C_n}{L_n}}}{\frac{2C_n}{L_n}} \tag{3-11}$$

Simplifying (3-10) and (3-11), the load resonant angular frequencies ω_o and ω_o' can be given in terms of resonant component ratios and series tank resonant frequency:

$$\omega_o = \omega_{op1} \sqrt{\frac{1 + L_n + C_n + \sqrt{(1 + L_n + C_n)^2 - 4L_nC_n}}{2C_n}} \tag{3-12}$$

$$\omega_o' = \omega_{op1} \sqrt{\frac{1 + L_n + C_n - \sqrt{(1 + L_n + C_n)^2 - 4L_nC_n}}{2C_n}} \tag{3-13}$$

with their ratio being given by,

$$\omega_r = \frac{\omega_o}{\omega_o'} = \sqrt{\frac{1 + L_n + C_n + \sqrt{(1 + L_n + C_n)^2 - 4L_nC_n}}{1 + L_n + C_n - \sqrt{(1 + L_n + C_n)^2 - 4L_nC_n}}} \tag{3-14}$$

Now, the characteristic resonant impedance of the un-damped resonant circuit, in Fig. 3.2(c), is defined as,

$$Z_o = \omega_o L_s \qquad (\Omega) \qquad (3\text{-}15)$$

thereafter, from (3-5), Z_o can be rewritten as,

$$Z_o = \frac{\omega_o}{\omega_{opl}} \times \frac{R_{eq}}{Q_{opl}} = \frac{R_{eq}}{Q_o} \qquad (\Omega) \qquad (3\text{-}16)$$

where Q_o is the load quality factor at the effective angular resonant frequency, ω_o.

At resonance, the input impedance of the tank, as seen from the perspective of the power switches, approaches zero, thereby forming the boundary between capacitive and inductive loading. From basic circuit analysis, the input impedence, Z_{in}, is given by:

$$\begin{aligned} Z_{in} &= \frac{s^4 L_s C_s L_p C_p R_{eq} + s^3 L_s C_s L_p + s^2 R_{eq}\left(L_s C_s + C_p L_p + C_s L_p\right) + sL_p + R_{eq}}{s^3 C_s C_p L_p R_{eq} + s^2 C_s L_p + sC_s R_{eq}} \\ &= \frac{\dfrac{s^4 C_n C_s{}^2 L_s{}^2 R_{eq}}{L_n} + \dfrac{s^3 C_s L_s{}^2}{L_n} + s^2 C_s L_s R_{eq}\left(1 + \dfrac{1}{L_n} + \dfrac{C_n}{L_n}\right) + \dfrac{sL_s}{L_n} + R_{eq}}{\dfrac{s^3 C_n C_s{}^2 L_s R_{eq}}{L_n} + \dfrac{s^2 C_s L_s}{L_n} + sC_s R_{eq}} = |Z_{in}| e^{j\beta_{in}} \end{aligned} \qquad (3\text{-}17)$$

where $s \rightarrow j\omega_s$. By recalling $\omega_{opl} = 1/\sqrt{L_s C_s}$ in (3-5), the input impedance Z_{in} can be rewritten as:

$$Z_{in} = Z_o Q_o \times \sqrt{\frac{\left[\dfrac{\omega_s{}^4 C_n}{\omega_{opl}{}^4 L_n} - \dfrac{\omega_s{}^2}{\omega_{opl}{}^2}\left(1 + \dfrac{1}{L_n} + \dfrac{C_n}{L_n}\right) + 1\right]^2 + \left[\dfrac{\omega_s L_s}{R_{eq} L_n}\left(1 - \dfrac{\omega_s{}^2}{\omega_{opl}{}^2}\right)\right]^2}{\dfrac{\omega_s{}^4}{\omega_{opl}{}^4 L_n{}^4} + \left[\omega_s C_s R_{eq}\left(1 - \dfrac{\omega_s{}^2 C_n}{\omega_{opl}{}^2 L_n}\right)\right]^2}} \qquad (3\text{-}18)$$

Finally, from (3-5) and (3-17), (3-18) can be re-arranged to give:

$$Z_{in} = Z_o Q_o \times \sqrt{\frac{\left[\left(\dfrac{\omega_o}{\omega_{opl}}\right)^4 \dfrac{C_n}{L_n} - \left(\dfrac{\omega_o}{\omega_{opl}}\right)^2 \left(1 + \dfrac{1}{L_n} + \dfrac{C_n}{L_n}\right) + 1\right]^2 + \left[\dfrac{1}{Q_o L_n}\left(1 - \left(\dfrac{\omega_o}{\omega_{opl}}\right)^2\right)\right]^2}{\left(\dfrac{\omega_o}{\omega_{opl}}\right)^4 \dfrac{1}{L_n{}^2} + \left[Q_o \left(\dfrac{\omega_o}{\omega_{opl}}\right)^2 \left(1 - \left(\dfrac{\omega_o}{\omega_{opl}}\right)^2 \dfrac{C_n}{L_n}\right)\right]^2}} \qquad (3\text{-}19)$$

at the resonant frequency, i.e. as $\omega_s \rightarrow \omega_o$. Consequently, the characteristic impedance, Z_o can be written as a function of Z_{in}, the ratio ω_o/ω_{op1}, component ratios C_n and L_n, and effective load quality factor Q_o, as follows,

$$Z_o = \frac{Z_{in}}{Q_o} \times \sqrt{\frac{\left(\frac{\omega_o}{\omega_{op1}}\right)^4 \frac{C_n}{L_n} - \left(\frac{\omega_o}{\omega_{op1}}\right)^2 \left(1 + \frac{1}{L_n} + \frac{C_n}{L_n}\right) + 1 + \left[\frac{1}{Q_o L_n}\left(1 - \left(\frac{\omega_o}{\omega_{op1}}\right)^2\right)\right]}{\left(\frac{\omega_o}{\omega_{op1}}\right)^4 \frac{1}{L_n^2} + \left[Q_o\left(\frac{\omega_o}{\omega_{op1}}\right)^2\left(1 - \left(\frac{\omega_o}{\omega_{op1}}\right)^2 \frac{C_n}{L_n}\right)\right]^2}} \tag{3-20}$$

and design values for series resonant inductance, L_s can be obtained from (3-14),

$$L_s = \frac{Z_o}{\omega_o} \tag{3-21}$$

and the series resonant capacitance from

$$\begin{aligned} C_s &= \frac{\omega_o^2 L_s}{\omega_{op1}^2 Z_o^2} \\ &= \frac{L_s}{Z_o^2} \times \frac{1 + L_n + C_n + \sqrt{(1 + L_n + C_n)^2 - 4L_n C_n}}{2C_n} \end{aligned} \tag{3-22}$$

Noting that (3-9), (3-19) and (3-20) are solely dependant on the two ratios C_n and L_n, the remaining parallel resonant tank components, C_p and L_p, are subsequently determined from the prior selection of C_n and L_n, viz.

$$L_p = \frac{L_s}{L_n} \tag{3-23}$$

and

$$C_p = C_s \times C_n \tag{3-24}$$

It should be noted, therefore, that whilst four reactive components exist in this converter topology, it is their ratios that are important from a design perspective, using the presented methodology, thereby eliminating the requirement for specific values early in the design procedure.

3.2. Resonant Circuit Analysis in Continuous Conduction Mode ($\omega_s \geq \omega_o$)

This mode, with continuous v_{Cp} and i_{Ls}, occurs when $\omega_s \geq \omega_o$ and under light load conditions. The turn-on losses in the switches are minimised since the switches turn on when i_{Ls} is of reverse polarity. Although this operating mode results in turn-off switching losses, ultimately, it is possible to reduce them by connecting a snubber capacitor in parallel with each power switches [C3].

Here then, continuous conduction operation is analyzed based on a Fundamental Mode transfer function. Circuit waveforms are shown in Fig. 3.3. The frequency content of a periodic signal $f(t)$ is obtained from a Fourier series expansion:

$$f(t) = \frac{a_0}{2} + \sum_{n=1,2,3...}^{\infty} c_n \sin\left(n\omega t + \phi_{v(n)}\right)$$

where

$$\begin{aligned} c_n &= \sqrt{a_n^{\,2} + b_n^{\,2}} \\ a_n &= 2/\mathrm{T}_s \int_o^{\mathrm{T}_s} f(t)\cos(n\omega t)dt \\ b_n &= 2/\mathrm{T}_s \int_o^{\mathrm{T}_s} f(t)\sin(n\omega t)dt \end{aligned} \tag{3-25}$$

The excitation voltage applied to the input of the tank network can be represented in terms of Fourier series components over a single switching cycle, of period $T_s=1/f_s$, where the amplitude and phase of the n-th harmonic is given by;

$$\begin{aligned} v_{i(n)} &= \frac{v_{DC}}{n\pi} \times \sqrt{a_n^{\,2} + b_n^{\,2}} \\ \phi_{vi(n)} &= \tan^{-1}\left(a_n / b_n\right) \end{aligned} \tag{3-26a}$$

where

$$\begin{aligned} a_n &= \sin(2\pi n\mathrm{D}) \\ b_n &= 1 - \cos(2\pi n\mathrm{D}) \end{aligned} \tag{3-26a}$$

and duty ratio D is the turn-on time, t_{on} of the power switches with respect to the switching period, T_s. Using FMA, the power switches and diodes are assumed ideal and the effects of the switches' internal capacitances, is neglected. The fundamental of a half-bridge square wave input excitation voltage (D=0.5) is therefore given by,

$$v_{i(1)} = \frac{2v_{DC}}{\pi} \tag{3-27}$$

A consequence of including an output filter inductor, L_f, is that whilst the voltage appearing at the input to the rectifier, v_R, is predominantly sinusoidal, the current, i_R exhibits a square-wave characteristic, see Fig. 3.3.

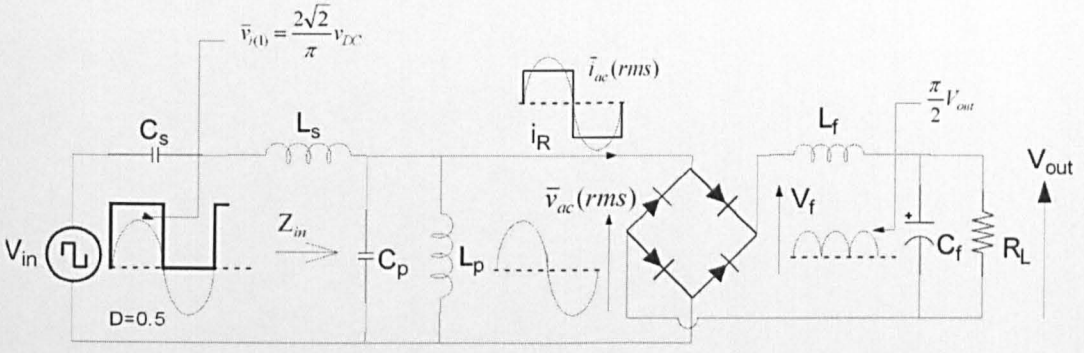

Figure 3.3 Current-output converter with key current and voltage waveforms.

The voltage across the resonant capacitor C_p is rectified, filtered, and then supplied to the load. To develop an equivalent circuit, the fundamental component of the voltage, and square-wave current, at the input of the rectifier, is used to derive an equivalent resistance R_{eq}. By assuming the resonant circuit adequately filters higher harmonics of the input voltage, the load resistance/output filter and rectifier can be modelled as an equivalent resistance (Steigerwald [C1]),

$$R_{eq} = \frac{\bar{v}_{ac(\mathrm{rms})}}{\bar{i}_{ac(\mathrm{rms})}} = \frac{\frac{\pi}{2\sqrt{2}}\left(V_{out} + 2v_{diode}\right)}{\frac{2\sqrt{2}}{\pi} i_{out}} = \frac{\pi^2}{8} R_L + \frac{\pi^2}{8} \frac{2v_{diode}}{i_{out}} \tag{3-28}$$

where $\bar{v}_{ac(\mathrm{rms})}$ and $\bar{i}_{ac(\mathrm{rms})}$ are the RMS voltage and current at the input of the rectifier, respectively.

For simplicity, the rectifier diode voltage, v_{diode}, can be neglected to give $R_{eq} = \frac{\pi^2}{8} R_L$, giving the FMA equivalent circuit shown in Fig. 3.4.

It is informative to obtain the frequency characteristics of the 4th-order resonant circuit of Fig. 3.4. The resonant frequency, ω_o, and characteristic impedance, Z_o, are defined by (3-13) and (3-16). In the presence of an equivalence load resistance, the load quality factor of the parallel resonant tank components are defined using standard notation (3-29):

$$Q_{op2} = \frac{R_{eq}}{\omega_{op2} L_p} = Q_{op1} \sqrt{L_n C_n} \tag{3-29}$$

and resonant frequency of the parallel resonant tank component is given by,

$$\omega_{op2} = \frac{1}{\sqrt{L_p C_p}} = \omega_{op1}\sqrt{\frac{L_n}{C_n}} \tag{3-30}$$

The ac input-to-output voltage relationship is given by the transfer function,

$$\frac{\bar{v}_{\mathrm{Re}}}{\bar{v}_{i(1)}} = \frac{\mathrm{s}^2 C_s L_p R_{eq}}{\mathrm{s}^4 C_s C_p L_s L_p R_{eq} + \mathrm{s}^3 C_s L_s L_p + \mathrm{s}^2 (C_p L_p R_{eq} + C_s L_s R_{eq} + C_s L_p R_{eq}) + \mathrm{s} L_p + R_{eq}}$$

$$= \frac{\dfrac{\mathrm{s}^2 Q_{op2}}{\omega_{op2}} \times \dfrac{C_s}{C_p}}{\dfrac{\mathrm{s}^4 Q_{op2}}{{\omega_{op1}}^2 \omega_{op2}} + \dfrac{\mathrm{s}^3}{{\omega_{op1}}^2} + \mathrm{s}^2\left(\dfrac{Q_{op2}}{\omega_{op2}} + \dfrac{R_{eq}}{{\omega_{op1}}^2 L_p} + \dfrac{Q_{op2}}{\omega_{op2}} \times \dfrac{C_s}{C_p}\right) + \mathrm{s} + \dfrac{R_{eq}}{L_p}}$$

$$= \frac{\dfrac{\mathrm{s}^2 C_n}{{\omega_{op1}}^2 L_n} \times \sqrt{L_n C_n}\, Q_{op1} \times \dfrac{1}{C_n}}{\left(\begin{array}{l} \dfrac{\mathrm{s}^4 C_n}{{\omega_{op1}}^4 L_n} \times \sqrt{L_n C_n}\, Q_{op1} + \dfrac{\mathrm{s}^3}{{\omega_{op1}}^3}\sqrt{\dfrac{C_n}{L_n}} \\ + \mathrm{s}^2\left(\dfrac{\sqrt{L_n C_n}\, Q_{op1} C_n}{{\omega_{op1}}^2 L_n} + \dfrac{\sqrt{L_n C_n}\, Q_{op1}}{{\omega_{op1}}^2} + \dfrac{\sqrt{L_n C_n}\, Q_{op1} C_n}{{\omega_{op1}}^2 L_n} \times \dfrac{1}{C_n}\right) + \dfrac{\mathrm{s}}{\omega_{op1}}\sqrt{\dfrac{C_n}{L_n}} + Q_{op1}\sqrt{L_n C_n} \end{array}\right)} \tag{3-31}$$

where $\mathrm{s} \rightarrow j\omega_s$.

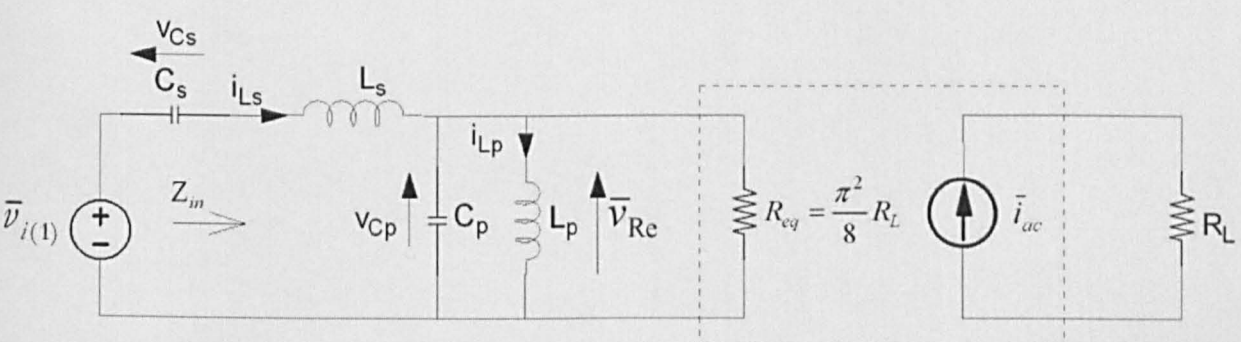

Figure 3.4 Equivalent circuit of the current-output resonant converter.

By deriving the describing function of the square-wave input voltage, V_{in}, and the output voltage, V_{out}, the input-to-output voltage transfer function, M_{vcr}, may be written as a function of the angular switching frequency, and the definitions given in (3-29),

$$M_{vcr} = \frac{V_{out}}{v_{DC}} = \frac{8}{\pi^2}\frac{\bar{v}_{\mathrm{Re}}}{\bar{v}_{i(1)}} = \frac{8}{\pi^2} \times \frac{\dfrac{s^2}{\omega_{op1}{}^2}\sqrt{\dfrac{C_n}{L_n}}Q_{op1}}{\left(\dfrac{s^4}{\omega_{op1}{}^4}\dfrac{C_n{}^{1.5}Q_{op1}}{\sqrt{L_n}} + \dfrac{s^3}{\omega_{op1}{}^3}\sqrt{\dfrac{C_n}{L_n}} + \dfrac{s^2}{\omega_{op1}{}^2} \times \sqrt{L_nC_n}\left(Q_{op1} + \dfrac{Q_{op1}}{L_n} + \dfrac{Q_{op1}C_n}{L_n}\right) + \dfrac{s}{\omega_{op1}}\sqrt{\dfrac{C_n}{L_n}} + Q_{op1}\sqrt{L_nC_n}\right)} \tag{3-32}$$

where the rms value for the resonant tank input and output voltage are,

$$\bar{v}_{\mathrm{Re}} = \frac{\pi}{2\sqrt{2}}V_{out}$$
$$\bar{v}_{i(1)} = \frac{2\sqrt{2}}{\pi}v_{DC} \tag{3-33}$$

Substituting (3-10) into (3-32) and introducing a design variable λ_r to represent the ratio of the effective resonant frequency, and the series resonant frequency, the input-to-output voltage transfer function for the current output resonant converter, can be rewritten as follows,

$$M_{vcr} = \frac{V_{out}}{v_{DC}} = \frac{8}{\pi^2} \times \frac{\dfrac{s^2}{\omega_o{}^2} \times \dfrac{\lambda_T{}^2\sqrt{C_n}Q_{op1}}{\sqrt{L_n}}}{\left[\dfrac{s^4}{\omega_o{}^4}\lambda_T{}^4\dfrac{C_n{}^{1.5}Q_{op1}}{\sqrt{L_n}} + \dfrac{s^3}{\omega_o{}^3}\lambda_T{}^3\sqrt{\dfrac{C_n}{L_n}} + \dfrac{s^2}{\omega_o{}^2}\lambda_T{}^2\sqrt{L_nC_n}\left(Q_{op1} + \dfrac{Q_{op1}}{L_n} + \dfrac{Q_{op1}C_n}{L_n}\right) + \dfrac{s}{\omega_o}\lambda_T\sqrt{\dfrac{C_n}{L_n}} + Q_{op1}\sqrt{L_nC_n}\right]} \tag{3-34}$$

where, from (3-10),

$$\lambda_T = \frac{\omega_o}{\omega_{op1}} = \sqrt{\frac{1 + \dfrac{1}{L_n} + \dfrac{C_n}{L_n} + \sqrt{\left(1 + \dfrac{1}{L_n} + \dfrac{C_n}{L_n}\right)^2 - \dfrac{4C_n}{L_n}}}{\dfrac{2C_n}{L_n}}}$$

It can be seen from (3-34) that the input-output characteristic is highly dependant on the choice of C_n, L_n, and Q_{op1}.

Table 3.1 Specification of a current-output converter.

Parameter	Value
Effective tank resonant frequency, f_o (kHz)	130
Effective resonant tank load quality factor, Q_o	2, 4, 6
Resonant capacitance ratio, C_n	0.5, 1, 2
Resonant inductance ratio, L_n	0, 0.5, 1

Figure 3.5 shows the input-to-output voltage conversion ratio obtained from SPICE simulations, with those predicted from (3-34), for a converter with the specifications given in Table 3.1. Each characteristic is for a different value of effective load quality factor, defined by $Q_o = Q_{op1}/\lambda_r$, giving another key design consideration for the converter.

The 4th-order resonant converter can provide step up, as well as a step down capability. However, it can be seen that the maximum gain V_{out}/V_{in} (Note: $V_{in}= 0.5v_{DC}$) occurs at approximately the same value as the effective quality factor, at resonance, if L_n and C_n are identical. Consequently, the output voltage, at resonance, is load dependent, and can rise to very high values under light- or no-load conditions.

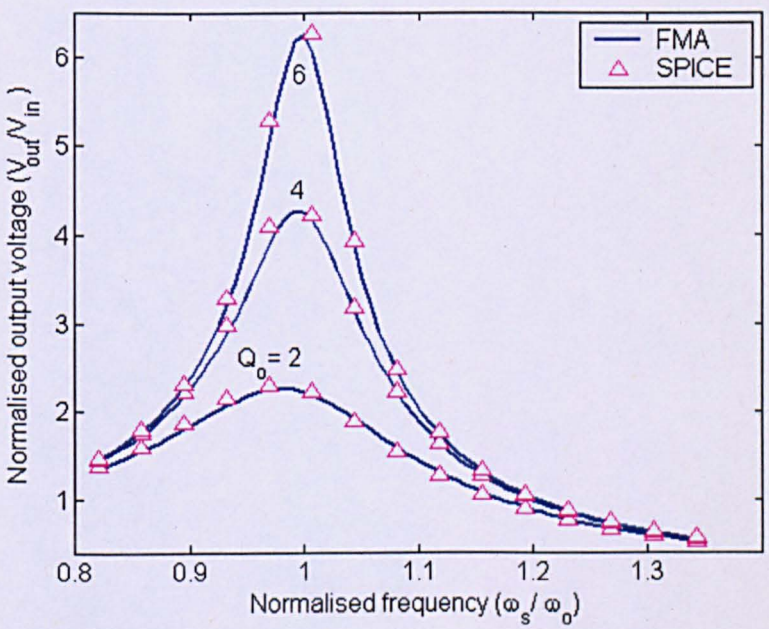

Figure 3.5 Frequency response of the example converter for varies Q_o (C_n= 0.5, L_n= 0.5)

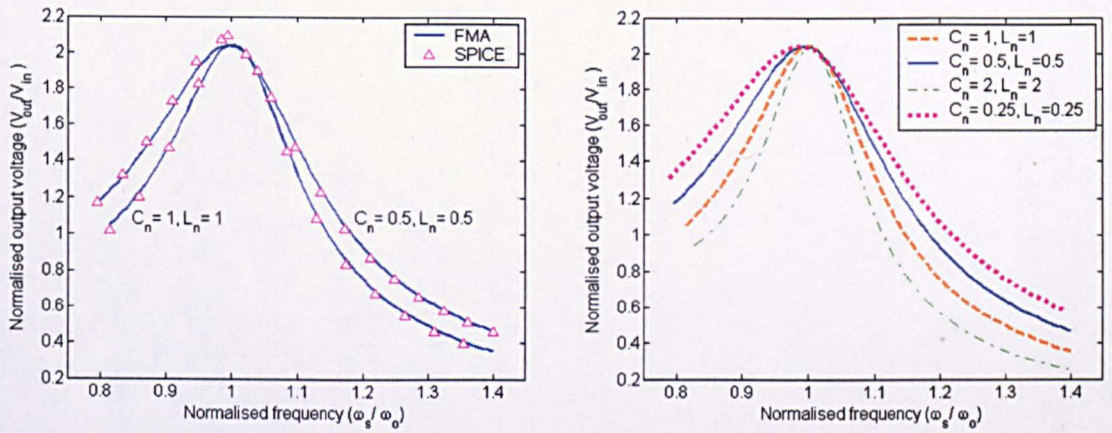

(a) (b)

Figure 3.6 Frequency response of the 4th-order current-output converter when C_n and L_n are varied (Q_o=2): (a) SPICE simulation and (b) FMA.

Figure 3.6 shows the converter's output voltage behaviour as a result of different component ratios, with the output load quality factor remaining fixed. If L_n and C_n are increased in the same manner, the control curves become 'steeper' toward the resonant peak. Figure 3.7 shows a similar characteristic when C_n remains constant and L_n is varied; whilst Fig. 3.8 compares the frequency response of the current-output converter for various C_n. From the results, it can be seen that if L_n and C_n are unequal, a smaller resonant inductance ratio L_n yields a greater voltage boost, close to resonance, and as L_n reduces towards zero, the converter begins to take on the characteristics of a 3rd-order converter. Moreover, as parallel resonant capacitor C_p becomes larger, relative to the series capacitor C_s, the frequency response has improved selectivity—therefore a smaller range of frequencies is required for controlled voltage regulation.

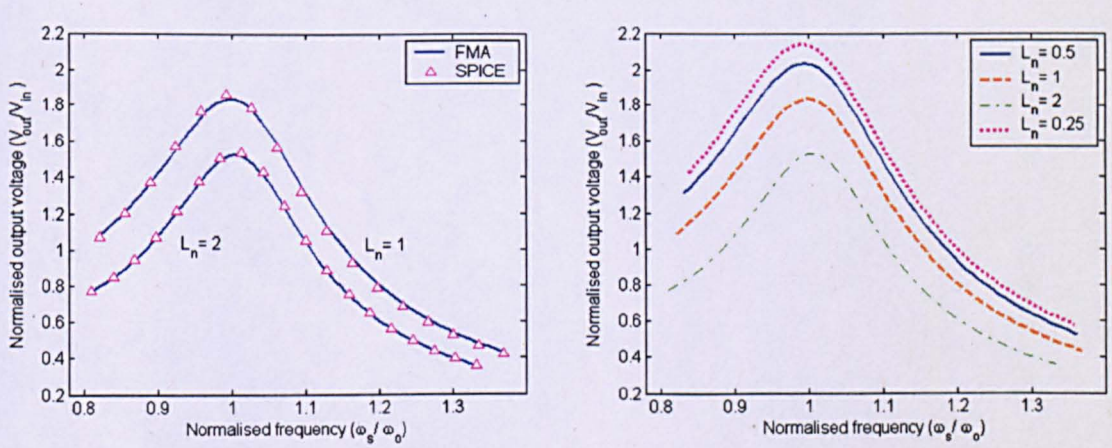

(a) (b)

Figure 3.7 Frequency sweep of converter at constant C_n=0.5 and Q_o=2: (a) SPICE and (b) FMA.

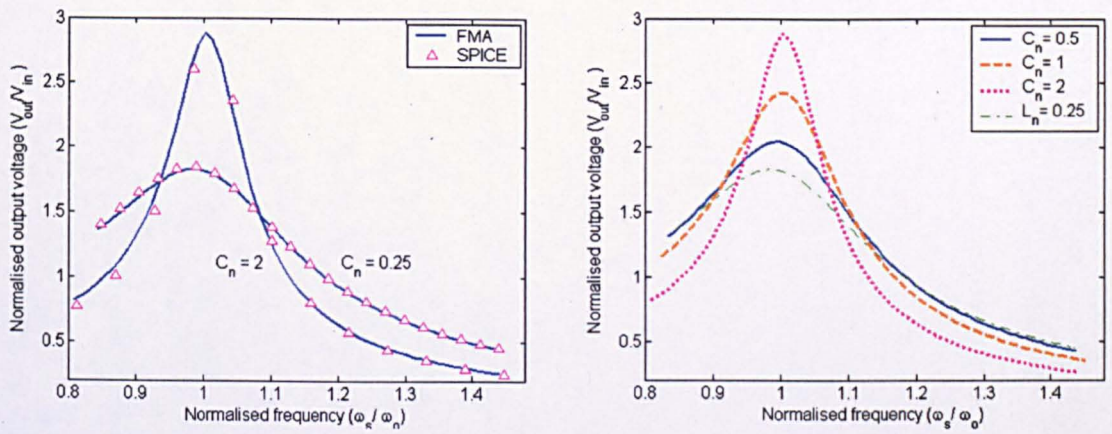

(a) (b)

Figure 3.8 Frequency sweep of LCLC current-output converter with varying C_n ratio (Q_o=2): (a) SPICE and (b) FMA.

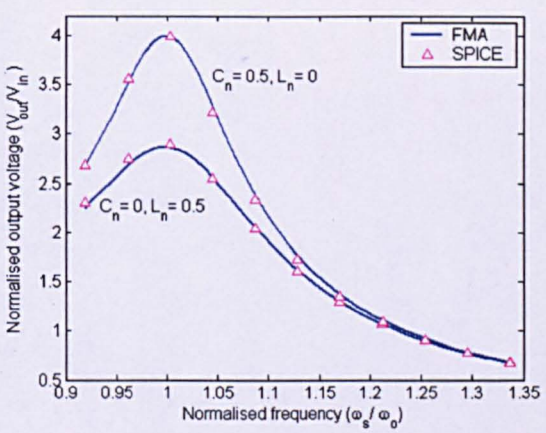

(a)

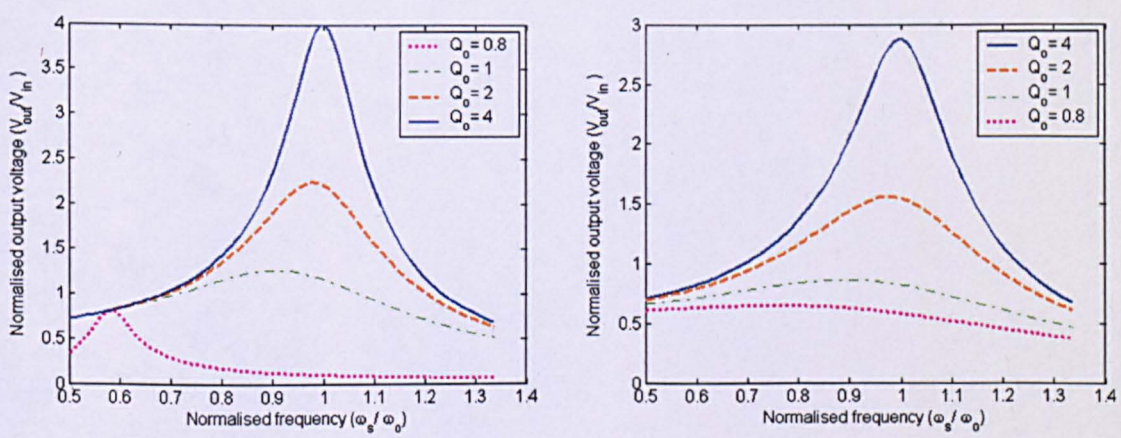

(b) (c)

Figure 3.9 Output voltage characteristics curves: (a) SPICE, (b) LCC topology under constant Q_o and (c) LLC topology under constant Q_o.

It is notable that (3-30) through to (3-33) can be constrained, and used, to describe the characteristics of other resonant converter topologies, such as the 3rd-order LCC and LLC resonant converter variants, which posses a single effective resonant frequency.

By way of example, when the parallel resonant inductance, L_p, is selected to be sufficiently large compared to series resonant inductance, L_s, then $L_n \to 0$, and the converter behaves like a 3rd-order LCC converter with the un-damped resonant frequency depending on C_n, and the effective tank frequency in (3-9) simplifies to (3-35a). As $L_p \to \infty$, $L_n \to 0$,

$$\omega_o = \omega_{op1}\sqrt{\frac{1+C_n}{C_n}} \tag{3-35a}$$

Similarly if the series capacitance is excluded, C_s is selected to be sufficiently large compared to C_p, thereby $C_s \to \infty$, $C_n \to 0$ and the effective resonant frequency simplifies to,

$$\omega_o = \omega_{op2}\sqrt{\frac{1+L_n}{L_n}} \tag{3-35b}$$

Numerical verification of (3-35) is obtained through a comparison with results obtained from SPICE simulations of LLC and LCC converters, in Fig. 3.9. In both cases, the second resonant frequency ω_o' equates to zero.

At low operating frequencies, the additional resonant peak of the LCLC resonant converter influences behaviour. Although the use of FMA assumes that the input current is sinusoidal, which still holds for regions around the second resonant frequency, ω_o', the output voltage can potentially be greater than expected (depending on values of C_n and L_n), with the tank components being subjected to higher electrical stresses. The characteristics of the converter about the secondary resonance are also governed by the relationship between the two effective resonant frequencies, $\omega_r = \omega_o/\omega_o'$.

Figure 3.10 shows the input-output characteristics of the converter as Q_o, L_n, C_n, are varied, with the switching frequency normalised to that of ω_o. It can be seen from Fig. 3.10(a) that the normalised output voltage M_{vcr} is equal to the effective load factor Q_o, at both resonant peaks, if L_n and C_n are varied together. In addition, the curves are narrower, and the two resonant frequencies are closer, if

both L_n and C_n are increased together. Conversely, if L_s is much smaller than L_p, a wider frequency bandwidth is required for output voltage regulation.

From Fig. 3.10(b), if the inductance and capacitance ratios are unequal, a higher L_n yields steeper curves with greater gain in the region of the secondary resonance, thereby allowing a higher voltage output to be obtained than can be achieved by operating about the 'effective resonance' of the whole circuit. Conversely, the maximum output voltage that can be obtained in the region of ω_o', is lower, if $L_n < C_n$.

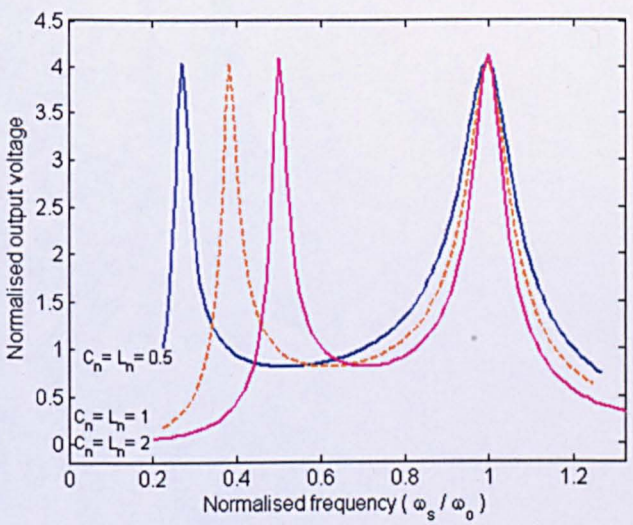

(a)

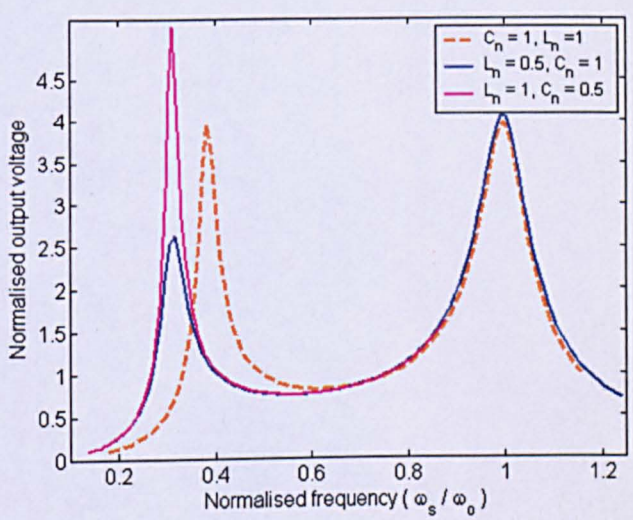

(b)

Figure 3.10 Output voltage characteristic curves of 4th-order resonant converter (a) at constant load factor Q_o=4 and, (b) with unequally varied C_n and L_n (Q_o=4)

3.3. Discontinuous Conduction Mode of Operation (DCM)

In this mode of operation, the parallel resonant capacitor voltage v_{Cp} remains at 0V for a period of time. Example steady state waveforms are given in Fig. 3.11. During steady state operation, the resonant tank inductor current $i_L(= i_{Ls}- i_{Lp})$ is initially zero and SW1 is turned on at $t = t_0$. So long as $|i_L| < i_{out}$, the output current circulates through the rectifier bridge, which appears as a short circuit across C_p, and keeps its voltage at 0V, as shown in Fig. 3.11. Therefore, v_{Cp} stays at zero for an interval that varies according the level of loading on the converter's output. When i_L exceeds i_{out}, the difference i_L-i_{out} flows into C_p causing v_{Cp} to increase. The boundary between CCM and the DCM can therefore be analytically determined.

Typical steady state waveforms used to find the boundary condition, are shown in Fig. 3.11(a), in which α_i [C4] is the phase difference between i_L and v_{Cp}. It can be observed from Fig. 3.11(a) that v_{Cp} is clamped at zero for a very short period of time under this condition. The fact that α_i is positive implies that the current leads the capacitor voltage. The boundary between CCM and DCM is governed by the state of v_{Cp} and $i_{out} > i_L$. Consequently, the condition required to provide continuous mode conduction, is given by $i_{out} < i_L \sin(\alpha_i)$. The equations used to find the boundary between CCM and DCM, have been given in [C4],

$$\tan(\alpha_i) > \frac{2}{\pi} \tag{3-36}$$

$$V_{out} = \frac{2i_L \sin(\alpha_i)}{2\pi^2 f_s C_p} \tag{3-37}$$

$$i_{out} = \frac{2i_L \cos(\alpha_i)}{\pi} \tag{3-38}$$

Substituting (3-37) and (3-38) into (3-36), the boundary condition for continuous conduction can be obtained as a function of resonant capacitance ratio, C_n, and angular frequency, ω_s,

$$\begin{aligned} &\frac{2\pi^2 f_s C_p V_{out}}{i_L} \times \frac{i_L}{\pi i_{out}} > \frac{2}{\pi} \\ &\omega_s C_s C_n R_L > \frac{2}{\pi} \end{aligned} \tag{3-39}$$

and substituting for Q_{op1} gives,

$$\frac{Q_{op1} C_n \omega_s}{\omega_{op1}} > \frac{\pi}{4} \tag{3-40}$$

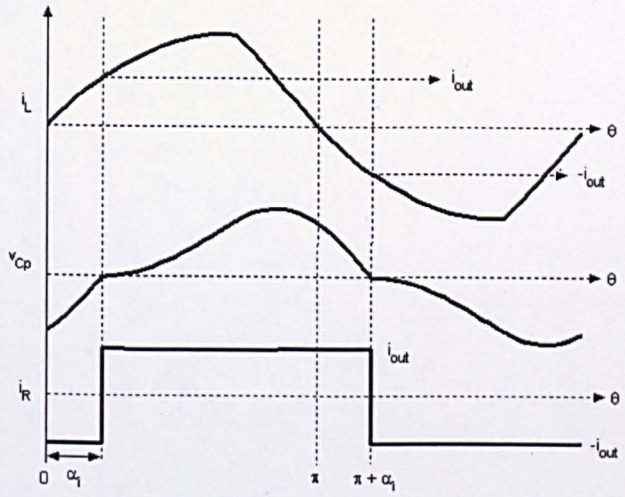

(a)

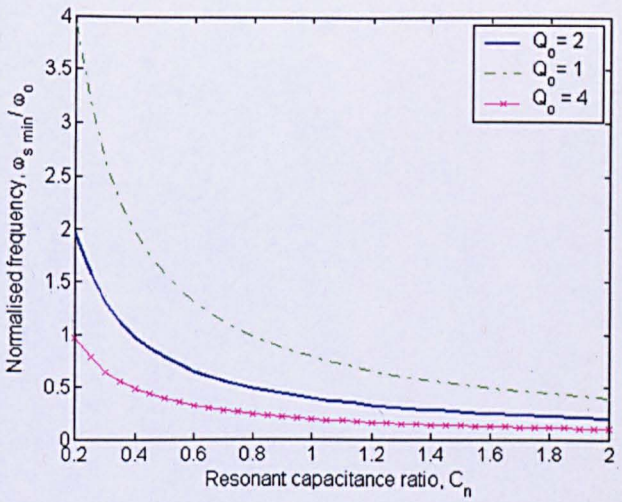

(b)

Figure 3.11 Boundary of DCM operational mode: (a) simulated key voltage and current waveforms and (b) minimum angular frequency, $\omega_{s\,min}$ for CCM.

Finally, (3-40) can be written in terms of the effective tank load quality factor, Q_o and angular resonant frequency, ω_o,

$$\frac{Q_o C_n \omega_s}{\omega_o} > \frac{\pi}{4} \tag{3-41}$$

When the angular switching frequency ω_s is reduced to a certain level, dictated by Q_o, C_n and ω_o, the parallel resonant capacitor voltage becomes discontinuous. Similarly, v_{Cp} has clamping intervals if the load quality factor Q_o is decreased to a particular level, dependant on ω_s, C_n and ω_o. Using (3-40) and

(3-41) to determine the minimum angular switching frequency, and minimum load quality factor, for continuous conduction, gives

$$\omega_{s\min} > \frac{\pi\omega_o}{4Q_oC_n}$$
$$Q_{o\min} > \frac{\pi\omega_o}{4C_n\omega_s} \tag{3-42}$$

As can be seen from Fig. 3.11(b), for a constant capacitance ratio C_n e.g. 0.4, the converter can be operated around its effective resonant frequency to sustain continuous conduction if Q_o= 2, whilst the converter has to be operated further away from resonance when Q_o is reduced to 1. In the case of high C_n, the converter is essentially always operating in continuous conduction mode if the switching frequency is above the resonant frequency.

3.4. Component Stresses Analysis

Here, the analysis results of previous sections are extended to include resonant component stresses. It is useful to know the relationship between the peak and average values of the circuit voltages and currents, and operating conditions (v_{DC}, V_{out}, ω_o, etc.). As previously discussed, the output characteristics of the converter are sensitive to the choice of C_n and L_n, implying that the electrical stresses on the tank components are also affected.

Electrical stresses can be analysed by consideration of the input impedance of the tank (re-written from (3-17) below, for clarity):

$$Z_{in} = Z_oQ_o \times \sqrt{\frac{\left[\left(\frac{\omega_o}{\omega_{opl}}\right)^4\frac{C_n}{L_n} - \left(\frac{\omega_o}{\omega_{opl}}\right)^2\left(1+\frac{1}{L_n}+\frac{C_n}{L_n}\right)+1\right]^2 + \left[\left(\frac{1}{Q_oL_n}\right)\left(1-\left(\frac{\omega_o}{\omega_{opl}}\right)^2\right)\right]^2}{\left(\frac{\omega_o}{\omega_{opl}}\right)^4\frac{1}{L_n^{\,2}} + \left[Q_o\left(\frac{\omega_o}{\omega_{opl}}\right)^2\left(1-\left(\frac{\omega_o}{\omega_{opl}}\right)^2\frac{C_n}{L_n}\right)\right]^2}} \tag{3-43}$$

Noting that the amplitude of the fundamental of the input voltage, when operating close to resonance, is $v_{i(1)} = (2/\pi)v_{DC}$ from (3-27), for the half-bridge converter configuration, the current through the tank consists mainly of the fundamental, and is approximately sinusoidal—hence, the peak switch current is equivalent to the peak series inductor current.

Having calculated the input impedance, the peak stress on L_s can be readily found from,

$$\hat{i}_{Ls} = \frac{v_{i(1)}}{|Z_{in}|} = \frac{2}{\pi} \times \frac{v_{DC}}{Z_o Q_o} \times \sqrt{\frac{\left(\frac{\omega_o}{\omega_{op1}}\right)^4 \frac{1}{L_n^2} + \left[Q_o\left(\frac{\omega_o}{\omega_{op1}}\right)^2\left(1-\left(\frac{\omega_o}{\omega_{op1}}\right)^2 \frac{C_n}{L_n}\right)\right]^2}{\left[\left(\frac{\omega_o}{\omega_{op1}}\right)^4 \frac{C_n}{L_n} - \left(\frac{\omega_o}{\omega_{op1}}\right)^2\left(1+\frac{1}{L_n}+\frac{C_n}{L_n}\right)+1\right]^2 + \left[\left(\frac{1}{Q_o L_n}\right)\left(1-\left(\frac{\omega_o}{\omega_{op1}}\right)^2\right)\right]^2}} \tag{3-44}$$

and the peak voltage across the series resonant capacitor, C_s, is consequently obtained from (3-45),

$$\hat{v}_{Cs} = \frac{\hat{i}_{Ls}}{\omega_s C_s} \tag{3-45}$$

The absolute value for the peak parallel resonant capacitor voltage $\hat{v}_{Cp}$ is equal to the output voltage of the equivalent circuit given in Fig. 3.4, which, from (3-34), is given by,

$$\hat{v}_{Cp} = \frac{\pi v_{DC}}{2} \times \frac{\frac{s^2 \lambda_r^2}{\omega_o^2}\sqrt{\frac{C_n}{L_n}}Q_{op1}}{\left(\frac{s^4}{\omega_o^4}\frac{\lambda_r^4 C_n^{1.5} Q_{op1}}{\sqrt{L_n}} + \frac{s^3 \lambda_r^3}{\omega_o^3}\sqrt{\frac{C_n}{L_n}}\right)\left(\frac{s^2\lambda_r^2}{\omega_o^2}\sqrt{L_n C_n}\left(Q_{op1}+\frac{Q_{op1}}{L_n}+\frac{Q_{op1}C_n}{L_n}\right)+\frac{s\lambda_r}{\omega_o}\sqrt{\frac{C_n}{L_n}}+Q_{op1}\sqrt{L_n C_n}\right)} \tag{3-46}$$

whilst the peak current amplitude flowing through the parallel resonant inductor, L_p is [C5],

$$\hat{i}_{Lp} = \frac{\hat{v}_{Cp}}{\omega_s L_p} \tag{3-47}$$

and the magnitude of the dc-output current of the converter is given by,

$$i_{out} = \frac{2\hat{v}_{Cp}}{\pi R_L} \tag{3-48}$$

Here, all analytical terms are now given in per-unit normalised form without change in notation. The following quantities are chosen as the bases for normalisation:

Voltage stress	v_{DC}
Current stress	v_{DC}/Z_o
Angular frequency	ω_o

A comparison of the normalised peak component stresses—$\frac{\hat{i}_{Ls}Z_o}{v_{DC}}$, $\frac{\hat{v}_{Cs}}{v_{DC}}$, $\frac{\hat{v}_{Cp}}{v_{DC}}$ and $\frac{\hat{i}_{Lp}Z_o}{v_{DC}}$, that are obtained from (3-44) to (3-48), with those from SPICE simulations, is given in Figs. 3.12 and 3.13, respectively. The prediction accuracy deteriorates for frequencies below resonance, or far away from resonance, due to the input current not exhibiting a dominant sinusoidal characteristic. As shown in Fig. 3.12(b), the waveform of the series resonant inductor current i_{Ls} becomes increasing triangular when the converter is operated at frequencies away from the effective resonant frequency. The overall results indicate that prediction accuracy comparable with SPICE, is possible, particularly around the resonant frequency, and above resonance. Furthermore, the magnitude of normalised peak i_{Ls} is shown in Fig. 3.12(c) when the load quality factor Q_o is varied. Similarly, Fig. 3.13(b) shows the magnitude of normalised peak voltage v_{Cp} for various load conditions.

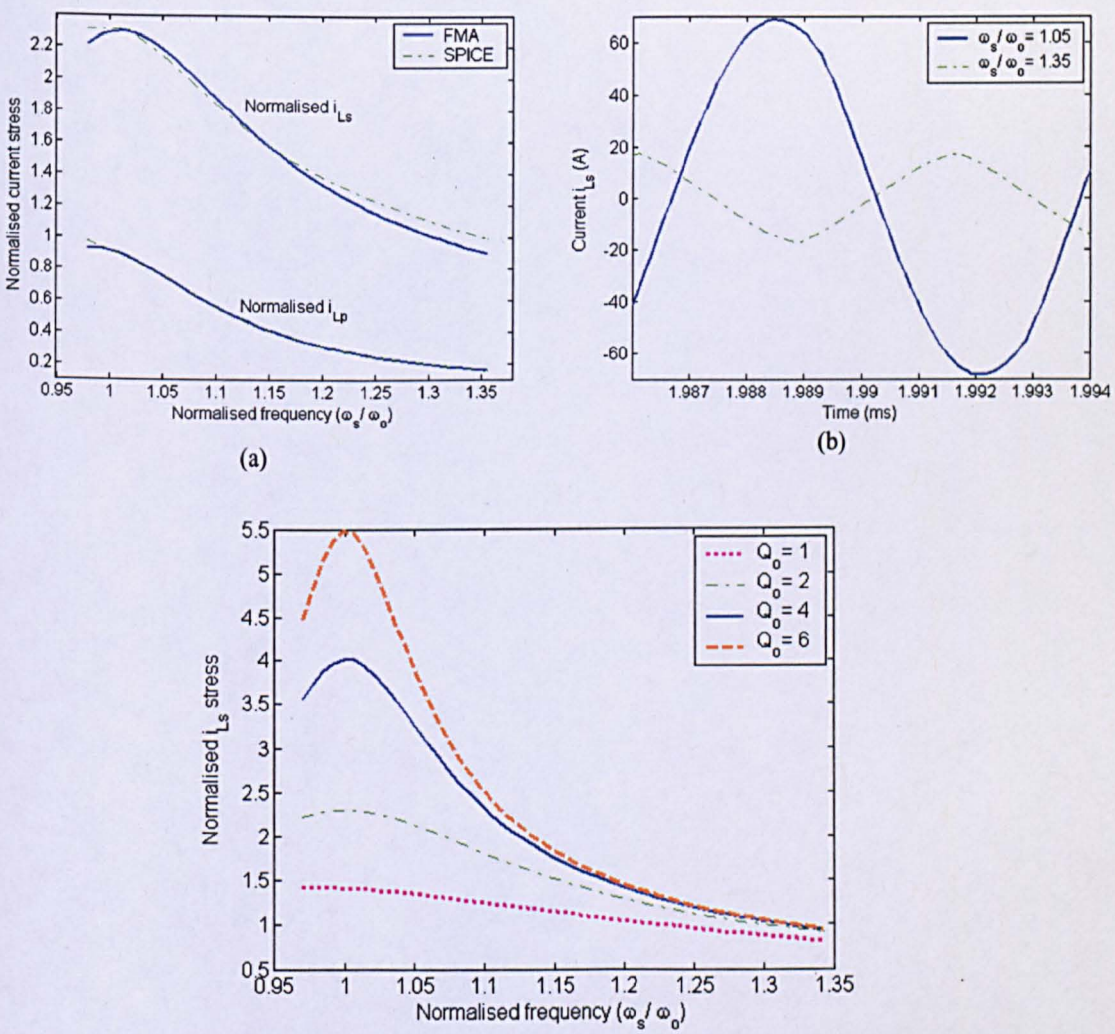

Figure 3.12 Resonant component current stresses at C_n =0.5, L_n=0.5 and Q_o=2: (a) SPICE against FMA, (b) Simulated waveform of i_{Ls} and (c) FMA.

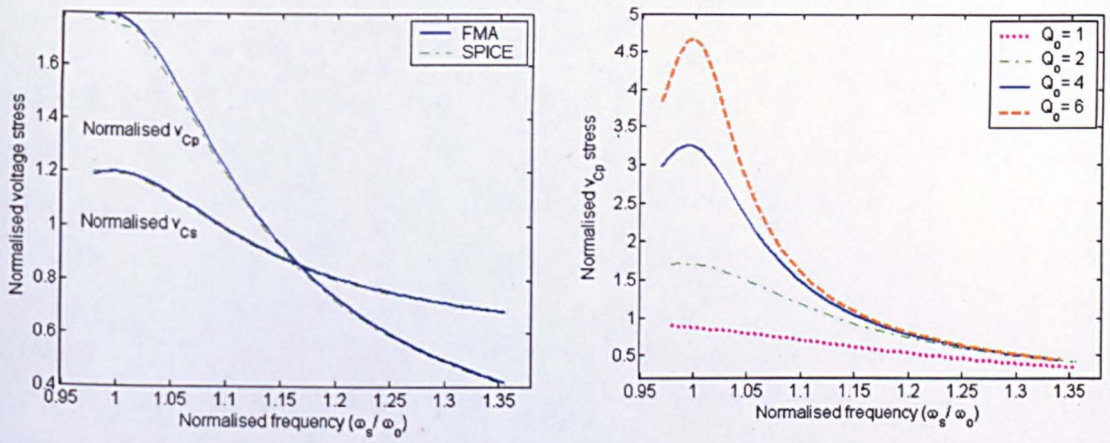

Figure 3.13 Resonant component current stresses (C_n =0.5 and L_n=0.5): (a) SPICE and (b) FMA predicted $\hat{v}_{Cp}/v_{DC}$.

From Fig. 3.14, the maximum normalised series inductor (L_s) current can be seen to increase as L_n decreases, indicating that current stresses on L_s can be reduced by either having large L_s or by decreasing L_p. The effect of increasing the parallel resonant capacitor, C_p, is also given in Fig. 3.15, from where it can be seen that an increase in C_n increases the voltage stress on C_p. For completeness, a comparison of maximum normalised peak switch current imposed on 3rd-order and 4th-order resonant converter variants, is shown in Fig. 3.16.

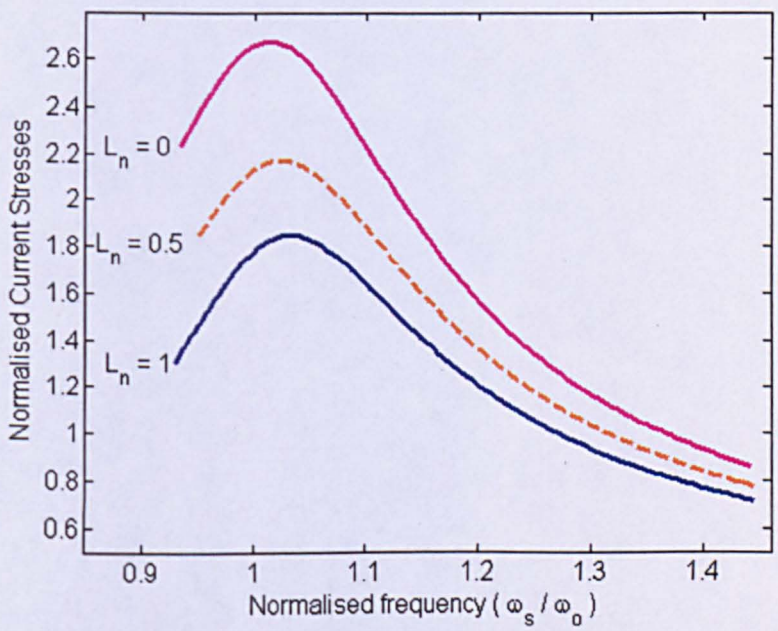

Figure 3.14 Characteristic curves of the series inductor current (C_n =0.5 and Q_o=2).

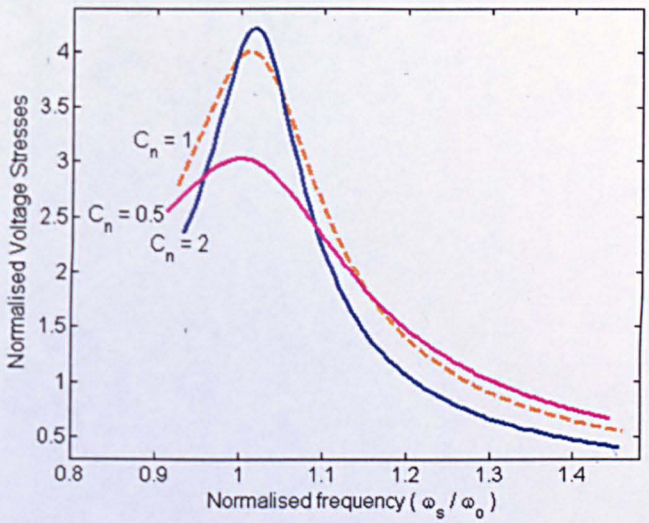

Figure 3.15 Maximum parallel capacitor voltages (L_n =0.5).

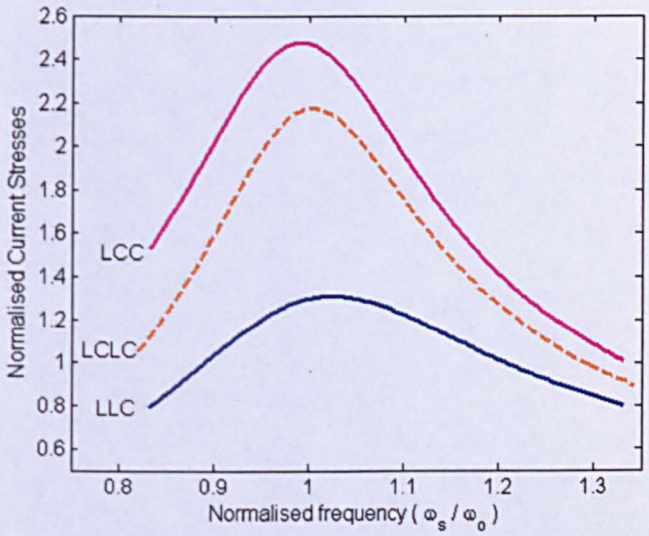

Figure 3.16 Comparison of maximum current stresses between different converter topology (Q_o= 2).

Figure 3.17 shows the normalised output current $i_{out}Z_o/v_{DC}$ versus normalised switching frequency, for C_n=0.5 and L_n=0.5. At resonance ($\omega_s/\omega_o = 1$), the output current of the resonant converter is seen to be independent of the output voltage, and the magnitude of the current is determined by the input voltage—the converter therefore exhibits a current source characteristic, and theoretically possesses infinite voltage gain for a constant output current [C2].

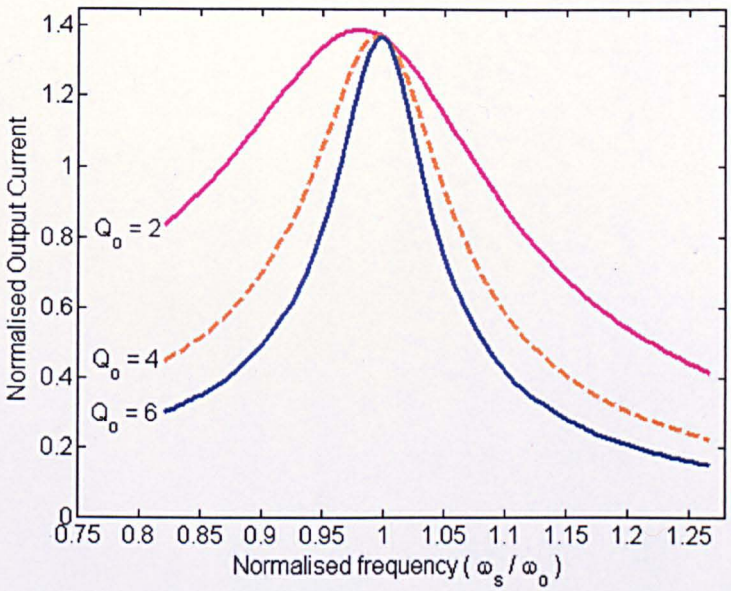

Figure 3.17 Normalised output current as a function of effective load quality factor.

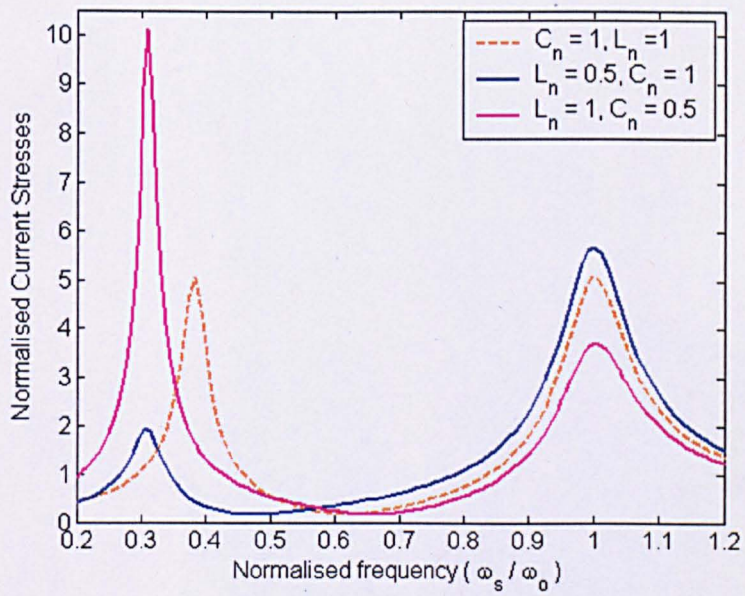

Figure 3.18 Frequency sweep of normalised series inductor/power switches input current for various L_n and C_n (Q_o=4).

The influence of L_n and C_n on the normalised inductor current magnitude, at the two resonant frequencies, is shown in Fig. 3.18. The normalised series inductor current $\hat{i}_{Ls}Z_o/v_{DC}$ is seen to be higher at $\omega_s = \omega_o$. Conversely, if $L_n >> C_n$, operation about the secondary resonant peak develops higher current stresses on L_s. A compromise is, therefore, required between high inductor current

stress levels, and the maximum output voltage magnitude, when operating in the region of the secondary resonant frequency.

When operating at the effective resonant frequency, the stresses imposed on the power switches SW1 and SW2 can be reduced by either decreasing the value of L_s, or increasing value of L_p, thereby lowering the L_n ratio. Similarly, a smaller inductance ratio L_n is essential for minimising the overall electrical stress if the system is operated at secondary resonant frequency. By way of example, a comparison between the predicted output voltage of the converter, V_{out}/V_{in} from (3.34), and those resulting from SPICE simulations, at steady state, is given in Fig. 3.19, with C_n=1 and L_n=0.5, thereby allowing an asymmetrical resonant component ratio (C_n>L_n) to facilitate a 'wider' frequency-controlled characteristic with higher gain at the effective resonant frequency.

For this example, a voltage gain of M_{vcr}=2.5 is obtained through operation above resonance at $\omega_s/\omega_o = 1.1$ (inductive conduction for ZVS), or by switching at ω_o'. At $\omega_s = \omega_o'$, the series resonant inductor current is in-phase with the input excitation voltage, and high power factor operation ensues. Furthermore, the associated current stress imposed on the series inductor is significantly lower at the secondary resonant frequency (i.e. $\hat{i}_{Ls}Z_o/v_{DC}$ =1.8 at ω_o' compared to 3.5 at effective resonance), with a consequential reduction in electrical stresses on power switches and resonant capacitor.

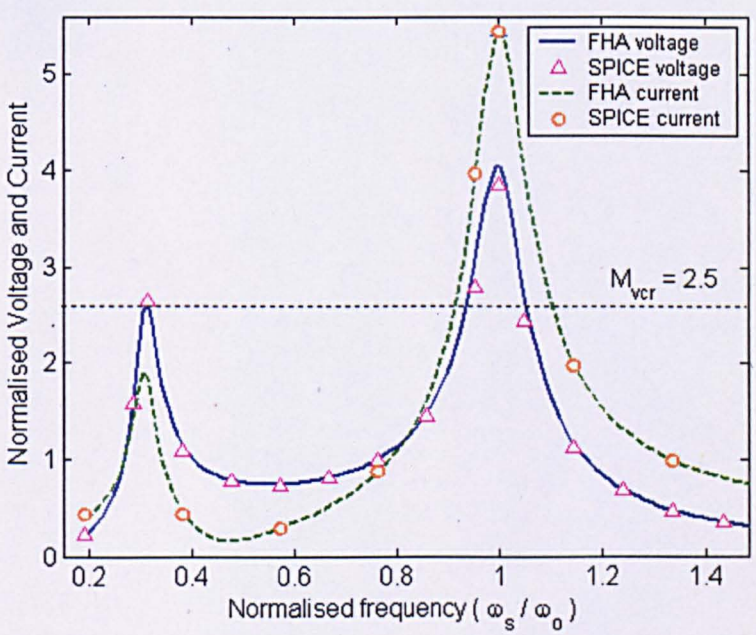

Figure 3.19 Comparison between FMA predictions and simulation results from SPICE (Q_o=4, C_n=1, L_n=0.5).

3.5. Summary

The derivation and verification of frequency domain models for the steady-state analysis of the 4th-order current-output resonant converter, has been presented. Results demonstrate the accuracy of the model to predict the dc output voltage from the converters, and to estimate voltage and current stresses on the resonant components. Morever, characteristics associated with mutli-resonance behaviour, for the two identified resonant frequencies, is considered, and operation of the resonant converter around the secondary resonant peak, is proposed, to faciltate a reduction in switching losses and operation at improved power factor.

References

[C1] R. L. Steigerwald, "A Comparison of Half-Bridge Resonant Converter Topologies", *IEEE Trans. on Power Electronics*, **3**, pp. 174-182, 1988.

[C2] M. K. Kazimierczuk and D. Czarkowski (1st Ed.), *Resonant Power Converters*, New York: John Wiley and Son, 1995.

[C3] N. Mohan, T. M. Undeland and W. P. Robbins (3rd Ed.), *Power Electronics*, USA: John Wiley and Son, 2003.

[C4] A. J. Forsyth, G. A. Ward and S. V. Mollov, "Extended Fundamental Frequency Analysis of LCC Resonant Converter", *IEEE Trans. on Power Electronics*, **18**, pp. 1286-1292, 2003.

[C5] Y. Ang, M. P. Foster, H. I. Sewell, C. M. Bingham and D. A. Stone, "Stress analysis of 4th-order LLCC resonant converters", *IEE Electronics Letters*, **38**, pp. 1585-1586, 2002.

CHAPTER 4

Cyclic Averaging Analysis of Current-Output Resonant Converters

Classically, resonant converters are analysed through the use of Fundamental Mode Approximation, as described in Chapter 3, or variants thereof, which can predict the steady-state behaviour of the converter to a degree of accuracy dictated by assumptions made during modelling. Large-signal state-variable modelling, introduced in Chapter 2, has been shown to provide very accurate transient time domain solutions, although the computational overhead (due to its reliance on integration) is often prohibitive, and impedes the use of such techniques in an interactive design environment.

These limitation can be accommodated to some degree by considering only steady-state solutions to the state-variable equations, which, as will be shown, provide analytical solutions for investigative and design validation purposes. Here then, the development and application of cyclic averaging techniques [D1, D2], based on derived state-variable dynamic models of the current-output LCLC converter, for determining the steady-state behaviour, is proposed. By comparison with previously published techniques, the method has the advantage of allowing any piecewise-linear state-space model describing the operation of a power converter, to be analytical solved without the pre-requisite of a transient-based simulation. Cyclic averaging therefore provides a rapid design and analysis aid.

Although the application of such techniques requires a-priori knowledge of the resonant converter's behaviour (operation in either continuous or discontinuous conduction modes, for instance), they are demonstrated to provide an attractive alternative to traditional FMA-based analysis for evaluating performance, and provide results of higher accuracy with commensurate computation overhead.

Comparisons between results of cyclic averaging and those obtained from SPICE simulations and experimental measurements from a prototype converter, are included, to show that accuracy comparable to SPICE is readily achievable whilst requiring only a fraction of the computation overhead.

Further, it is shown that, by suitable manipulation, the resulting models can be directly employed to analytically predict the voltage and current stresses on the resonant components, which is a key feature in the design of resonant converters since they tend to be higher compared to their hard-switched counterparts.

4.1. The Cyclic Modes

A power converter is considered to operate in a cyclic-mode when the state vector $x(t)$, at any time t, is equal to $x(t+n\mathrm{T})$, where T is the switching period of the converter and n is a positive integer, i.e. $x(t+n\mathrm{T})=x(t)$. For resonant converters, each cycle is comprised of multiple operating modes, M_i, each dependent on the state of the input voltage and the rectifier input/output voltages and currents. When considering operation in a cyclic-mode, a system of piecewise linear (state-space) equations that describe the converter's behaviour, in each of the modes, during a cycle, can be derived, viz.:

$$\dot{x}_i = \mathrm{A}_i x_i + \mathrm{B}_i \tag{4-1}$$

where x_i is the state vector, A_i represents the dynamics and B_i is the excitation matrix during the i^{th} operating mode.

For the i^{th} mode, (4-1) can be solved analytically to give:

$$x_i(t) = e^{\mathrm{A}_i t} x_i(t_0) + \int_0^t e^{\mathrm{A}_i(t-\tau)} \mathrm{B}_i \, d\tau = \Phi_i x_i(t_0) + \mathrm{T}_i \tag{4-2}$$

where $\Phi_i = \Phi(t,t_0) = e^{\mathrm{A}_i t}$, $\mathrm{T}_i = \int_0^t e^{\mathrm{A}_i(t-\tau)} \mathrm{B}_i \, d\tau$, and $x_i(t_0)$ are the initial conditions for the i^{th} mode.

By noting that the time during which the circuit operates in the i^{th} mode is $d_i\mathrm{T}$, where d_i is the duty, the complete solution for the converter can be obtained by employing the state vector at time $d_i\mathrm{T}$ as the initial condition for the subsequent dynamics of the $(i+1)^{th}$ mode.

The need to evaluate the integral in (4-2) is a key cause of computational overhead when analysing the system in this manner. However, by combining A_i and B_i to form an augmented dynamics matrix, (4-3), the integration overhead can be eliminated at the expense of obtaining only the 'cyclic' steady-state solution [D1]:

$$\frac{d}{dt}\begin{pmatrix} x_i(t) \\ \hline 1 \end{pmatrix} = \left(\begin{array}{c|c} \mathrm{A}_i & \mathrm{B}_i \\ \hline 0 & 1 \end{array}\right)\begin{pmatrix} x_i(t) \\ \hline 1 \end{pmatrix} \quad \text{or} \quad \frac{d}{dt}\hat{x}_i(t) = \hat{\mathrm{A}}_i \hat{x}_i(t) \tag{4-3}$$

Now, if mode 1 corresponds to the time period between t_0 and t_1, and mode 2 corresponds to the time period between t_1 and t_2, the solution for the state vector at the transition time between modes 1 & 2, t_1, is given by:

$$\hat{x}_1(t_1) = e^{\hat{A}_1 d_1 T} \hat{x}_1(t_0) = \hat{\Phi}_1 \hat{x}_1(t_0) \tag{4-4}$$

Similarly, the state vector at the transition time between modes 2 and 3, t_2, is,

$$\hat{x}_2(t_2) = e^{\hat{A}_2 d_2 T} \hat{x}_2(t_0) = \hat{\Phi}_2 \hat{\Phi}_1 \hat{x}_1(t_0) \tag{4-5}$$

In general, for the i^{th} mode:

$$\hat{x}(t_i) = \hat{\Phi}_i \hat{\Phi}_{i-1} \cdots \hat{\Phi}_1 \hat{x}(t_0) = \hat{\Phi}_{tot} \hat{x}(t_0) \tag{4-6}$$

where $\hat{\Phi}_{tot} = \left(\begin{array}{c|c} \Phi_{tot} & T_{tot} \\ \hline 0 & 1 \end{array}\right)$, and $\hat{x}(t_i)$ is the state-vector at time t_i for an initial condition $\hat{x}(t_0)$, and, therefore, by definition of the cyclic mode, is equivalent to the initial condition for the cyclic solution.

Since behaviour in the cyclic mode necessarily presumes periodic steady-state operation, the initial condition for operation in a cyclic mode is given by,

$$x_{per}(t_0) = \left(I^n - \Phi_{tot}\right)^{-1} T_{tot} \tag{4-7}$$

and the state-variables at any subsequent time are obtained from (4-6).

4.1.1. Averaged Steady State Solutions

The mean output voltage of the converter is obtained by averaging the state-variables over a complete cycle:

$$x_{av} = \frac{1}{T} \int_{t_0}^{t_0+T} x(t)\ dt \tag{4-8}$$

Again, the requirement for evaluating the integral is prohibitive to rapid analysis. However, by augmenting the state-vector with $\dot{x}_{av}(t) = x(t)/T$, the solution of the resulting system can be simplified. Consider, for example, the dynamics of the converter during the i^{th} mode of a cycle,

$$\dot{x}_i = A_i x_i + B_i \tag{4-9}$$

and

$$\dot{x}_{i\_av} = \frac{d_i}{T} x_i \tag{4-10}$$

The resulting dynamic description is:

$$\frac{d}{dt}\begin{pmatrix} x_i(t) \\ \hline 1 \\ \hline x_{i\_av}(t) \end{pmatrix} = \left(\begin{array}{c|c|c} \mathrm{A}_i & \mathrm{B}_i & 0 \\ \hline 0 & 0 & 0 \\ \hline d_i/\mathrm{T}\times I^n & 0 & 0 \end{array}\right)\begin{pmatrix} x_i(t) \\ \hline 1 \\ \hline x_{i\_av}(t) \end{pmatrix} \tag{4-11}$$

or

$$\dot{z}_i(t) = \tilde{\mathrm{A}}_i z_i(t) \tag{4-12}$$

and the initial condition for the cyclic mode is:

$$z(t_0) = \begin{pmatrix} x_{per}(t_0) \\ \hline 1 \\ \hline 0 \end{pmatrix} \tag{4-13}$$

In a similar manner to that presented in the previous section, the averaged state-vector is obtained as:

$$z(t_0 + \mathrm{T}) = \tilde{\Phi}_m \tilde{\Phi}_{m-1} \cdots \tilde{\Phi}_1 z(t_0) \tag{4-14}$$

$$z(t_0 + \mathrm{T}) = \begin{pmatrix} x_{per}(t_0) \\ \hline 1 \\ \hline x_{av} \end{pmatrix}$$

from which the average output voltage (or current) of the converter, together with the average voltages (or currents) across (through) the reactive components in the circuit, can be determined.

4.2. Cyclic Mode Analysis of Current-Output Converter in Continuous Conduction Mode

Classically, to obtain time-domain descriptions of the resonant converter, the non-linear differential equations have had to be solved numerically to find the cyclic-mode initial conditions. However, if the transition times between modes are known, initial conditions can be successfully obtained using cyclic analysis without the necessity of performing complex integration. Subsequently, the initial conditions are applied to determine average steady-state solution of the converter output voltage.

However, due to the complexity of operation, involving different numbers of modes associated with low and high loading, the model matrices, and related duty times, are derived separately for each case.

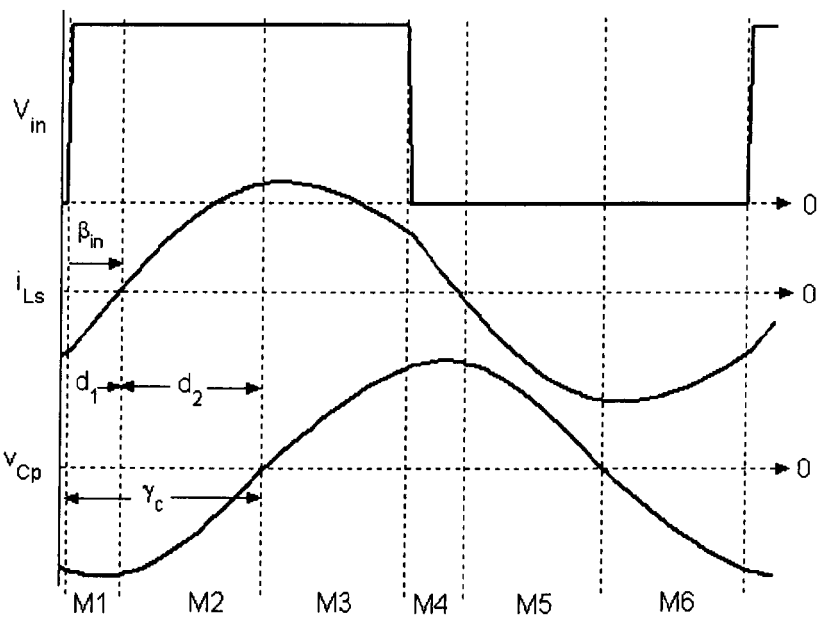

Figure 4.1 Dominant operating modes of a 4th-order current-output resonant converter under light load (operated above resonance).

Since Zero Voltage Switching (ZVS) is necessary for efficient operation, cyclic averaging is only considered here for frequencies above the system resonance (which is the norm). For operation above resonance, then, the current-output LCLC converter exhibits six modes of operation within each switching period, for light load conditions.

The modes are defined with respect to the polarity of the input voltage, V_{in}, and the state of the series resonant inductor current i_{Ls} and the parallel resonant capacitor voltage v_{Cp}. These are:

Mode 1 (M1)	$V_{in}>0$	$v_{Cp}<0$	$i_{Ls}<0$
Mode 2 (M2)	$V_{in}>0$	$v_{Cp}<0$	$i_{Ls}>0$
Mode 3 (M3)	$V_{in}>0$	$v_{Cp}>0$	$i_{Ls}>0$
Mode 4 (M4)	$V_{in}=0$	$v_{Cp}>0$	$i_{Ls}>0$
Mode 5 (M5)	$V_{in}=0$	$v_{Cp}>0$	$i_{Ls}<0$
Mode 6 (M6)	$V_{in}=0$	$v_{Cp}<0$	$i_{Ls}<0$

As previously described (Chapter 2), a state-variable description of the circuit can be obtained by separating the dynamics into fast- and slow- sub-systems.

The combined state-variable model and coupling equations are ultimately given by (4-15).

$$\begin{bmatrix} \dot{v}_{Cp} \\ \dot{v}_{Cs} \\ \dot{i}_{Lp} \\ \dot{i}_{Ls} \\ \dot{v}_{Cf} \\ \dot{i}_{Lf} \end{bmatrix} = \begin{bmatrix} 0 & 0 & -\frac{1}{C_p} & \frac{1}{C_p} & 0 & 0 \\ 0 & 0 & 0 & \frac{1}{C_s} & 0 & 0 \\ \frac{1}{L_p} & 0 & 0 & 0 & 0 & 0 \\ -\frac{1}{L_s} & -\frac{1}{L_s} & \frac{r_{cp}}{L_s} & -\frac{r_{ds}+r_{cs}+r_{ls}+r_{cp}}{L_s} & 0 & 0 \\ 0 & 0 & 0 & 0 & -\frac{1}{C_f(R_L+r_{cf})} & \frac{R_L}{C_f(R_L+r_{cf})} \\ 0 & 0 & 0 & 0 & -\frac{R_L}{L_f(R_L+r_{cf})} & -\frac{r_{lf}(R_L+r_{cf})+R_L r_{cf}}{L_f(R_L+r_{cf})} \end{bmatrix} \begin{bmatrix} v_{Cp} \\ v_{Cs} \\ i_{Lp} \\ i_{Ls} \\ v_{Cf} \\ i_{Lf} \end{bmatrix} + \begin{bmatrix} -\frac{i_R}{C_p} \\ 0 \\ 0 \\ \frac{V_{in}}{L_s}+\frac{r_{cp}i_R}{L_s} \\ 0 \\ \frac{v_f}{L_f} \end{bmatrix} \tag{4-15a}$$

$$\begin{aligned} i_R &= i_{Lf}\,\mathrm{sgn}(v_{Cp}) \\ v_f &= |v_R| - 2v_{diode} \end{aligned} \tag{4-15b}$$

and the output voltage equation is given by,

$$V_{out} = \frac{R_L}{R_L + r_{cf}} \times v_{Cf} + \frac{R_L r_{cf}}{R_L + r_{cf}} \times i_{Lf} \tag{4-16}$$

There is no clamping action on the parallel capacitor voltage so the input voltage to the rectifier simplifies to:

$$v_R = v_{Cp} + r_{cp}(i_{Ls} - i_{Lp} - i_R) \tag{4-17}$$

During each mode, the dynamics matrices A_i and the input excitation matrices, B_i, are obtained by substituting the appropriate elements of the coupling equation into the state-variable dynamic model, and considering the polarity of the input voltage and the direction of the rectifier current [D3].

For instance, during mode M1, $V_{in} > 0$, $i_{Ls} < 0$ and $v_{Cp} < 0$, and consequently, the rectifier current is negative. The coupling equations in (4-15b) therefore reduce to:

$$\begin{aligned} i_R &= -i_{Lf} \\ v_R &= v_{Cp} + r_{cp}i_{Ls} + r_{cp}i_{Lf} - r_{cp}i_{Lp} \\ v_f &= -v_{Cp} - r_{cp}i_{Ls} - r_{cp}i_{Lf} - r_{cp}i_{Lp} - 2v_{diode} \end{aligned} \tag{4-18}$$

Substituting (4-18) into (4-15), the particular piecewise linear state-equation for mode M1 is given by the matrices,

$$A_1=\begin{bmatrix} 0 & 0 & -\frac{1}{C_p} & \frac{1}{C_p} & 0 & \frac{1}{C_p} \\ 0 & 0 & 0 & \frac{1}{C_s} & 0 & 0 \\ \frac{1}{L_p} & 0 & 0 & 0 & 0 & 0 \\ -\frac{1}{L_s} & -\frac{1}{L_s} & \frac{r_{cp}}{L_s} & -\frac{r_{ds}+r_{cs}+r_{ls}+r_{cp}}{L_s} & 0 & -\frac{r_{cp}}{L_s} \\ 0 & 0 & 0 & 0 & -\frac{1}{C_f(R_L+r_{cf})} & \frac{R_L}{C_f(R_L+r_{cf})} \\ -\frac{1}{L_f} & 0 & -\frac{r_{cp}}{L_f} & -\frac{r_{cp}}{L_f} & -\frac{R_L}{L_f(R_L+r_{cf})} & -\frac{r_{lf}(R_L+r_{cf})+r_{cp}(R_L+r_{cf})+R_Lr_{cf}}{L_f(R_L+r_{cf})} \end{bmatrix} \quad B_1=\begin{bmatrix} 0 \\ 0 \\ 0 \\ \frac{V_{in}}{L_s} \\ 0 \\ -\frac{2v_{diode}}{L_f} \end{bmatrix} \tag{4-19}$$

Similarly, the dynamics matrix, A_2, and the input matrix, B_2, for mode M2 ($V_{in} > 0$, $i_{Ls} > 0$, $v_{Cp} < 0$) are given by,

$$A_2=\begin{bmatrix} 0 & 0 & -\frac{1}{C_p} & \frac{1}{C_p} & 0 & \frac{1}{C_p} \\ 0 & 0 & 0 & \frac{1}{C_s} & 0 & 0 \\ \frac{1}{L_p} & 0 & 0 & 0 & 0 & 0 \\ -\frac{1}{L_s} & -\frac{1}{L_s} & \frac{r_{cp}}{L_s} & -\frac{r_{ds}+r_{cs}+r_{ls}+r_{cp}}{L_s} & 0 & -\frac{r_{cp}}{L_s} \\ 0 & 0 & 0 & 0 & -\frac{1}{C_f(R_L+r_{cf})} & \frac{R_L}{C_f(R_L+r_{cf})} \\ -\frac{1}{L_f} & 0 & \frac{r_{cp}}{L_f} & \frac{r_{cp}}{L_f} & -\frac{R_L}{L_f(R_L+r_{cf})} & -\frac{r_{lf}(R_L+r_{cf})+r_{cp}(R_L+r_{cf})+R_Lr_{cf}}{L_f(R_L+r_{cf})} \end{bmatrix} \quad B_2=\begin{bmatrix} 0 \\ 0 \\ 0 \\ \frac{V_{in}}{L_s} \\ 0 \\ -\frac{2v_{diode}}{L_f} \end{bmatrix} \tag{4-20}$$

whilst the modal equations describing operation during M3 ($V_{in} > 0$, $i_{Ls} > 0$, $v_{Cp} > 0$) are:

$$A_3=\begin{bmatrix} 0 & 0 & \frac{1}{C_p} & \frac{1}{C_p} & 0 & -\frac{1}{C_p} \\ 0 & 0 & 0 & \frac{1}{C_s} & 0 & 0 \\ \frac{1}{L_p} & 0 & 0 & 0 & 0 & 0 \\ \frac{1}{L_s} & \frac{1}{L_s} & \frac{r_{cp}}{L_s} & \frac{r_{ds}+r_{cs}+r_{ls}+r_{cp}}{L_s} & 0 & \frac{r_{cp}}{L_s} \\ 0 & 0 & 0 & 0 & \frac{1}{C_f(R_L+r_{cf})} & \frac{R_L}{C_f(R_L+r_{cf})} \\ \frac{1}{L_f} & 0 & \frac{r_{cp}}{L_f} & \frac{r_{cp}}{L_f} & \frac{R_L}{L_f(R_L+r_{cf})} & \frac{r_{cf}(R_L+r_{cf})-r_{cp}(R_L+r_{cf})+R_Lr_{cf}}{L_f(R_L+r_{cf})} \end{bmatrix} \quad B_3=\begin{bmatrix} 0 \\ 0 \\ 0 \\ \frac{V_{in}}{L_s} \\ 0 \\ \frac{2v_{diode}}{L_f} \end{bmatrix} \tag{4-21}$$

Due to symmetry, the modal and excitation matrices for converter operation in M4 ($V_{in} = 0$, $i_{Ls} > 0$, $v_{Cp} > 0$) and M5 ($V_{in} = 0$, $i_{Ls} < 0$, $v_{Cp} > 0$) and M6 ($V_{in} = 0$, $i_{Ls} < 0$, $v_{Cp} < 0$) are given by:

$$A_4 = A_3$$

$$A_5 = \begin{bmatrix} 0 & 0 & -\frac{1}{C_p} & \frac{1}{C_p} & 0 & -\frac{1}{C_p} \\ 0 & 0 & 0 & \frac{1}{C_s} & 0 & 0 \\ \frac{1}{L_p} & 0 & 0 & 0 & 0 & 0 \\ -\frac{1}{L_s} & -\frac{1}{L_s} & \frac{r_{cp}}{L_s} & -\frac{r_{ds}+r_{cs}+r_{ls}+r_{cp}}{L_s} & 0 & \frac{r_{cp}}{L_s} \\ 0 & 0 & 0 & 0 & -\frac{1}{C_f(R_L+r_{cf})} & \frac{R_L}{C_f(R_L+r_{cf})} \\ \frac{1}{L_f} & 0 & -\frac{r_{cp}}{L_f} & -\frac{r_{cp}}{L_f} & -\frac{R_L}{L_f(R_L+r_{cf})} & -\frac{r_{lf}(R_L+r_{cf})-r_{cp}(R_L+r_{cf})+R_L r_{cf}}{L_f(R_L+r_{cf})} \end{bmatrix}$$

$$A_6 = A_1$$

$$B_4 = \begin{bmatrix} 0 & 0 & 0 & 0 & 0 & -\frac{2v_{diode}}{L_f} \end{bmatrix}^T = B_6 = B_5$$

(4-22)

Initial conditions $x_{per}(t_0)$ can be obtained by substituting (4-19) through to (4-22) into (4-11), (4-13) and (4-14) along with the transition times associated with each mode.

4.2.1. Determining the Duty-times of Each Mode

To describe the steady-state behaviour of the converter operating in a cyclic mode, the cyclic modal matrices, together with their corresponding time periods, are substituted into (4-11) and (4-13). Although accurate determination of the duty-times is critical for correct determination of initial conditions, FMA is now initially considered sufficient for the purpose when the converter is operating in continuous conduction mode, and when the output-filter inductance is considered sufficient to provide a ripple-free output. In this case, the voltage waveform presented to the rectifier bridge is considered sinusoidal, and the rectifier input current is considered to be square-wave. Since, using FMA, the rectifier and output filter of the resonant converter are modelled by an equivalent resistance $R_{eq} = \pi^2 R_L/8$, a simplified equivalent circuit of the resonant converter is shown in Fig. 4.2.

When operating above the system resonance, the impedance of the resonant tank appears high to the input-voltage harmonics if the load quality factor Q is high, and the series resonant inductor current, which coincides with the input switch current, is approximately sinusoidal.

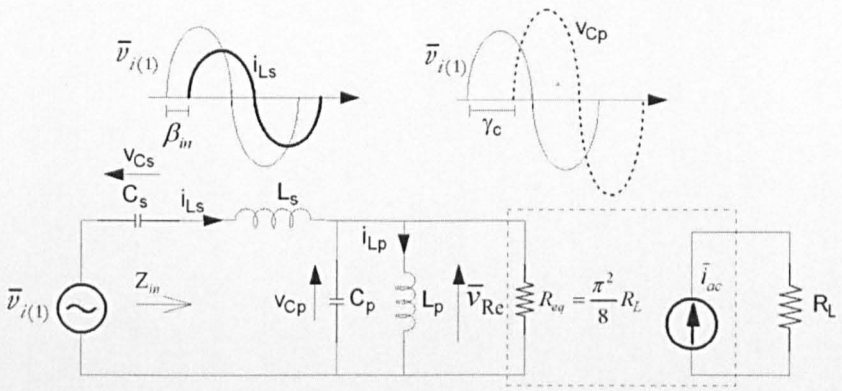

Figure 4.2 An FMA equivalent circuit modelling the fundamental components of the resonant tank waveforms.

The input impedance, Z_{in}, of the resonant circuit in Fig. 4.2 is given by,

$$Z_{in} = \frac{s^4\left(\frac{Q_{op2}}{\omega_{op1}^2\omega_{op2}}\right) + s^3\left(\frac{1}{\omega_{op1}^2}\right) + s^2\left(\frac{R_{eq}}{\omega_{op1}^2 L_p} + \frac{Q_{op2}}{\omega_{op2}} + \frac{C_s Q_{op2}}{C_p\omega_{op2}}\right) + s + \frac{R_{eq}}{L_p}}{s^3\left(\frac{C_s Q_{op2}}{\omega_{op2}}\right) + s^2 C_s + s\left(\frac{C_s R_{eq}}{L_p}\right)} = |Z_{in}|e^{j\beta_{in}} \tag{4-23}$$

where normalised parameters are employed for brevity, as given below:

$$\begin{aligned} \omega_{op1} &= 1/\sqrt{L_s C_s} \\ \omega_{op2} &= 1/\sqrt{L_p C_p} \\ Q_{op1} &= \frac{R_{eq}}{\omega_{op1} L_s} \\ Q_{op2} &= \frac{R_{eq}}{\omega_{op2} L_p} \end{aligned} \tag{4-24}$$

Making the substitution $s \to j\omega_s$, the phase angle between the fundamental of the input voltage V_{in} and the fundamental of series inductor current i_{Ls} is,

$$\beta_{in} = \tan^{-1}\left[\frac{-\omega_s^2 C_s}{\omega_s\left(\frac{C_s R_{eq}}{L_p} - \omega_s^2\left(\frac{C_s Q_{op2}}{\omega_{op2}}\right)\right)}\right] - \tan^{-1}\left[\frac{\omega_s^4\left(\frac{Q_{op2}}{\omega_{op1}^2\omega_{op2}}\right) - \omega_s^2\left(\frac{R_{eq}}{\omega_{op1}^2 L_p} + \frac{Q_{op2}}{\omega_{op2}} + \frac{Q_{op2}}{C_n\omega_{op2}}\right) + \frac{R_{eq}}{L_p}}{\omega_s\left(1 - \frac{\omega_s^2}{\omega_{op1}^2}\right)}\right] \tag{4-25}$$

At $t = t_1$, defined as the time at which the series resonant inductor current passes through zero (end of M1), duty d_1 is obtained from the phase angle (4-25) and is normalised by dividing by 2π:

$$d_1 = \frac{\beta_{in}}{2\pi} \tag{4-26}$$

The duty for M2, d_2, is derived by finding the phase difference, γ_c, between the fundamental of the input voltage and that of the parallel capacitor voltage, from the equivalent circuit of Fig. 4.2. Neglecting parasitic resistances for the moment, the parallel capacitor voltage $v_{Cp}(s)$ is described, in the Laplace domain, by:

$$\frac{v_{Cp}}{V_{in}}(s) = \frac{2}{\pi}\left[\frac{s^2\left(\frac{Q_{op2}}{\omega_{op2}C_n}\right)}{s^4\left(\frac{Q_{op2}}{\omega_{op1}^{\ 2}\omega_{op2}}\right)+s^3\left(\frac{1}{\omega_{op1}^{\ 2}}\right)+s^2\left(\frac{R_{eq}}{\omega_{op1}^{\ 2}L_p}+\frac{Q_{op2}}{\omega_{op2}C_n}+\frac{Q_{op2}}{\omega_{op2}}\right)+s+\frac{R_{eq}}{L_p}}\right] \tag{4-27}$$

Again making the substitution $s \rightarrow j\omega_s$, γ_c in polar representation (4-27) is sufficient to determine the mode length for M2 (normalised to angles between 0 and 2π), as follows:

$$d_2 = \begin{cases} -\frac{1}{2\pi}\times\tan^{-1}\left[\frac{\omega_s^{\ 4}\left(\frac{Q_{op2}}{\omega_{op1}^{\ 2}\omega_{op2}}\right)+\omega_s^{\ 2}\left(\frac{R_{eq}}{\omega_{op1}^{\ 2}L_p}+\frac{Q_{op2}}{C_n\omega_{op2}}+\frac{Q_{op2}}{\omega_{op2}}\right)+\frac{R_{eq}}{L_p}}{\omega_s\left[1-\frac{\omega_s^{\ 2}}{\omega_{op1}^{\ 2}}\right]}\right]-d_1 & \text{for } \omega_s\left[1-\left(\frac{\omega_s}{\omega_{op1}}\right)^2\right]\geq 0 \\ -\frac{1}{2}+\frac{1}{2\pi}\times\tan^{-1}\left[\frac{\omega_s^{\ 4}\left(\frac{Q_{op2}}{\omega_{op1}^{\ 2}\omega_{op2}}\right)+\omega_s^{\ 2}\left(\frac{R_{eq}}{\omega_{op1}^{\ 2}L_p}+\frac{Q_{op2}}{C_n\omega_{op2}}+\frac{Q_{op2}}{\omega_{op2}}\right)+\frac{R_{eq}}{L_p}}{\omega_s\left[1-\left(\frac{\omega_s}{\omega_{op1}}\right)^2\right]}\right]-d_1 & \text{for } \omega_s\left[1-\left(\frac{\omega_s}{\omega_{op1}}\right)^2\right]<0 \end{cases} \tag{4-28}$$

The remaining duty times are found through symmetry.

$$\begin{aligned} d_3 &= 0.5 - d_1 - d_2 \\ d_4 &= d_1 \\ d_5 &= d_2 \\ d_6 &= d_3 \end{aligned} \tag{4-29}$$

Equations (4-25) and (4-28) are therefore sufficient for analysing the behaviour of the converter when only the fundamental makes a significant contribution, and the load quality factor is high, and the circuit is operated in the region of the system resonant frequency. For higher operating frequencies, however, the parallel capacitor voltage becomes increasingly distorted (non-sinusoidal), and errors when calculating the duty-times (due to the existence of higher harmonic components) can have a significant effect on the accuracy of the calculated initial conditions, and hence, output voltage predictions.

The contribution of additional harmonics in the analysis, can significantly enhance the accuracy, at the expense of much greater complexity. However, simulation studies show that harmonics beyond the 5th do not make any significant contribution. By way of example, denoting V_{in} as the amplitude of the input square-wave excitation voltage, and the n-th frequency component of V_{in}, a frequency-based summation can be employed to describe v_{Cp} (assuming linearity), (note $j\omega$ is replaced by s for convenience):

$$v_{Cp} = \frac{2V_{in}}{\pi} \times \sum_{n=1,3,5\ldots}^{\infty} \frac{1}{n} \left[\frac{(sn)^2 \times \dfrac{Q_{op2}}{\omega_{op2} C_n}}{(sn)^4 \left(\dfrac{Q_{op2}}{\omega_{op1}{}^2 \omega_{op2}} \right) + (sn)^3 \left(\dfrac{1}{\omega_{op1}{}^2} \right) + (sn)^2 \left(\dfrac{R_{eq}}{\omega_{op1}{}^2 L_p} + \dfrac{Q_{op2}}{C_n \omega_{op2}} + \dfrac{Q_{op2}}{\omega_{op2}} \right) + sn + \dfrac{R_{eq}}{L_p}} \right] \tag{4-30}$$

Furthermore, it is known that omitting parasitic resistances can have a significant effect on the accuracy of the predictions obtained from cyclic averaging (when comparing with experimental measurements), due primarily to the sensitivity on the predicted phase angles β_{in} and γ_c. Improvement in the accuracy of duty-time calculations can be made by the inclusion of components associated series parasitic resistances, giving:

$v_{Cp}(s)$

$$= \frac{2V_{in}}{\pi} \times \sum_{n=1,3,5\ldots}^{\infty} \frac{1}{n} \frac{\dfrac{snC_s R_{eq}}{\omega_{op2}{}^2 C_p} \left[(sn)^2 C_p r_{cp} + sn\left(1 + \dfrac{C_p r_{cp} r_{lp}}{L_p} \right) + \dfrac{r_{lp}}{L_p} \right]}{\left\{ \left[\dfrac{(sn)^2 (r_{cp} + R_{eq})}{\omega_{op2}{}^2} + snC_p \left(R_{eq} r_{lp} + R_{eq} r_{cp} + r_{cp} + \dfrac{L_p}{C_p} \right) + R_{eq} + r_{lp} \right] \left(\dfrac{(sn)^2}{\omega_{op2}{}^2} + snC_s R_{tot} + 1 \right) \right\}} \tag{4-31}$$

$$\left\{ + \frac{snC_s R_{eq}}{\omega_{op2}{}^2 C_p} \left[(sn)^2 C_p r_{cp} + sn\left(1 + \frac{C_p r_{cp} r_{lp}}{L_p} \right) + \frac{r_{lp}}{L_p} \right] \right\}$$

where the total parasitic resistance related to the series resonant tank, $R_{tot} = r_{ds} + r_{ls} + r_{cs}$.

The phase-angles, and hence, the mode duties, are again found after substituting $s \rightarrow j\omega_s$. The steady-state behaviour of the converter is determined from the averaging of cyclic modal matrices for each operating mode along with their corresponding duties.

4.2.2. Component Stresses Analysis

As previously discussed, whilst the soft-switching characteristics of resonant converters serves to enhance efficiency compared to equivalent hard-switched converters, the electrical stresses to which the resonant components are exposed can be much higher than those found in traditional hard-switched counterparts. An assessment of electrical stresses is, therefore, of significant importance during the design of resonant power supplies [D4].

Conveniently, the cyclic-averaging method provides a ready means of calculating steady state values of voltage and current stress on the resonant components. Although the stress level imposed on the resonant components and switching devices are higher in transient operation, e.g. during start-up and output load change, the transient voltage and current only flows through the resonant converter for a short period of time, as shown in Fig. 4.3. Although higher start-up current caused thermal 'hot-spot' to build up on the centre of inductor core that leads to increased core loss, forced cooling can be achieved using fan mounted on the inductor itself to mitigate the thermal effect. Therefore, steady state current stress values are considered sufficient for establishing the required inductor rating during design stage. It is observed from Fig. 4.3 that, the maximum start-up voltage stress can rise up to 1.8 times the normal stress levels in steady state. The higher voltage stress on the dielectric material can reduce capacitor life-time, and significantly compromise the reliability of resonant capacitors, thus additional safety margin is necessary to ensure reliable operation of a resonant power supply.

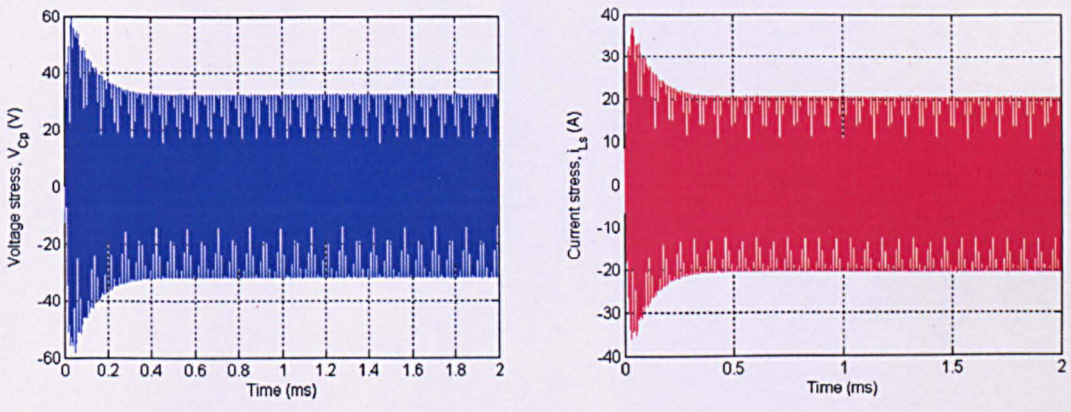

(a) (b)

Figure 4.3 Current and voltage waveforms at f_s=140 kHz and R_L=5Ω (a) v_{Cp} and, (b) i_{Ls}.

The following analysis considers excitation of the converter above resonance (the normal operating condition).

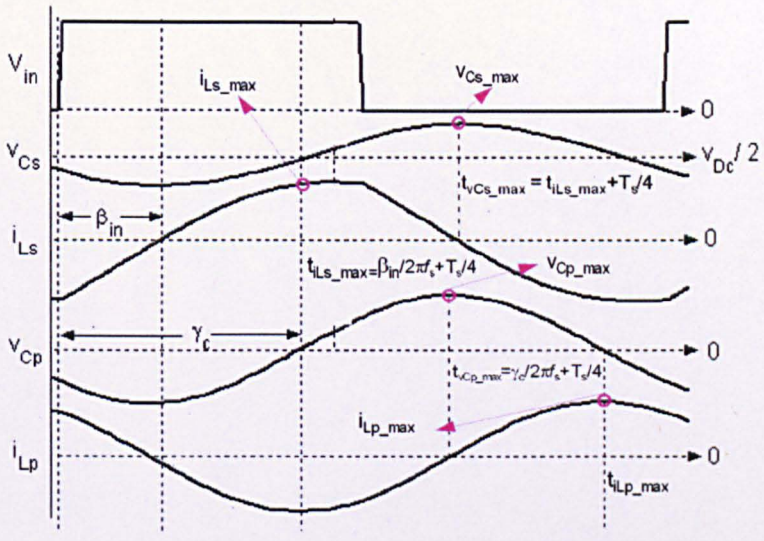

Figure 4.4 Cyclic mode analysis current and voltage waveforms.

Referring to simulated steady-state current and voltage waveforms in Fig. 4.4, and ignoring parasitic resistances, the resonant inductor current, i_{Ls} and the resonant capacitor voltage, v_{Cs} are displaced in phase by $\pi/2$ rads. Hence, the maximum voltage across capacitor C_s occurs when $i_{Ls}=0$.

Taking the input voltage vs. current phase lag β_{in} in (4-25) and normalising through division by 2π, the time at which $i_{Ls}=0$, and the time at which v_{Cs} is a maximum, is in mode M4, i.e.

$$t_{vCs\_\max} = \frac{\beta_{in}}{2\pi f} \tag{4-32}$$

From (4-6), the maximum series capacitor voltage is given by:

$$\hat{v}_{Cs} = \begin{bmatrix}0 & 1 & 0 & 0 & 0 & 0 & 0\end{bmatrix} e^{\hat{A}_4 t_{vCs\_\max}} e^{\hat{A}_3 d_3 T_s} e^{\hat{A}_2 d_2 T_s} e^{\hat{A}_1 d_1 T_s} \hat{x}_{per}(t_0) \tag{4-33}$$

where T_s is the switching period.

The maximum series inductor current is phase-shifted by $\pi/2$ from $\hat{v}_{Cs}$, hence, i_{Ls} is a maximum at time $t_{iLs\_max}= t_{vCs\_max}-(T_s/4)$ and can occur in either M2 or M3 (depending on operating frequency). The time at which i_{Ls} is a maximum ($\hat{i}_{Ls}$) is therefore given by,

$$\hat{x}(t_{iLs\_max})$$

$$= \begin{cases} \hat{x}(t_{iLs\_max\_mode1}) = e^{\hat{A}_1(t_{iLs\_max}-d_1T_s)} e^{\hat{A}_1 d_1 T_s} \hat{x}_{per}(t_0) & \text{for } t_{iLs\_max} \le (d_1+d_2)T_s \\ \hat{x}(t_{iLs\_max\_mode2}) = e^{\hat{A}_3(t_{iLs\_max}-(d_1+d_2)T_s)} e^{\hat{A}_2 d_2 T_s} e^{\hat{A}_1 d_1 T_s} \hat{x}_{per}(t_0) & \text{for } t_{iLs\_max} \le \dfrac{T_s}{2} \end{cases} \tag{4-34}$$

and

$$\hat{i}_{Ls} = [0 \quad 0 \quad 0 \quad 1 \quad 0 \quad 0 \quad 0]\hat{x}(t_{iLs\_max}) \tag{4-35}$$

{Note: with increasing switching frequency the series inductor current becomes increasingly triangular, and the time required for the current waveform to reach its maximum value ultimately increases to $t_{iLs\_max}= (d_1+d_2+d_3)\ T_s$}. Referring to Fig. 4.4, the maximum voltage across the parallel resonant capacitor ($\hat{v}_{Cp}$) is phase-shifted from d_2 by $\pi/2$ rads.

Hence, the maximum parallel capacitor voltage $\hat{v}_{Cp}$ occurs in either M3 ($V_{in} > 0$, $v_{Cp} > 0$) or M4 ($V_{in} = 0$, $v_{Cp} > 0$) depending on the switching frequency, and, using FMA, occurs at time:

$$t_{vCp\_max}$$

$$= \begin{cases} t_{vCp\_max\_mode3} = \dfrac{T_s}{4} - \dfrac{T_s}{2\pi}\tan^{-1}\left(\dfrac{\dfrac{\omega_s^4 Q_{op2}}{\omega_{op1}^2 \omega_{op2}} + \omega_s^2\left(\dfrac{R_{eq}}{\omega_{op1}^2 L_p} + \dfrac{C_s Q_{op2}}{C_p \omega_{op2}} + \dfrac{Q_{op2}}{\omega_{op2}}\right) + \dfrac{R_{eq}}{L_p}}{\omega_s\left[1 - \dfrac{\omega_s^2}{\omega_{op1}^2}\right]} \right) \\ t_{vCp\_max\_mode4} = \dfrac{T_s}{4} - \dfrac{T_s}{2\pi}\left(\pi - \tan^{-1}\left(\dfrac{\dfrac{\omega_s^4 Q_{op2}}{\omega_{op1}^2 \omega_{op2}} + \omega_s^2\left(\dfrac{R_{eq}}{\omega_{op1}^2 L_p} + \dfrac{C_s Q_{op2}}{C_p \omega_{op2}} + \dfrac{Q_{op2}}{\omega_{op2}}\right) + \dfrac{R_{eq}}{L_p}}{\omega_s\left[1 - \dfrac{\omega_s^2}{\omega_{op1}^2}\right]} \right) \right) \end{cases} \tag{4-36}$$

Substituting (4-36) into (4-6), the peak stress across the parallel capacitor, $\hat{v}_{Cp}$, is given by,

$$\hat{x}(t_{vCp\_\max})$$

$$= \begin{cases} \hat{x}(t_{vCp\_\max\_\mathrm{mod}e3}) = e^{\tilde{A}_3(t_{vCp\_\max}-d_1\mathrm{T}_s-d_2\mathrm{T}_s)}e^{\tilde{A}_2 d_2\mathrm{T}_s}e^{\tilde{A}_1 d_1\mathrm{T}_s}\hat{x}_{per}(t_0) & \text{for } t_{vCp\_\max} < \dfrac{\mathrm{T}_s}{2} \\ \hat{x}(t_{vCp\_\max\_\mathrm{mod}e4}) = e^{\tilde{A}_4(t_{vCp\_\max}-0.5\mathrm{T}_s)}e^{\tilde{A}_3 d_3\mathrm{T}_s}e^{\tilde{A}_2 d_2\mathrm{T}_s}e^{\tilde{A}_1 d_1\mathrm{T}_s}\hat{x}_{per}(t_0) & \text{for } t_{vCp\_\max} > \dfrac{\mathrm{T}_s}{2} \end{cases} \tag{4-37}$$

and

$$\hat{v}_{Cp} = [1 \quad 0 \quad 0 \quad 0 \quad 0 \quad 0 \quad 0]\hat{x}(t_{vCp\_\max}) \tag{4-38}$$

With reference to Fig. 4.4, the maximum current $\hat{i}_{Lp}$ flows through parallel resonant inductor L_p, at time $t_{iLp\_\max}=d_5\mathrm{T}_s$ and occurs in M5. The state at which i_{Lp} is a maximum ($\hat{i}_{Lp}$) is therefore given by,

$$\hat{x}(t_{iLp\_\max}) = e^{\tilde{A}_5(t_{iLp\_\max})}e^{\tilde{A}_4 d_4\mathrm{T}_s}e^{\tilde{A}_3 d_3\mathrm{T}_s}e^{\tilde{A}_2 d_2\mathrm{T}_s}e^{\tilde{A}_1 d_1\mathrm{T}_s}\hat{x}_{per}(t_0) \tag{4-39}$$

and

$$\hat{i}_{Lp} = [0 \quad 0 \quad 1 \quad 0 \quad 0 \quad 0 \quad 0]x(t_{iLp\_\max}) \tag{4-40}$$

As previously discussed, the calculated initial conditions are sensitive to the accuracy of duty-times, implying that the electrical stresses on the tank components are also affected. Higher harmonics component of the input voltage can be added into the analysis in a similar manner to (4-30), to enhance the accuracy, at the expense of much greater complexity.

4.3. Cyclic Mode Analysis of Current-Output Converter in Discontinuous Conduction Mode (DCM)

Discontinuous conduction operation occurs when the current-output converter is heavily loaded. Ultimately, when the load on the converter is high, the resonant network cannot supply sufficient current to maintain conduction to the load when the rectifier commutates, and results in distorted rectifier currents when the tank current flows through the rectifier diodes, until $i_{Ls} - i_{Lp} > I_{out}$. Under such circumstances, the input voltage across the bridge rectifier v_R becomes discontinuous, and, for a short period of time, parallel capacitor voltage v_{Cp} is clamped to ≈0V.

Two additional modes of operation, see Fig. 4.5, are therefore included to account for this discontinuous behaviour, when v_{Cp}=0. Again, the variables in the cyclic modal matrices are the states of the input voltage V_{in} and parallel capacitor voltage. Whilst there are two states for the input voltage, the parallel capacitor voltage now has three states to describe the discontinuous conduction mode.

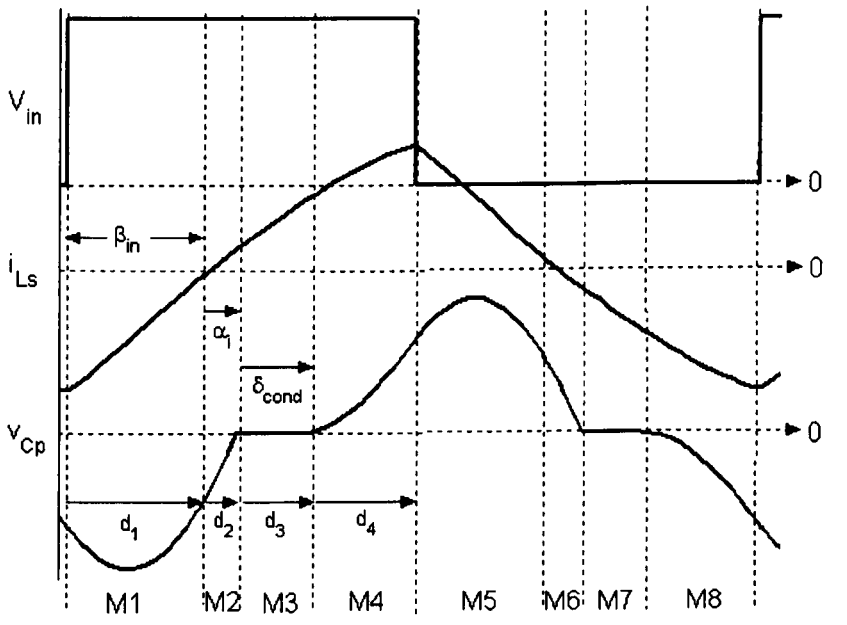

Figure 4.5 Dominant operating modes in discontinuous conduction mode.

Consequently, by assuming a positive input voltage transition marks the start of a cycle, the convention for mode description becomes,

Mode 1 (M1)	$V_{in}>0$	$v_{Cp}<0$	$i_{Ls}<0$
Mode 2 (M2)	$V_{in}>0$	$v_{Cp}<0$	$i_{Ls}>0$
Mode 3 (M3)	$V_{in}>0$	$v_{Cp}=0$	$i_{Ls}>0$
Mode 4 (M4)	$V_{in}>0$	$v_{Cp}>0$	$i_{Ls}>0$
Mode 5 (M5)	$V_{in}=0$	$v_{Cp}>0$	$i_{Ls}>0$
Mode 6 (M6)	$V_{in}=0$	$v_{Cp}>0$	$i_{Ls}<0$
Mode 7 (M7)	$V_{in}=0$	$v_{Cp}=0$	$i_{Ls}<0$
Mode 8 (M8)	$V_{in}=0$	$v_{Cp}<0$	$i_{Ls}<0$

As before, the dynamics and input excitation matrices are found by substituting the coupling equations into the state-variable dynamic model, and considering the state of the two variables. Accounting for the behaviour of the distorted capacitor voltage, the coupling equation simplifies to,

$$i_R = \begin{cases} i_{Lf}\,\mathrm{sgn}(v_{Cp}) & \text{for } |i_L| \geq i_{Lf} \\ i_L & \text{for } |i_L| < i_{Lf} \end{cases} \qquad (4\text{-}41)$$

$$v_R = v_{Cp} + r_{cp}\left(i_{Ls} - i_{Lp} - i_R\right)$$

During M1, $V_{in} > 0$, $v_{Cp} < 0$ and $i_{Ls} < 0$, and consequently, the rectifier current is negative, and the particular piecewise linear state-equation is dictated by the matrices,

$$\mathbf{A}_1 = \begin{bmatrix} 0 & 0 & -\frac{1}{C_p} & \frac{1}{C_p} & 0 & \frac{1}{C_p} \\ 0 & 0 & 0 & \frac{1}{C_s} & 0 & 0 \\ \frac{1}{L_p} & 0 & 0 & 0 & 0 & 0 \\ -\frac{1}{L_s} & -\frac{1}{L_s} & \frac{r_{cp}}{L_s} & -\frac{r_{ds}+r_{cs}+r_{ls}+r_{cp}}{L_s} & 0 & -\frac{r_{cp}}{L_s} \\ 0 & 0 & 0 & 0 & -\frac{1}{C_f(R_L+r_{cf})} & \frac{R_L}{C_f(R_L+r_{cf})} \\ -\frac{1}{L_f} & 0 & -\frac{r_{cp}}{L_f} & -\frac{r_{cp}}{L_f} & -\frac{R_L}{L_f(R_L+r_{cf})} & -\frac{r_{lf}(R_L+r_{cf})+r_{cp}(R_L+r_{cf})+R_L r_{cf}}{L_f(R_L+r_{cf})} \end{bmatrix} \quad \mathbf{B}_1 = \begin{bmatrix} 0 \\ 0 \\ 0 \\ \frac{V_{in}}{L_s} \\ 0 \\ -\frac{2v_{diode}}{L_f} \end{bmatrix}$$

(4-42)

During M2, $V_{in} > 0$, $v_{Cp} < 0$ and $i_{Ls} > 0$ giving,

$$A_2 = \begin{bmatrix} 0 & 0 & -\frac{1}{C_p} & \frac{1}{C_p} & 0 & \frac{1}{C_p} \\ 0 & 0 & 0 & \frac{1}{C_s} & 0 & 0 \\ \frac{1}{L_p} & 0 & 0 & 0 & 0 & 0 \\ -\frac{1}{L_s} & -\frac{1}{L_s} & \frac{r_{cp}}{L_s} & -\frac{r_{ds}+r_{cs}+r_{ls}+r_{cp}}{L_s} & 0 & -\frac{r_{cp}}{L_s} \\ 0 & 0 & 0 & 0 & -\frac{1}{C_f(R_L+r_{cf})} & \frac{R_L}{C_f(R_L+r_{cf})} \\ -\frac{1}{L_f} & 0 & \frac{r_{cp}}{L_f} & \frac{r_{cp}}{L_f} & -\frac{R_L}{L_f(R_L+r_{cf})} & -\frac{r_{lf}(R_L+r_{cf})+r_{cp}(R_L+r_{cf})+R_L r_{cf}}{L_f(R_L+r_{cf})} \end{bmatrix} \quad B_2 = \begin{bmatrix} 0 \\ 0 \\ 0 \\ \frac{V_{in}}{L_s} \\ 0 \\ -\frac{2v_{diode}}{L_f} \end{bmatrix} \tag{4-43}$$

In M3, $V_{in} > 0$ and $i_L < i_{Lf}$, hence, $v_{Cp} = 0$. The excess current from the output filter/load now circulates through the rectifier bridge, and the coupling equation reduces to:

$$\begin{aligned} i_R &= i_{Ls} - i_{Lp} \\ v_R &= 0 \end{aligned} \tag{4-44}$$

The particular piecewise linear state-equation for M3 is therefore given by,

$$A_3 = \begin{bmatrix} 0 & 0 & 0 & 0 & 0 & 0 \\ 0 & 0 & 0 & \frac{1}{C_s} & 0 & 0 \\ \frac{1}{L_p} & 0 & 0 & 0 & 0 & 0 \\ -\frac{1}{L_s} & -\frac{1}{L_s} & 0 & -\frac{r_{ds}+r_{cs}+r_{ls}}{L_s} & 0 & 0 \\ 0 & 0 & 0 & 0 & -\frac{1}{C_f(R_L+r_{cf})} & \frac{R_L}{C_f(R_L+r_{cf})} \\ 0 & 0 & 0 & 0 & -\frac{R_L}{L_f(R_L+r_{cf})} & -\frac{r_{lf}(R_L+r_{cf})+R_L r_{cf}}{L_f(R_L+r_{cf})} \end{bmatrix}, B_2 = \begin{bmatrix} 0 \\ 0 \\ 0 \\ \frac{V_{in}}{L_s} \\ 0 \\ -\frac{2v_{diode}}{L_f} \end{bmatrix} \tag{4-45}$$

and the dynamics matrix, A_4, and the input matrix, B_4, for M4 ($V_{in} > 0$, $v_{Cp} > 0$, $i_{Ls} > 0$) are given by:

$$A_4 = \begin{bmatrix} 0 & 0 & -\frac{1}{C_p} & \frac{1}{C_p} & 0 & -\frac{1}{C_p} \\ 0 & 0 & 0 & \frac{1}{C_s} & 0 & 0 \\ \frac{1}{L_p} & 0 & 0 & 0 & 0 & 0 \\ -\frac{1}{L_s} & -\frac{1}{L_s} & \frac{r_{cp}}{L_s} & -\frac{r_{ds}+r_{cs}+r_{ls}+r_{cp}}{L_s} & 0 & \frac{r_{cp}}{L_s} \\ 0 & 0 & 0 & 0 & -\frac{1}{C_f(R_L+r_{cf})} & \frac{R_L}{C_f(R_L+r_{cf})} \\ \frac{1}{L_f} & 0 & \frac{r_{cp}}{L_f} & \frac{r_{cp}}{L_f} & -\frac{R_L}{L_f(R_L+r_{cf})} & \frac{r_{cf}(R_L+r_{cf})-r_{cp}(R_L+r_{cf})+R_L r_{cf}}{L_f(R_L+r_{cf})} \end{bmatrix} \quad B_4 = \begin{bmatrix} 0 \\ 0 \\ 0 \\ \frac{V_{in}}{L_s} \\ 0 \\ -\frac{2V_{diode}}{L_f} \end{bmatrix} \tag{4-46}$$

Again, using symmetry, the modal and excitation matrices for converter operation in the subsequent half switching cycle, are given by,

$A_5 = A_4$,

$$A_6 = \begin{bmatrix} 0 & 0 & -\frac{1}{C_p} & \frac{1}{C_p} & 0 & -\frac{1}{C_p} \\ 0 & 0 & 0 & \frac{1}{C_s} & 0 & 0 \\ \frac{1}{L_p} & 0 & 0 & 0 & 0 & 0 \\ -\frac{1}{L_s} & -\frac{1}{L_s} & \frac{r_{cp}}{L_s} & -\frac{r_{ds}+r_{cs}+r_{ls}+r_{cp}}{L_s} & 0 & \frac{r_{cp}}{L_s} \\ 0 & 0 & 0 & 0 & -\frac{1}{C_f(R_L+r_{cf})} & \frac{R_L}{C_f(R_L+r_{cf})} \\ \frac{1}{L_f} & 0 & -\frac{r_{cp}}{L_f} & -\frac{r_{cp}}{L_f} & -\frac{R_L}{L_f(R_L+r_{cf})} & -\frac{r_{cf}(R_L+r_{cf})-r_{cp}(R_L+r_{cf})+R_L r_{cf}}{L_f(R_L+r_{cf})} \end{bmatrix},$$

$A_7 = A_3, A_8 = A_1$

$$B_5 = B_6 = B_7 = B_8 = \begin{bmatrix} 0 & 0 & 0 & 0 & 0 & -\frac{2v_{d\,iode}}{L_f} \end{bmatrix}^T$$

(4-47)

As before, the cyclic-mode initial condition, $x_{per}(t_0)$, for the converter subjected to heavy load conditions is obtained through substitution of the piecewise linear equations from (4-42) through to (4-47), into (4-11) to (4-14), along with the switching transition times associated with each operating mode.

4.3.1. Determination of Mode Duty-times during Discontinuous Operation

Fundamentally, when the converter is subjected to high loads the resonant network cannot supply sufficient current to maintain conduction to C_p when the rectifier commutates, and results in distortion of the rectifier voltage, and $v_R \approx 0$. Whilst the transition time in continuous conduction mode operation can be approximated through FMA, or similar frequency-domain techniques, significant errors are incurred when estimating the duty times during heavy loading. In an effort to overcome such deficiencies, the 'Extended Fundamental Frequency Analysis' reported by Forsyth *et al.* in [D5] for 3rd-order LCC resonant converter, is modified and extended here, for the more complex LCLC converter counterpart.

In [D5], the non-conduction phase angle δ_{cond} is introduced as a measure of the interval when v_{Cp} remains at zero, and where, at the end angle $\theta = \delta_{cond}$, the rectifier resumes normal conduction. α_i now

denotes the phase-angle between the input current i_{Ls} and capacitor voltage v_{Cp}. Using basic network theory, v_{cp} can be expressed as a function of the two key angles δ_{cond} and α_i. Having obtained a suitable description of v_{Cp}, the fundamental impedance $Z_{Cp(1)}$ of the parallel combination of C_p and rectifier, can be derived from Ohms law.

An equivalent circuit for the converter is obtained by replacing the bridge rectifier, output filter and load with $Z_{Cp(1)}$ as shown in Fig. 4.6, and the impedance of the resulting equivalent circuit is used to calculate the input voltage vs. current phase angle β_{in} and all the remaining duties.

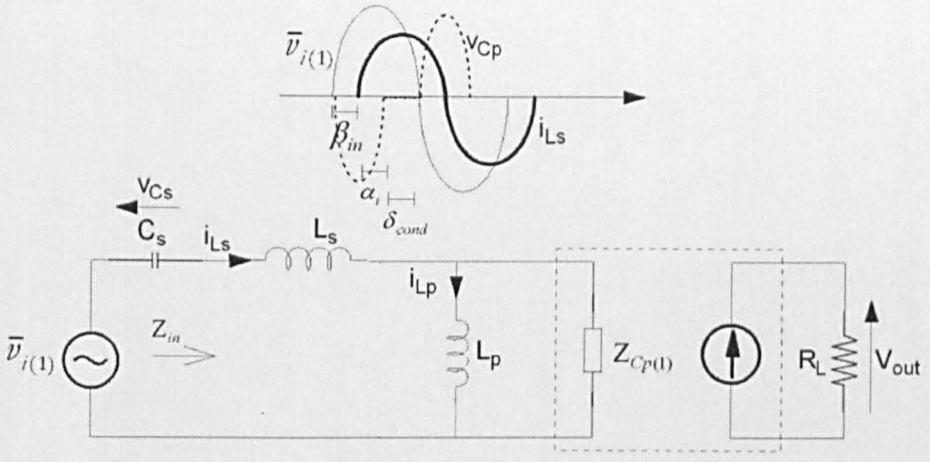

Figure 4.6 Equivalent circuit modelling the fundamental components of converter waveforms in DCM.

At the beginning of a cycle, when v_{Cp} commutates to zero at $t = t_0$, the resonant network cannot supply sufficient current to maintain conduction at the output, and the current waveform into the rectifier bridge i_R is equal to that of current flowing out of the inductor L_s-L_p network. Since the difference between the currents flows into C_p, v_{Cp} remains at zero within the interval δ_{cond} until the current i_L exceeds the output current i_{Lf}. At the end of the interval $0 \le \theta < \delta_{cond}$, the rectifier resumes normal conduction. The parallel capacitor voltage, v_{Cp}, can be expressed as a function of angle θ by considering the positive half cycle of the waveform shown in Fig. 4.7.

During the normal conduction interval $\delta_{cond} \le \theta < \pi$, v_{Cp} is given by,

$$v_{Cp}(\theta) = \frac{1}{2\pi f_s C_p} \int_{\delta_{cond}}^{\theta} \hat{i}_L \sin(\theta + \alpha_i) - i_{out} d\theta \tag{4-48}$$

where $\hat{i}_L \sin(\theta + \alpha_i) = i_{Ls} - i_{Lp}$ is the resonant tank link current.

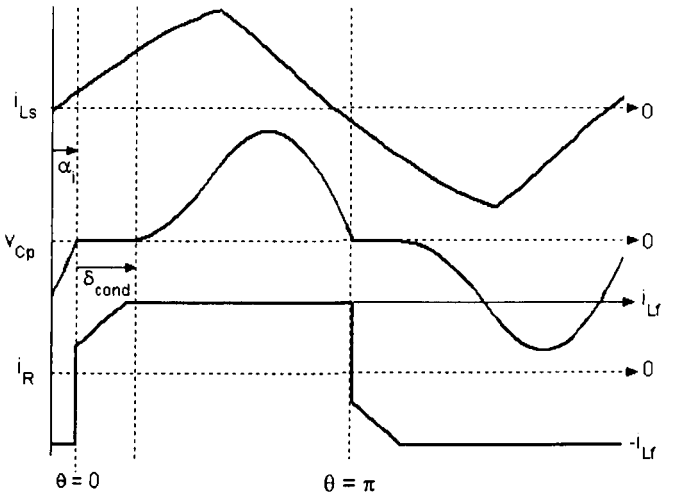

Figure 4.7 Waveforms during DCM operation.

Employing trigonometric functions, $\cos(\alpha+\beta)=\cos(\alpha)\cos(\beta)-\sin(\alpha)\sin(\beta)$ and evaluating the integral in (4-48) yields,

$$v_{Cp}(\theta)=\frac{-i_L\cos(\theta+\alpha_i)+i_L\cos(\delta_{cond}+\alpha_i)+i_{out}(\delta_{cond}-\pi)}{2\pi f_s C_p} \tag{4-49}$$

Exploiting symmetry between the positive- and negative-half cycles of operation, the parallel capacitor voltage can be expressed as a function of angle,

$$v_{Cp}(\theta)=\begin{cases} 0 & \text{for} \quad 0<\theta\le\delta_{\text{cond}} \\ \dfrac{-i_L\cos(\theta+\alpha_i)+i_L\cos(\delta_{cond}+\alpha_i)+i_{out}(\delta_{cond}-\pi)}{2\pi f_s C_p} & \text{for} \quad \delta_{\text{cond}}<\theta\le\pi \\ 0 & \text{for} \quad \pi<\theta\le\pi+\delta_{\text{cond}} \\ \dfrac{i_L\cos(\theta+\alpha_i)-i_L\cos(\delta_{cond}+\alpha_i)-i_{out}(\delta_{cond}-\pi)}{2\pi f_s C_p} & \text{for} \quad \pi+\delta_{\text{cond}}<\theta\le 2\pi \end{cases} \tag{4-50}$$

To determine the boundary defining the capacitor-charging period, it is noted that $v_{Cp}(t_0)=0$ and $v_{Cp}(\pi)=0$, and expressions for the parallel capacitor v_{Cp} when it tends to 0V, can be obtained,

$$\theta=0\rightarrow v_{Cp}(0)=\frac{-i_L\cos(\alpha_i)+i_L\cos(\delta_{cond}+\alpha_i)+i_{out}\delta_{cond}}{2\pi f_s C_p}=0 \tag{4-51}$$

and

$$\theta=\pi\rightarrow v_{Cp}(\pi)=\frac{-i_L\cos(\pi+\alpha_i)+i_L\cos(\delta_{cond}+\alpha_i)+i_{out}(\delta_{cond}-\pi)}{2\pi f_s C_p}=0 \tag{4-52}$$

Under steady state conditions, the output voltage (V_{out}) from the converter, can be determined, by calculating the average voltage across the bridge rectifier during a complete cycle. Since the resonant current charges the parallel capacitor during intervals $\delta_{cond} \le \theta < \pi$ and $\pi + \delta_{cond} \le \theta < 2\pi$, the output voltage can be determined from,

$$V_{out} = \frac{1}{2\pi}\left\{ \int_{\delta_{cond}}^{\pi} v_{Cp}(\theta) + \int_{\pi+\delta_{cond}}^{2\pi} -v_{Cp}(\theta) \right\} \tag{4-53}$$

Again, exploiting symmetry over half a switching cycle, substituting (4-52) into (4-53) and evaluating the integral allows the solution for V_{out}, as follows:

$$V_{out} = \frac{1}{\pi}\int_{\delta_{cond}}^{\pi} \frac{-i_L \cos(\theta+\alpha_i) + i_L \cos(\delta_{cond}+\alpha_i) + i_{out}(\delta_{cond}-\pi)}{2\pi f_s C_p} d\theta$$

$$= \frac{i_L \sin(\alpha_i) + (\pi - \delta_{cond}) i_L \cos(\delta_{cond}+\alpha_i) + i_L \sin(\delta_{cond}+\alpha_i) + i_{out}\left(\frac{2\pi\delta_{cond} - \pi^2 - \delta_{cond}^2}{2}\right)}{2\pi^2 f_s C_p} \tag{4-54}$$

By noting that the output current is described by $i_{out} = i_L \sin(\alpha_i + \delta_{cond})$, and the output voltage by $V_{out} = i_{out} R_L$, (4-54) can be rearranged to give,

$$i_{out} R_L = \frac{i_L \sin(\alpha_i) + (\pi - \delta_{cond}) \times i_L \cos(\delta_{cond}+\alpha_i) + i_L \sin(\alpha_i+\delta_{cond}) \times \left(1 + \pi\delta_{cond} - \frac{(\pi^2 + \delta_{cond}^2)}{2}\right)}{2\pi^2 f_s C_p}$$

$$\sin(\alpha_i) + (\pi - \delta_{cond})\cos(\delta_{cond}+\alpha_i) + \left(1 + \pi\delta_{cond} - \frac{(\pi^2+\delta_{cond}^2)}{2} - 2\pi^2 f_s R_L C_p\right) = 0 \tag{4-55}$$

The key step in determining the three mode transition-times is to obtain the phase-angles δ_{cond} and α_i. Equations (4-52) and (4-55) can be solved numerically for these angles,

$$\sin(\alpha_i) + (\pi - \delta_{cond})\cos(\delta_{cond}+\alpha_i) + \left(1 + \pi\delta_{cond} - \frac{(\pi^2+\delta_{cond}^2)}{2} - 2\pi^2 f_s R_L C_p\right) = 0$$

$$-\cos(\pi+\alpha_i) + \cos(\delta_{cond}+\alpha_i) + (\delta_{cond}-\pi)\sin(\alpha_i+\beta_{in}) = 0 \tag{4-56}$$

Having established satisfactory values of δ_{cond} and α_i, from (4-49) the fundamental frequency component of the parallel capacitor voltage, $v_{Cp(1)}$ is given by,

$$\begin{aligned} v_{Cp(1)} &= \frac{2}{\pi}\int_{\delta_{cond}}^{\pi} v_{Cp}(\theta)e^{-j\theta}d\theta \\ &= \frac{2}{\pi}\int_{\delta_{cond}}^{\pi} \frac{-i_L\cos(\theta+\alpha_i)+i_L\cos(\delta_{cond}+\alpha_i)+i_{out}(\delta_{cond}-\pi)}{2\pi f_s C_p}\times e^{-j\theta}d\theta \end{aligned} \tag{4-57}$$

The 'extended fundamental frequency analysis' equivalent impedance, modelling the non-linear behaviour of the parallel capacitor voltage and filter, is therefore given by,

$$\begin{aligned} &Z_{Cp(1)} \\ &= \frac{1}{2\pi^2 f_s C_p}\left[\begin{array}{c} 2\sin(\alpha_{in}+\delta_{cond})\sin(\alpha_{in})-\cos^2(\alpha_{in})-\cos^2(\alpha_{in}+\delta_{cond})+2 \\ +j\sin(\alpha_{in}+\delta_{cond})(2\cos(\alpha_{in})+\cos(\alpha_{in}+\delta_{cond}))+\sin(\alpha_{in})\cos(\alpha_{in})+\delta_{cond}-\pi \end{array}\right] \end{aligned} \tag{4-58}$$

The overall system impedance Z_{in} of the equivalent circuit is,

$$Z_{in} = j\omega_s L_s + \frac{1}{j\omega_s C_s} + 1 \Big/ \left(\frac{1}{j\omega_s L_p} + \frac{1}{Z_{Cp(1)}}\right) \tag{4-59}$$

The M1 transition duty (d_1), is defined as the time when input current i_{Ls} =0, and can be derived from knowledge of Z_{in}. Taking the input voltage vs. current phase angle β_{in}, and subsequently normalising by 2π, yields:

$$d_1 = \frac{1}{2\pi}\times\tan^{-1}\left(\frac{\omega_s^2\left(L_sC_sZ_{Cp(1)}+L_pC_sZ_{Cp(1)}\right)-Z_{Cp(1)}}{\omega_s(\omega_s^2 L_sL_pC_s-L_p)}\right) \tag{4-60}$$

Exploiting symmetry over a half switching cycle, the remaining duties are found to be:

$$\begin{aligned} d_2 &= \frac{\alpha_i}{2\pi} \\ d_3 &= \frac{\delta_{cond}}{2\pi} \\ d_4 &= 0.5 - d_1 - d_2 - d_3 \\ d_5 &= d_1 \\ d_6 &= d_2 \\ d_7 &= d_3 \\ d_8 &= d_4 \end{aligned} \tag{4-61}$$

4.4. Accuracy of Cyclic Averaging Analysis

The accuracy of the cyclic-analysis, and the related averaging method, for predicting the steady-state behaviour of 4th-order inductor-loaded converter, is now demonstrated by comparison with measurements from a prototype converter, Fig. 4.8, with components given in Table 2.1, over a range of operating conditions.

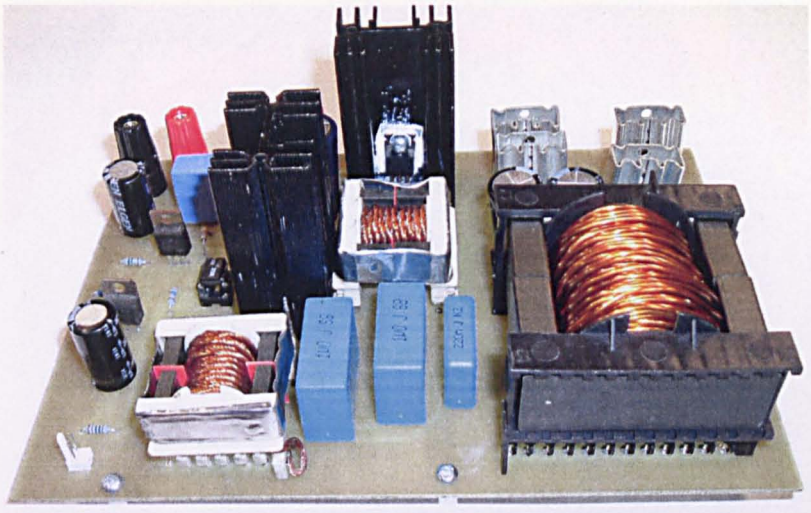

Figure 4.8 Experimental setup for current-output 4th-order resonant converter.

Table 2.1 Voltage-output converter model parameters.

Parameters	Values
DC link input voltage, v_{DC} (V)	20, 25, 30
Series resonant inductance, L_s (μH)	2.7
Series resonant capacitance, C_s (μF)	2
Parallel resonant inductance, L_p (μH)	5.4
Parallel resonant capacitance, C_p (μF)	1
Switching devices internal on resistance, r_{ds} (Ω)	0.04
Inductor L_s series resistance, r_{ls} (Ω)	0.1
Inductor L_p series resistance, r_{lp} (Ω)	0.15
Instantaneous diode forward voltage drop, v_{diode} (V)	0.85
Output filter inductance, L_f (mH)	1
Output filter capacitance, C_f (μF)	33
Output load Resistance, R_L (Ω)	2.5, 5
Nominal operating frequency, f_s (kHz)	140

By way of example, Fig. 4.9 compares predictions and measured output voltages, for two light load conditions, whilst Fig. 4.10 shows the resulting electrical stresses on tank components. For comparison purposes, Fig. 4.10(c) shows experimental waveforms of measured voltage/current across/through the resonant capacitors and inductors, whilst operating in the region of the resonant frequency.

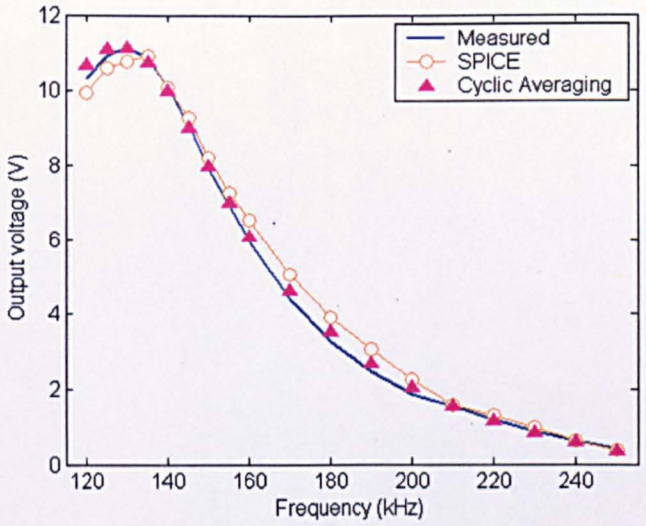

(a)

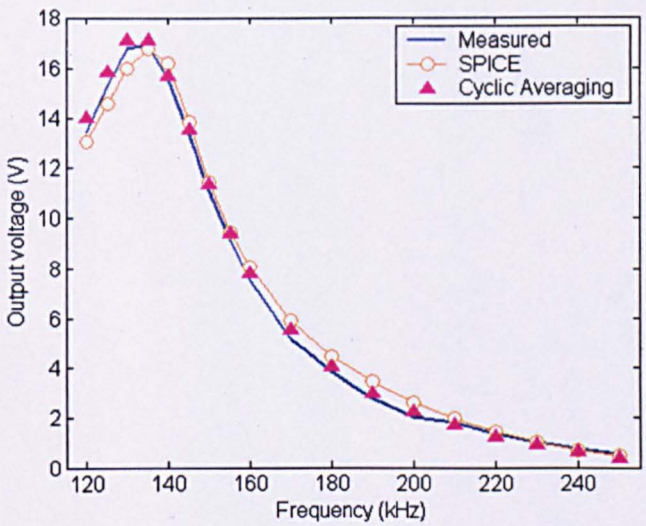

(b)

Figure 4.9 Output voltage of current-output LCLC converter (a) R_L= 5Ω and (b) R_L= 2.5Ω.

Also, for completeness, the variation of output voltage, with excitation frequency, derived using cyclic averaging, is compared with practical measurements from the experimental converter, loaded with R_L = 5Ω for two input voltage levels, in Fig. 4.11. In each case it can be seen that a good correlation between predictions and measurements exists.

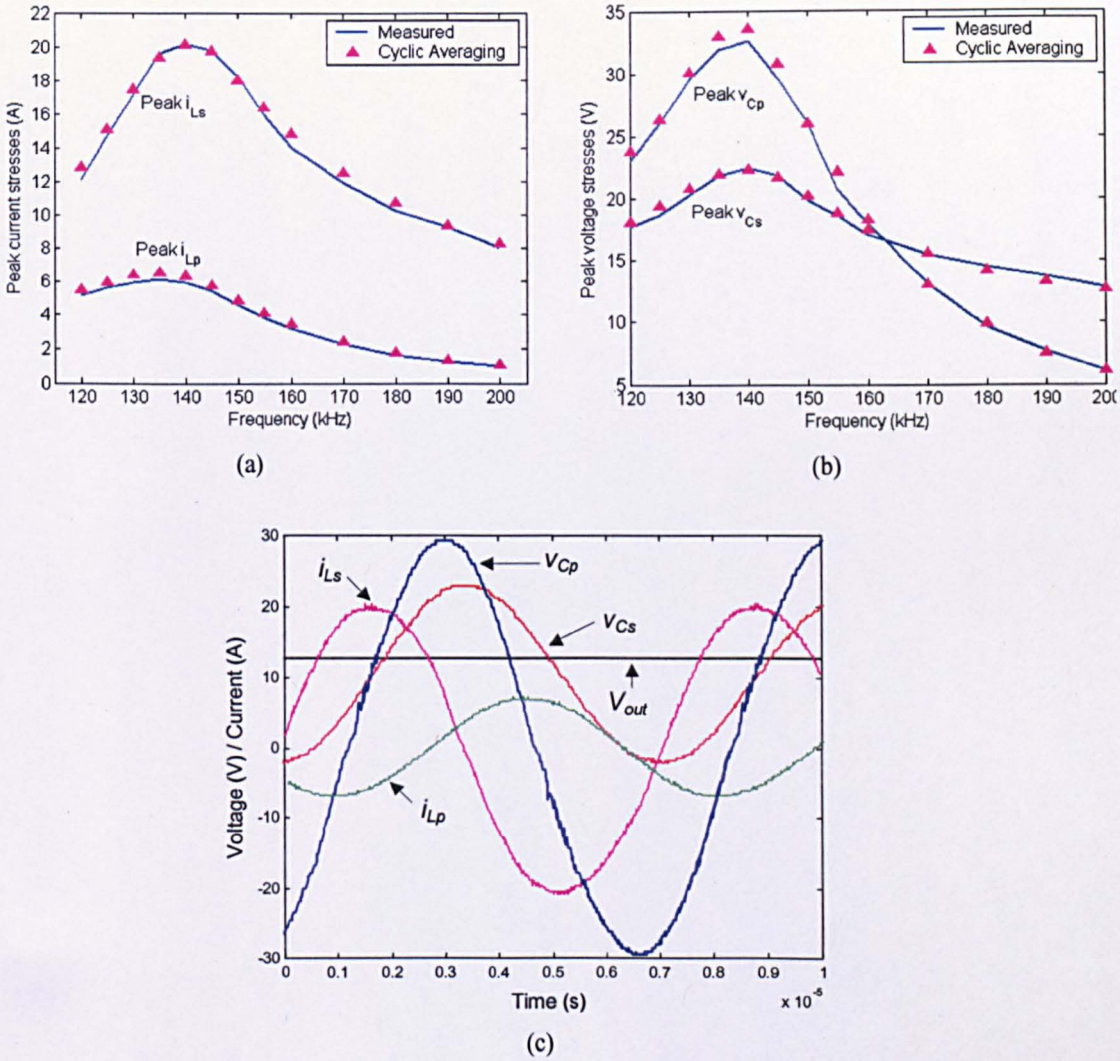

Figure 4.10 Currents and voltages of current-output LCLC converter: (a) Predicted and measured current stresses (b) Voltage stresses and (c) Experimental waveforms of the current-output LCLC converter.

An example state-space portrait showing the converter's behaviour (during continuous conduction operation), from cyclic analysis, is given in Fig. 4.11(c). From an execution speed perspective, the cyclic-based averaging predictions take ≈10ms in MATHWORKS® MATLAB to analyze the current-

output converter at one frequency point, compared to an execution time of 73s for the SPICE transient analysis (5ms to steady state with maximum step size of $1/10 f_s$).

In general, it is notable that the overall calculation time for generating a frequency sweep of the output voltage using cyclic averaging, is typically $1/10{,}000^{th}$ of that for the generation of similar results using SPICE. Likewise, the execution time is at least $1/1000^{th}$ of that for the integration-based state-variable model simulations.

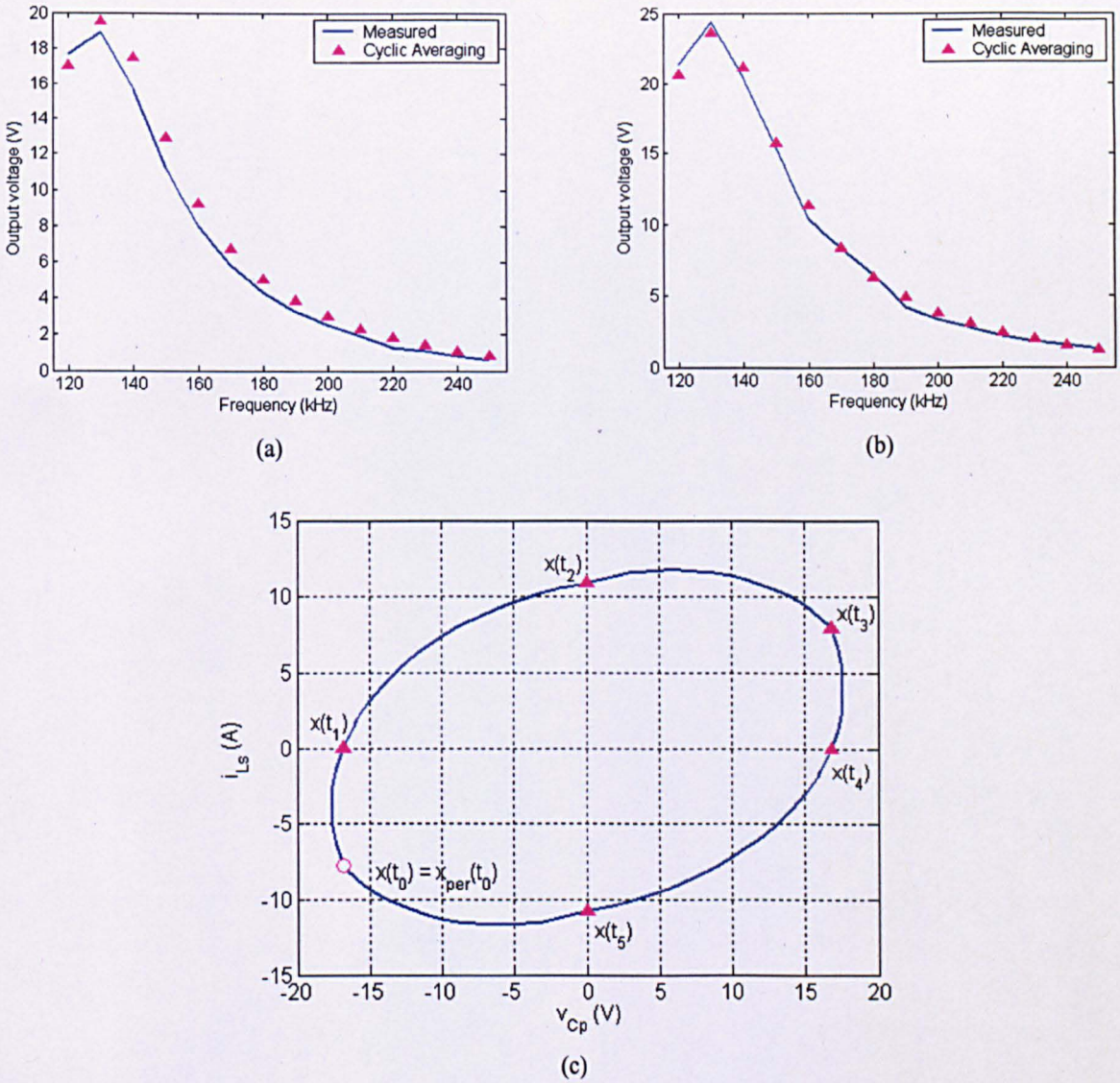

Figure 4.11 Predicted output voltage from cyclic averaging: (a) V_{in} = 25V, (b) V_{in} = 30V and (c) State plane trajectory predicted by the cyclic averaging.

For completeness, Fig. 4.12 gives a demonstration of accuracy of cyclic-analysis for predicting the output voltage of the converter when it is subjected to heavy loading conditions. The output voltages determined from state-space model simulations are compared with those obtained from cyclic-analysis, and confirm the accuracy of the proposed methodology.

As a matter of interest, Fig. 4.12(c) shows an example state-plane portrait of the series resonant inductor current, i_{Ls} against the parallel capacitor voltage v_{Cp} during discontinuous conduction mode.

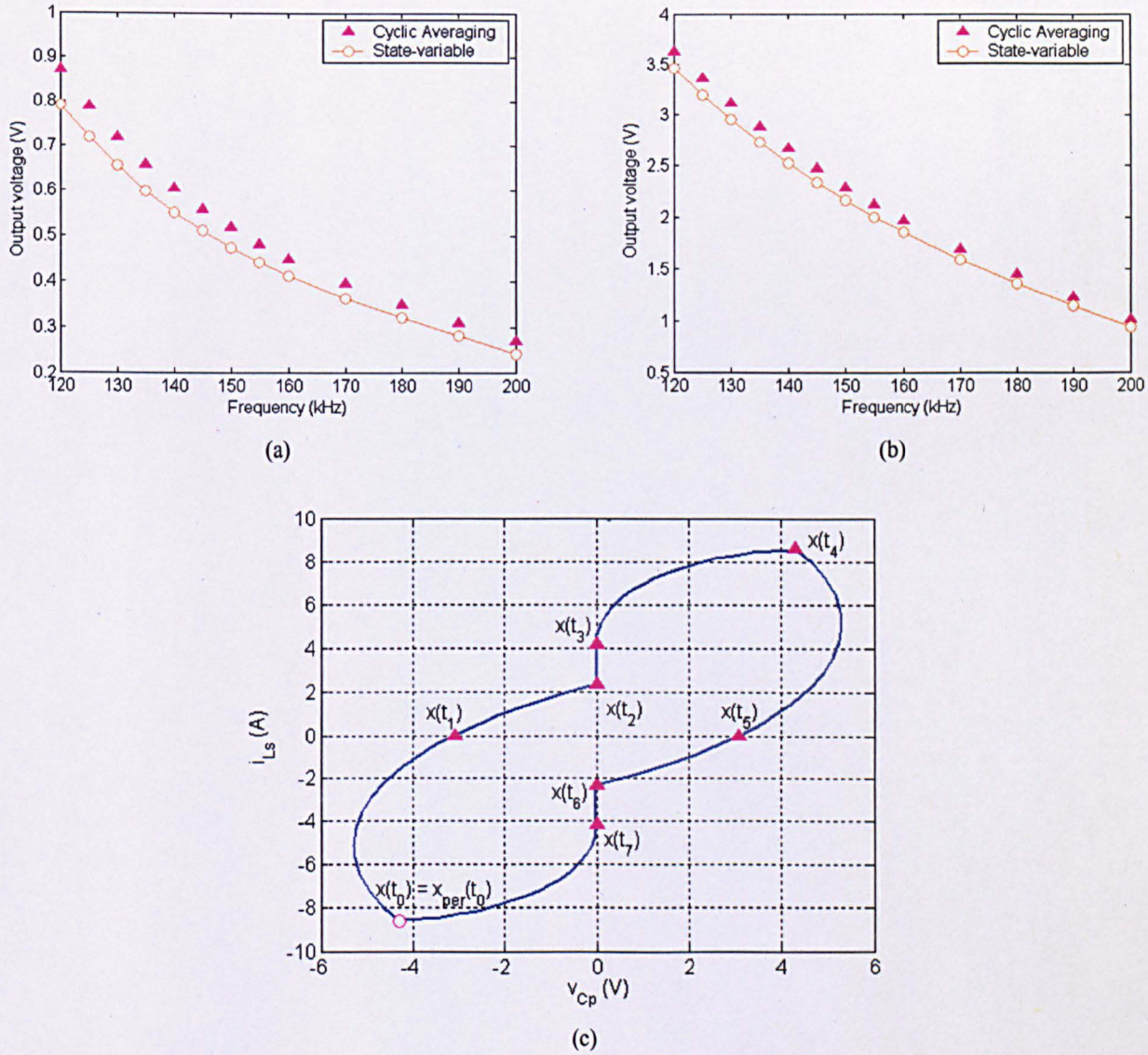

Figure 4.12 Cyclic averaging analysis estimated output voltage (a) R_L= 0.1Ω and (b) R_L= 0.5Ω and (c) State plane trajectory of the resonant converter.

4.5. Summary

A methodology based on cyclic-averaging techniques to facilitate the high-speed, steady-state analysis of current-output resonant power converters, has been presented, and its virtues have been demonstrated by comparing predictions with measurements from a 4th-order converter. State-variable dynamic descriptions for each operating mode, have been derived, and analytical formulae have been employed to estimate the mode duties for converters operating in both continuous (CCM) and discontinuous conduction modes (DCM).

The subsequent peak electrical stresses have also been estimated using an extension to the cyclic-analysis methods. The accuracy of the proposed analysis methodologies has also been demonstrated by comparisons with practical measurements, SPICE simulations, and the results from the non-linear state variable model, and are shown to require significantly less computation overhead at the expense of only obtaining steady-state solutions.

References

[D1] H. R. Visser and P. J. Bosch, "Modelling of Periodically Switching Networks", in *22nd IEEE Power Electronics Specialists Conference Rec.*, 1991, pp. 67-73.

[D2] M. P. Foster, H. I. Sewell, C. M. Bingham, D. A. Stone, D. Hente and D. Howe, "High speed Analysis of Resonant Power converters", *IEE Proc. Electric Power Applications*, **150,** pp. 62-70, 2003.

[D3] Y. Ang, M. P. Foster, C. M. Bingham, D. A. Stone, H. I. Sewell and D. Howe, "Analysis of 4th-order LCLC Resonant Power Converters", *IEE Proc. Electric Power Applications*, **151**, pp. 169-181, 2004.

[D4] J. Cheng and A. F. Witulski, "Analytic Solutions for LLCC Parallel Resonant Converter Simplify Use of Two- and Three-Element Converters", *IEEE Trans. on Power Electronics*, **13**, pp. 235-242, 1998.

[D5] A. J. Forsyth, G. A. Ward and S. V. Mollov, "Extended Fundamental Frequency Analysis of LCC Resonant Converter", *IEEE Trans. on Power Electronics*, **18**, pp. 1286-1292, 2003.

CHAPTER 5

Case study: LCLC Converters for Capacitively-Coupled Electronic Lamp Ballasts

Features of the 4th-order LCLC resonant converter, have been considered in Chapter 3. From the input-to-output voltage transfer function, in Fig. 3.5, it can be seen that for $\omega_s/\ \omega_o = 0.85$ to 1.3, load regulation is relatively poor, especially near resonant, at $\omega_s/\ \omega_o = 1$. If good load regulation is desired, then the converter has to be operated above $\omega_s/\ \omega_o = 1.3$. Operation far below resonance also leads to the influence of the secondary resonance, or discontinuous mode operation.

Although such features can make LCLC converters ill-suited for some classical power supply applications, they can be employed to particular advantage in specialized applications. One such use, is for fluorescent lamp ballasts, and, here, a prototype 12V:300V ballast is considered as a case-study example. The electronic ballast normally requires a very high no-load voltage, prior to lamp ignition, and subsequently, a lower converter output voltage at full load.

Methodologies for analyzing and designing an LCLC resonant ballast, operating at 2.63MHz, are given, with the high operating frequency being shown to facilitate capacitive discharge and appropriate filtering for EMI, with near-resonance switching, at high load quality factor, promoting high efficiency operation.

State-variable dynamic descriptions of the converter, are derived, and subsequently employed to rapidly determine the steady-state cyclic behavior of the ballast during nominal operation, and, importantly, provide estimates of the voltage and current stresses on resonant tank components. Furthermore, from the frequency domain analysis equations, a structured design procedure to realize 4th-order electronic ballasts, is given. Simulation and experimental measurements from a prototype ballast circuit driving a 60cm, 8W T5 fluorescent lamp, are included, to demonstrate the accuracy of the modeling and design methodologies.

5.1. Fluorescent Lighting—Background

Fluorescent illumination takes a major role in today's lighting requirements (with around 1.2 billion units being produced per annum) due to benefits afforded by crisp white light output compared to traditional incandescent and high intensity discharge lamps. Fluorescent lamps also provide a higher Lumens/Watt output, and higher efficiency, particularly when excited at high frequencies, typically 30-50kHz, by virtue of there being insufficient time between each half cycle of the supply for a significant number of mercury ions in the discharge to re-combine (and thereby necessitating a re-strike), as occurs with standard mains frequency excitation, for instance.

The affect of this non-linear frequency dependence of lamp voltage and current can be seen from a comparison of Figs. 5.1(a) & 5.1(b), which show the voltage vs. current relationship for an 8W, 60cm, T5 fluorescent tube excited by 50Hz and 50kHz input voltage, respectively. The relative 'loop area' shows that less re-combination occurs within the lamp between each half cycle of the input voltage when high frequency excitation is employed.

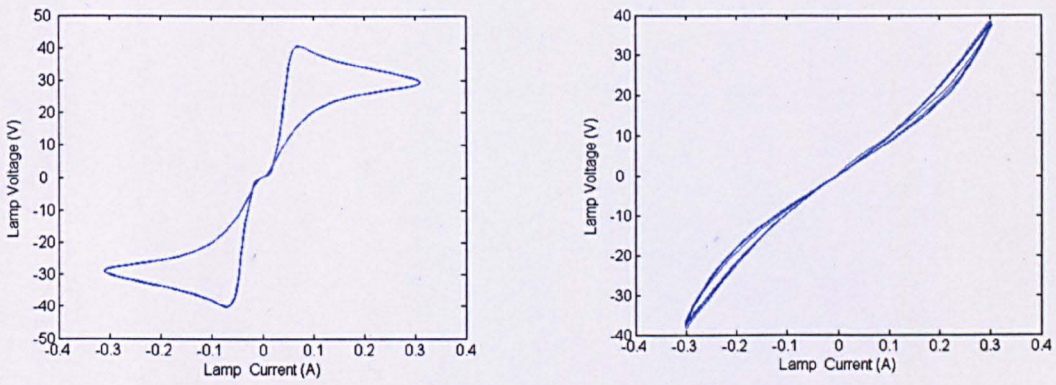

(a) (b)

Figure 5.1 Lamp voltage vs. current: (a) 50Hz excitation; (b) 50 kHz excitation.

Typically, fluorescent lamps are constructed with an oxide coated, tungsten filament electrode. Passing current through the electrode prior to striking, to heat it (termed pre-heating), lowers the electrode work function, thereby allowing electrons to be emitted more readily. This consequently allows the lamp to strike at a lower voltage than would normally be required, which in-turn reduces damage to the electrode from ion bombardment during the ignition event. Despite electrode pre-heating, however, the most common lamp failure mechanism is due to breakdown of the coating on the electrodes, giving rise to a blackening at one end of the tube, and the lamp subsequently acting with similar characteristics to that of a gas diode.

To circumvent this problem, and ultimately increase lamp lifetime, electrode-less lamps have been developed with various techniques being employed to sustain the arc viz. RF induction and capacitive discharge, by Wharmby [E1], that usually require excitation frequencies in the MHz range. Bakker *et al.* [E2] also demonstrate the use of impedance measurements to understand the non-linear effects of stray impedances associated with RF discharge. Along with increasing lifetime, electrode-less excitation also removes the loss associated with electrode heating, and, therefore, encourages higher operating efficiency. Although RF discharges are extremely stable, the lack of inexpensive, efficient electronic ballasts has impeded the development of commercially viable capacitive discharge lamps. Nevertheless, such lamps (for example the 2.5MHz GE Lighting *Genura* 23W, and 2.65MHz Philips QL 85W commercially available induction coupled lamps) are increasingly becoming preferred candidates for use in inaccessible environments (high-ceiling sports halls, for instance) and where low maintenance is a requirement.

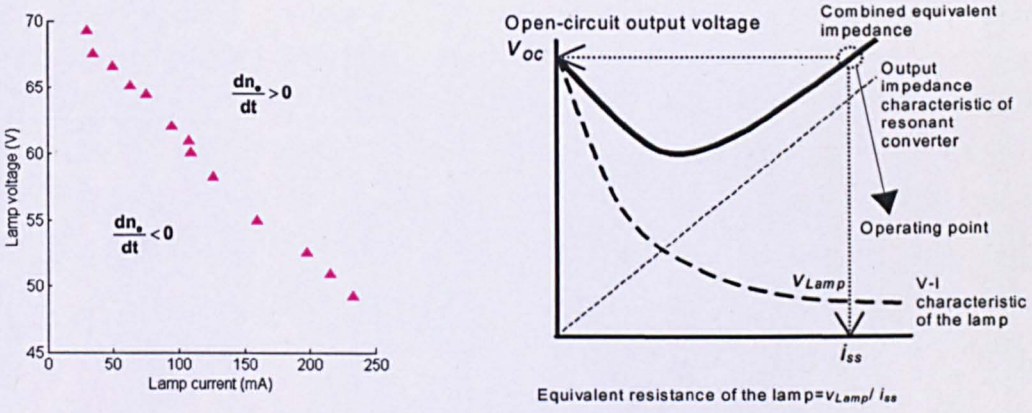

(a) (b)

Figure 5.2 Lamp characteristics (a) Measured voltage and current characteristics and (b).

To provide ignition and sustained light output from the lamp, an electronic ballast must develop sufficiently high voltage, typically between 400V and 1000V, for striking, and subsequently provide current limiting to promote stable operation. The latter issue is a key motivator for adopting resonant converters for lamp ballasts, since, after striking, the lamp exhibits a negative incremental impedance characteristic, as shown in Fig. 5.2(a) for an 8W lamp. The output impedance of resonant converter naturally acts to counter this destabilizing characteristic and encourages steady continuous operation. For example, Fig. 5.2(b) shows the effect of output impedance of resonant converter in stabilizing the lamp current. Before the lamp is ignited, the resistance of fluorescent tube presented to the output of the ballast, is infinite i.e. the output stage is essentially an open-circuit. A very high voltage, V_{oc} is required to achieve gaseous discharge.

Upon application of ignition voltage to the lamp-ballast system and establishment of ionization, the lamp voltage decreases whilst the lamp current increases. The internal impedance seen by the lamp, $R_{lamp}=v_{Lamp}/\ \underline{i_{ss}}$ has negative incremental characteristic. As illustrated in Fig. 5.2(b), the output impedance characteristic of the resonant converter has a positive gradient, and the resulting operating characteristic of the lamp-ballast system will also have positive impedance gradient. Consequently, the ballast stabilizes the lamp characteristic.

When operating without electrodes, the requirement for high frequency excitation also provides the additional benefit of reducing the volume envelope requirements of the reactive components of the ballast; although this is at the expense of significantly complicating the design of the ballast since circuit behaviour can become dominated by parasitic elements.

5.1.1. High Voltage Resonant Electronics Ballast Selection

Electronic ballasts with half-bridge series resonant inverters are relatively straightforward to design, and have been widely reported e.g. [E3, E4, E5], along with more complicated 3rd-order LCC inverter variants [E6]. More generally, however, for applications that are battery powered or require battery backup facilities, for instance, the low DC input voltage must be 'boosted' for lamp ignition through the incorporation of a step-up transformer [E7]. Time domain mathematical models used to describe compact fluorescent ballasts have been previously reported in [E8, E9], where theoretical results of series-resonant and series-parallel LCC electronic ballasts are shown to provide good agreement with measured data, at the expense of requiring significant computation overhead. More often therefore, designers resort to Fundamental Mode Approximation (FMA) [E10, E11] for simplifying and speeding-up the design and analysis process, at the expense of neglecting the important harmonic and sub-harmonic content of the circuit voltages and currents.

The 4th-order resonant converter shown in Fig. 5.3 is particularly suited to high voltage electronic ballast applications, where, on the account of the high frequency behaviour of the fluorescent lamp, the gas discharge can be modelled by resistor. In such cases, the subsequent effects of the high-frequency transformer's leakage inductance and inter-winding capacitance can have profound effect on circuit behaviour, and are best represented by a model of a LCLC inverter. The 4th-order resonant inverter avoids problems such as current and voltage spikes associated with leakage inductance and winding capacitance, by incorporating them directly into the resonant tank elements, thereby eliminating the effect caused by transformer parasitic, and allowing the converter to operate efficiently and reliably. Indeed, other low order resonant converter topologies, such as the series and parallel inverter variants,

when used in high voltage and high frequency applications, with a non-ideal transformer, are likely to exhibit 4th-order characteristics.

As described previously, the widespread adoption of such high-order resonant inverters, has been impeded by and the lack of suitable design methodologies that can provide an accurate and rapid analysis of the circuit at the design stage; particularly those that consider the significant effects that parasitic resistances, capacitances and inductances have on the resonant tank behaviour. Here then, *cyclic mode analysis* is again considered as a candidate technique for the rapid analysis and design of an inverter, suitable for use as an electronic ballast, with the lamp providing a suitable candidate application for exploitation and verification of the analysis methodology.

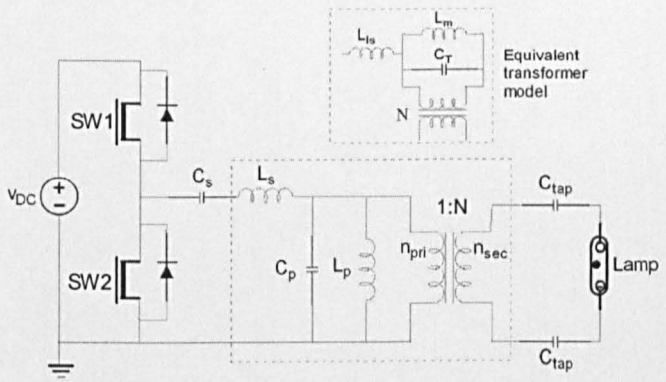

Figure 5.3 Proposed resonant inverter for fluorescent lamp ballast applications.

5.2. Analysis of Resonant Inverter in Cyclic Mode

Figure 5.4 shows the proposed electronic ballast in terms of idealised reactive components along with their associated series parasitic resistances. At very high frequencies, the reactance of the low value capacitances, C_{tap} become very small. This allows the impedance of the capacitances to be modelled as part of the internal impedance of the converter. Upon ignition, the output impedance of the resonant converter compensates the negative incremental resistance effect of the fluorescent lamp, thus the inverter's output can then be conveniently modelled as a pure (apparent) resistance, R_i. In high frequency inverters, such as considered here, the parallel resonant components, L_p and C_p, are designed to be the magnetising inductance and parasitic capacitance of a step-up transformer, whilst the series resonant component, L_s, takes advantage of the transformer leakage inductance. In this way, the high order circuit is achieved with few additional passive components.

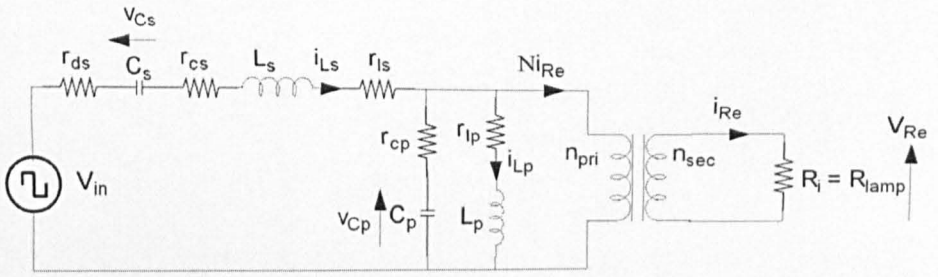

Figure 5.4 Simplified circuit of electronic ballast.

A state-variable dynamic model of the circuit can be derived by considering the resonant tank components and power switches:

$$\begin{aligned}
\frac{dv_{Cp}}{dt} &= \frac{i_{Ls} - i_{Lp} - \mathrm{N}i_{\mathrm{Re}}}{C_p} \\
\frac{dv_{Cs}}{dt} &= \frac{i_{Ls}}{C_s} \\
\frac{di_{Lp}}{dt} &= \frac{v_{Cp} - i_{Lp}\left(r_{cp} + r_{lp}\right) + r_{cp}i_{Ls} - \mathrm{N}r_{cp}i_{\mathrm{Re}}}{L_p} \\
\frac{di_{Ls}}{dt} &= \frac{V_{in} - v_{Cs} - v_{Cp} - i_{Ls}\left(r_{ds} + r_{cp} + r_{cs} + r_{ls}\right) + r_{cp}i_{Lp} + \mathrm{N}r_{cp}i_{\mathrm{Re}}}{L_s}
\end{aligned} \tag{5-1}$$

with the resonant inverter's output voltage v_{Re} and load current i_{Re} given by:

$$\begin{aligned}
v_{\mathrm{Re}} &= \mathrm{N}\left(v_{Cp} + r_{cp}\left(i_{Ls} - i_{Lp} - \mathrm{N}i_{\mathrm{Re}}\right)\right) \\
i_{\mathrm{Re}} &= \mathrm{N}\left(\frac{v_{Cp} + r_{cp}(i_{Ls} - i_{Lp})}{(R_i + \mathrm{N}^2 r_{cp})}\right)
\end{aligned} \tag{5-2}$$

The resulting state-variable model is therefore:

$$\begin{bmatrix} \dot{v}_{Cp} \\ \dot{v}_{Cs} \\ \dot{i}_{Lp} \\ \dot{i}_{Ls} \end{bmatrix} = \begin{bmatrix} 0 & 0 & -\frac{1}{C_p} & \frac{1}{C_p} \\ 0 & 0 & 0 & \frac{1}{C_s} \\ \frac{1}{L_p} & 0 & -\frac{r_{cp} + r_{lp}}{L_p} & \frac{r_{cp}}{L_p} \\ -\frac{1}{L_s} & -\frac{1}{L_s} & \frac{r_{cp}}{L_s} & -\frac{r_{ds} + r_{cs} + r_{cp} + r_{ls}}{L_s} \end{bmatrix} \begin{bmatrix} v_{Cp} \\ v_{Cs} \\ i_{Lp} \\ i_{Ls} \end{bmatrix} + \begin{bmatrix} -\frac{\mathrm{N}i_{\mathrm{Re}}}{C_p} \\ 0 \\ -\frac{\mathrm{N}r_{cp}i_{\mathrm{Re}}}{L_p} \\ \frac{V_{in}}{L_s} + \frac{\mathrm{N}r_{cp}i_{\mathrm{Re}}}{L_s} \end{bmatrix} \tag{5-3}$$

To demonstrate the accuracy of the model, a prototype 4th-order LCLC inverter (v_{DC} = 12V, L_s = 2.6μH, L_p = 4μH, C_s = 6nF and C_p = 3nF, R_i = 470Ω) is considered. A step-up high-frequency toroidal transformer with secondary-to-primary turns ratio of N = 2, is also incorporated. Figure 5.5(a) shows the predicted steady-state operating waveforms from the state-variable model, and Fig. 5.5(b) compares the output voltage derived from state-variable model (simulated to steady state) with measurements taken from the experimental ballast. Although the state-variable description can accurately model the transient behaviour of the 4th order inverter, as before, the execution time remains prohibitive due to the requirement for integration. As discussed in detail in Chapter 4, this drawback can be abated to some degree by only considering the steady-state behaviour of the circuit, thereby allowing analytical solutions from the state equations to be obtained for investigative and design validation purposes.

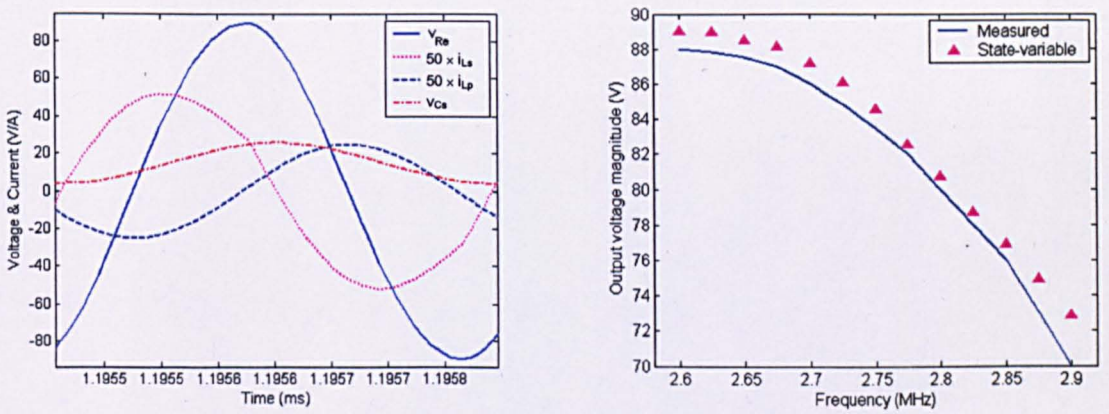

(a) (b)

Figure 5.5 State-variable model simulation result of the 4th-order LCLC resonant inverter (a) Voltage and current waveform and (b) Output voltage against frequency.

In particular, cyclic modelling, which has been employed previously for 4th-order current-output resonant converters in Chapter 3, provides a convenient methodology to facilitate the rapid solution of the steady state voltages and currents for the 4th-order ballast considered here. For operation above resonance, which is the norm, by describing the input voltage as a bipolar square wave, it is possible to see, that, for a particular resonant inverter, the initial conditions can be found from just two dominant modes, termed Mode 1 (M1) and Mode 2 (M2), which are defined with respect to the polarity of input voltage V_{in} [E12], see Fig. 5.6.

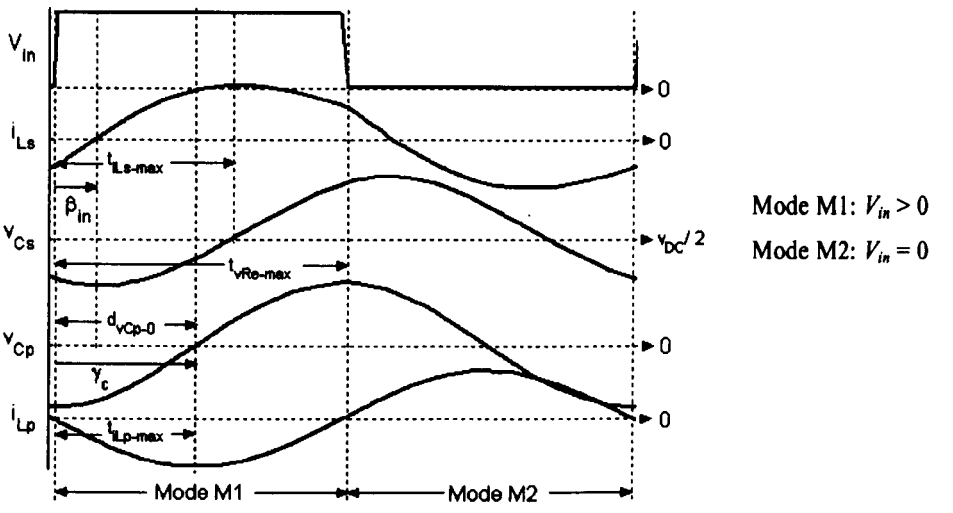

Figure 5.6 Dominant operating modes and definitions of phase angles.

Cyclic mode descriptions of circuit behaviour are given by the dynamics matrices A_i and the input excitation matrices, B_i for each mode. During M1, the state of input excitation voltage is $V_{in} > 0$, and the piecewise linear state-equation is defined by the matrices:

$$A_1 = \begin{bmatrix} -\frac{N^2}{C_p \times (R_i + N^2 r_{cp})} & 0 & -\frac{1}{C_p} + \frac{N^2 r_{cp}}{C_p \times (R_i + N^2 r_{cp})} & \frac{1}{C_p} - \frac{N^2 r_{cp}}{C_p \times (R_i + N^2 r_{cp})} \\ 0 & 0 & 0 & \frac{1}{C_s} \\ \frac{1}{L_p} - \frac{N^2 r_{cp}}{L_p \times (R_i + N^2 r_{cp})} & 0 & -\frac{r_{cp} + r_{lp}}{L_p} & \frac{r_{cp}}{L_p} \\ -\frac{1}{L_s} + \frac{N^2 r_{cp}}{L_s \times (R_i + N^2 r_{cp})} & -\frac{1}{L_s} & \frac{r_{cp}}{L_s} - \frac{N^2 r_{cp}^2}{L_s \times (R_i + N^2 r_{cp})} & -\frac{r_{ds} + r_{cs} + r_{cp} + r_{ls}}{L_s} + \frac{N^2 r_{cp}^2}{L_s \times (R_i + N^2 r_{cp})} \end{bmatrix}, B_1 = \begin{bmatrix} 0 \\ 0 \\ 0 \\ \frac{V_{in}}{L_s} \end{bmatrix} \quad (5\text{-}4)$$

Due to symmetry, the dynamics matrix A_2 and the input matrix, B_2, for inverter operation in M2 (V_{in} = 0) is given by:

$$A_2 = A_1 \text{ and, } B_2 = 0_{4x1} \quad (5\text{-}5)$$

It is desirable to solve for the initial operating condition, and subsequently, the steady state output characteristics of the resonant circuit, from (5-4) and (5-5).

However, this can lead to high computational overhead due to requirement for integration, but is considerably simplified when cyclic mode analysis, presented in Chapter 4, is used. In this case, then,

operation of the resonant inverter in a cyclic-mode can be described by a system of piecewise linear (state-space) equations viz.:

$$\dot{x}_i = \mathrm{A}_i x_i + \mathrm{B}_i \tag{5-6}$$

where x_i is the state vector, A_i and B_i represent the dynamics and input excitation matrices, given in (5-4) and (5-5), respectively, during i^{th}=1, 2 operating mode.

During M1, (5-6) can be solved analytically, giving:

$$x_1(t) = e^{\mathrm{A}_1 t} x_1(t_0) + \int_0^t e^{\mathrm{A}_1 (t-\tau)} \mathrm{B}_1 \, d\tau = \Phi_1 x_1(t_0) + \mathrm{T}_1 \tag{5-7}$$

where $\Phi_1 = \Phi(t, t_0) = e^{\mathrm{A}_1 t}$, $\mathrm{T}_1 = \int_0^t e^{\mathrm{A}(t-\tau)} \mathbf{B}_1 \, d\tau$, and $x_1(t_0)$ are the initial conditions. By de-noting the time during which the circuit operates in M1, as d_1/f_s, where d_1 is the duty and f_s is the operating frequency, the complete solution for the system can be obtained by employing the state vector at time d_1/f_s as the initial condition for the subsequent dynamics of M2.

As described in Chapter 4, by combining A_1 and B_1 to form an augmented dynamics matrix, (5-8), the integration overhead can be eliminated at the expense of obtaining only the 'cyclic' steady-state description:

$$\frac{d}{dt}\begin{pmatrix} x_1(t) \\ \hline 1 \end{pmatrix} = \left(\begin{array}{c|c} \mathrm{A}_1 & \mathrm{B}_1 \\ \hline 0 & 0 \end{array}\right)\begin{pmatrix} x_1(t) \\ \hline 1 \end{pmatrix} \tag{5-8}$$

Now, if M1 corresponds to the time period between t_0 and t_1, and M2 the time period between t_1 and t_2, the solution for the state vector at end of M1, t_1, is given by:

$$\hat{x}_1(t_1) = e^{\hat{\mathrm{A}}_1 \times d_1/f_s} \hat{x}_1(t_0) = \hat{\Phi}_1 \hat{x}_1(t_0) \tag{5-9}$$

Similarly, the state vector at the transition time between M1 and M2, t_2, is

$$\hat{x}_2(t_2) = e^{\hat{\mathrm{A}}_2 \times d_2/f_s} \hat{x}_2(t_0) = \hat{\Phi}_2 \hat{\Phi}_1 \hat{x}_1(t_0) \tag{5-10}$$

In general, for the m^{th} mode:

$$\hat{x}(t_i) = \hat{\Phi}_i \hat{\Phi}_{i-1} \cdots \hat{\Phi}_1 \hat{x}(t_0) = \hat{\Phi}_{tot} \hat{x}(t_0) \tag{5-11}$$

where $\hat{\Phi}_i = \left(\begin{array}{c|c} \Phi_i & \mathrm{T}_i \\ \hline 0 & 1 \end{array}\right)$, and $\hat{x}(t_i)$ is the state-vector at time t_m for an initial condition $\hat{x}(t_0)$, and, therefore, by definition of the cyclic mode, is equivalent to the initial condition for the cyclic solution.

Since behaviour in the cyclic mode necessarily presumes periodic steady-state operation, the initial condition for operation in a cyclic mode is given by,

$$x_{per}(t_0) = \left(I^n - \Phi_{tot}\right)^{-1} \mathrm{T}_{tot} \tag{5-12}$$

Since only two dominant modes are considered, depending on the state of the input excitation voltage, symmetry dictates that the duty of each mode is $0.5\mathrm{T}_s$, where T_s is the period for one cycle i.e. $d_1 = 0.5, \quad d_2 = 0.5$. Substituting (5-4) and (5-5) along with the mode duties, into (5-9), (5-10) and (5-12), therefore provides the initial operating condition of the circuit in steady-state and an analytical solution for circuit behaviour.

5.2.1. Cyclic Mode Analysis: Component Electrical Stresses

For the resonant inverter circuit considered, the peak component stresses depend phase angles, β_{in} and γ_c, defined in Fig. 5.6. Assuming v_{cp} is predominantly sinusoidal, and neglecting resonant component parasitic, for brevity, the Laplace transfer function of the circuit is:

$$\frac{v_{Cp}}{V_{in}}(\mathrm{s}) = \frac{2}{\pi}\left[\frac{\dfrac{\mathrm{s}^2 Q_{op2}}{\omega_{op2} C_n}}{\dfrac{\mathrm{s}^4 Q_{op2}}{\omega_{op1}^{\ 2}\omega_{op2}} + \dfrac{\mathrm{s}^3}{\omega_{op1}^{\ 2}} + \mathrm{s}^2\left(\dfrac{R_{eq}}{\omega_{op1}^{\ 2} L_p} + \dfrac{Q_{op2}}{\omega_{op2} C_n} + \dfrac{Q_{op2}}{\omega_{op2}}\right) + \mathrm{s} + \dfrac{R_{eq}}{L_p}}\right] \tag{5-13}$$

where

$$\begin{aligned} \omega_{op1} &= 1/\sqrt{L_s C_s} \\ Q_{op} &= \frac{R_{eq}}{\omega_{op2} L_p} = \omega_{op2} C_p R_{eq} \end{aligned} \tag{5-14}$$

and

$$R_{eq} = \frac{R_i}{\mathrm{N}^2} = \frac{R_{lamp}}{\mathrm{N}^2} \tag{5-15}$$

Substituting $\mathrm{s} \rightarrow j\omega_s$, the phase angle γ_c, as a function of the operating frequency, is sufficient to determine the normalised duty—d_{vCp_0} therefore denotes the duty when v_{Cp} goes to zero, as follows:

$$d_{vCp\_0} = \begin{cases} -\dfrac{1}{2\pi} \times \tan^{-1}\left[\dfrac{\omega_s^{\ 2}\left(\dfrac{\omega_s^{\ 2} Q_{op2}}{\omega_{op1}^{\ 2}\omega_{op2}} + \dfrac{\mathrm{N}^2 R_i}{\omega_{op1}^{\ 2} L_p} + \dfrac{C_n Q_{op2}}{\omega_{op2}} + \dfrac{Q_{op2}}{\omega_{op2}}\right) + \dfrac{\mathrm{N}^2 R_i}{L_p}}{\omega_s \times \left(1 - \dfrac{\omega_s^{\ 2}}{\omega_{op1}^{\ 2}}\right)}\right] & \text{for } 1 - \dfrac{\omega_s^{\ 2}}{\omega_{op1}^{\ 2}} \geq 0 \\ -\dfrac{1}{2} + \dfrac{1}{2\pi} \times \tan^{-1}\left[\dfrac{\omega_s^{\ 2}\left(\dfrac{\omega_s^{\ 2} Q_{op2}}{\omega_{op1}^{\ 2}\omega_{op2}} + \dfrac{\mathrm{N}^2 R_i}{\omega_{op1}^{\ 2} L_p} + \dfrac{C_n Q_{op2}}{\omega_{op2}} + \dfrac{Q_{op2}}{\omega_{op2}}\right) + \dfrac{\mathrm{N}^2 R_i}{L_p}}{\omega_s \times \left(1 - \dfrac{\omega_s^{\ 2}}{\omega_{op1}^{\ 2}}\right)}\right] & \text{for } 1 - \dfrac{\omega_s^{\ 2}}{\omega_{op1}^{\ 2}} < 0 \end{cases} \tag{5-16}$$

Referring to Fig. 5.6, the magnitude of output voltage ($\hat{v}_{\mathrm{Re}}$) is seen to be phase-shifted from the end of the duty time d_{vCp_0}, by $\pi/2$ rad., by virtue of the voltage v_{Re} being sinusoidal and in-phase with v_{Cp}. Notably, $\hat{v}_{\mathrm{Re}}$ can occur in either M1 ($V_{in} > 0$) or M2 ($V_{in} = 0$) depending on operating frequency.

From (5-16), the maximum voltage $\hat{v}_{\mathrm{Re}}$ occurs at,

$$t_{v\mathrm{Re\_max}} = \begin{cases} t_{vCp\_max\_model} \\ = \dfrac{T_s}{4} - \dfrac{T_s}{2\pi}\tan^{-1}\left[\dfrac{\omega_s^{\,2}\left(\dfrac{\omega_s^{\,2}Q_{op2}}{\omega_{op1}^{\,2}\omega_{op2}} + \dfrac{N^2R_i}{\omega_{op1}^{\,2}L_p} + \dfrac{C_nQ_{op2}}{\omega_{op2}} + \dfrac{Q_{op2}}{\omega_{op2}}\right) + \dfrac{N^2R_i}{L_p}}{\omega_s \times \left(1 - \dfrac{\omega_s^{\,2}}{\omega_{op1}^{\,2}}\right)}\right] & \text{for } 1 - \dfrac{\omega_s^{\,2}}{\omega_{op1}^{\,2}} \geq 0 \\ t_{vCp\_max\_model2} \\ = -\dfrac{T_s}{4} + \dfrac{T_s}{2\pi}\tan^{-1}\left[\dfrac{\omega_s^{\,2}\left(\dfrac{\omega_s^{\,2}Q_{op2}}{\omega_{op1}^{\,2}\omega_{op2}} + \dfrac{N^2R_i}{\omega_{op1}^{\,2}L_p} + \dfrac{C_nQ_{op2}}{\omega_{op2}} + \dfrac{Q_{op2}}{\omega_{op2}}\right) + \dfrac{N^2R_i}{L_p}}{\omega_s \times \left(1 - \dfrac{\omega_s^{\,2}}{\omega_{op1}^{\,2}}\right)}\right] & \text{for } 1 - \dfrac{\omega_s^{\,2}}{\omega_{op1}^{\,2}} < 0 \end{cases} \tag{5-17}$$

Substituting (5-15) into (5-11) the states and the output v_{Re} at $t = t_{v\mathrm{Re\_max}}$, can be obtained:

$$\hat{x}(t_{v\mathrm{Re\_max}}) = \begin{cases} \hat{x}(t_{v\mathrm{Re\_max\_model}}) = e^{\hat{\mathbf{A}}_1(t_{vCp\_max})}\hat{x}_{per}(t_0) & \text{for } t_{v\mathrm{Re\_max}} < 0.5 \\ \hat{x}(t_{v\mathrm{Re\_max\_model2}}) = e^{\hat{\mathbf{A}}_2(t_{vCp\_max} - d_1T_s)}e^{\hat{\mathbf{A}}_1 d_1 T_s}\hat{x}_{per}(t_0) & \text{for } t_{v\mathrm{Re\_max}} > 0.5 \end{cases}$$

and

$$\hat{v}_{\mathrm{Re}} = [\mathrm{N} \quad 0 \quad 0 \quad 0 \quad 0]\hat{x}(t_{v\mathrm{Re\_max}}) \tag{5-18}$$

The magnitude of voltage stress across C_p immediately follows from $\hat{v}_{\mathrm{Re}}/\mathrm{N}$. The input voltage vs. current phase angle, β_{in}, after normalising by 2π is:

$$d_{vCs\_max} = \frac{1}{2\pi} \times \tan^{-1}\left[\frac{\omega_s \times \left(1 - \dfrac{\omega_s^{\,2}}{\omega_{op1}^{\,2}}\right)}{\dfrac{\omega_s^{\,4}Q_{op2}}{\omega_{op1}^{\,2}\omega_{op2}} - \omega_s^{\,2}\left(\dfrac{R_{eq}}{\omega_{op1}^{\,2}L_p} + \dfrac{Q_{op2}}{\omega_{op2}} + \dfrac{Q_{op2}}{C_n\omega_{op2}}\right) + \dfrac{R_{eq}}{L_p}}\right] - \frac{1}{2\pi} \times \tan^{-1}\left[\frac{\dfrac{\omega_s C_s R_{eq}}{L_p} - \dfrac{\omega_s^{\,3}C_sQ_{op2}}{\omega_{op2}}}{-\omega_s^{\,2}C_s}\right] \tag{5-19}$$

Referring again to Fig. 5.6, the series resonant inductor current, i_{Ls}, and the resonant capacitor voltage, v_{Cs}, are displaced by $\pi/2$ rad. v_{Cs} is a maximum at the zero crossing of i_{Ls}, which always occurs in M2 by virtue of operating the tank inductively, hence, the time at which v_{Cs} experiences the maximum voltage stress is given by $t_{vCs\_max} = d_{vCs\_max}T_s$.

From (5-11) and (5-19), the maximum series resonant capacitor voltage is therefore given by:

$$\hat{v}_{Cs} = [0 \;\; 1 \;\; 0 \;\; 0 \;\; 0] e^{\hat{\mathbf{A}}_2 t_{vCs\_\max}} e^{\hat{\mathbf{A}}_1 d_1 T_s} \hat{x}_{per}(t_0) \tag{5-20}$$

The maximum series inductor current is phase-shifted from $\hat{v}_{Cs}$ by $\pi/2$. Hence, i_{Ls} is a maximum at $t_{iLs\_\max} = t_{vCs\_\max}$ - (T_s/4) and can occur in either M1 or M2 (depending on operating frequency). The state vector when i_{Ls} is a maximum is therefore given by,

$$\hat{x}(t_{iLs\_\max}) = \begin{cases} \hat{x}(t_{iLs\_\max\_mode1}) = e^{\hat{\mathbf{A}}_1 (t_{iLs\_\max})} \hat{x}_{per}(t_0) & \text{for } t_{iLs\_\max} \le 0.5T_s \\ \hat{x}(t_{iLs\_\max\_mode2}) = e^{\hat{\mathbf{A}}_2 (t_{iLs\_\max} - 0.5T_s)} e^{\hat{\mathbf{A}}_1 d_1 T_s} \hat{x}_{per}(t_0) & \text{for } t_{iLs\_\max} \ge 0.5T_s \end{cases} \tag{5-21}$$

and

$$\hat{i}_{Ls} = [0 \;\; 0 \;\; 0 \;\; 1 \;\; 0] \hat{x}(t_{iLs\_\max}) \tag{5-22}$$

Observation from Fig. 5.6 indicates that the peak parallel inductor current ($\hat{i}_{Lp}$) occurs at $t_{iLp\_\max} = d_{vCp\_0} T_s$ in M1. The state vector when i_{Lp} reaches its maximum, and the magnitude of the current, are therefore given by,

$$\hat{x}(t_{iLp\_\max}) = e^{\hat{\mathbf{A}}_1 (t_{iLp\_\max})} \hat{x}_{per}(t_0) \tag{5-23}$$

and

$$\hat{i}_{Lp} = [0 \;\; 0 \;\; -1 \;\; 0 \;\; 0] \hat{x}(t_{iLp\_\max}) \tag{5-24}$$

5.3. Design Procedure for Electronic Ballasts

Here, the design and realisation of a 4th-order electronic ballast to drive a capacitive-coupled fluorescent lamp, for battery backup emergency lighting (issues relating to general lamp dimming is not considered), is considered. Although four resonant elements in the 4th-order resonant electronic ballast need to be designed, they can be combined into two resonant component ratios, namely C_n and L_n for initial design purposes, as discussed in Chapter 3.

Initial specifications, such as the resonant capacitance and inductance ratios, L_n and C_n, and load quality factor Q_{op1}, are selected, and the ratio of the nominal operating frequency to effective resonance frequency, is chosen to determine the required operating point—the operating frequency is selected to be above, and in the region of, the resonant frequency, to promote high-efficiency operation.

The corresponding normalised output voltage as a function of component ratios L_n, C_n, quality factor Q_{op1} and normalised frequency ω_s/ω_o, is:

$$M_{inv} = \frac{\frac{2\sqrt{2}}{\pi}\times\frac{s^2}{\omega_o{}^2}\times\frac{\lambda_T{}^2\sqrt{C_n}Q_{op1}}{\sqrt{L_n}}}{\frac{s^4}{\omega_o{}^4}\frac{\lambda_T{}^4 C_n{}^{1.5}Q_{op1}}{\sqrt{L_n}}+\frac{s^3}{\omega_o{}^3}\lambda_T{}^3\sqrt{\frac{C_n}{L_n}}+\frac{s^2}{\omega_o{}^2}\lambda_T{}^2\sqrt{L_nC_n}\left(Q_{op1}+\frac{Q_{op1}C_n{}^2}{L_n}+\frac{Q_{op1}C_n}{L_n}\right)+\frac{s}{\omega_o}\lambda_T\sqrt{\frac{C_n}{L_n}}+Q_{op1}\sqrt{L_nC_n}} \quad (5\text{-}25)$$

and

$$\lambda_T=\frac{\omega_o}{\omega_{op1}}=\sqrt{\frac{\left(1+\frac{1}{L_n}+\frac{C_n}{L_n}\right)+\sqrt{\left(1+\frac{1}{L_n}+\frac{C_n}{L_n}\right)^2-4\left(\frac{C_n}{L_n}\right)}}{\frac{2C_n}{L_n}}} \quad (5\text{-}26)$$

Note: λ_T is the ratio of the effective resonant frequency and series tank component resonant frequency. The series load quality factor Q_{op1} and switching to resonant frequency ratio, can be selected to adjust the attainable output voltage at the desired operating point, and the required transformer turns ratio. Further, it will be shown that the desired load quality factor and resonant frequency uniquely determine the values of resonant components. The transformer secondary to primary turn ratio, N is determined from,

$$N = v_{Lamp}/v_{DC}\times M_{inv} \quad (5\text{-}27)$$

Based on the terminology developed in Chapter 3, the effective load quality factor of the circuit is given by:

$$Q_o = Q_{op1}/\lambda_T \quad (5\text{-}28)$$

and the characteristic input impedance of the overall resonant circuit, Z_o, is:

$$Z_o = R_{lamp}/Q_oN^2 \quad (5\text{-}29)$$

The value of series resonant inductance L_s and series resonant capacitance C_s follow,

$$L_s = Z_o/\omega_o = Z_o/2\pi f_o \quad (5\text{-}30)$$

and

$$C_s=\frac{L_s\lambda_T{}^2}{2Z_o{}^2}=\frac{L_s}{Z_o{}^2}\times\frac{1+L_n+C_n+\sqrt{(1+L_n+C_n)^2-4L_nC_n}}{2C_n} \quad (5\text{-}31)$$

Thereafter, the parallel resonant inductance and parallel resonant capacitance are,

$$C_p = C_s \times C_n$$
$$L_p = L_s / L_n \tag{5-32}$$

The peak electrical stresses on the components can be assessed by substituting the component values from (5-30) through to (5-32), into (5-18), (5-20), (5-21) and (5-23). As discussed in Chapter 3, the input-output characteristic is very sensitive to the choice of C_n and L_n. This implies that the resonant component electrical stresses should also be a function of these two factors.

Current stress on the series inductor L_s and switching devices can be reduced by increasing the value of L_s or decreasing the value of parallel inductor L_p; thereby, increasing the L_n ratio. In a similar manner, a decrease in C_n can decrease the voltage stress imposed on C_p. Here, it is proposed that the two ratios are varied until the level of component stresses, calculated from cyclic analysis, are deemed satisfactory. Moreover, to promote high-efficiency operation, it is important to minimise the circulating energy by designing the load quality factor of the resonant circuit to be within the range of 4 to 6 at full load [E13].

As previously discussed, any candidate electronic ballast must provide sufficient voltage to promote ignition, and a current limiting capability thereafter. Before the lamp is ignited, it can be assumed that the resistance presented to the output of the ballast, is infinite i.e. the output stage is essentially an open-circuit. Consequently, the resonant inverter behaves as a tank circuit with a high effective load quality factor to facilitate ionization of the gas within the tube. Of note, is that the minimum capacitive discharge voltage decreases with increasing frequency, when the capacitive coupling reactance becomes small. Once gaseous breakdown has occurred, the resistance decreases as the lamp conducts current and the lamp represents a pure resistance at high frequencies.

From the experimentally measured lamp characteristics of Fig. 5.3(b), the RMS value of the voltage across, and current through, the lamp at full power (8W), in steady state, are v_{Lamp} (RMS) = 65V and i_{Lamp} (RMS) = 0.136A, respectively. Hence, the resistance of the lamp is ≈470Ω. The lamp is chosen to operate at a frequency of 2.63MHz for optimal efficiency and reduced EMI. A summary of specifications for the ballast is given in Table 1.

Table 5.1 Initial specifications for electronic ballast.

Parameters	Values
Input dc voltage, v_{DC}(V)	12
Nominal lamp resistance at 8W (Ω)	470
Resonant capacitance ratio, C_n	0.5
Resonant inductance ratio, L_n	0.5
Effective load quality factor, Q_o	6
Frequency ratio, λ_r	1.935
Nominal operating frequency, f_o (MHz)	2.63
Ratio of nominal to resonant frequency, f_s / f_o	1.02

Having chosen values for C_n, L_n and f_s/f_o, the numerical values for the four resonant elements can be determined. The calculated and realised component values, are given in Table 5.2. Although the effective load quality factor should ideally be within the range of 4 to 6, Q_o is selected to be 6 in this design to facilitate the utilisation of a small transformer turns ratio without compromising the overall system stability and reliability. Further, the electronic ballast is operated at a constant frequency of 2.65 MHz, and thereby does not have the large circulating energy problem normally associated with frequency modulation of resonant circuits. A Ni-Mn toroid core is used to construct the 17.6μH transformer. The toroid core has the advantage of being more compact than ETD core structures and provide higher magnetic coupling, thus lowering stray leakage flux, and promoting greater efficiency. The secondary leakage inductance of the transformer is sufficiently small so as to be neglected in the following analysis. In this case, the equivalent L_p incorporating the magnetising inductance L_m of the transformer, is measured to be 4μH.

Table 5.2 Electronics ballast component values.

Parameters	Values
Series resonant inductance, L_s (μH)	2.6
Series resonant capacitance, C_s (nF)	6
Parallel resonant inductance, L_p (μH)	4
Parallel resonant capacitance, C_p (μF)	3
Transformer magnetising inductance, L_m	17.3
Leakage inductance, L_{ls} (μH)	0.06

The accuracy of the proposed cyclic-based analysis techniques for predicting the steady-state behaviour of the 4th-order resonant inverter, is now demonstrated by comparison with results from SPICE simulations and the prototype experimental converter, over a range of operating conditions.

By way of example, Fig. 5.7 compares predicted and measured output voltages for the inverter for two load conditions, whilst Fig. 5.8 shows predicted and measured steady-state electrical stresses on the resonant components, at 470Ω. It can be seen that an excellent correlation between the cyclic and experimental results, is evident.

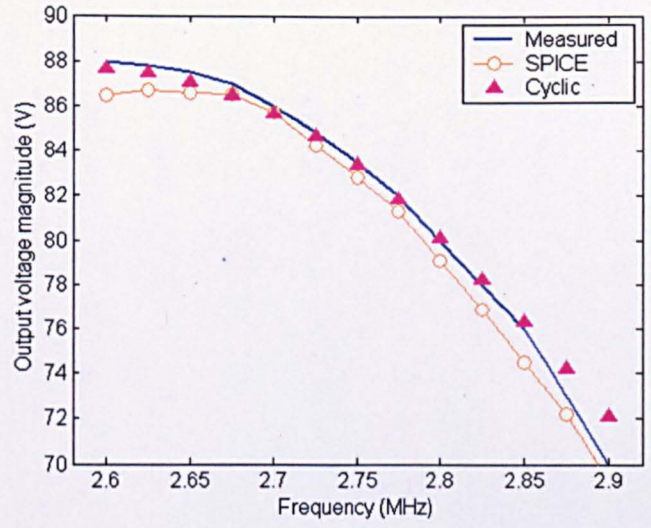

(a)

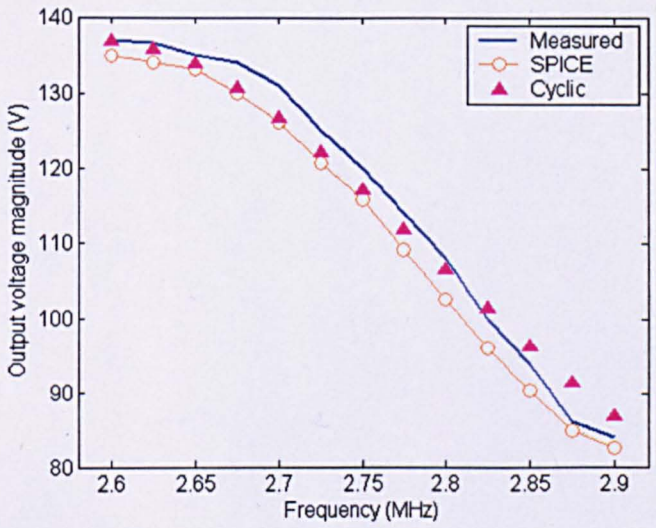

(b)

Figure 5.7 Comparison of maximum output voltage obtained from cyclic averaging, Spice simulations, and measurements from the experimental ballast, for (a) $R_L = 470\Omega$ and (b) $R_L = 940\Omega$.

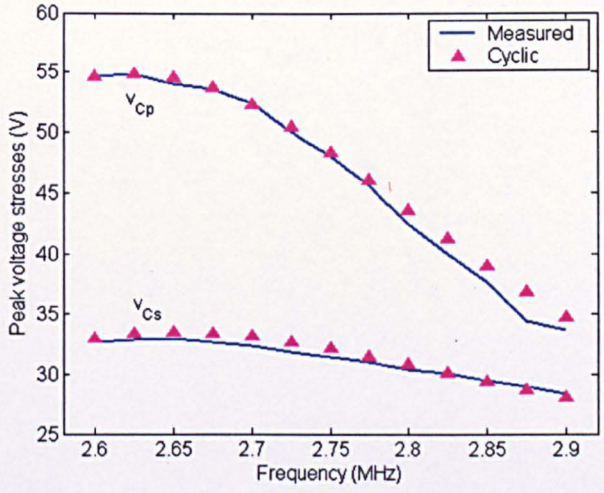

(a)

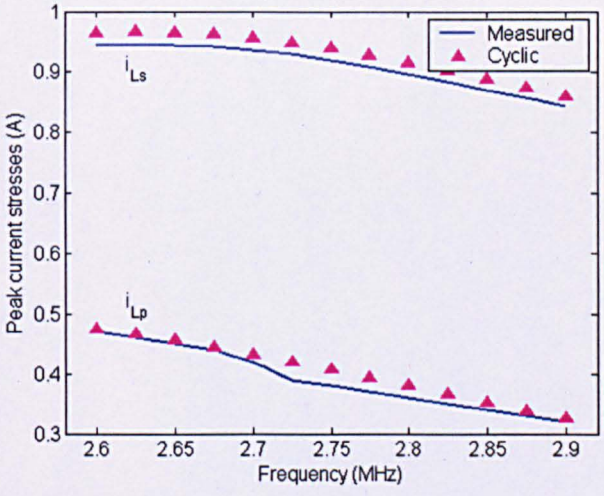

(b)

Figure 5.8 Comparison of predictions and measurements (a) voltage stresses and (b) current stresses on resonant components, with load R_l= 940Ω.

The proposed electronic ballast, see Fig. 5.9(a), is connected to a fluorescent lamp through a small length of adhesive copper tape connected to both ends of the discharge tube, such that capacitance is created between the copper tape and the gas, which are separated by the dielectric glass wall—see Fig. 5.9(b) (the manufacturers electrodes are not electrically connected). Although the initial understanding of how the system work (see Fig. 5.3) provides the platform for converter prototyping, the stray capacitance of the high frequency transformer is not sufficiently large to achieve the desired voltage boosting effect. Thereby, additional discrete capacitor is placed on the secondary side of the transformer in parallel with the fluorescent lamp to obtain the desired converter characteristic.

Moreover, due to practical issue related to construction of practical high frequency transformer, an ideal transformer magnetising inductance value cannot be obtained in this case. This can be compensated by having a discrete parallel resonant inductor, L_p on the secondary side of the transformer, and to allow the primary side leakage inductance to be absorbed into the series inductor L_s. The characteristic of the resulting circuit in Fig. 5.9(a) is now equivalence to that of the initial design shown in Fig. 5.3. Hence, the high-frequency ballast achieves the required voltage for ignition without an associated auxiliary preheating mechanism.

Upon establishment of ionization, the discharge now lies in the domain of positive dn_e/dt, and the lamp current increases until it reaches nominal operating point, where v_{Lamp} (RMS) = 65V and i_{Lamp} (RMS) = 0.136A. When operated above the effective resonant frequency, the resonant tank behaves like inductive impedance in series with the fluorescent tube. A further increase of the lamp current would move the operating point into the region of negative dn_e/dt, the resonant ballast reacts by forcing the current back to i_{Lamp} (RMS) to promote stable operation.

A basic approximation, useful for determining the value of internal capacitance c_{tap} formed by the proximity of the copper tape and gas, separated by the fluorescent tube wall, is given in [E14]:

$$c_{tap} = 8.85\times10^{-12}\,\frac{\varepsilon_r \pi d_{\text{tube}}\,\ell_{\text{tube}}}{t_i} \qquad (5\text{-}33)$$

where
ε_r = dielectric constant of the fluorescent tube
d_{tube} = internal diameter of fluorescent tiub
ℓ_{tube} = copper tap width
t_i = fluorescent tube thickness

For the case of the 8W fluorescent lamp, the value for c_{tap} is approximately 60pF, and the effective resistance, R_i across the output of the electronic ballast is given by,

$$R_i = \sqrt{\left(\frac{2}{2\pi f_s c_{tap}}\right)^2 + R_{lamp}{}^2} = 2.03\text{k} \quad (\Omega) \qquad (5\text{-}34)$$

Subsequently, the required ignition voltage for the capacitively-coupled ballast is,

$$v_{Lamp}(\text{rms}) = i_{Lamp}(\text{rms}) \times R_i = 273 \quad (\text{V}) \qquad (5\text{-}35)$$

For completeness, the measured output voltage for R_i = 2.03kΩ, is compared with cyclic analysis predictions in Fig. 5.10(a). Once again, the predictions are in good agreement with experimental

results. The discrepancy between the results is attributed to effect of non-linearities that exists within the high-frequency transformer.

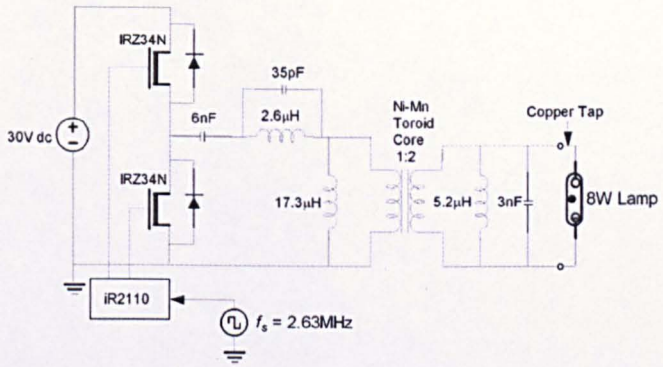

(a)

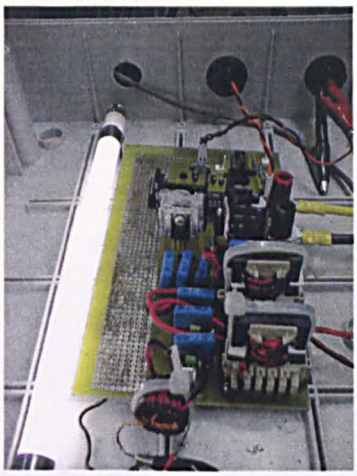

(b)

Figure 5.9 Capacitive coupled fluorescent ballast: (a) Circuit schematics and (b) Prototype lamp ballast.

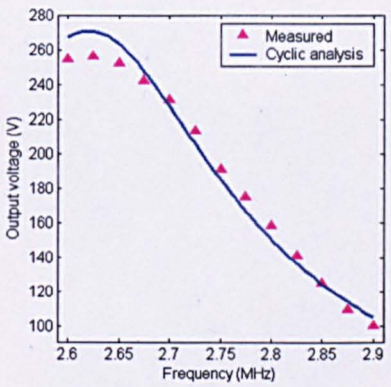

(a)

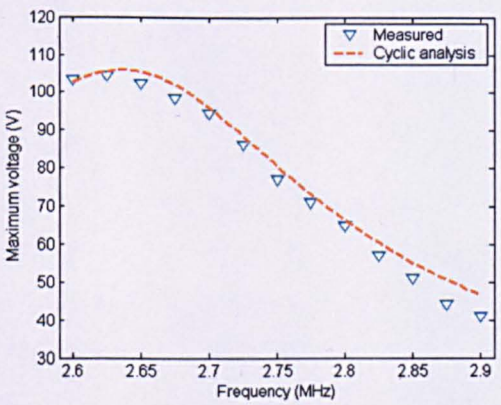

(b)

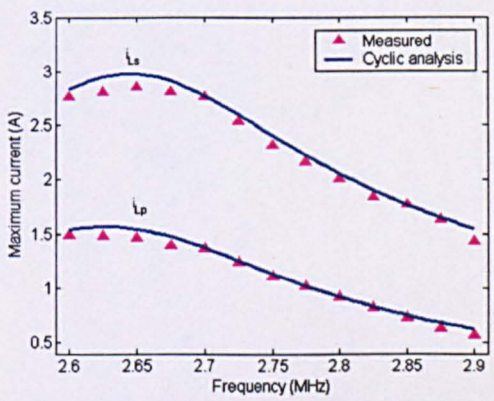

(c)

Figure 5.10 Comparison of predictions and measurements: (a) Output voltage (rms), (b) voltage stresses and (c) current stresses on resonant components, with R_L=2.03k.

Finally, Figs. 5.10(b) and (c) demonstrate the accuracy of predicting resonant components stresses, which are at a maximum prior to lamp ignition. It can be seen that the cyclic modelling technique provides a useful tool for estimating stresses, and, characteristically, tends to produce conservative estimates, particularly around the resonant frequency where the designer has to accommodate the greatest margin of safety. It is notable that the power switches employed in the ballast are IRZ34N, driven by square-wave signal from the high frequency IR2110 gate driver. There is no preheating prior to discharge, therefore incurring no input power losses for heating up the electrodes. The ignition frequency is fixed to the switching frequency, for steady-state operation, in order to maintain constant frequency during commutation from one mode to the other.

5.4. Summary

State-variable dynamic descriptions of a resonant power inverter, used as a fluorescent lamp ballast, have been presented. The model is subsequently used to obtain a steady-state cyclic description of the circuit, and the derivation of analytical formulae to calculate the electrical stresses on the resonant tank components, is given. The accuracy of the proposed techniques has been demonstrated by comparisons with both Spice simulations, and from measurements from an experimental 8W, capacitive-coupled, fluorescent lamp, with good agreement being shown. It is notable that, whilst the state-variable dynamic model requires a commensurate computational overhead to that of Spice simulations, the presented cyclic analysis method is typically $10^4\times$ faster.

Finally, a structured design procedure, is presented, based on a user defined ratio of operating frequency to nominal switching frequency, and a desired Q factor, to realise an inverter for lamp ballast applications, although, notably, the method is ultimately applicable to other fields such as induction heating and plasma generation systems. This inverter is powered from a low DC voltage source at a switching frequency corresponding to the highest boost capability. Thus, the size of the transformer in the ballast circuit is greatly reduced.

In addition, circuit parameters are designed so that ZVS of the power devices is preserved, to promote high efficiency operation. Although during high frequency operation the circuit incurred losses attributed to the non-ideally designed discrete energy storage components, overall, system efficiency of around 80% was achieved during nominal operation.

References

[E1] D. O. Wharmby, "Electrodeless lamps for lighting: a review", *IEE Proceedings-A*, **140**, pp. 465-473, 1993.

[E2] L. P. Bakker, G. M. W. Kroesen and F. J. D. Hoog, " RF Discharge Impedance Measurement using a New method to Determine the Stray Impedances", *IEEE Trans. on Plasma Science*, **27**, pp. 384-395, 1999.

[E3] M. K. Kazimierczuk and W. Szaraniec, "Electronics Ballast for Fluorescent Lamps", *IEEE Trans. on Power Electronics*, **8**, pp. 384-395, 1993.

[E4] C. Chang, J. Chang and G. W. Bruning, "Analysis of the Self-Oscillating Series Resonant Inverters for Electronics Ballasts", *IEEE Trans. on Power Electronics*, **14**, pp. 533-540, 1999.

[E5] S. Y. R. Hui, L. M. Lee, H. Chung and Y. K. Ho, "An Electronics ballast with Wide Dimming High PF, and Low EMI", *IEEE Trans. on Power Electronics*, **16**, pp. 465-471, 2001.

[E6] M. C. Cosby and R. M. Nelms, "A Resonant Inverter for Electronics Ballast Applications", *IEEE Trans. on Industrial Electronics*, **41**, pp. 418-425, 1994.

[E7] C. S. Moo, W. M. Chen, and H. K. Hsieh, "Electronic Ballast with Piezoelectric Transformer for Cold Cathode Fluorescent Lamps", *IEE Proc. Electric Power Applications*, **150**, pp. 278-282, 2003.

[E8] L. R. Nerone, "A Mathematical Model of the Class D Converter for Compact Fluorescent Ballast", *IEEE Trans. on Power Electronics*, **10**, pp. 708-715, 1995.

[E9] S. Yaakov, M. Shvartsas and J. Lester, "A Behavioural SPICE Compatible Model of an Electrodeless Fluorescent Lamp", in *17th Annual IEEE Applied Power Electronics Conference Proc.*, 2002, pp. 948-954.

[E10] J. Alonso, C. Blanco, E. Lopez, A. J. Calleja, and M. Rico, "Analysis, Design, and Optimization of the LCC Resonant Inverter as a High-Intensity Discharge lamp Ballast", *IEEE Trans. on Power Electronics*, **13**, pp. 573-585, 1998.

[E11] T. Wu, T. Yu and M. Chiang, "Single-Stage Electronic Ballast with Dimming Feature and unity Power Factor", *IEEE Trans. on Power Electronics*, **13**, pp. 586-596, 1998.

[E12] Y. Ang, D. A. Stone, C. M. Bingham and M. P. Foster, "Analysis & Design of High-Frequency LCLC Resonant Converters for Electrode-Less Fluorescent Lamp Ballasts", in *2nd IEE International Conference on Power Electronics, Machines and Drives*, Edinburgh, 2004, pp. 137-142.

[E13] J. A. Donahue and M. M. Jovanovic, "The LCC inverter as a cold cathode fluorescent lamp driver", in *9th Annual IEEE Applied Power Electronics Conference Proc.*, 1994, pp. 427-433.

[E14] J. L. Duarte, J. Wijntjens and J. Rozenboom, "Getting more from fluorescent lamps through resonant converters", in *Industrial Electronics, Control, Instrumentation, and Automation Conference Proc.*, 1992, pp. 560-563.

CHAPTER 6

Design Orientated Analysis of 4th-Order Voltage-Output Resonant Converters

Here, properties of the voltage-output 4th-order LCLC resonant converter, are investigated. Harmonics of the switching frequency are neglected, and the resonant tank waveforms are assumed to be purely sinusoid, thereby allowing an 'Extended Fundamental Mode Analysis' to be derived for the resonant tank, rectifier and output filter of the converter, whose discontinuous conduction mode operation can then be analysed using linear ac techniques. A key result of the proposed approach is that, the output voltage under discontinuous conduction mode operation, is readily obtained. The influence of resonant tank component losses and rectifier diode non-idealities, on the output voltage, is also assessed.

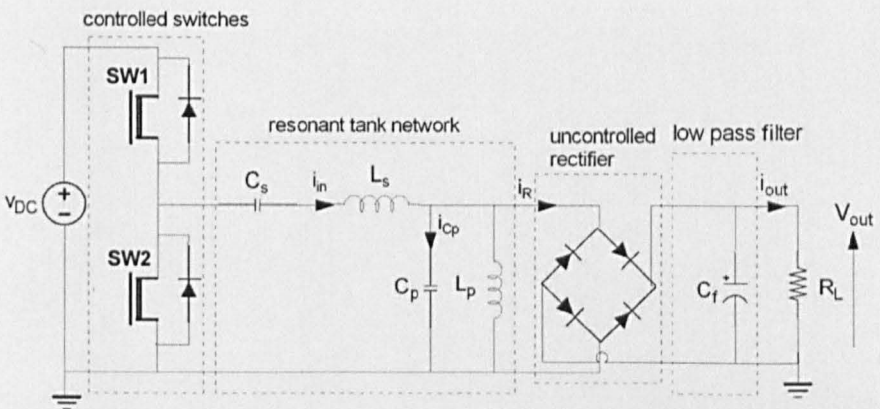

Figure 6.1 4th-order voltage-output LCLC converters (excluding reactive components parasitic).

The exclusion of the output filter inductor, L_f, as shown in Fig. 6.1, significantly complicates the steady-state behavioural analysis of the series-parallel voltage-output resonant converter, since there are periods of discontinuous conduction of the bridge rectifier due to limiting of dv/dt at the rectifier input, which then dynamically decouples the output filter/load from the resonant tank circuitry.

Although simplified equivalent circuits have been previously proposed for the analysis of resonant converters based on FMA [F1-F3], in which an equivalent resistor models the combined rectifier, output filter and load network, these have only addressed parallel LC and series-parallel LCC and

LCLC-type converters with an inductive output filter. Alternative analysis techniques, presented in [F4, F5], based on a state-space approach, have also allowed steady-state solutions to be obtained, specifically for the LCC, and LCLC resonant converter variants. However, whilst providing improved prediction accuracy compared to FMA, ultimately, the computation time is compromised due to the increased complexity.

To date, the most accurate methodologies for the rapid analysis of resonant converters have been based on variants of Rectifier–Compensated FMA (RCFMA) [F6, F7, F8, F9], in which, in addition to the use of an 'equivalent resistor' to model the effects of the rectifier and output filter (as in classical FMA), other components, specifically an additional equivalent capacitor, are also included to improve modelling accuracy.

Although RCFMA allows the underlying attributes of FMA to be applied to the more complex voltage-output converter, whilst still allowing rapid analysis by virtue of employing the fundamental mode principle, structured design procedures, based on the resulting analysis techniques, have yet to be reported.

This chapter, therefore, extends the FMA principle to accommodate the non-linear interaction that occurs between the parallel resonant capacitor and the bridge rectifier of the LCLC voltage-output resonant converter, and results in a relatively straightforward analytical solution for steady-state analysis. In addition, knowledge of the effects of various parameters on the steady-state characteristics of the converter allows four design synthesis procedures, to be derived, based on the resulting analytical solutions.

6.1. Operation and Steady State Behaviour

In [F2], the voltage and current characteristics of the rectifier in a resonant converter are modelled by an 'equivalent' resistor. However, the non-linear voltage clamping action of the parallel capacitor/bridge rectifier, which occurs when higher-order resonant tank circuits are employed, does not, in general, allow such a simple approximation to be employed if accurate results are required. An extended equivalent circuit is, therefore, proposed for the LCLC voltage-output converter that incorporates an additional resistance in series with a capacitor to account for the coupling/decoupling effect that arises from the rectifier conduction/non-conduction periods. Although this has been previously reported for LCC converters in [F8, F9], its application to 4th-order resonant converters is now considered for the first time.

The non-linear interaction between C_p and C_f, means that the voltage presented to the rectifier cannot be assumed to be a square-wave due to the significant capacitor charging/discharging intervals. By way of example, typical voltage and current waveforms for a 4th-order converter, in the steady state, are shown in Fig. 6.2.

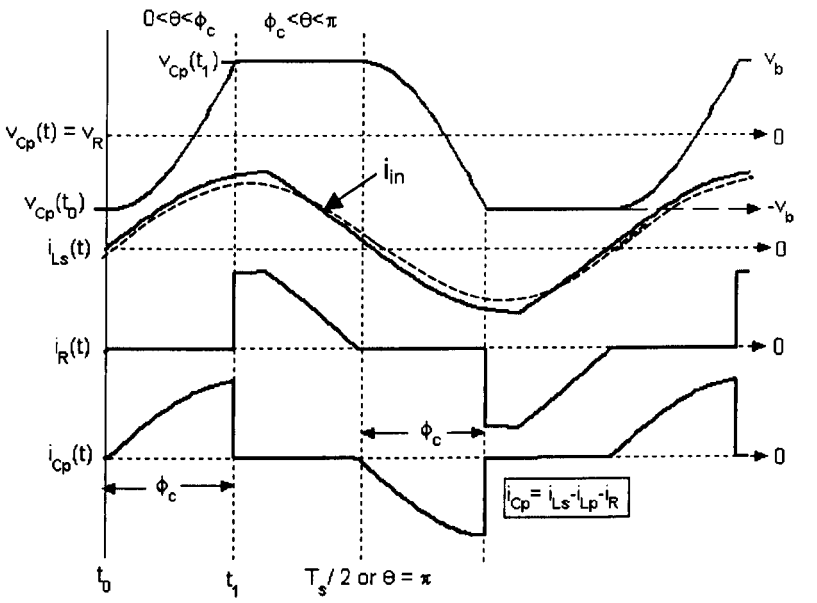

Figure 6.2 Voltage and current waveforms of the voltage-output converter.

At the start of a cycle, at t_0, the rectifier is non-conducting and no current flows into it. Capacitor C_p is, therefore, charged to $v_{Cf} = v_{out}$ (plus the bridge rectifier voltage drop), at which time rectifier conduction commences once again. During the charging of C_p, v_{Cp} is given by:

$$v_{Cp}(t) = v_{Cp}(t_0) + \frac{1}{C_p}\int_{t_0}^{t_1} \hat{i}_{in} \sin(2\pi f_s t)dt \tag{6-1}$$

Evaluating the integral in (6-1) with the initial rectifier input voltage, $v_R(t_0) = v_{Cp}(t_0) = -(V_{out} + 2v_{diode})$ gives:

$$v_{Cp}(t) = -v_b + \frac{\hat{i}_{in}}{2\pi f_s C_p} \times (1 - \cos(2\pi f_s t_1)) \tag{6-2}$$

where $v_b = V_{out} + 2v_{diode}$.

To determine the boundary that defines the capacitor charging period, it is noted that $v_{Cp}(t_1) = v_b$ which yields the rectifier non-conduction angle ϕ_c :

$$t_1 = \frac{1}{2\pi f_s}\cos^{-1}(\phi_c) \tag{6-3}$$

where

$$\phi_c = \cos^{-1}\left(1 - \frac{4\pi v_b f_s C_p}{\hat{i}_{in}}\right)$$

The voltage across the parallel resonant capacitor v_{Cp} can now be expressed as a function of angle θ ;

$$v_{Cp}(\theta) = \begin{cases} -v_b + \dfrac{\hat{i}_{in}}{2\pi f_s C_p} \times (1 - \cos(\theta)) & \text{for } 0 \le \theta < \phi_c \\ v_b & \text{for } \phi_c \le \theta < \pi \\ v_b - \dfrac{\hat{i}_{in}}{2\pi f_s C_p} \times (1 - \cos(\theta)) & \text{for } \pi \le \theta < \pi + \phi_c \\ -v_b & \text{for } \pi + \phi_c \le \theta < 2\pi \end{cases} \tag{6-4}$$

During the interval $0 \le \theta < \phi_c$, the resonating inductor current, i_{in}, increases, and the rectifier is non-conducting. This results in a decoupled resonant circuit comprised only of the resonant-tank reactive components (and power switches). At the end of the charging interval, when the rectifier voltage attempts to increase beyond v_b , conduction of the rectifier resumes and the voltage across the capacitor is clamped to v_b . At $\theta = \pi$, the resonant current reverses, switching off the bridge rectifier and consequently discharging C_p from v_b to $-v_b$, and subsequently clamping the rectifier voltage at $-v_b$ at $\theta = \pi + \phi_c \ldots 2\pi$.

Under steady-state conditions, the average output current, i_{out}, from the converter, can be determined by calculating the average current flowing through the bridge rectifier during a complete cycle. Therefore, since the rectifier current flows to the output filter and load during intervals $\phi_c \le \theta < \pi$ and $\pi + \phi_c \le \theta < 2\pi$, the output current can be determined from:

$$i_{out} = \frac{1}{2\pi}\left\{\int_{\phi_c}^{\pi} \hat{i}_{in}\sin(\theta)d\theta + \int_{\pi+\phi_c}^{2\pi} -\hat{i}_{in}\sin(\theta)d\theta\right\} \tag{6-5}$$

Substituting (6-3) into (6-5) and evaluating the integral provides the solution for i_{out}, viz.:

$$i_{out} = \frac{\hat{i}_{in}}{\pi} \times (1 + \cos(\phi_c)) = \frac{2(\hat{i}_{in} - 2\pi v_b f_s C_p)}{\pi} \tag{6-6}$$

Equations (6-3) and (6-6) can be used to derive the bridge rectifier non-conduction angle ϕ_c as follows:

$$\begin{aligned} \phi_c &= \cos^{-1}\left(1 - \frac{8\pi v_b f_s C_p}{\pi i_{out} + 4\pi v_b f_s C_p}\right) \\ &= \cos^{-1}\left(\frac{i_{out} + 4\pi v_b f_s C_p - 8\pi v_b f_s C_p}{\pi i_{out} + 4\pi v_b f_s C_p}\right) \\ &= \cos^{-1}\left(\frac{\pi i_{out} - 4\pi v_b f_s C_p}{\pi i_{out} + 4\pi v_b f_s C_p}\right) \end{aligned} \tag{6-7}$$

The output voltage from the converter can be determined by assuming that the output filter capacitance $C_f >> C_p$ is sufficiently large to impart negligible output voltage ripple. In this case (full derivation details in Appendix A):

$$\begin{aligned} V_{out} = i_{out} R_L &= \frac{\hat{i}_{in} R_L}{\pi} \times (1 + \cos(\phi_c)) \\ &= \frac{2R_L(\hat{i}_{in} - 4\pi f_s C_p v_{diode})}{\pi(1 + 4R_L f_s C_p)} \end{aligned} \tag{6-8}$$

6.1.1. *Determining Equivalent Passive Components*

Having determined the steady-state voltage and current characteristics of the converter, a describing function is now derived to model the non-linear interaction between the rectifier/output filter and parallel capacitor. Via a transformation, the fundamental frequency component of the voltage across capacitor C_p (Figure 6.2) is described by an equivalent resistance and capacitance. This then facilitates the rapid analysis of the resulting passive circuit. Referring to (6-4), the voltage across the capacitor can be divided into two intervals during each half-cycle, viz. the period when the capacitor is being charged, and the period when the voltage clamping action occurs.

Given that the negative half cycle is the mirror image of the positive half cycle, the voltage during the period when the rectifier is conducting (i.e. the clamping period) is given by v_{Cp_clamp}:

$$v_{Cp\_clamp} = \begin{cases} v_b & \text{for} \quad \phi_c \le \theta < \pi \\ -v_b & \text{for} \quad \pi + \phi_c \le \theta < 2\pi \end{cases} \tag{6-9}$$

From a Fourier series analysis, the fundamental component of v_{Cp_clamp} can be shown to be:

$$v_{Cp\_clamp(1)} = \frac{1}{\pi}\left[\int_{\phi_c}^{\pi} v_b e^{-j\theta} d\theta - \int_{\pi+\phi_c}^{2\pi} v_b e^{-j\theta} d\theta\right] \tag{6-10}$$

By matching the boundary condition ($v_{Cp}(\phi_c) = v_b$) at the end of the interval $0 \le \theta < \phi_c$, v_b can be described in terms of $\hat{i}_{in}$ by rearrangement of (6-3),

$$v_b = \frac{\hat{i}_{in}}{4\pi f_s C_p} \times (1 - \cos(\phi_c)) \tag{6-11}$$

Substituting (6-11) into (6-10) and evaluating the integral yields:

$$\begin{aligned} v_{Cp\_clamp(1)} &= \frac{2v_b(1 + \cos(\phi_c) - j\sin(\phi_c))}{j\pi} \\ &= \frac{\hat{i}_{in}}{j2\pi^2 f_s C_p} \times (1 - \cos(\phi_c))(1 + e^{-j\phi_c}) \end{aligned} \tag{6-12}$$

Using complex notation for the Fourier series expansion of the input current leads to the fundamental being described by:

$$i_{in(1)} = \frac{2}{\pi}\int_0^{\pi} \hat{i}_{in} \sin(\theta) e^{-j\theta} d\theta = -j\hat{i}_{in} \tag{6-13}$$

An equivalent resistance, $\Re_{Cp\_clamp}$, that models the capacitor voltage clamping effect is, therefore, given by,

$$\Re_{Cp\_clamp} = \frac{v_{Cp\_clamp(1)}}{i_{in(1)}} = \frac{1 + e^{-j\phi_c}}{2\pi^2 f_s C_p} \times (1 - \cos(\phi_c)) \tag{6-14}$$

A similar procedure can be used to determine the equivalent passive components that model the parallel capacitor voltage, during the period when the rectifier is non-conducting, and the input current discharges/charges C_p. The effect of charging C_p is described by:

$$v_{Cp\_charge} = \begin{cases} -v_b + \dfrac{\hat{i}_{in}}{2\pi f_s C_p}(1 - \cos(\theta)) & \text{for} \quad 0 \le \theta < \phi_c \\ v_b - \dfrac{\hat{i}_{in}}{2\pi f_s C_p}(1 - \cos(\theta)) & \text{for} \quad \pi \le \theta < \pi + \phi_c \end{cases} \tag{6-15}$$

Exploiting symmetry and the trigonometric relationship—$\cos(\theta)=\left(e^{j\theta}+e^{-j\theta}\right)/2$, a Fourier series expansion of (6-15) yields the fundamental component,

$$v_{Cp\_charge(1)}=\frac{1}{\pi}\int_0^{\phi_c}\left(-v_b+\frac{\hat{i}_{in}}{2\pi f_s C_P}\times(1-\cos(\theta))\right)e^{-j\theta}d\theta+\frac{1}{\pi}\int_{\pi}^{\pi+\phi_c}\left(v_b-\frac{\hat{i}_{in}}{2\pi f_s C_P}\times(1-\cos(\theta))\right)e^{-j\theta}d\theta$$

$$=\frac{2}{\pi}\int_0^{\phi_c}\left(-v_b+\frac{\hat{i}_{in}}{2\pi f_s C_P}(1-\cos(\theta))\right)e^{-j\theta}d\theta$$

$$=\frac{\hat{i}_{in}}{\pi^2 f_s C_p}\int_0^{\phi_c}\left(e^{-j\theta}-\left(\frac{1+e^{-j2\theta}}{2}\right)\right)d\theta-\frac{2}{\pi}\int_0^{\phi_c}v_b e^{-j\theta}d\theta$$

$$=\frac{\hat{i}_{in}}{\pi^2 f_s C_p}\left[je^{-j\phi_c}-\frac{\phi_c}{2}-j\frac{e^{-j2\phi_c}}{4}-j\frac{3}{4}\right]-\frac{j\hat{i}_{in}}{2\pi^2 f_s C_p}\times(1-\cos(\phi_c))(1-e^{-j\phi_c}) \tag{6-16}$$

The fundamental of the voltage across C_p can, therefore, be described by summing the contributions of (6-12) and (6-16), which, after simplifying yields:

$$\begin{aligned}v_{Cp(1)}&=v_{Cp\_charge(1)}+v_{Cp\_clamp(1)}\\&=\frac{\hat{i}_{in}}{4\pi^2 f_s C_p}\left[\sin(2\phi_c)-2\phi_c+j(\cos(2\phi_c)-1)\right]\end{aligned} \tag{6-17}$$

Derivation details of (6-17) are given in the Appendix A, for brevity. An equivalent passive resistance, $\Re_e$ which models the *Re*al term of $v_{Cp(1)}$ is obtained by dividing (6-17) by $i_{in(1)}$ as follows:

$$\begin{aligned}Z_{vCp(1)}&=\frac{v_{Cp(1)}}{i_{in(1)}}=\frac{1}{-j\hat{i}_{in}}\times\frac{\hat{i}_{in}}{4\pi^2 f_s C_p}\left[\sin(2\phi_c)-2\phi_c+j(\cos(2\phi_c)-1)\right]\\&=-\frac{1}{4\pi^2 f_s C_p}\left[\frac{\sin(2\phi_c)-2\phi_c}{j}+(\cos(2\phi_c)-1)\right]\end{aligned} \tag{6-18}$$

$$\Re_e=\mathrm{Re}\left(\frac{v_{Cp(1)}}{i_{in(1)}}\right)=\frac{1}{-j\hat{i}_{in}}\times\frac{j\hat{i}_{in}(\cos(2\phi_c)-1)}{4\pi^2 f_s C_p}=\frac{(1-\cos(2\phi_c))}{4\pi^2 f_s C_p}$$

and an equivalent capacitance C_e, can be derived from the *Im*aginary term in $v_{Cp(1)}$:

$$\begin{aligned}\frac{1}{j2\pi f_s C_e}&=\mathrm{Im}\left(\frac{v_{Cp(1)}}{i_{in(1)}}\right)=\frac{2\phi_c-\sin(2\phi_c)}{j4\pi^2 f_s C_p}\\\frac{1}{2\pi f_s C_e}&=\frac{1}{4\pi^2 f_s C_p}\times(2\phi_c-\sin(2\phi_c))\\\therefore C_e&=\frac{2\pi C_p}{2\phi_c-\sin(2\phi_c)}\end{aligned} \tag{6-19}$$

The resulting equivalent circuit of the voltage-output converter, is shown in Fig. 6.3, with the values for the equivalent passive components being given by (6-18) and (6-19).

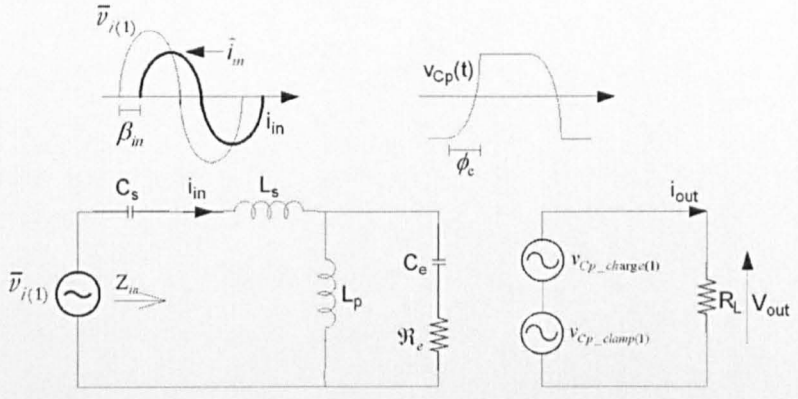

Figure 6.3 RTFMA Equivalent circuit of LCLC converter.

6.2. Circuit Analysis

The input voltage to the resonant tank that results from switching the half-bridge V_{in} is a square-wave of magnitude v_{DC} given by:

$$V_{in} = \begin{cases} v_{DC} & \text{for} \quad 0 < \theta < \pi \\ 0 & \text{for} \, \pi < \theta < 2\pi \end{cases} \tag{6-20}$$

The fundamental of V_{in} has an amplitude $v_{i(1)} = \frac{2}{\pi} v_{DC}$. An initial estimate of the rectifier non-conduction angle in (6-7) can be established from:

$$\begin{aligned} \phi_c &= \cos^{-1}\left(\frac{\pi - 4\pi R_L f_s C_p}{\pi + 4\pi R_L f_s C_p}\right) = \cos^{-1}\left(\frac{\pi - 4\pi R_L f_s C_s C_n}{\pi + 4\pi R_L f_s C_s C_n}\right) \\ &= \cos^{-1}\left(\frac{\pi - 2\omega_s \omega_{op1} L_s Q_{op1} C_s C_n}{\pi + 2\omega_s \omega_{op1} L_s Q_{op1} C_s C_n}\right) = \cos^{-1}\left(\frac{\pi - \dfrac{2\omega_s Q_{op1} C_n}{\omega_{op1}}}{\pi + \dfrac{2\omega_s Q_{op1} C_n}{\omega_{op1}}}\right) \\ &= \cos^{-1}\left(\frac{\pi - 2\omega_n Q_{op1} C_n}{\pi + 2\omega_n Q_{op1} C_n}\right) \end{aligned} \tag{6-21}$$

where $Q_{op1} = \dfrac{R_L}{\omega_{op1} L_s}$.

An initial estimate of the equivalent passive components subsequently follows by substituting (6-21) into (6-18) and (6-19), and the effective ratio of the resonant tank capacitances, C_{neff}, is given by:

$$C_{neff} = \frac{C_e}{C_s} = \frac{2\pi C_p}{C_s(2\phi_c - \sin)2\phi_c))} = \frac{2\pi C_n}{(2\phi_c - \sin(2\phi_c))} \tag{6-22}$$

Using the component values derived in (6-18) and (6-19), the capacitive-output LCLC resonant converter is now reduced to an equivalent 4th-order inverter, for which, using FMA, the effective input impedance, Z_{in}, of the equivalent circuit is (refer to the Appendix A for complete derivation):

$$\begin{aligned} Z_{in} &= j\omega_s L_s + \frac{1}{j\omega_s C_s} + \frac{1}{\dfrac{-\omega_s{}^2 L_p C_e + (j\omega_s C_e \Re_e + 1)}{(j\omega_s L_p - \omega_s{}^2 L_p C_e \Re_e)}} \\ &= \frac{\dfrac{R_L\omega_n}{Q_{op1}L_n}\left[\begin{array}{c} -C_n\omega_n{}^2\left(\dfrac{2\pi}{2\phi_c - \sin(2\phi_c)}\right) + L_n\left(1 - \dfrac{1}{\omega_n{}^2}\right) + C_n\left(\dfrac{2\pi}{2\phi_c - \sin(2\phi_c)}\right) + 1 \\ + j\left[\dfrac{1-\cos(2\phi_c)}{2\phi_c - \sin(2\phi_c)}\left(L_n - \dfrac{L_n}{\omega_n{}^2} - 1\right)\right] \end{array}\right]}{\dfrac{1-\cos(2\phi_c)}{2\phi_c - \sin(2\phi_c)} + j\left(\dfrac{2\pi\omega_n{}^2 C_n}{L_n(2\phi_c - \sin(2\phi_c))} - 1\right)} \end{aligned} \tag{6-23}$$

thereby allowing the amplitude of the input resonant current, $\hat{i}_{in}$, to be determined,

$$\hat{i}_{in} = \frac{2v_{DC}}{\pi|Z_{in}|} = \frac{2v_{DC}Q_{op1}L_n}{\pi R_L\omega_n} \times \frac{\left|\dfrac{1-\cos(2\phi_c)}{2\phi_c - \sin(2\phi_c)} + j\left(\dfrac{2\pi\omega_n{}^2 C_n}{L_n(2\phi_c - \sin(2\phi_c))} - 1\right)\right|}{\left|\begin{array}{c} -C_n\omega_n{}^2\left(\dfrac{2\pi}{2\phi_c - \sin(2\phi_c)}\right) + L_n\left(1 - \dfrac{1}{\omega_n{}^2}\right) + C_n\left(\dfrac{2\pi}{2\phi_c - \sin(2\phi_c)}\right) \\ +1 + j\left[\dfrac{1-\cos(2\phi_c)}{2\phi_c - \sin(2\phi_c)}\left(L_n - L_n\left(\dfrac{1}{\omega_n{}^2}\right) - 1\right)\right] \end{array}\right|} \tag{6-24}$$

The output voltage is subsequently obtained by substituting (6-24) into (6-8), giving,

$$V_{out} = \frac{\hat{i}_{in}R_L}{\pi} \times (1 + \cos(\phi_c)) = \frac{\dfrac{2v_{DC}Q_{op1}L_n}{\pi^2\omega_n} \times (1 + \cos(\phi_c)) \times \left|\dfrac{1-\cos(2\phi_c)}{2\phi_c - \sin(2\phi_c)} + j\left(\dfrac{2\pi\omega_n{}^2 C_n}{L_n(2\phi_c - \sin(2\phi_c))} - 1\right)\right|}{\left|\begin{array}{c} -C_n\omega_n{}^2\left(\dfrac{2\pi}{2\phi_c - \sin(2\phi_c)}\right) + L_n\left(1 - \dfrac{1}{\omega_n{}^2}\right) + C_n\left(\dfrac{2\pi}{2\phi_c - \sin(2\phi_c)}\right) \\ +1 + j\left[\dfrac{1-\cos(2\phi_c)}{2\phi_c - \sin(2\phi_c)}\left(L_n - L_n\left(\dfrac{1}{\omega_n{}^2}\right) - 1\right)\right] \end{array}\right|} \tag{6-25}$$

Although the above describing functions provide a suitable mechanism for estimating the output voltage, a primary source of error is related to inaccurate modelling of the rectifier on-state voltage, v_{diode}. Hence, using an iterative procedure, a more accurate estimate of the rectifier non-conduction angle ϕ_c can be obtained by substituting (6-25) into (6-7) (together with the diode on-state voltage drop, v_{diode})— and subsequently returning to (6-25) to refine the converter output voltage estimate. The iterative calculation procedure is shown in Fig. 6.4, for clarity.

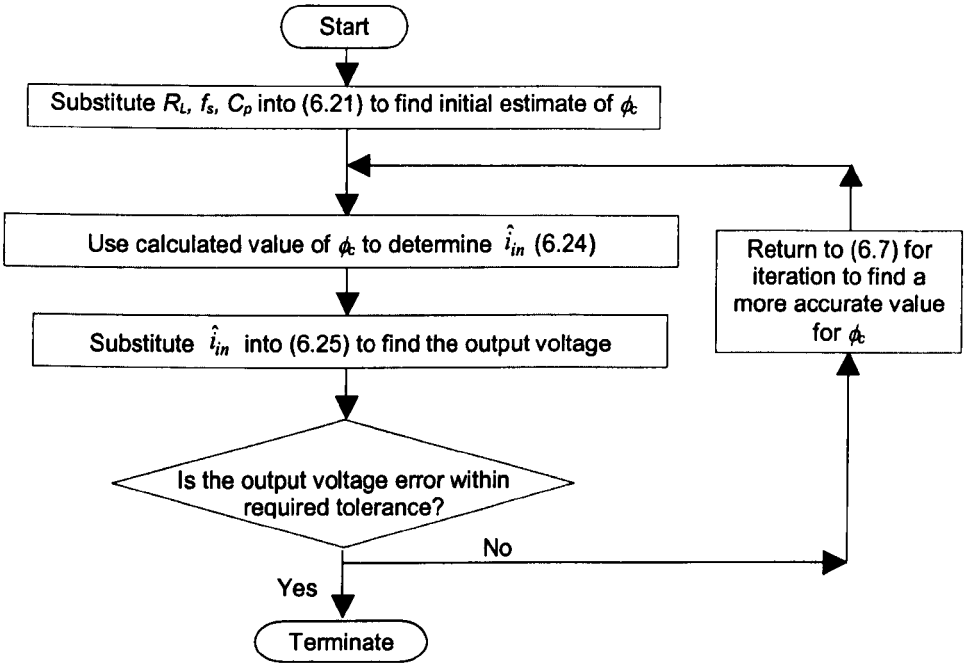

Figure 6.4 Flow-chart describing the iterative calculation procedure.

Figure 6.5 shows the variation of the normalised output-voltage versus normalised switching frequency, for a range of series quality factors, Q_{op1}, as predicted from the foregoing equivalent circuit transformation technique, for specific values of resonant component ratios L_n and C_n. For a low load quality factor, it can be seen that the converter behaves in a similar manner to a series resonant converter, and is suitable for step-down operation, whilst for higher quality factors the voltage-boosting characteristic of the converter (possible due to the inclusion of capacitor C_p) becomes dominant, thereby facilitating step-up operation. At low output loads, a high-load quality factor also results in a sharper resonant peak and the effective resonant frequency moving away from the series resonant frequency, ω_{op1}. The operating frequency should, therefore, be increased to maintain

inductive switching of the power devices when the converter is operated at light load. Moreover, the higher resonant frequency will result in higher conduction and turn-off losses in the power devices, whilst the voltage conversion ratio will rise, leading to the converter being operated far away from the effective resonance in order to maintain a constant output voltage.

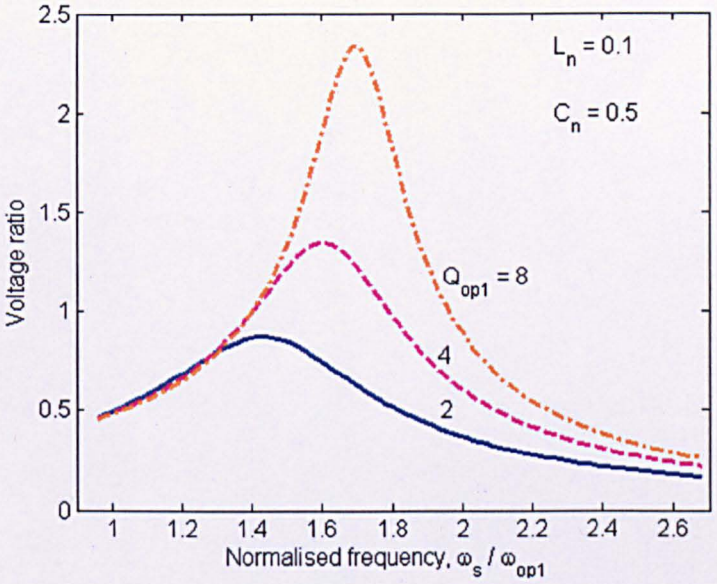

Figure 6.5 Variation of voltage gain with normalised frequency.

The main observation from the presented analysis is that the effective resonant frequency f_{oeff} of the converter is highly dependent on load resistance, by virtue of the dependence on the rectifier conduction angle ϕ_c, see (6-21). The resonant frequency, ω_{op1}, of the series resonant tank components, as a function of the effective resonant frequency of the converter, ω_{oeff}, is given by,

$$\omega_{op1} = \left[\frac{\omega_{oeff}^{\,2}\left(1+\frac{1}{L_n}+\frac{C_{neff}}{L_n}\right)}{2\left(\frac{C_{neff}}{L_n}\right)\omega_{oeff}^{\,4}} + \sqrt{\frac{\omega_{oeff}^{\,4}\left(1+\frac{1}{L_n}+\frac{C_{neff}}{L_n}\right)^2 - 4\left(\frac{C_{neff}}{L_n}\right)\omega_{oeff}^{\,4}}{4\left(\frac{C_{neff}}{L_n}\right)^2\omega_{oeff}^{\,8}}} \right]^{-\frac{1}{2}} \tag{6-26}$$

In particular, re-arranging (6-26) provides the ratio of the effective resonant frequency of the circuit, to the series resonant frequency,

$$\lambda_r^{\,2} = \left(\frac{\omega_{oeff}}{\omega_{op1}}\right)^2 = \frac{\left(1+\frac{1}{L_n}+\frac{C_{neff}}{L_n}\right)+\sqrt{\left(1+\frac{1}{L_n}+\frac{C_{neff}}{L_n}\right)^2 - 4\left(\frac{C_{neff}}{L_n}\right)}}{2\left(\frac{C_{neff}}{L_n}\right)} \tag{6-27}$$

The effective load quality factor of the equivalent circuit, Q_{oeff}, which is generally higher than the series load quality factor, Q_{op1}, is a non-linear function of f_s, the rectifier non-conduction angle, ϕ_c, and the load resistance, R_L.

$$Q_{oeff} = \frac{\Re_e}{\omega_{oeff} L_s} = C_s \Re_e \omega_{oeff} \left(\frac{\omega_{op1}}{\omega_{oeff}} \right)^2 = C_s \Re_e \omega_{oeff} \lambda_\tau^{\,2} \tag{6-28}$$

From Fig. 6.6, it is notable that the effective resonant frequency of the overall circuit moves with increasing load quality factor. Furthermore, the value of C_{neff} also varies as a function of load. In particular, as the series load quality factor, Q_{op1}, decreases, the effective resonant capacitance ratio, C_{neff}, increases, for constant C_n and L_n, as shown, from (6-22), in Fig. 6.6.

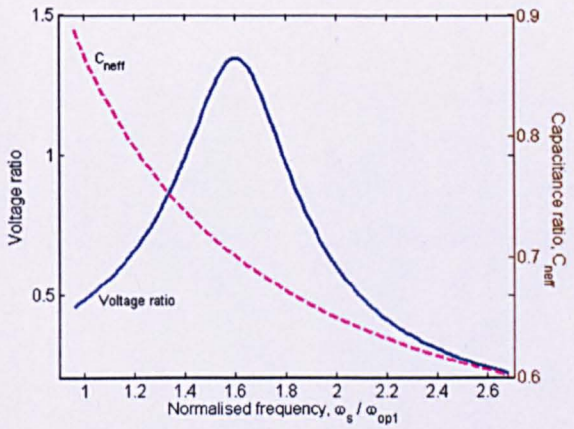

(a)

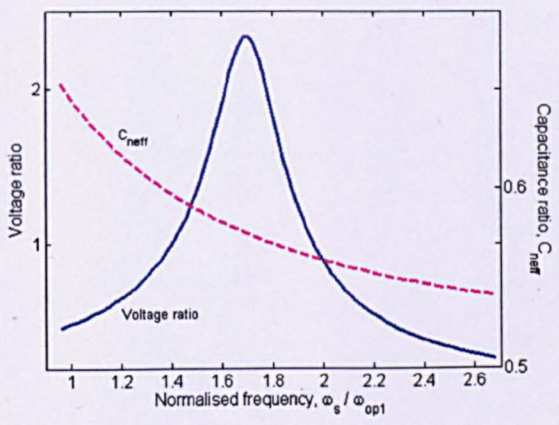

(b)

Figure 6.6 Normalised output voltage and equivalent resonant capacitance ratio at L_n=0.1 and C_n=0.5 (a) Q_{op1}=4 (b) Q_{op1}=8.

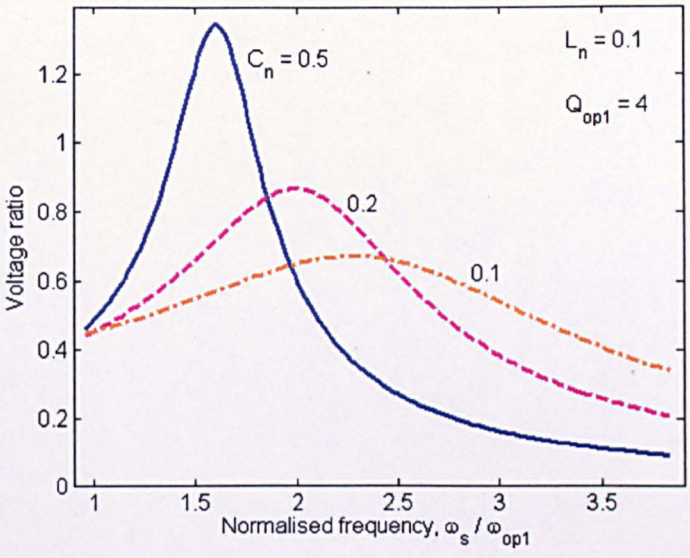

(a)

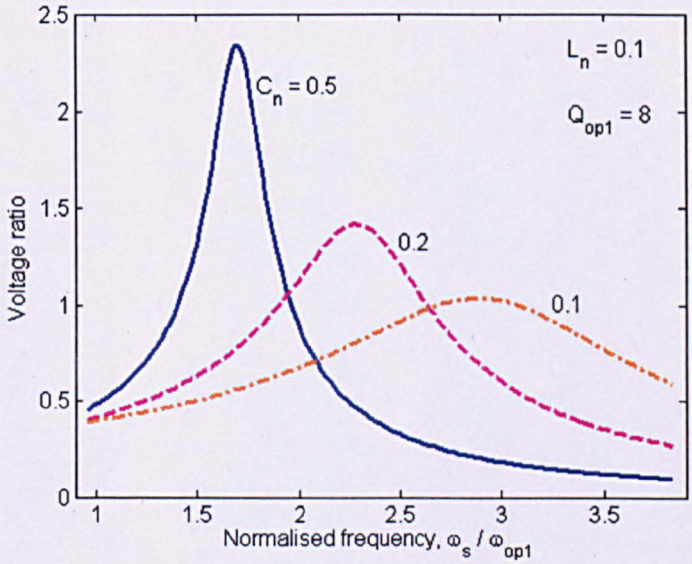

(b)

Figure 6.7 Output voltage characteristics for various values of C_n (=0.1, 0.2 and 0.5) at (a) Q_{op1}=4 and (b) Q_{op1}=8.

Figure 6.7 shows examples of the calculated input-output voltage conversion ratio, V_{out}/v_{DC} as a function of the normalised switching frequency, ω_n, for a range of resonant capacitance ratios C_n, from which, it will be seen that for high values of C_n, the output voltage about the resonant frequency increases, facilitating voltage-boost operation. However, for low values of C_n, the input-output voltage characteristic exhibits a smoother frequency response with a reduced resonant peak. The sharper

resonant peak which results as C_n is increased implies that the output voltage regulation when the converter is subjected to variations in supply voltage, can be achieved through smaller changes in the operating frequency, i.e. the effective forward path gain is higher, and, hence, less control action is required.

The influence of C_p on the predicted output voltage of the converter is shown in Fig. 6.8(a). As expected from the previous discussions, the maximum attainable output voltage increases as C_p is increased, albeit increasing the input current and imparting higher electrical stresses on the resonant components, for the same output voltage.

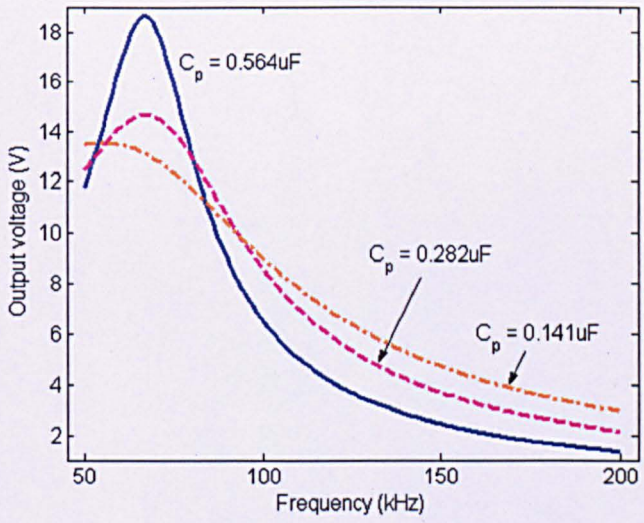

(a)

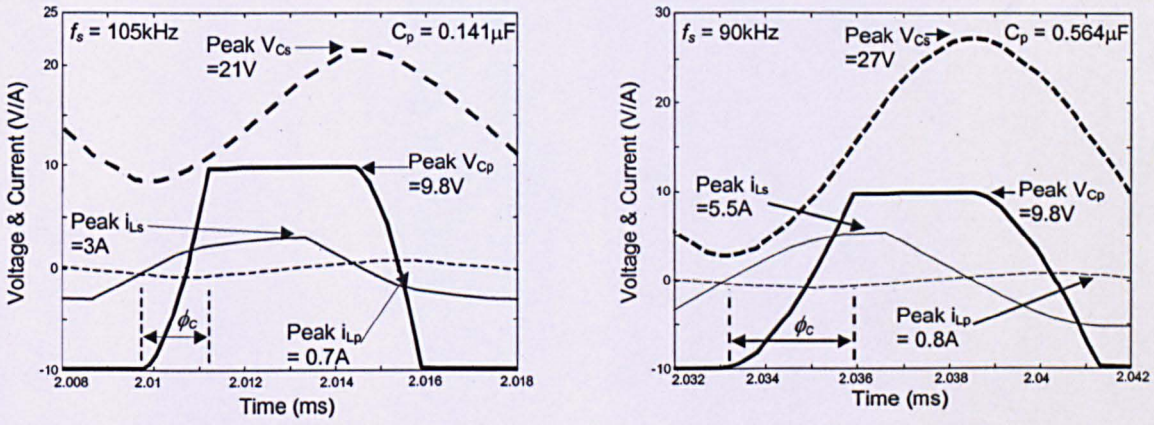

(b)

Figure 6.8 Variation of output voltage with parallel resonant capacitor C_p (a) frequency sweep and (b) voltage and current stresses.

Figure 6.8(b) shows the predicted time-domain voltage and current waveforms to highlight the fact that the electrical stresses and the rectifier non-conduction angle, seen by converters with a similar output voltage, depend on the value of resonant capacitor C_p. Specifically, it can be seen that for lower values of C_p, the rectifier non-conduction angle essentially becomes negligible, and the rectifier/output filter is presented with a square-wave voltage waveform.

The accuracy of the proposed analysis techniques for predicting the steady-state behaviour of the converter is now demonstrated by comparing predictions with results from SPICE simulations and from measurements from a prototype converter (see Figure 6.9), with measured component values for providing 5-12V output voltages, given in Table 6.1. The Half-bridge MOSFETS are IRLZ34N, and are driven by IR2108 gate drivers.

Table 6.1 Experiment voltage-output LCLC resonant converter specifications.

Parameters	Values
DC link input voltage, v_{DC} (V)	30
Series resonant inductance, L_s (μH)	12.6
Parallel resonant inductance, L_p (μH)	25
Series resonant capacitance, C_s (μF)	0.737
Parallel resonant capacitance, C_p (μF)	0.141, 0.282, 0.564
Load Resistance, R_L (Ω)	5, 10

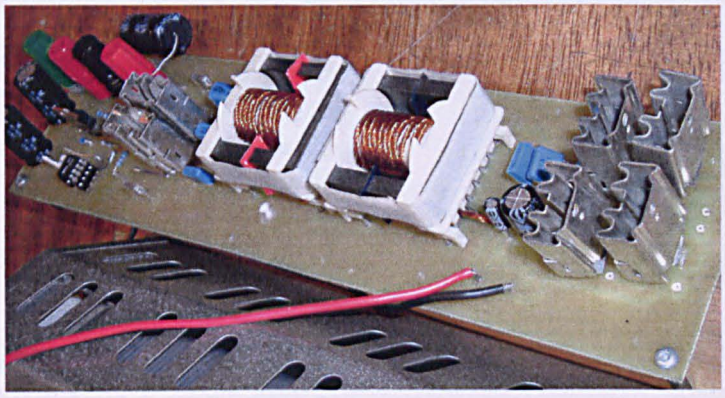

Figure 6.9 Experimental 4th-order capacitive-output resonant converter.

Figure 6.10 compares the predicted variation in output voltage, with switching frequency, using the proposed analysis procedure, (6-7), (6-21), (6-24), and (6-25), with the measured variation, Fig. 6.10(a), and with the variation predicted from FMA, Fig. 6.10(b), for two different loads.

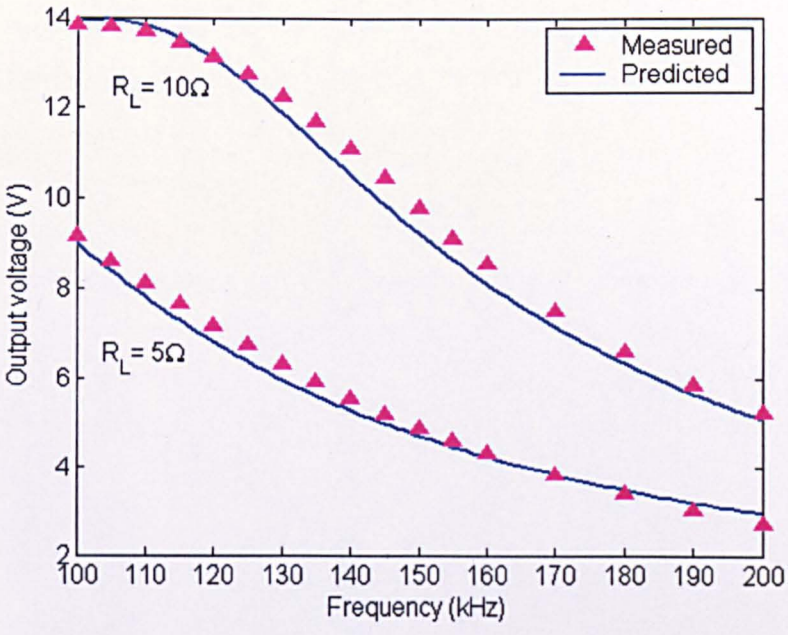

(a)

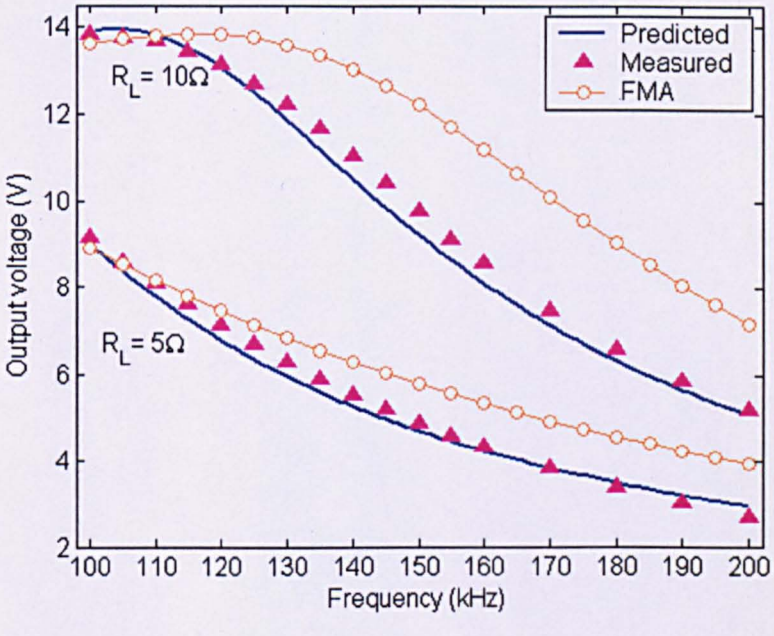

(b)

Figure 6.10 Predicted output voltage from proposed analysis procedure compared with (a) measurements on prototype converter (b) results from FMA.

In each case, it can be seen that the proposed analytical model accurately describes the steady-state operation of the converter. The discrepancy in output voltage predictions using FMA is due to the

assumption that the equivalent resistance—$R_{eq} = \frac{8}{\pi^2} R_L$ is sufficient to accurately model the interaction of the rectifier and capacitor output filter networks, which, as has been demonstrated, is not the case.

From (6-18), (6-21), as the angle $\phi_c \to 0$, the equivalent capacitance due to the rectifier/output filter coupling effect, also tends to zero, i.e. $C_e \to 0$. By way of example, from (6-18), (6-21), and employing the trigonometric relationship—$\cos\left[2\cos^{-1}(\theta)\right] = 2\theta^2 - 1$, it can be shown that the equivalent output resistance, $\Re_e$, is given by:

$$\Re_e = \frac{1}{4\pi^2 f_s C_p} \times \left(1 - \cos(2\phi_c)\right) = \frac{1}{4\pi^2 f_s C_p}\left(1 - 2\left(\frac{\pi - 4\pi^2 f_s C_p R_L}{\pi + 4\pi^2 f_s C_p R_L}\right)^2 + 1\right)$$

$$= \frac{1}{4\pi^2 f_s C_p}\left(\frac{32\pi^2 f_s C_p R_L}{\pi^2 + 8\pi^2 f_s C_p R_L + 16\pi^2 {C_p}^2 {R_L}^2}\right) \tag{6-29}$$

$$C_p \to 0, \quad \Re_e \to \frac{8R_L}{\pi^2}.$$

thereby, if $C_p \to 0$, then equivalent resistor $\Re_e \to \frac{8R_L}{\pi^2}$.

Consequently, the characteristic of the converter then becomes similar to that of a 3rd-order CLL series-loaded resonant converter. For example, Fig. 6.11 shows the calculated input-output voltage conversion ratio, as a function of the normalised switching frequency, ω_n, for various values of the resonant capacitance ratio, C_n, and resonant inductance ratio, L_n, for a constant value of Q_{opl}.

It can be seen from Fig. 6.11(a) that for the same value of C_n, the output-voltage boosting effect of a 3rd-order LCC-type resonant converter (L_n is assumed to be zero) is more significant than for the LCLC voltage-output counterpart. In contrast, the maximum voltage conversion ratio at resonance, which is attainable from the LCLC voltage-output converter, is comparable to that for a CLL converter in which C_n is small enough to be neglected, whilst requiring a smaller range of switching frequency for output voltage regulation.

Figure 6.11(b) shows that as the value of resonant capacitance ratio C_n, for the LCC converter, is halved, the maximum voltage conversion ratio is similar for all three converters at the effective

resonant frequency. It will also be seen that LCLC voltage-output converter has a sharper curve around resonance, which implies a better output voltage control characteristic.

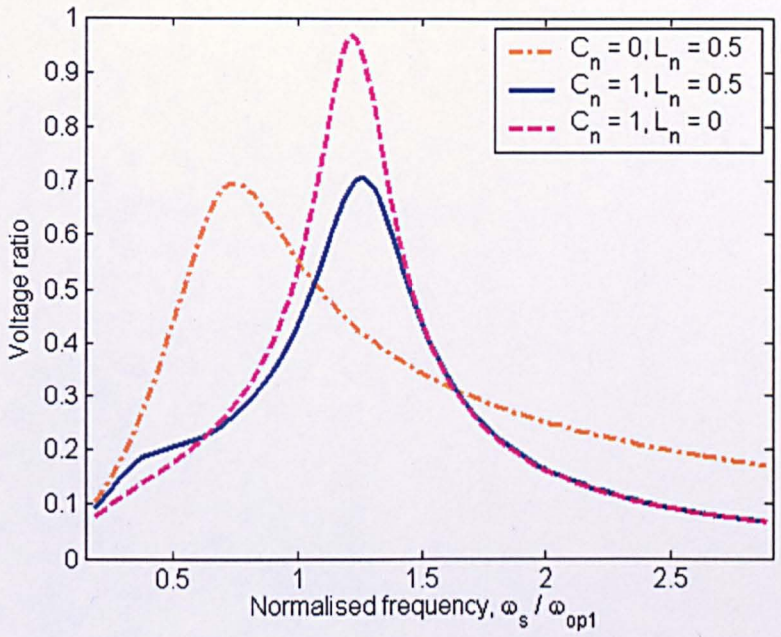

(a)

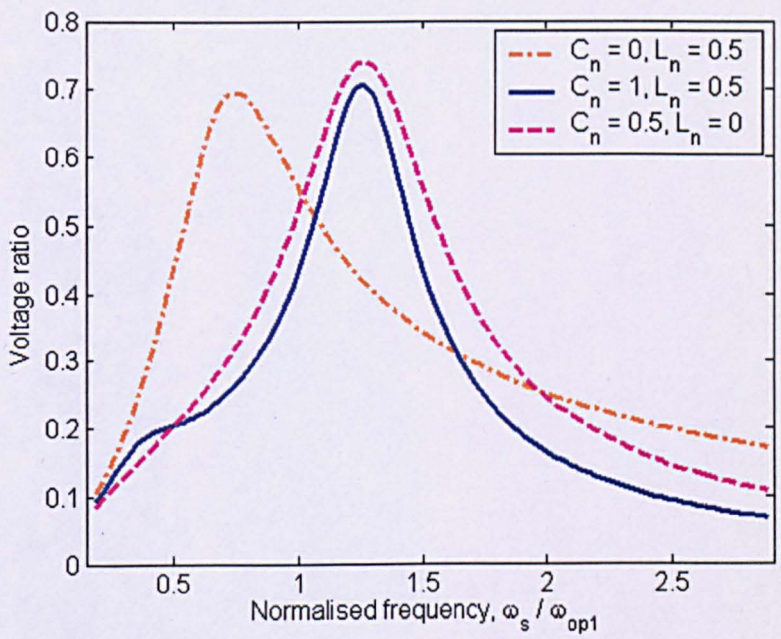

(b)

Figure 6.11 Output voltage characteristic for various values of C_n and L_n at constant Q_{op1}=1.2.

6.3. Design Methodologies

The presented analytical equations describing the characteristics of the 4th-order LCLC converter are now employed as a basis for deriving various design/synthesis procedures, the equivalent circuit parameters $\Re_e$ and C_e being fundamental to the calculation of specific circuit component values. Four methodologies are presented, viz.:

i) Output voltage constraint method
ii) Parallel capacitor constraint method
iii) Rectifier non-conduction angle constraint method
iv) Input voltage versus input current phase-angle constraint method

Of the methodologies, the output voltage constraint methodology is likely to be the most useful, by virtue of requiring a minimal amount of user-supplied information [F11]. The method essentially comprises a reformulation of the analysis techniques presented in Section 6.2, and allows the response of a converter to be independently evaluated for given values of the resonant component values, C_n, L_n, and Q_{op1}.

The requirement to constrain the value of parallel capacitance, C_p, arises primarily because of the possibility of exploiting parasitic elements (predominantly the inter-winding capacitance of a transformer or the rectifier diode junction capacitance) to realise an appropriate value. In addition, it also permits large values of C_p to be chosen to achieve a voltage-boosting effect around the effective resonant frequency, or, in contrast, small values of C_p to be employed in order to reduce electrical component stresses.

The rectifier non-conduction angle constraint design methodology is essentially a complement to the parallel capacitor design methodology, in that it relates the influence of the C_p charging period to the attainable DC voltage output. A large rectifier non-conduction angle, ϕ_c, is essential to provide a high-voltage conversion ratio, since it allows C_p to be charged/discharged for longer periods within each half-cycle, whilst a small value can be selected to facilitate step-down voltage operation, albeit compromising the output voltage regulation if the load falls below some design-specific minimum value.

As discussed in the previous section, important factors that influence the design of voltage-output converters, are their operational efficiency and component stresses. Therefore, since reducing the stress on the switching devices is a key incentive for resonant operation, the input voltage versus current phase angle constraint methodology, is the most useful approach for realising a power supply for which low switching stresses are a priority, i.e. exhibits a high power factor, even at high switching frequencies.

6.3.1. Output Voltage Constraint Method

This method enables converter component values to be chosen to achieve a given voltage conversion ratio and load quality factor Q_{op1}. The procedure numerically sweeps the normalised switching frequency, $\omega_n = \omega_s/\omega_{op1}$, and equates the normalised output voltage, V_{out}/v_{DC}, to the required voltage conversion ratio, M_{vcr}. Specifically, after values for the resonant capacitance ratio, C_n, and the series load quality factor, Q_{op1}, have been selected, to obtain a desirable frequency response for the normalised output voltage, by rearranging (6-25), the normalised output voltage is found by sweeping the value of the normalised switching frequency, $\omega_n = \omega/\omega_{op1}$ —an example being shown in Fig. 6.5, with V_{out}/v_{DC} given by:

$$\frac{V_{out}}{v_{DC}} = \frac{\dfrac{2Q_{op1}L_n}{\pi^2\omega_n}\times\left(1+\cos(\phi_c)\right)\times\left|\dfrac{1-\cos(2\phi_c)}{2\phi_c-\sin(2\phi_c)}+j\left(\dfrac{2\pi\omega_n{}^2C_n}{L_n(2\phi_c-\sin(2\phi_c))}-1\right)\right|}{\left|\begin{array}{c}-C_n\omega_n{}^2\left(\dfrac{2\pi}{2\phi_c-\sin(2\phi_c)}\right)+L_n\left(1-\dfrac{1}{\omega_n{}^2}\right)+C_n\left(\dfrac{2\pi}{2\phi_c-\sin(2\phi_c)}\right)\\ +1+j\left[\dfrac{1-\cos(2\phi_c)}{2\phi_c-\sin(2\phi_c)}\left(L_n-L_n\left(\dfrac{1}{\omega_n{}^2}\right)-1\right)\right]\end{array}\right|} \tag{6-30}$$

The numerical sweep procedure enables the operating frequency of the converter or the required switching frequency to resonant frequency ratio, to be found, by equating the resulting magnitude of the equivalent circuit transfer function (6-30) to the voltage conversion ratio specification, M_{vcr}. Having established suitable values for C_n, Q_{op1} and ω_n, the effective characteristic impedance, Z_{oeff} of the 4th-order resonant circuit, which is also influenced by the rectifier action, is obtained from:

$$Z_{oeff} = \omega_{oeff}L_s = \left(\frac{\omega_{oeff}}{\omega_{op1}}\right)\omega_{op1}L_s = \lambda_r\sqrt{\frac{L_s}{C_s}} = \lambda_r Z_{op1} \tag{6-31}$$

where the characteristic impedance of the series resonant tank is:

$$Z_{op1} = \frac{R_L}{Q_{op1}} \tag{6-32}$$

Since the ratio $\lambda_r = \omega_{oeff} / \omega_{op1} \geq 1$, then $Z_{oeff} > Z_{op1}$, implying that the characteristic impedance is increased. Using (6-31) and (6-32), the required value of series inductor is determined from the desired nominal switching frequency:

$$L_s = \frac{Z_{oeff}}{2\pi f_{oeff}} = \frac{Z_{op1}\lambda_r}{2\pi f_{oeff}} = \frac{R_L \lambda_r}{2\pi f_{oeff} Q_{op1}} = \frac{R_L}{\omega_{op1} Q_{op1}} = \frac{R_L \omega_n}{2\pi f_s Q_{op1}} \tag{6-33}$$

Finally, the required series resonant capacitance is found from the required resonant frequency and $\overline{\omega}_{eff}$, as follows:

$$C_s = \frac{\lambda_r^{\,2}}{4\pi^2 f_{oeff}^{\,2} L_s} = \frac{\omega_n^{\,2}}{4\pi^2 f_s^{\,2} L_s} \tag{6-34}$$

whilst parallel resonant capacitance C_p follows, by definition, from $C_p = C_s \times C_n$ and $L_p = L_s / L_n$.

6.3.2. *Parallel Capacitor Constraint Method*

To calculate values for the resonant components, this method requires that C_p, V_{out}, v_{DC}, the output power rating p_{out}, the rectifier diode voltage drop, the effective resonant frequency, f_{oeff}, the switching frequency, f_s, and both C_n and L_n, are specified. From the specification, the nominal output load resistance is:

$$R_L = \frac{V_{out}^{\,2}}{p_{out}} \tag{6-35}$$

The rectifier non-conduction angle ϕ_c is determined by substituting given values of f_s and C_p into (6-7), and rearranging, to give:

$$\phi_c = \cos^{-1}\left(\frac{\pi i_{out} - 4\pi v_b f_s C_p}{\pi i_{out} + 4\pi v_b f_s C_p}\right) = \cos^{-1}\left(\frac{\pi - 4\pi R_L f_s C_p - \dfrac{8\pi v_{diode} f_s C_p}{i_{out}}}{\pi + 4\pi R_L f_s C_p + \dfrac{8\pi v_{diode} f_s C_p}{i_{out}}}\right) \tag{6-36}$$

where $i_{out} = \frac{p_{out}}{V_{out}}$ is the output current and $v_b = V_{out} + 2v_{diode}$ is the peak voltage across the rectifier. Since the equivalent passive components, $\Re_e$ and C_e are dependant on the design parameters, C_p, R_L, f_s and, ϕ_c, (6-36) is substituted into (6-18) and (6-19) to find their 'equivalent' values. The required value of series capacitance C_s needed to provide the desired C_n and ϕ_c, is then found from (6-37),

$$C_s = \frac{C_e C_n (2\phi_c - \sin(2\phi_c))}{2\pi} \tag{6-37}$$

From (6-22), (6,27) and (6.34), the series inductance is given by:

$$L_s = \frac{\lambda_r^2}{4\pi^2 f_{oeff}^2 C_s} \tag{6-38}$$

and $L_p = L_s / L_n$ and $C_p = C_s C_n$.

6.3.3. Rectifier Non-Conduction Angle Constraint Method

Here, the resonant component values are determined for a specified rectifier non-conduction angle ϕ_c, values for V_{out}, v_{DC}, p_{out}, v_{diode}, f_{oeff}, f_s, C_n and L_n also being specified. From (6-11), the value of parallel resonant capacitor could be calculated from knowledge of the peak input current $\hat{i}_{in}$:

$$C_p = \frac{\hat{i}_{in}}{4\pi f_s v_b} \times (1 - \cos(\phi_c)) \tag{6-39}$$

However, since $\hat{i}_{in}$ is rarely known a-priori, at the design synthesis stage, it is generally more appropriate to determine C_p from output quantities. Thus, substituting (6-6) into (6-39) and rearranging gives:

$$C_p = \frac{i_{out}}{4 f_s v_b} \times \frac{1 - \cos(\phi_c)}{1 + \cos(\phi_c)} \tag{6-40}$$

where $i_{out} = \frac{p_{out}}{V_{out}}$ and $v_b = V_{out} + 2v_{diode}$ is the peak voltage across the bridge rectifier.

The value of the series resonant capacitance follows from $C_s = C_p / C_n$, and the series and parallel inductances are determined, respectively, from $L_s = \frac{\lambda_r^2}{4\pi^2 f_{oeff}^2 C_s}$ and $L_p = L_s / L_n$.

6.3.4. *Input Voltage Versus Current Phase Angle Constraint Method*

Here, resonant components are chosen based on the requirement for achieving a given phase-angle, β_{vcr}, between the input voltage and input current. The procedure is driven by a compromise between ensuring zero-voltage switching (ZVS) of the power devices to facilitate high efficiency operation (i.e. the circuit appears to be inductive from the perspective of the power switches), whilst also maximising the voltage conversion ratio and power factor (which are ultimately a maximum at resonance).

The phase difference between the fundamental frequency components of the input voltage and the input current is, from (6-23):

$$\beta_{in} = \tan^{-1}\left(\frac{\frac{1-\cos(2\phi_c)}{2\phi_c-\sin(2\phi_c)}\times\left(L_n-\frac{L_n}{\omega_n^{\,2}}-1\right)}{-\frac{2\pi}{2\phi_c-\sin(2\theta_c)}\left(C_n\omega_n^{\,2}\right)+L_n\left(1-\frac{1}{\omega_n^{\,2}}\right)+\frac{2\pi}{2\phi_c-\sin(2\phi_c)}(C_n)+1}\right)-\tan^{-1}\left(\frac{\frac{2\pi}{2\phi_c-\sin(2\phi_c)}\left(\frac{C_n\omega_n^{\,2}}{L_n}\right)-1}{\frac{1-\cos(2\phi_c)}{2\phi_c-\sin(2\phi_c)}}\right) \quad (6\text{-}41)$$

The normalised frequency $\omega_n = \omega_s/\omega_{op1}$ is swept numerically to determine the required value for β_{in} to equal the specified value β_{vcr}, for given values of Q_{op1}, C_n and L_n. By way of example, Fig. 6.12 enables the required switching frequency to resonant frequency ratio, ω_n, to obtain a specified value of β_{in}. Whilst soft-switching of the resonant converter power switches serves to enhance efficiency compared to equivalent hard-switched converters, the electrical stresses to which the tank components are exposed can be much higher by virtue of the currents, which are imposed on them, being essentially sinusoidal at high Q_{op1}.

Figure 6.13 shows the normalised input current obtained from the simplified equivalent circuit of Fig. 6.14, for various values of load quality factor, viz. $Q_{op1} = 2,4,8$. An advantage of the LCLC converter topology is that the input current decreases as the load quality factor decreases, which reduces the losses in the switching devices, thereby enabling a high efficiency to be achieved even for low loads. Substituting the required design parameters ϕ_c, V_{out} into (6-24) and solving for the peak series resonant current, $\hat{i}_{in}$, leads to the required value of capacitance C_p:

$$C_p = \frac{\hat{i}_{in}}{4\pi f_s(V_{out}+2v_{diode})}\times(1-\cos(\phi_c)) \quad (6\text{-}42)$$

Resonant components C_s and L_s are subsequently found, respectively, from (6-37) and (6-38). Finally, the required input voltage rating is given by,

$$v_{DC} = \frac{\pi \hat{i}_{in} Z_{in}}{2} \tag{6-43}$$

It should be noted that this methodology is also useful for producing numerical sweeps of the peak resonant current versus the normalised frequency, $\omega_n = \omega_s / \omega_{op1}$ for specified values of v_{DC} and V_{out}.

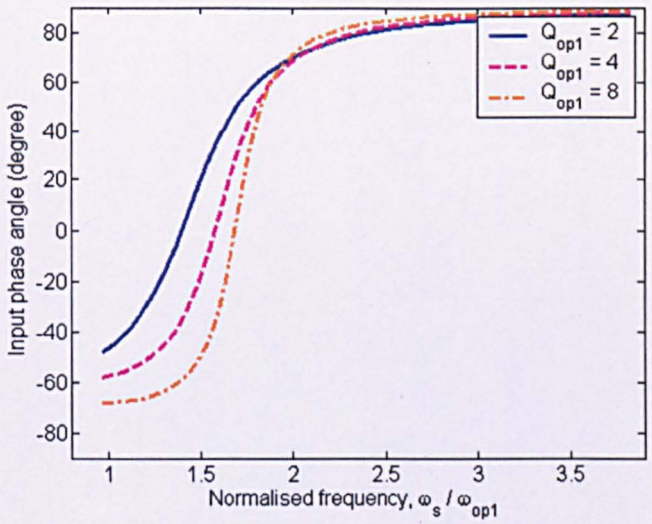

(a)

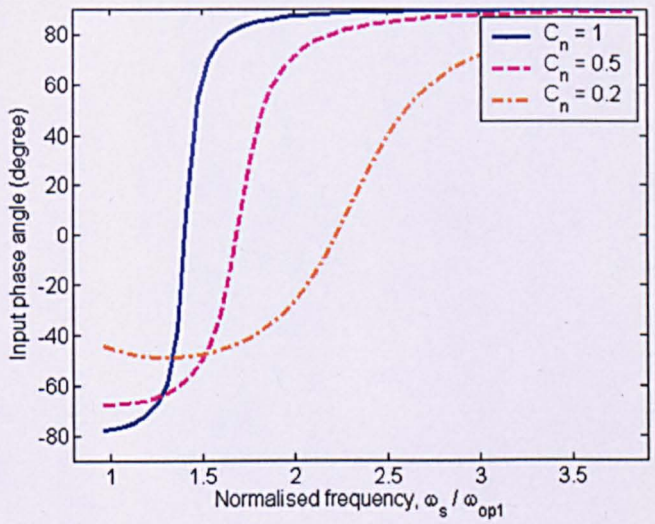

(b)

Figure 6.12 Input phase angle of the resonant circuit versus normalised switching frequency, for (a) specified resonant component ratios C_n=0.5 (b) a specified load quality factor Q_{op1}=8.

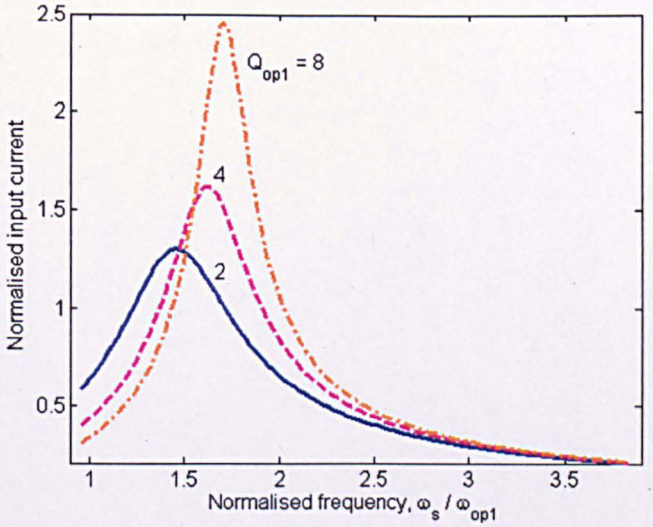

Figure 6.13 Variation of normalised input current (C_n = 0.5, L_n = 0.1).

6.4. Summary

A method based on the derivation of a describing function to model the complex interaction between the parallel capacitor and rectifier/output-filter, has been developed, to facilitate rapid steady-state analysis of a capacitor–loaded 4th-order resonant power converter. Predictions of the output voltage, as a function of load resistance, and the regulation of output voltage as a function of switching frequency, have been compared with measurements on a prototype LCLC voltage-output converter, and with results from SPICE simulations. They confirm that excellent accuracy is afforded by the proposed analysis methods, which, due to their very low computational overhead, are eminently suitable for routine use during the design of high-order LCLC converters.

From the presented results, the advantages of the LCLC voltage-output converter, for operation above resonance, have been shown to be i) the peak input resonant current decreases with load current, thereby maintaining efficiency from full load to light load ii) a good compromise is achievable between the control characteristics, component values, efficiency and electrical stresses iii) a decrease in losses compared to those of the LCLC current-output converter due to the elimination of the output smoothing inductor. Finally, the presented describing functions have been employed to facilitate the derivation of 4-design synthesis methodologies, each satisfying different user-defined constraints to aid in the design of LCLC converters. Conditions under which each methodology might be employed, and the qualities they subsequently impart to a converter design, have also been discussed.

References

[F1] I. Batarseh, "Resonant converter topologies with three and four energy storage elements", *IEEE Trans. on Power Electronics*, **9**, pp. 64-73, 1994.

[F2] R. L. Steigerwald, "A Comparison of half-bridge resonant converter topologies", *IEEE Trans. on Power Electronics*, **3**, pp. 174-182, 1988.

[F3] H. M. Suryawanshi and S. G. Tarnekar, "Modified LCLC-type series resonant converter with improved performance", *IEE Proc. Electric Power Applications*, **143**, pp. 354-360, 1996.

[F4] A. K. S. Bhat, "Analysis and design of a series-parallel resonant converter with capacitive output filter", *IEEE Trans. on Industrial Applications*, **27**, pp. 523-534, 1991.

[F5] Y. A. Ang, M. P. Foster, C. M. Bingham, D. A. Stone, H. I. Sewell and D. Howe, "Analysis of 4th-order LCLC resonant power converters", *IEE Proc. Electric Power Applications*, **151**, pp. 169-181, 2004.

[F6] G. Ivensky, A. Kats and S. Yaakov, "An RC load model of parallel and series-parallel resonant DC-DC converters with capacitive output filter", *IEEE Trans. on Power Electronics*, **14**, pp. 515-521, 1999.

[F7] J. G. Hayes and M. G. Egan, "Rectifier-compensated fundamental mode approximation analysis of the series parallel LCLC family of resonant converters with capacitive output filter and voltage-source load", in *30th IEEE Power Electronics Specialist Conference Rec.*, 1999, pp. 1030-1036.

[F8] A. J. Forsyth and S. V. Mollov, "Simple equivalent circuit for the series-loaded resonant converter with voltage boosting capacitor", *IEE Proc. Electric Power Applications*, **145**, pp.301-306, 1998.

[F9] H. I. Sewell, M. P. Foster, C. M. Bingham, D. A. Stone, D. Hente and D. Howe, "Analysis of voltage output LCC resonant converters, including boost mode operation", *IEE Proc. Electric Power Applications*, **150**, pp.673-679, 2003.

[F10] C. Gould, D. A. Stone, M. P. Foster and C. M. Bingham, "State-variable modelling of CLL resonant converters", in *2nd IEE Power Electronics, Machines & Drives Conference Proc.*, Edinburgh, 2004, pp.214-219.

[F11] Y. Ang, C. M. Bingham, M. P. Foster, D. A. Stone and D. Howe, "Design Orientated Analysis of 4th-Order LCLC Converters with Capacitive Output Filter", *IEE Proc. Electric Power Applications*, **152**, pp. 310-322, 2005.

CHAPTER 7

Cyclic Averaging Analysis of Voltage-Output Converters

As in the case of the current-output converter, here, the large-signal state-variable model, developed in Chapter 2, is now transformed into a cyclic model description, by decomposing it into several piecewise linear (PWL) equations, based on the state of resonant tank current and voltage, and rectifier current.

Whilst the duty-times required for cyclic analysis of the 4th-order current-output resonant converter, have been derived through the use of a FMA equivalent circuit, this technique often proves inaccurate, and renders undesirable cyclic mode results. Thus, the enhanced describing function concept from Chapter 6 will be adopted to determine the required duties for cyclic averaging. The parallel resonant capacitor voltage v_{Cp} of the converter, Fig. 7.1, is saturated at the modulus of the output voltage plus the rectifier on-state voltage drop, v_{diode}, during the clamping period, thereby incurring six operating modes during each switching cycle, as shown in the example waveforms of Fig. 7.2.

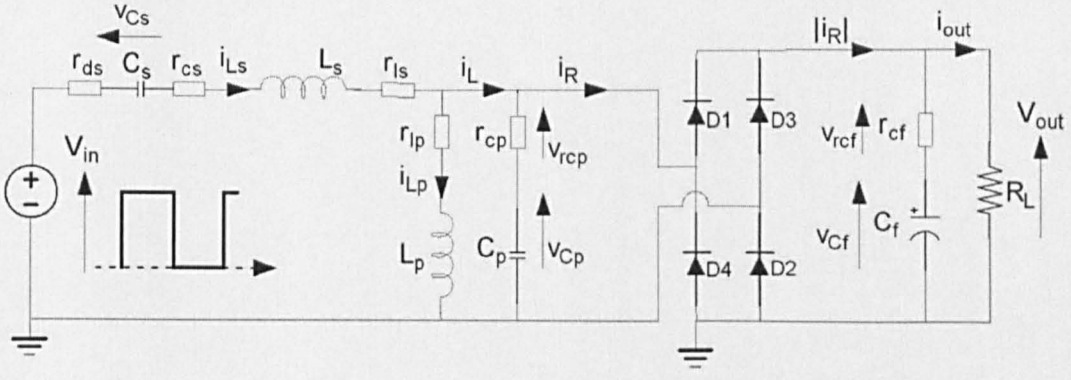

Figure 7.1 Simplified circuit of 4th-order voltage-output resonant converter.

7.1. Cyclic Mode Analysis of Voltage-Output Resonant Converters

Analysis of the behaviour of the voltage-output 4th-order resonant converter (Fig. 7.1) (operated above resonance) for switching frequencies above, and in the region of, the resonant frequency, shows that there are six dominant modes of operation in each switching cycle, defined with respect to the polarity of the input excitation voltage and state of the rectifier bridge current [G1], as shown in Fig. 7.2.

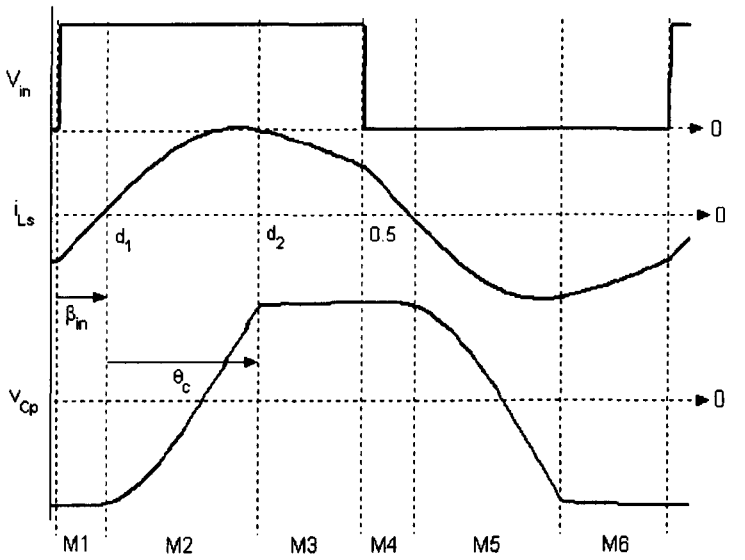

Figure 7.2 Voltage and current waveforms of a voltage output LCLC resonant converter.

Two of the modes are defined with respect to the polarity of MOSFET half-bridge input voltage. The remaining modes are determined by the conduction state of the rectifier input current, i_R, i.e. when $v_{Cp}>0$ and the rectifier is conducting positive current, or $v_{Cp}<0$ and the rectifier conducts negative current, or otherwise, the rectifier is not conducting and the resonant circuit is essentially decoupled from the rectifier. The modes are summarised below:

Mode 1 (M1)	$V_{in}>0$	$i_R<0$
Mode 2 (M2)	$V_{in}>0$	$i_R=0$
Mode 3 (M3)	$V_{in}>0$	$i_R>0$
Mode 4 (M4)	$V_{in}=0$	$i_R>0$
Mode 5 (M5)	$V_{in}=0$	$i_R=0$
Mode 6 (M6)	$V_{in}=0$	$i_R<0$

For reasons highlighted previously, modelling of the cyclic mode for this converter is complicated by the rectifier current being a highly non-linear function of the resonant current and filter capacitor voltage. The state-variable model of the converter is derived by partitioning the converter dynamics into 'fast' and 'slow' sub-systems that are coupled by the rectifier current.

The combined state-variable models, and coupling equation, are ultimately given by (7-1) (full derivation details have been previously given in Chapter 2).

$$\begin{bmatrix} \dot{v}_{Cp} \\ \dot{v}_{Cs} \\ \dot{i}_{Lp} \\ \dot{i}_{Ls} \\ \dot{v}_{Cf} \end{bmatrix} = \begin{bmatrix} 0 & 0 & -\frac{1}{C_p} & \frac{1}{C_p} & 0 \\ 0 & 0 & 0 & \frac{1}{C_s} & 0 \\ \frac{1}{L_p} & 0 & 0 & 0 & 0 \\ -\frac{1}{L_s} & -\frac{1}{L_s} & \frac{r_{cp}}{L_s} & -\frac{r_{ds}+r_{cp}+r_{cs}+r_{ls}}{L_s} & 0 \\ 0 & 0 & 0 & 0 & -\frac{1}{C_f(R_L+r_{cf})} \end{bmatrix} \begin{bmatrix} v_{Cp} \\ v_{Cs} \\ i_{Lp} \\ i_{Ls} \\ v_{Cf} \end{bmatrix} + \begin{bmatrix} -\frac{i_R}{C_p} \\ 0 \\ 0 \\ \frac{V_{in}}{L_s}+\frac{r_{cp}i_R}{L_s} \\ \frac{|i_R|R_L}{C_f(R_L+r_{cf})} \end{bmatrix} \tag{7-1a}$$

$$i_R = \frac{C_f}{\mathrm{sgn}(i_L)C_p + C_f} i_L + \mathrm{sgn}(i_L)\frac{C_p}{\mathrm{sgn}(i_L)C_p + C_f}\frac{v_{Cf}}{R_L} \tag{7-1b}$$

and the output voltage of the converter is given by,

$$V_{out} = \frac{R_L r_{cf}|i_R|}{R_L + r_{cf}} + \frac{R_L v_{Cf}}{R_L + r_{cf}} \tag{7-2}$$

However, by assuming the output filter capacitance C_f is sufficiently larger than C_p, for preserving low ripple level on the output voltage, (7-1b) reduces to,

$$i_R = \begin{cases} \frac{C_f}{C_p + C_f} i_L & \text{for} \quad |v_{Cp}| = V_{out} + 2v_{diode} \\ 0 & \text{for} \quad |v_{Cp}| < V_{out} + 2v_{diode} \end{cases} \tag{7-3}$$

In a similar manner to that used for analysing the current-output variant (see Chapter 4), the dynamic matrices, A_i and the input excitation matrices, B_i are found by substituting the coupling equation (7-3) into (7-1a) and considering the polarity of the input voltage and direction of the rectifier current. During M1, V_{in} is positive and i_R is negative whilst parallel resonant capacitor voltage, v_{Cp}, is clamped to V_{out} (plus the on-state rectifier voltage drop).

The resulting piecewise linear dynamic matrix equation is, therefore, given by,

$$A_1 = \begin{bmatrix} 0 & 0 & -\frac{1}{C_p}+\frac{C_f}{C_p(C_f+C_p)} & \frac{1}{C_p}-\frac{C_f}{C_p(C_f+C_p)} & 0 \\ 0 & 0 & 0 & \frac{1}{C_s} & 0 \\ \frac{1}{L_p} & 0 & 0 & 0 & 0 \\ -\frac{1}{L_s} & -\frac{1}{L_s} & \frac{r_{cp}}{L_s}-\frac{r_{cp}C_f}{L_s(C_f+C_p)} & -\frac{r_{ds}+r_{cp}+r_{cs}+r_{ls}}{L_s}+\frac{r_{cp}C_f}{L_s(C_f+C_p)} & 0 \\ 0 & 0 & \frac{R_L C_f}{C_f(R_L+r_{cf})(C_f+C_p)} & -\frac{R_L C_f}{C_f(R_L+r_{cf})(C_f+C_p)} & -\frac{1}{C_f(R_L+r_{cf})} \end{bmatrix} \tag{7-4}$$

The excitation matrix, $B_1 = \begin{bmatrix} 0 & 0 & 0 & \frac{V_{in}}{L_s} & 0 \end{bmatrix}^T$ and the coupling equation is $|i_R| = -\frac{C_f}{C_f+C_p} i_L$.

During M2 ($V_{in} > 0$, $i_R = 0$), the output rectifier is decoupled from the resonant tank, giving the dynamic and excitation matrices, respectively, as A_2 and B_2:

$$A_2 = \begin{bmatrix} 0 & 0 & -\frac{1}{C_p} & \frac{1}{C_p} & 0 \\ 0 & 0 & 0 & \frac{1}{C_s} & 0 \\ \frac{1}{L_p} & 0 & 0 & 0 & 0 \\ -\frac{1}{L_s} & -\frac{1}{L_s} & \frac{r_{cp}}{L_s} & -\frac{r_{ds}+r_{cp}+r_{cs}+r_{ls}}{L_s} & 0 \\ 0 & 0 & 0 & 0 & -\frac{1}{C_f(R_L+r_{cf})} \end{bmatrix}, \text{and } B_2 = \begin{bmatrix} 0 \\ 0 \\ 0 \\ \frac{V_{in}}{L_s} \\ 0 \end{bmatrix} \tag{7-5}$$

and similarly, during the time when $V_{in}>0$ and $i_R>0$ (M3), the system is described by:

$$A_3 = \begin{bmatrix} 0 & 0 & -\frac{1}{C_p}+\frac{C_f}{C_p(C_f+C_p)} & \frac{1}{C_p}-\frac{C_f}{C_p(C_f+C_p)} & 0 \\ 0 & 0 & 0 & \frac{1}{C_s} & 0 \\ \frac{1}{L_p} & 0 & 0 & 0 & 0 \\ -\frac{1}{L_s} & -\frac{1}{L_s} & \frac{r_{cp}}{L_s}-\frac{r_{cp}C_f}{L_s(C_f+C_p)} & -\frac{r_{ds}+r_{cp}+r_{cs}+r_{ls}}{L_s}+\frac{r_{cp}C_f}{L_s(C_f+C_p)} & 0 \\ 0 & 0 & -\frac{R_L C_f}{C_f(R_L+r_{cf})(C_f+C_p)} & \frac{R_L C_f}{C_f(R_L+r_{cf})(C_f+C_p)} & -\frac{1}{C_f(R_L+r_{cf})} \end{bmatrix}$$

$B_3 = B_1$

(7-6)

Exploiting symmetry between half switching cycles, the modal matrices for converter operating in M4 (V_{in}=0, i_R>0), M5 (V_{in}=0, i_R=0) and M6 (V_{in}=0, i_R<0) are equivalent to those in M3, M2, and M1, respectively, viz.:

$$\begin{aligned} A_4 &= A_3 \\ A_5 &= A_2 \\ A_6 &= A_1 \\ B_4 &= B_5 = B_6 = [0 \;\; 0 \;\; 0 \;\; 0 \;\; 0]^T \end{aligned} \tag{7-7}$$

7.1.1. Determining the Duty of Each Mode

As before, the cyclic-mode initial condition $x_{per}(t_0)$, for voltage-output converter, can be obtained by substituting the piecewise linear equations for different modes in (7-4), (7-5), (7-6) and (7-7) into the augmented cyclic mode equations in Chapter 4 viz. (4-6), (4-7) and (4-12), along with the mode transition times associated with each. Investigations have previously shown that the time-periods associated with each mode, required to predict the cyclic-mode initial conditions, can be successfully predicted using the Rectifier Transformed FMA equivalent circuits, derived in Chapter 6.

Moreover, the procedures presented are subjected to iteration to permit the effects of rectifier on-state voltage drop to be incorporated. Derivation details for obtaining the equivalent model can be found in the previous chapter. Here, just the results are employed.

The rectifier and capacitive output filter can be approximated by a combination of equivalent resistance and capacitance, as illustrated, for clarity, in Fig. 7.3.

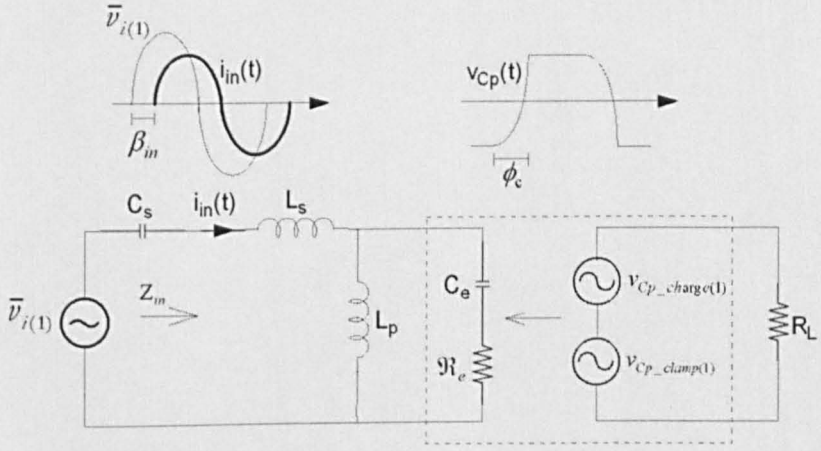

Figure 7.3 Equivalent circuit of voltage-output LCLC resonant converter.

In this case, the rectifier non-conduction angle is given, approximately, by,

$$\phi_c = \cos^{-1}\left(\frac{\pi - 4\pi R_L f_s C_p}{\pi + 4\pi R_L f_s C_p}\right) \tag{7-8}$$

The output filter and rectifier, when decoupled from the resonant tank circuit, are modelled by an equivalent resistance and an equivalent capacitance, whose values are given by [G2]:

$$\begin{aligned} \Re_e &= \frac{1-\cos(2\phi_c)}{4\pi^2 f_s C_p} \\ C_e &= \frac{2\pi C_p}{2\phi_c - \sin(2\phi_c)} \end{aligned} \tag{7-9}$$

Throughout the analysis, the resonant tank input current $i_{in}(t)$, which flows from the network of series resonant components, into the rectifier bridge circuit, is assumed to be predominantly sinusoidal, i.e.:

$$i_{in}(t) = \hat{i}_{in}\sin(2\pi f_s t) \tag{7-10}$$

Now, as before, β_{in} is the phase angle between the input voltage and the fundamental harmonic component of the series inductor current. The duty d_1 associated with M1 is obtained by assuming that the output voltage is ripple-free, and the current through the rectifier follows that of $i_{in}(t)$. d_1 is therefore defined as the time when series resonant inductor current i_{Ls}= 0, and is obtained from knowledge of the overall impedance, Z_{in}, of the equivalent circuit of Fig. 7.3, viz.:

$$|Z_{in}| = \frac{R_L\omega_n}{Q_{op1}L_n} \times \left| \frac{-\dfrac{2\pi C_n\omega_n^{\,2}}{2\phi_c - \sin(2\phi_c)} + L_n\left(1-\dfrac{1}{\omega_n^{\,2}}\right) + \dfrac{2\pi C_n}{2\phi_c - \sin(2\phi_c)} + 1 + j\left(\dfrac{1-\cos(2\phi_c)}{2\phi_c - \sin(2\phi_c)}\right)\left(L_n - \dfrac{L_n}{\omega_n^{\,2}} - 1\right)}{\dfrac{1-\cos(2\phi_c)}{2\phi_c - \sin(2\phi_c)} + j\left(\dfrac{2\pi\omega_n^{\,2}C_n}{L_n(2\phi_c - \sin(2\phi_c))} - 1\right)} \right| \tag{7-11}$$

Taking the phase angle of (7-11), and subsequently normalising by dividing by 2π, yields the duty for M1, as follows:

$$d_1 = \frac{1}{2\pi} \times \tan^{-1}\left[\frac{\dfrac{1-\cos(2\phi_c)}{2\phi_c - \sin(2\phi_c)}}{\dfrac{2\pi\omega_n^{\,2}C_n}{L_n(2\phi_c - \sin(2\phi_c))} - 1}\right] - \frac{1}{2\pi} \times \left[\frac{-\dfrac{2\pi C_n\omega_n^{\,2}}{2\phi_c - \sin(2\phi_c)} + L_n\left(1-\dfrac{1}{\omega_n^{\,2}}\right) + \dfrac{2\pi C_n}{2\phi_c - \sin(2\phi_c)} + 1}{\dfrac{1-\cos(2\phi_c)}{2\phi_c - \sin(2\phi_c)} \times L_n - \dfrac{L_n}{\omega_n^{\,2}} - 1}\right] \tag{7-12}$$

The fact that β_{in} is positive implies that the first harmonic of the inductor current lags the input voltage when operating above the resonant frequency. During the rectifier non-conducting interval, the inductor current flows into C_p, charging it to $v_{Cf} = V_{out}$ (plus the bridge rectifier voltage drop v_{diode}), at which time rectifier conduction resumes once again.

It is noted that T_s is the period for one switching cycle, and v_{Cp} during charging of C_p is given by:

$$v_{Cp} = v_{Cp}(d_1 T_s) + \frac{1}{C_p} \times \int_{d_1 T_s}^{(d_2+d_1)T_s} \hat{i}_{in} \sin(\omega_s t) dt$$
$$v_{Cp}(d_1 T_s) = -v_b = -V_{out} - 2v_{diode} \tag{7-13}$$

The duty d_2 for M2 is, therefore, found by evaluating the integral in (7-13) to give:

$$v_{Cp} = -v_b + \hat{i}_{in} \times \frac{1 - \cos(\omega_s d_2 T_s)}{2\pi f_s C_p} \tag{7-14}$$

To determine the boundary time that defines the entire capacitor-charging period, it is noted that $v_{Cp} = v_R$ at $t = d_2 T_s$. From (7-14), solving for duty d_2 yields:

$$d_2 = \frac{1}{2\pi} \times \cos^{-1}\left(1 - \frac{4\pi v_b f_s C_p}{\hat{i}_{in}}\right) \tag{7-15}$$

where the amplitude of the resonant tank input current, $\hat{i}_{in}$, can be determined from,

$$\hat{i}_{in} = \frac{2v_{DC}}{\pi |Z_{in}|} \tag{7-16}$$

The switching transition times for the remaining operating modes are found, by symmetry, to be:

$$\begin{aligned} d_3 &= 0.5 - d_1 - d_2 \\ d_4 &= d_1 \\ d_5 &= d_2 \\ d_6 &= d_3 \end{aligned} \tag{7-17}$$

7.2. Component Electrical Stresses

Here, the techniques presented in the previous sections are now extended to include an analysis of component stresses. During the design stage, consideration of electrical stresses imposed

on the tank components are of utmost important to the designer. It will be shown that cyclic-averaging provides a convenient and accurate means for addressing this issue.

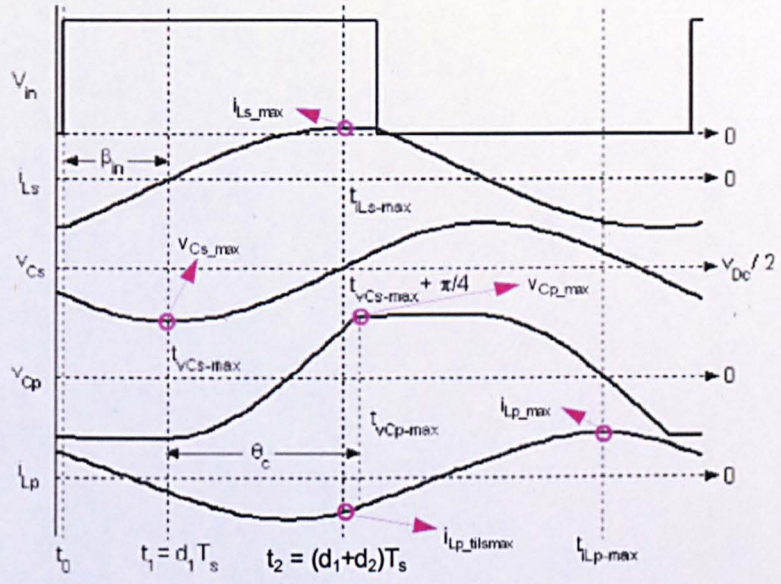

Figure 7.4 Sketched current and voltage waveforms.

With reference to Fig. 7.4, it can be seen that the series inductor current, i_{Ls}, which coincides with the power switch input current, and the series capacitor voltage v_{Cs} are phase-displaced by $\pi/2$ rad, and the maximum voltage across C_s occurs when $i_{Ls}(t) \to 0$, when operating in M4 and occurs at time $t_{vCs\_max} = d_4 T_s = d_1 T_s$. From (7-12) $\hat{v}_{Cs}$ is given by substituting t_{vCs_max} into (4-6):

$$\hat{v}_{Cs} = \begin{bmatrix} 0 & 1 & 0 & 0 & 0 & 0 \end{bmatrix} e^{\hat{A}_4 t_{vCs\_max}} e^{\hat{A}_3 d_3 T_s} e^{\hat{A}_2 d_2 T_s} e^{\hat{A}_1 d_1 T_s} \hat{x}_{per}(t_0) \tag{7-18}$$

Similarly, noting that the maximum series resonant inductor current i_{Ls} occurs at time $t_{iLs\_max} = d_1 T_s + (T_s/4)$, in M2 or M3 (depending on the operating frequency), the state transition matrix of the converter is,

$$\hat{x}(t_{iLs\_max}) = \begin{cases} \hat{x}(t_{iLs\_max\_mode2}) = e^{\hat{A}_2 (t_{iLs\_max} - d_1 T_s)} e^{\hat{A}_1 d_1 T_s} \hat{x}_{per}(t_0) & \text{for } t_{iLs\_max} \le (d_1 + d_2) T_s \\ \hat{x}(t_{iLs\_max\_mode3}) = e^{\hat{A}_3 (t_{iLs\_max} - (d_1+d_2) T_s)} e^{\hat{A}_2 d_2 T_s} e^{\hat{A}_1 d_1 T_s} \hat{x}_{per}(t_0) & \text{for } t_{iLs\_max} \le T_s/2 \end{cases} \tag{7-19}$$

and, thereafter, the peak value of resonant inductor current $\hat{i}_{Ls}$ is given by,

$$\hat{i}_{Ls} = \begin{bmatrix} 0 & 0 & 0 & 1 & 0 & 0 \end{bmatrix} \hat{x}(t_{iLs\_max}) \tag{7-20}$$

When the converter is operated further away from the effective resonant frequency, the assumption previously made that the current through series resonant inductor L_s, is sinusoidal, does not hold, as the waveform becomes increasingly triangular at higher frequencies. In this case, the time required for the current to reach its maximum value ultimately increases to $t_{iLs\_max} = 0.5T_s$. It is therefore necessary to modify (7-19) to account for this, in the following way,

$$\hat{x}(t_{iLs\_max}) = e^{\hat{A}_3 0.5T_s} e^{\hat{A}_2 d_2 T_s} e^{\hat{A}_1 d_1 T_s} \hat{x}_{per}(t_0) \quad \text{for } t_{iLs\_max} \geq T_s/2 \tag{7-21}$$

When the rectifier/filter sub-system is diode-coupled to the parallel resonant tank, $|v_{Cp}|$ is clamped to the modulus of $V_{out} + 2v_{diode}$. The peak positive voltage occurs when the bridge rectifier begins to conduct forward current ($i_R > 0$), as operation enters M3, at $t_{vCp\_max} = d_3 T_s$. From (7-14), $\hat{v}_{Cp}$ is then given by,

$$\hat{v}_{Cp} = \begin{bmatrix} 1 & 0 & 0 & 0 & 0 & 0 \end{bmatrix} e^{\hat{A}_3 t_{vCp\_max}} e^{\hat{A}_2 d_2 T_s} e^{\hat{A}_1 d_1 T_s} \hat{x}_{per}(t_0) \tag{7-22}$$

With increasing excitation frequency, the period during which the parallel capacitor voltage is clamped becomes shorter, and gradually migrates toward the beginning of the negative half cycle of the input voltage, V_{in}. The time at which $\hat{v}_{Cp}$ occurs, is, therefore, in M4, and $t_{vCp\_max} = d_4 T_s$.

$$\hat{v}_{Cp} = \begin{bmatrix} 1 & 0 & 0 & 0 & 0 & 0 \end{bmatrix} e^{\hat{A}_4 t_{vCp\_max}} e^{\hat{A}_3 d_3 T_s} e^{\hat{A}_2 d_2 T_s} e^{\hat{A}_1 d_1 T_s} \hat{x}_{per}(t_0) \tag{7-23}$$

Again, with reference to Fig. 7.4, the maximum current flows through the parallel resonant inductor ($\hat{i}_{Lp}$) when the voltage across the parallel capacitor, v_{Cp}, reduces to zero. The time at which $v_{Cp} = 0$, t_{iLp_max}, can be found by solving (7-13) to give:

$$\begin{aligned} 0 &= -v_R + \hat{i}_{in} \times \frac{1 - \cos \omega_s (t_{iLp\_max})}{2\pi f_s C_p} \\ t_{iLp\_max} &= \cos^{-1}\left(1 - \frac{2\pi v_b f_s C_p}{\hat{i}_{in}}\right) \end{aligned} \tag{7-24}$$

The maximum inductor current i_{Lp} occurs in M5 and the peak value of the parallel resonant inductor current, $\hat{i}_{Lp}$ is then given by:

$$\hat{i}_{Lp} = \begin{bmatrix} 0 & 0 & 1 & 0 & 0 & 0 \end{bmatrix} e^{\hat{A}_5 t_{iLp\_max}} e^{\hat{A}_4 d_4 T_s} e^{\hat{A}_3 d_3 T_s} e^{\hat{A}_2 d_2 T_s} e^{\hat{A}_1 d_1 T_s} \hat{x}_{per}(t_0) \tag{7-25}$$

The steady-state stresses imposed on the resonant tank components are thus analyzed by considering (7-18) through to (7-25). Since the cyclic model can now be used, together with mode duty times, for finding the initial conditions, $x_{per}(t_0)$, cyclic averaging techniques can be employed to provide both accurate predictions of the converter's output voltage, and all the primary steady state stresses.

An example state-plane trajectory for a complete switching period, obtained using cyclic averaging, is given in Fig. 7.5. The tank circuit voltage and current solutions follow circular arcs and the trajectory for the M2 sub-interval occurs when v_{Cp} is clamped to the output voltage.

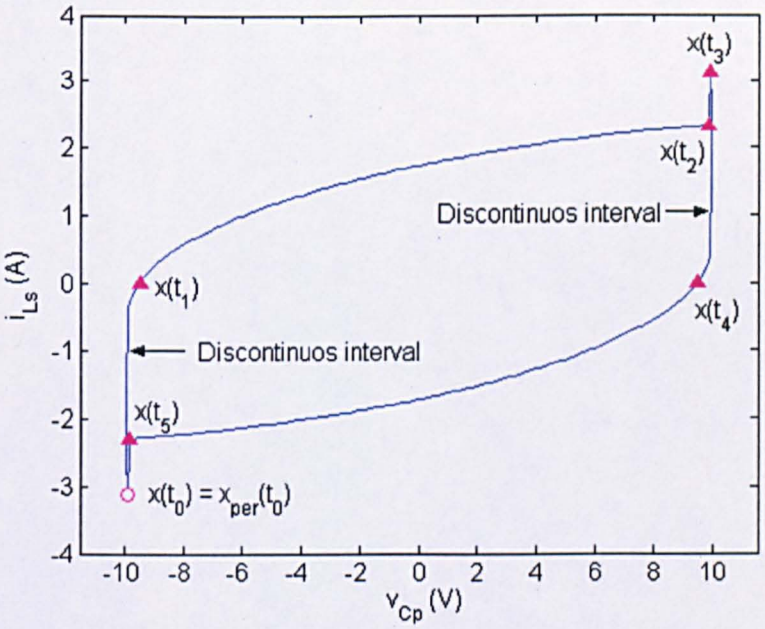

Figure 7.5 State-plane trajectory predicted by the cyclic averaging analysis.

A problem encountered whilst applying the cyclic averaging algorithm to the voltage-output converter is that the parallel resonant capacitor voltage can be either higher or lower than the output voltage, thereby contradicting the voltage clamping action of the bridge rectifier. As an example of this, Fig. 7.6 shows the discrepancy produced when the duty-cycle is incorrect. Although describing functions provide a suitable mechanism for estimating the modal duty times, the main reasons for the voltage discrepancy are attributed to inaccuracies in the original estimation of rectifier non-conduction angle, which could arise due to excluding the effects of the non-linear rectifier on-state voltage, or the sinusoidal waveform assumptions associated with the RTFMA analysis.

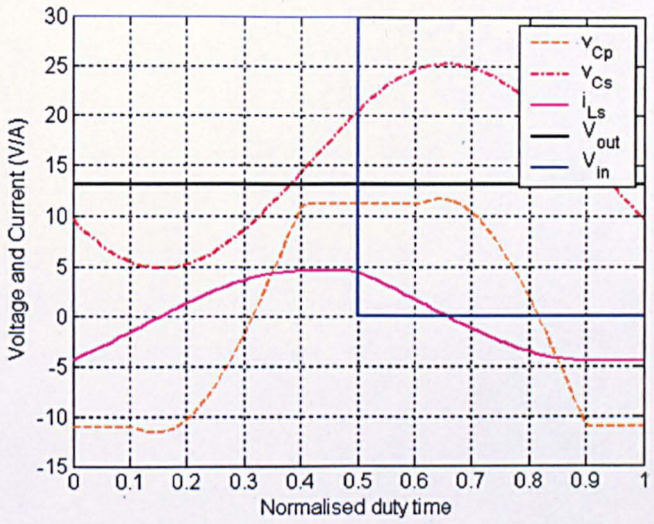

(a)

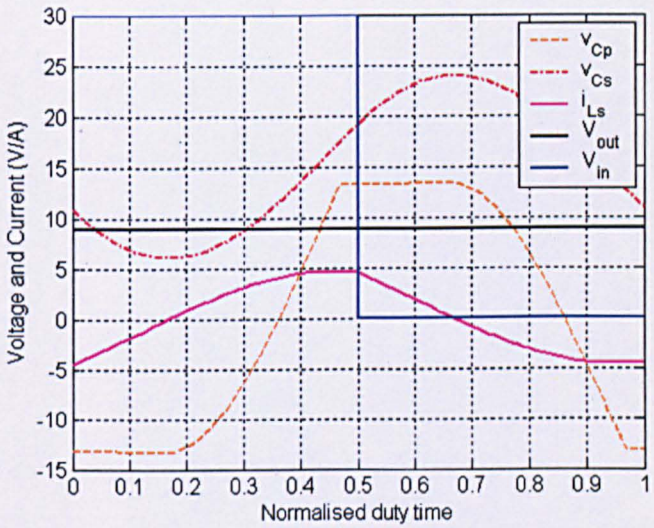

(b)

Figure 7.6 Circuit voltages and currents from RTFMA predictions: (a) $v_{Cp}(d_2T_s) < V_{out}$ and (b) $v_{Cp}(d_2T_s) > V_{out}$.

Moreover, in RTFMA, the magnitude of the parallel tank capacitor charging/discharging current, i_{Cp} assumes the magnitude of series resonant inductor current, i_{Ls}. This assumption normally holds in cases when the value of parallel resonant inductor L_p dominates the series resonant inductor L_s and parallel resonant capacitor C_p, thus behaving like a large current-limiting impedance.

Most of the resonant tank input current then flows from L_s into the rectifier and capacitor C_p, whilst L_p will only conduct a small portion of the total current. However, in the case when the value of inductor L_p is not sufficiently larger than L_s, the current carried by L_p cannot be neglected.

Again referring to Fig. 7.4, that the maximum series resonant inductor current i_{Ls} occurs at time $t_{iLs\_max} = t_{vCs\_max} + (T_s/4)$ in either M3 or M4, depending on operating frequency. From (7-19) and (7-21), the state transition matrix of the resonant converter at t_{iLs_max}, is given by,

$$\hat{x}(t_{iLs\_max}) = \begin{cases} e^{\hat{A}_2(t_{iLs\_max}-d_1T_s)}e^{\hat{A}_1 d_1 T_s}x_{per}(t_0) & \text{for } t_{iLs\_max} < (d_1+d_2)T_s \\ e^{\hat{A}_3(t_{iLs\_max}-(d_1+d_2)T_s)}e^{\hat{A}_2 d_2 T_s}e^{\hat{A}_1 d_1 T_s}x_{per}(t_0) & \text{for } t_{iLs\_max} \le 0.5T_s \\ e^{\hat{A}_3 0.5T_s}e^{\hat{A}_2 d_2 T_s}e^{\hat{A}_1 d_1 T_s}x_{per}(t_0) & \text{for } t_{iLs\_max} > 0.5T_s \end{cases} \tag{7-26}$$

Therefore, current $i_{Lp\_tiLsmax}$ flowing through parallel resonant inductor is,

$$i_{Lp\_tiLs\,max} = [0 \quad 0 \quad 1 \quad 0 \quad 0 \quad 0]\hat{x}(t_{iLs\_max}) \tag{7-27}$$

Assuming that the current, which flows into Cp, is small compared to that which flows in L_s and L_p during the rectifier conduction period, the voltage at the rectifier is dependent on the direction of the link-current flowing from the resonant tank circuit $i_L = i_{Ls} - i_{Lp}$.

Hence, the amplitude of the link current $\hat{i}_{in}$ in (7-16) can be determined from the initial cyclic mode analysis solution in (7-20) and (7-25),

$$\hat{i}_{in} = i_{Ls\_max} - i_{Lp\_tiLs\,max} \tag{7-28}$$

The refined magnitude of resonant tank link current is then substituted into (7-15) to enhance the accuracy of the boundary time that defines the capacitor-charging period at $t = d_2T_s$.

Although significant improvements in prediction accuracy can obtained by appropriately including the effect of the parallel inductor current and v_{diode} using the iterative refinement procedure described in Chapter 6, errors still persist at switching frequencies away from the resonant frequency due to the assumption of sinusoidal series resonant inductor currents. Instead, it will be demonstrated that for this particular converter topology, the cyclic process itself can be utilised in conjunction with knowledge of

boundary conditions on the discontinuity of the parallel capacitor voltage, to provide enhanced analysis accuracy.

Through modifications to the scheme presented for finding the duty time and initial conditions of the cyclic system, it can be shown that the cyclic analysis can be employed to conduct a localised search to provide more accurate estimation of the second duty cycle, d_2. Improvement of the duty-cycle accuracy can be obtained by noting that M1 ends, and M2 begins, at the point when parallel capacitor voltage v_{Cp} is clamped, implying that $v_{Cp} = V_{out}+2v_{diode}$. However, errors in the calculation of d_2 results in solutions that do not satisfy this condition.

By iteratively sweeping the duty from the initial estimate of d_2, the correct duty can be found when the cyclic analysis solution satisfied the above condition. In summary, the initial estimate d_{2_ini} is calculated from the RCFMA equivalent circuit using (7-15), and localised iterative search shown in Fig. 7.7 is terminated when the parallel capacitor voltage at the end of M1 at time d_2T_s, satisfies the boundary condition at time $d_2T_s - |v_{Cp}|-V_{out}-2v_{diode} = 0$.

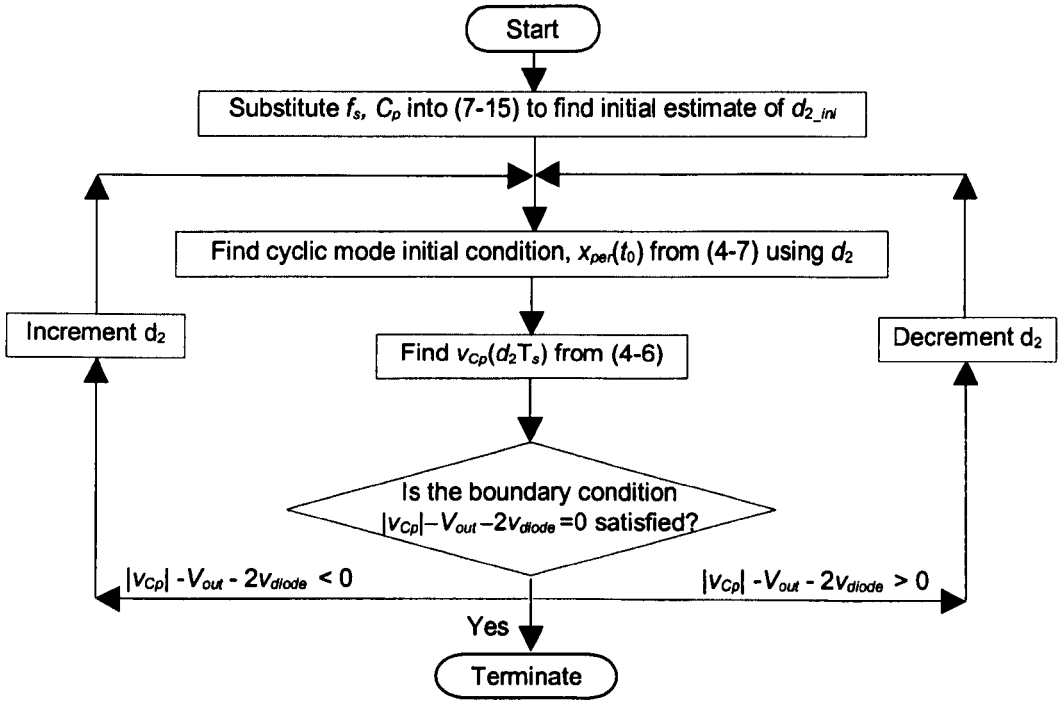

Figure 7.7 Flow-chart describing the iterative localised sweep procedure.

7.3. Accuracy of Cyclic Averaging Analysis for Voltage-Output Resonant Converters

The prototype converter in Fig. 7.8, with specifications given in Table 7.1, is used as a demonstration of the application of the presented techniques. Figure 7.9 compares the measured output voltages from the prototype converter with those derived from the state-variable model, and cyclic-averaging, for various operating frequencies and load conditions—a good correspondence between the results being shown in all cases. Some discrepancy in the predictions of output voltage are attributed to non-linearities of the switching devices i.e. gate driver dead-time etc.

Table 2.2 Voltage-output converter model parameters.

Parameters	Values
DC link input voltage, v_{DC} (V)	30
Series resonant inductance, L_s (μH)	12.6
Series resonant capacitance, C_s (μF)	0.737
Parallel resonant inductance, L_p (μH)	25
Parallel resonant capacitance, C_p (μF)	0.141
Switching devices internal on resistance, r_{ds} (Ω)	0.04
Inductor L_s series resistance, r_{ls} (Ω)	0.1
Inductor L_p series resistance, r_{lp} (Ω)	0.15
Instantaneous diode forward voltage drop, v_{diode}	0.7
Output filter capacitance, C_f (μF)	100
Output load Resistance, R_L (Ω)	5, 10
Nominal resonant frequency, f_o (kHz)	90

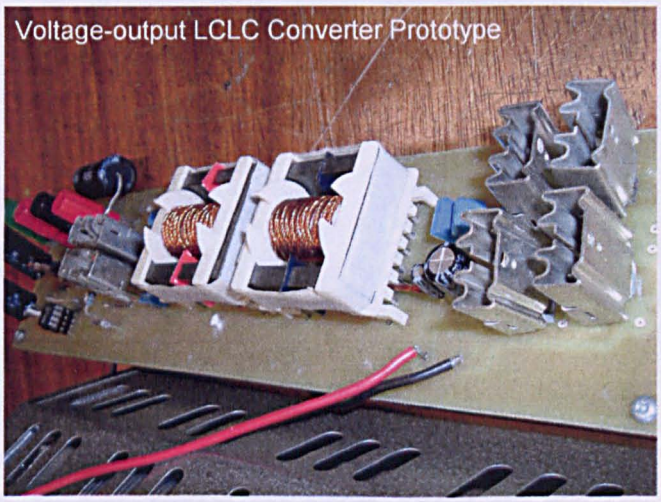

Figure 7.8 Prototype 4th-order voltage-output resonant converter.

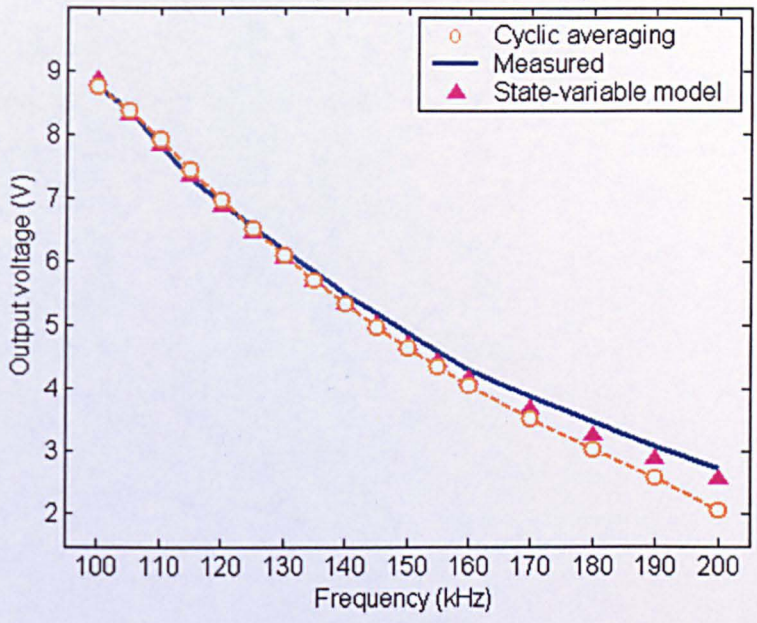

(a)

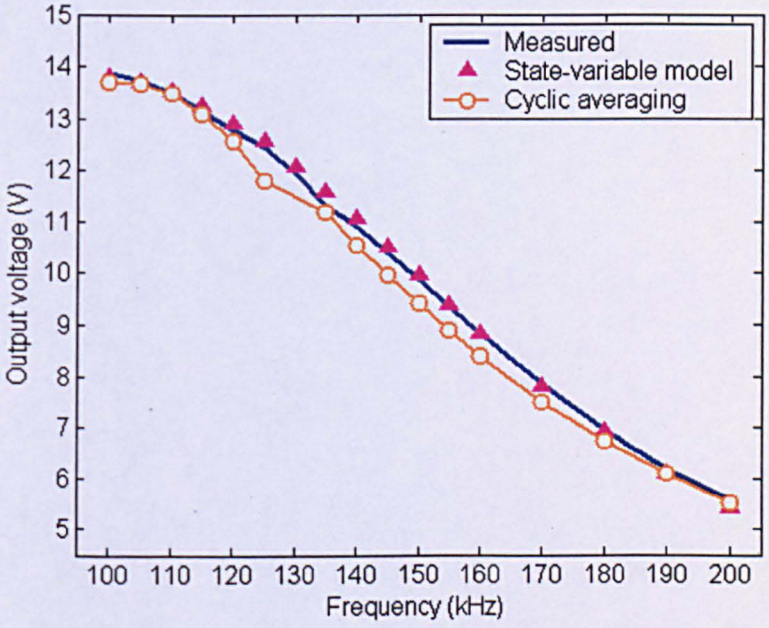

(b)

Figure 7.9 Comparison of predicted output voltage from cyclic averaging and state-variable models with measurements on voltage-output LCLC converter: (a) R_L=5Ω and (b) R_L=10Ω.

Further, the electrical component stresses predicted by cyclic-averaging, compared with measurements taken from the prototype converter, are given in Fig. 7.10, with Fig. 7.11 also showing experimental waveforms from the converter operating just above the resonant frequency.

Again, it is seen that cyclic-averaging provides an accurate method to model the steady-state behaviour of the converter over a wide dynamic operating range. It is interesting to note that the parallel capacitor voltage, v_{cp}, is demonstrated to be only 'weakly' clamped during the rectifier on-periods, as a result of the effects of parasitic inductances around the bridge circuit.

Nevertheless, cyclic-averaging is still seen to provide accurate estimates of component stresses. It is also notable that the calculation time for obtaining the results using cyclic-averaging is, typically, only 10^{-4} of that required for SPICE simulations.

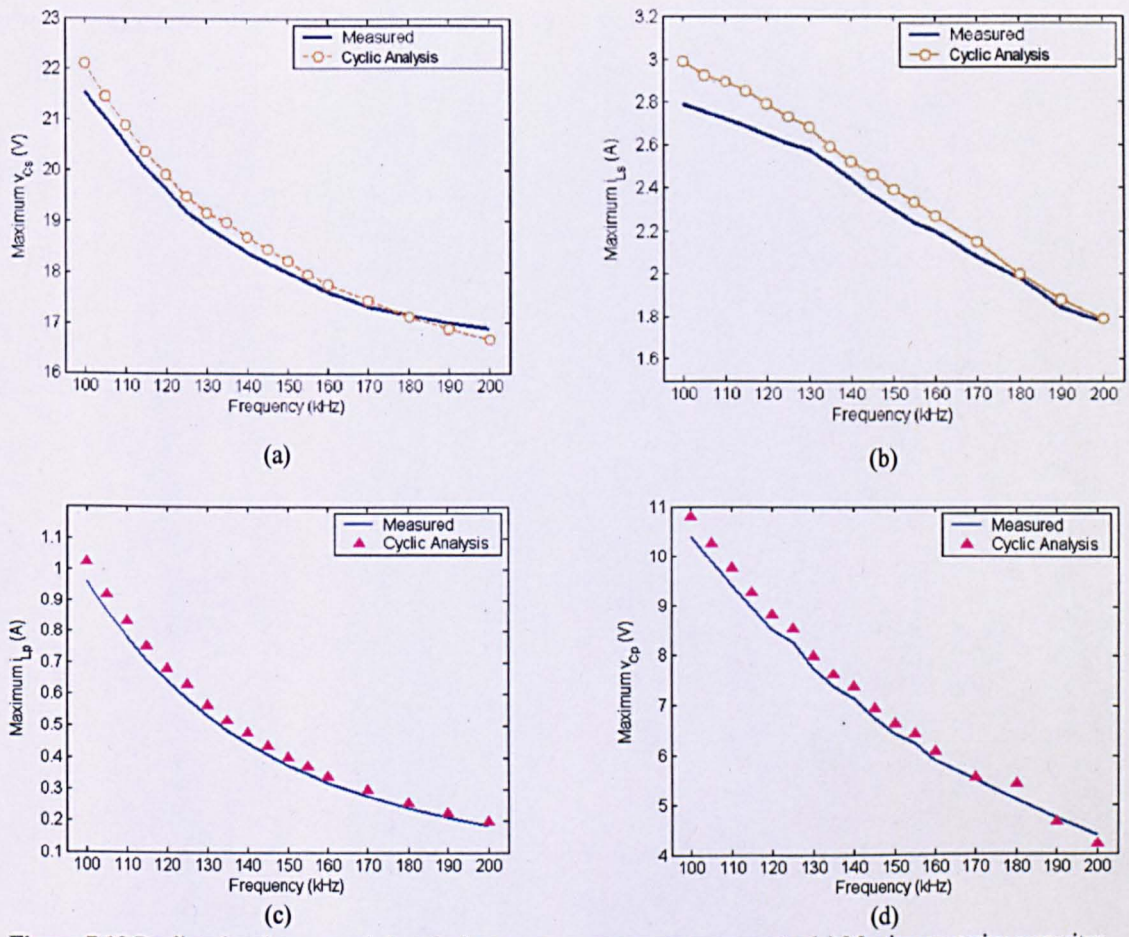

Figure 7.10 Predicted and measured electrical stresses on resonant components: (a) Maximum series capacitor voltage, (b) Maximum series inductor current, (c) Maximum parallel capacitor voltage and (d) maximum parallel inductor current.

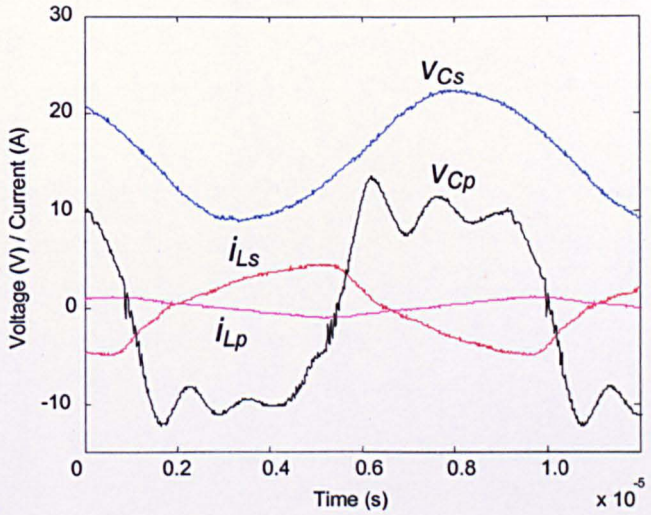

Figure 7.11 Measurements from the prototype voltage-output LCLC converter.

7.4. Summary

Cyclic mode analysis and averaging techniques have been applied to the 4th-order voltage-output resonant power converter to facilitate high-speed analysis of the output voltage and stresses on components. Its virtues have been demonstrated by comparing predictions with measurements on a prototype converter operating above resonance. State-variable dynamic descriptions of circuits and their subsequent use for determining the piece-wise linear cyclic model, have been presented, and analytical formulae have been derived to calculate the electrical stresses on the resonant components.

New methods relying on localised searches and a refined iteration procedure for estimating the mode duties, have also been proposed. The methods are shown to provide accurate duties for a wide range of switching frequencies, compared to previously reported methods, particularly for low output voltage converters, where the effect of rectifier on-state voltage cannot be ignored. The accuracy of the proposed methodology has also been demonstrated by comparisons with SPICE simulations, which typically require $\approx 10^4\times$ greater computation time.

References

[G1] Y. Ang, M. P. Foster, C. M. Bingham, D. A. Stone, H. I. Sewell and D. Howe, "Analysis of 4th-order LCLC Resonant Power Converters", *IEE Proc. Electric Power Applications*, **151**, pp. 169-181, 2004.

[G2] Y. Ang, C. M. Bingham, M. P. Foster, D. A. Stone and D. Howe, "Design Orientated Analysis of 4th-Order LCLC Converters with Capacitive Output Filter", *IEE Proc. Electric Power Applications*, **152**, pp. 310-322, 2005.

CHAPTER 8

Dual-Load Resonant Converters

Increasing pressure on manufacturers to provide high-density power converters is spawning significant interest in converter topologies that can provide multiple regulated outputs—particular growth areas being the telecommunications and computer and microprocessor industries, with mobile phones, PDAs and handheld products typically requiring 3.3V, 5V, ±12V and ±15V supplies for various interfaces. To date, fly-back converters remain the low-cost solution for providing a single regulated output [H1] along with additional semi-regulated auxiliary outputs. Other candidate converters include buck [H2], forward [H3, H4, H5], and current fed push-pull converters [H6], all having their relative merits. Such converters employ a transformer with multiple secondary windings, and the designer chooses to regulate one of the outputs using Pulse-Width-Modulation or excite the transformer at a fixed duty-cycle. However, cross regulation error that accompanies output load variations, where the regulation of one output voltage impacts on the performance of others, is a significant limitation for voltage sensitive electronic systems. If regulation is needed on all outputs, the designer will generally employ a post-regulation technique, based on linear regulators, individual step-down DC/DC converters or magnetic amplifiers. Although cross-regulation error can be abated to some extend using such techniques, the required additional circuitry often precludes their use for cost-critical applications.

The emergence of enabling technologies such as high-frequency, high-power switching devices, and low cost digital processing ICs, has recently lead to resonant converters being considered as potential candidates for DC-DC conversion to deliver multiple stabilized outputs, due to their high efficiency, limited electromagnetic/radio frequency sensitivity and reduced switching stresses compared to classical hard-switched counterparts. Again, however, the use of a transformer with multiple secondary windings, with only one output being regulated through closed-loop control, and the remaining being unregulated or requiring secondary-side post-regulation, is commonplace.

The development of multiple-output supplies typically requires substantial design effort, with a need for improved understanding of the behaviour of resonant converter solutions. Current and voltage waveforms of the resulting transformer-isolated converters can differ significantly from their non-

isolated parent counterparts, and classical models do not accurately predict their dynamic characteristics, primarily due to the complexities of modelling the magnetic coupling between outputs.

Here then, the analysis, design and control of the 4^{th}-order LCLC voltage-output resonant converter (SPRC), specifically for the provision of multiple regulated outputs, is explored. State-variable concepts are employed, and new analysis techniques developed to establish operating-mode boundaries in order to describe the internal behaviour of a candidate dual-output resonant supply. A step-by-step procedure is given to guide the designer through the most important criterion for obtaining a satisfactory converter realisation, and the impact of the proposed choices on the ultimate performance of the supply. Results are included that compare predictions from the resulting models with those from SPICE simulations and measurements from a prototype power supply under closed-loop control.

8.1. Multiple-Output Resonant Converter Topologies

Resonant converters utilising a single primary power stage and generating more than one isolated output voltage, are termed multiple-output resonant converters. To-date, several approaches have been explored to address cross-regulation issues, complexity and overall circuit performance of such converters, with solutions now being divided into three distinct groups. The first regulates a single primary output using closed-loop feedback, with the auxiliary outputs being semi-regulated and therefore subject to cross-regulation error. Cross-regulation error has been sub-divided into dynamic- and static-behaviour, by Agrawal [H7], with improvements being shown through careful design of the output filters. However, a drawback of such techniques (also given in Agrawal and Batarseh [H8]) is the requirement for large filter inductors and capacitors, high turns-ratio transformers, leading to significant parasitic effects, and a high-valued series resonant inductance. Furthermore, another disadvantage associated with the requirement for a wide switching frequency range, normally required for frequency regulation, is poor cross regulation of multiple output converters. The work proposed by Batarseh *et al.* [H9] therefore also suggests that the use of constant frequency PWM can be beneficial as a means of reducing cross-regulation, through optimisation of all components to operate at a single frequency.

A number of more complex techniques for use with high-order resonant converters (3^{rd} and 4^{th}-order) have been reported in [H10, H11], with designs employing centre-tapped transformers that are terminated through full-wave rectification and inductor-type output filters. A significant disadvantage of this configuration, however, is the relatively high diode count accompanying full-bridge rectification. Moreover, once again, the feedback loop is closed around only one of the outputs with frequency control often being used for regulation.

The second category of solutions considers precise post-regulation of each output using either linear regulators or hard-switched dc-dc converters. Although relatively straightforward to design, such circuits are rarely used in practice due to cost constraints.

The third category of solutions is specific to applications that require only two regulated voltage outputs, such as commonly found in signal-processing and microprocessor based systems. They avoid the need for post-regulation by utilising two closed-loop feedback configurations. A 3^{rd}-order LLC converter with two independently controlled outputs has been considered by Elfrich and Duerbaum [H12]. However, an in-depth analysis to provide optimum performance characteristics has yet to be forthcoming, primarily due to the significant complexity associated with the highly non-linear

behaviour and the interaction between the various outputs as a function of load. Nevertheless, it is solutions that broadly fall within this third category that are investigated in the remainder of this Chapter.

Specifically, a detailed investigation into the behaviour of dual-output resonant converters, that combine the benefits of high-efficiency and flexibility, is given in Sections 8.2 and 8.3, with the LCLC variant, Fig. 8.1, being used to provide a focus to the study. Realisation of a prototype LCLC converter operating from a standard 15V input and developing two independently-regulated outputs, via the use of dual-loop feedback, is demonstrated. Control of each output is achieved by switching the power devices asymmetrically over each half switching cycle using a combination of PWM and frequency control.

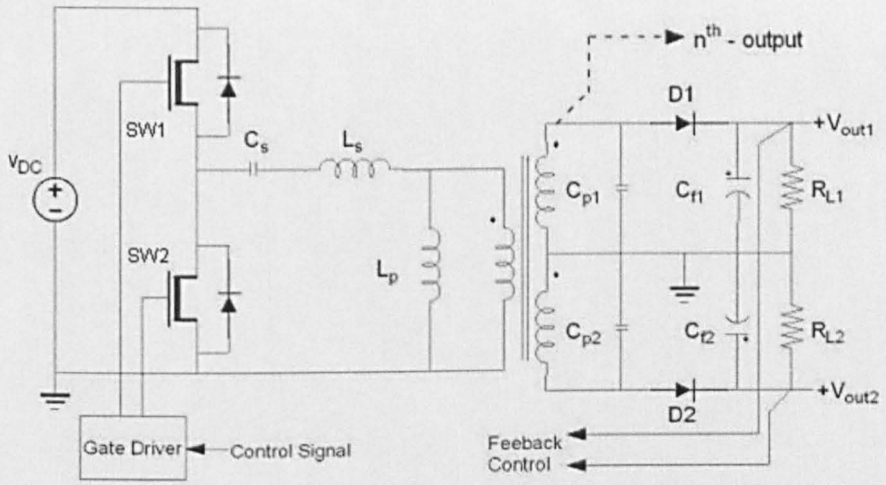

Figure 8.1 Dual-load LCLC resonant converter with feedback control

8.2. Circuit Model of the Dual-Load LCLC-SPRC

Fourth-order resonant converters with capacitive output filters have been considered in previous Chapters. From the result therein, it was shown that all variants provided beneficial attributes compared to 2nd-order SRC and PRC counterparts, by combining their best features, i.e. they can be regulated over a wide load range with reduced circulating power. Moreover, parasitic elements that are normally problematic for other converter designs, can be readily absorbed into the resonant network, to enhance performance and reduce mass and volume.

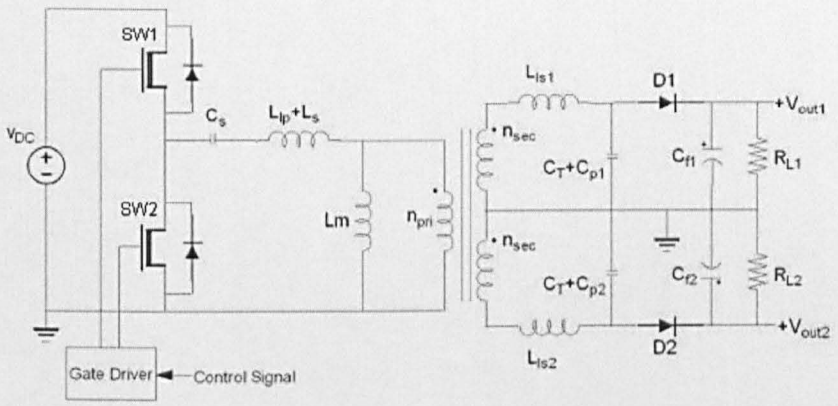

(a)

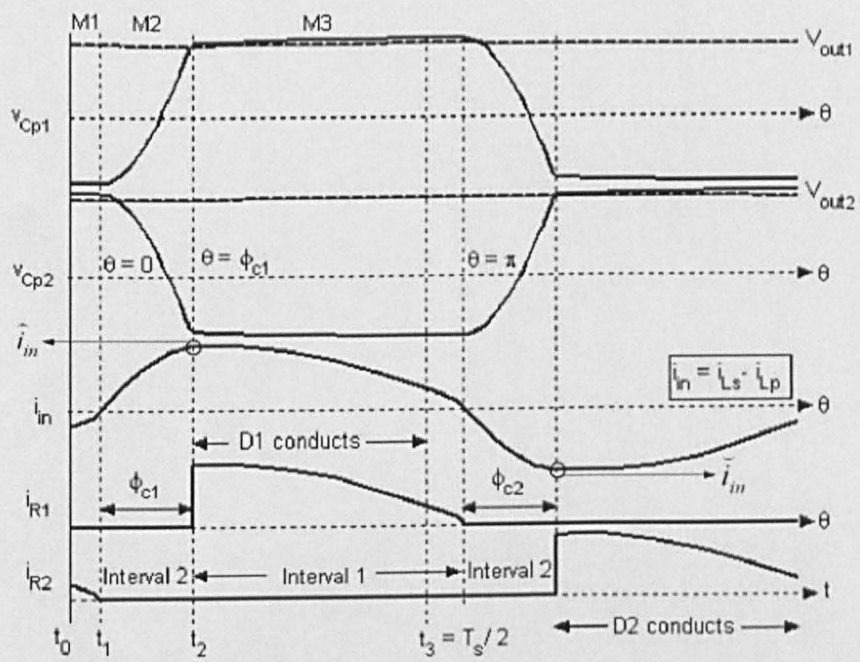

(b)

Figure 8.2 Dual-load 4th-order resonant converter (a) schematic (b) typical operating waveforms.

A schematic of a half-bridge LCLC-SPRC with two outputs is shown in Fig. 8.2(a). By changing the full bridge rectifier to a dual-complementary rectifier, the resulting dual-load converter combines the benefits of requiring a minimum number of rectifier diodes and the ability for multi-output regulation. The rectifier is most efficient under balanced high- and low-side output loading, and, is typically used together with capacitor-type output filters for low current rating applications.

The transformer in Fig. 8.2(a) can be modelled as an ideal voltage conversion component with a magnetising inductance, L_m, series primary leakage inductance, L_{lp} and secondary series leakage inductances, L_{ls1} and L_{ls2}. Since the primary leakage inductance of a well-designed ferrite transformer is much smaller than the magnetising inductances, L_m, it can be absorbed into the resonant tank series inductor, L_s. The value of the series resonant inductance can be increased by adding discrete components, if required, to satisfy pre-determined design constraints.

To demonstrate the ability of the converter to deliver unsymmetrical output voltages, under balanced load conditions, the transformer is constrained to have unity turns-ratios in both output windings, and the high- and low-side parallel resonant capacitors, C_{p1} and C_{p2}, are selected to have identical values. The output filter capacitors, C_{f1} and C_{f2}, are assumed to be large enough so the voltages they are subjected to can be considered constant over a switching period.

Since current flows through the primary side of the transformer to the top- and bottom-sides of the rectifier, during different half-cycles of tank excitation, see Fig. 8.2(b), each output is replenished with energy alternately. During the positive half-cycle of the parallel resonant capacitor voltage waveform, v_{Cp}, the resonant current flows toward the top-side rectifier through to output, R_{L1}, resulting in the voltage V_{out1}; whilst the resonant current then supplies power to V_{out2} when the polarity of the resonant capacitor voltage changes. Diodes D1 and D2 clip the parallel capacitor voltage to $+V_{out1}$ or $-V_{out2}$.

Classically, either the high-side or low-side output will be closed-loop regulated through frequency modulation. However, variations in line voltage or load resistance then yield cross regulation errors [H7-H11] on the unregulated output. Moreover, an asymmetric output voltage distribution is not achievable, in general, under balanced output load conditions, regardless of switching frequency. It is therefore proposed that the converter is operated asymmetrically through variation of input voltage duty cycle, and frequency, to facilitate regulation of both output voltages.

8.3. Principle of Operation

Here, the converter operating in discontinuous voltage conduction mode, is considered. To achieve zero-voltage switching, the converter is assumed to operate on the negative slope of the input-output magnitude characteristic, above resonance.

When operating in this region, the resulting waveforms can be sub-divided into two distinct time intervals (Interval 1 and Interval 2—see Fig. 8.2(b)):

Interval 1 Clamping of the parallel capacitor voltage. Here, the series inductor L_s and C_s provide resonant behaviour whilst the voltage across L_p and C_p is clamped by the output voltage. As the current through the series inductor, L_s, decays to zero, C_p begins to contribute to resonant behaviour, and operation enters the second designated interval.

Interval 2 Decoupling of the rectifier and output filter. Here, all tank components contribute to resonant behaviour, with the rectifier effectively becoming reverse biased. Current into both high- and low-side diodes remain at zero, and the parallel capacitors are charged until their voltage is clamped at either $+V_{out1}$ or $-V_{out2}$, thereby providing the boundary at the end of this designated time interval.

In this respect, the dual-load resonant converter, as shown, constitutes a multi-resonant system since the effective resonant frequency varies during different time-intervals—one being determined by the resonant components L_s, C_s, L_p and C_p, and the other by the resonant components and load condition. With reduced load the resonant frequencies become higher. A more detailed description of the behaviour is now given.

A half-cycle of converter operation can be modelled by three Modes, M1...M3, as shown in Fig. 8.2(b).

Circuit Mode M1 ($t_0 \le t < t_1$). With reference to Figs. 8.2 and 8.3, at the start of M1, SW2 is turned off at t_0. At this time, the series inductor current, i_{Ls}, is negative and flows through the internal body diode of SW1, thereby facilitating ZVS of SW1. Also during this period, i_{Ls} allows D2 to conduct and transfer energy to support the output voltage, V_{out2}, whilst the voltage on C_{p2} is clamped to V_{out2}—all the rectifier current therefore flows to the load. At the end of M1, the rectifier current i_{R2} has decayed

to zero, and both high- and low-side rectifiers, and the output filter, are effectively decoupled from the resonant tank. This marks the beginning of Mode M2.

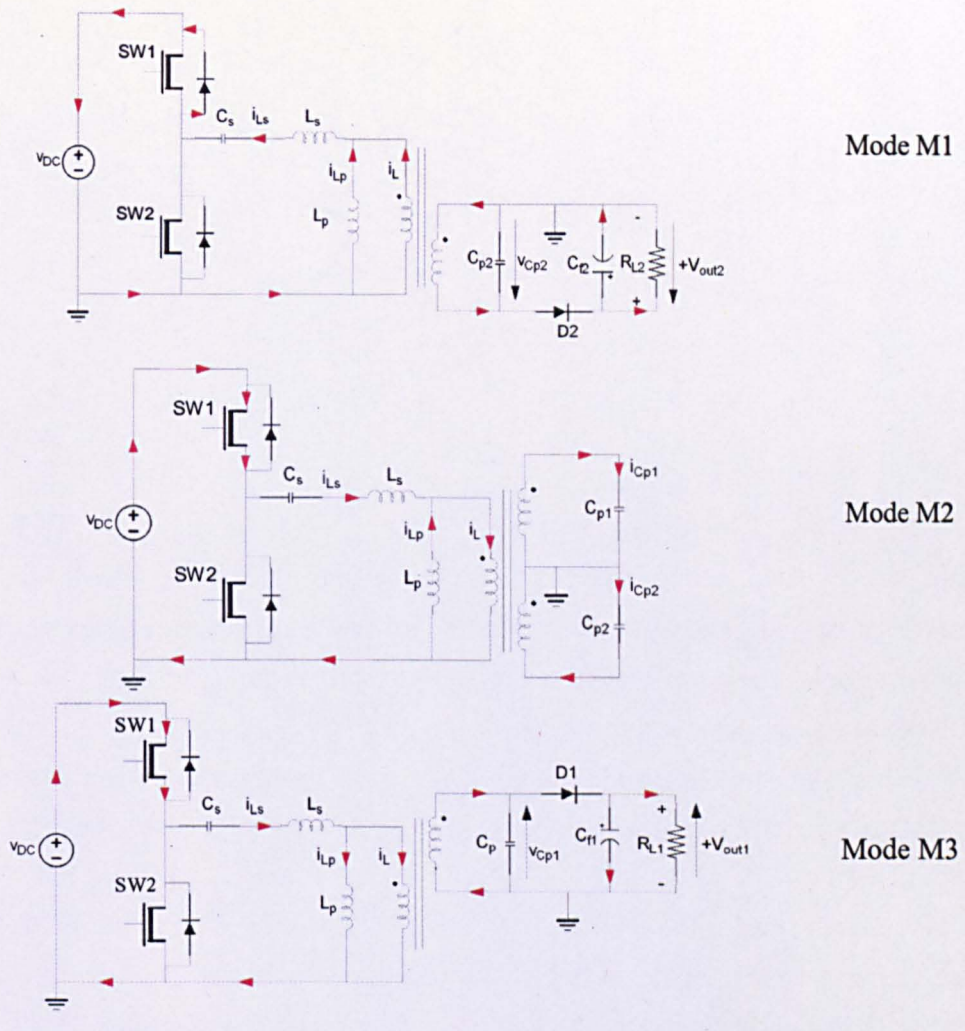

Figure 8.3 Circuit modes.

Circuit Mode M2 ($t_1 \le t < t_2$). Here, the series resonant inductor current i_{Ls} starts becoming positive. Since SW1 was turned on during M1, current flow is now through SW1. Initial conditions for this mode are that i_{Ls}=0 and v_{cp2}= V_{out2}. The inductor current i_{Ls} and parallel resonant capacitor voltages now take on sinusoidal characteristics. Since the outputs are effectively disconnected from the tank, both C_{p1} and C_{p2} contribute to resonant behaviour. Both rectifier currents are therefore zero and the converter outputs are in an 'idle' state, being supplied solely by the charge on the filter capacitors.

By initially neglecting the rectifier on-state voltage, and noting that the effective parallel resonant capacitance C_p is the sum of shunt network capacitances C_{p1} and C_{p2}, v_{Cp1} during the capacitor charging period is described by [H13]:

$$v_{Cp1}(t) = v_{Cp1}(t_1) + \frac{1}{C_p}\int_{t_1}^{t_2} \tilde{i}_{in} \sin(2\pi f_s t)dt \tag{8-1}$$

where $\tilde{i}_{in} = i_{Ls} - i_{Lp}$. Evaluating (8-1) with initial conditions $v_R(t_1) = v_{Cp1}(t_1) = -V_{out2}$ yields:

$$v_{Cp1}(t_2) = -V_{out2} + \tilde{i}_{in} \times \frac{1 - \cos(2\pi f_s(t_2 - t_1))}{2\pi f_s C_p} \tag{8-2}$$

The boundary for the end of the capacitor-charging period is $v_{Cp1}(t_2) = +V_{out1}$, which yields the rectifier non-conduction angle, ϕ_{c1}, associated with positive polarity of current, i_R, through the high side rectifier:

$$\begin{aligned} t_2 - t_1 &= \frac{1}{2\pi f_s} \times \cos^{-1}(\phi_{c1}) \\ \phi_{c1} &= \cos^{-1}\left(1 - \frac{2\pi f_s C_p v_{tot}}{\tilde{i}_{in}}\right) \end{aligned} \tag{8-3}$$

where $v_{tot} = V_{out1} + V_{out2}$. This mode ends when SW1 turns off.

Circuit Mode M3 ($t_2 \le t < T_s/2$). At t=t_2, D1 becomes forward-biased and D2 reverse-biased. The rectifier diode current i_{R2} remains zero throughout the duration of M3, and D1 clamps the capacitor voltage, v_{cp1} to $+V_{out1}$ until i_{Ls} decays to zero, at which time the second half-cycle of operation commences.

For 50% duty-cycle excitation, the 2nd half-cycle of operation is the mirror image of the first. However, for asymmetrical excitation, the output rectifier diode (D2) non-conduction angle, associated with the series resonant inductor current being of negative polarity, is given by:

$$\phi_{c2} = \cos^{-1}\left(1 - \frac{2\pi f_s C_p v_{tot}}{\tilde{i}_{in}}\right) \tag{8-4}$$

where $\tilde{i}_{in} = i_{Ls} - i_{Lp}$.

The voltage, v_{cp1}, across the parallel resonant capacitor can therefore be expressed as a function of the angle θ —see Fig. 8.2(b):

$$v_{Cp1}(\theta) = \begin{cases} -V_{out2} + \dfrac{\hat{i}_{in}}{2\pi f_s C_p} \times (1 - \cos(\theta)) & \text{for } \theta = 0 \ldots \phi_{c1} \\ +V_{out1} & \text{for } \theta = \phi_{c1} \cdots \pi \\ V_{out1} - \dfrac{\hat{i}_{in}}{2\pi f_s C_p} \times (1 - \cos(\theta)) & \text{for } \theta = \pi \ldots \pi + \phi_{c2} \\ -V_{out2} & \text{for } \theta = \pi + \phi_{c2} \ldots 2\pi \end{cases} \tag{8-5}$$

Under steady-state conditions, the mean output current i_{out1} flowing through D1 towards the output filter and load, can be determined from the mean current flowing through the rectifier when it is of positive polarity. Since this occurs during the interval $\phi_{c1} \le \theta < \pi$, i_{out1} is given by:

$$i_{out1} = \frac{1}{2\pi} \times \int_{\phi_{c1}}^{\pi} \hat{i}_{in} \sin(\theta) d\theta \tag{8-6}$$

Substituting (8-3) into (8-6) and evaluating the integral provides the solution for i_{out1} as follows:

$$i_{out1} = \frac{\hat{i}_{in}}{2\pi} \times (1 + \cos(\phi_{c1})) = \frac{\hat{i}_{in} - \pi f_s C_p v_{tot}}{\pi} \tag{8-7}$$

Simple mathematical manipulation of (8-3) and (8-7) then gives the corresponding rectifier non-conduction angle ϕ_{c1}:

$$\phi_{c1} = \cos^{-1}\left(\frac{\pi i_{out1} - \pi f_s C_p v_{tot}}{\pi i_{out1} + \pi f_s C_p v_{tot}} \right) \tag{8-8}$$

V_{out1} is determined by assuming the output filter capacitance C_f is sufficiently large to impart negligible output voltage ripple. In this case:

$$\begin{aligned} V_{out1} = i_{out1} R_{L1} &= \frac{\hat{i}_{in} R_{L1}}{2\pi} \times (1 + \cos(\phi_{c1})) \\ &= \frac{R_{L1}(\hat{i}_{in} - \pi f_s C_p v_{tot})}{\pi} \\ &= \frac{R_{L1}}{\pi} \times \frac{\hat{i}_{in} - \pi f_s C_p V_{out2}}{1 + R_L f_s C_p} \end{aligned} \tag{8-9}$$

Equations (8-6) to (8-9) can be further manipulated to provide the complementary D2 non-conduction angle, ϕ_{c2}, and the output current, i_{out2}, and output voltage V_{out2}, as follows:

$$\begin{aligned} i_{out2} &= \frac{\bar{i}_{in}}{2\pi} \times (1 + \cos(\phi_{c2})) \\ V_{out2} &= \frac{R_{L2}}{\pi} \times \frac{\bar{i}_{in} - \pi f_s C_p V_{out1}}{1 + R_L f_s C_p} \end{aligned} \tag{8-10}$$

Notably, a high-sensitivity and inter-dependence between the high- and low-side output voltage distributions, and $\bar{i}_{Ls}$ and $\bar{i}_{Ls}$, has been observed, and will be discussed in detail in later sections.

8.4. State-Variable Model for Dual-Load Resonant Converter

A state-variable model describing the behaviour of the dual-load converter can be obtained by considering the electrical network in Fig. 8.4. The model is derived by separating the converter dynamics into 'fast' and 'slow' sub-systems, with their interaction related by a set of coupling equations. The leakage inductances of a well designed ferrite transformer are normally small compared to its magnetising inductance. For this reason, their effects are initially neglected for brevity.

State variables are selected based on voltages and currents that govern the operation of the resonant tank. The fast sub-system is therefore considered to describe the dynamics of the resonant tank and power switches (8-11)—the underlying equations exclude the effects of parasitics.

$$\begin{aligned} \frac{dv_{Cs}}{dt} &= \frac{i_{Ls}}{C_s} \\ \frac{di_{Ls}}{dt} &= \frac{V_{in} - v_{Cs} - v_{Lp}}{L_s} \\ \frac{di_{Lp}}{dt} &= \frac{v_{Lp}}{L_p} \\ \frac{dv_{Cp1}}{dt} &= \frac{i_{Ls} - i_{Lp} - i_{R1} - i_{Cp2} - i_{R2}}{C_{p1}} \\ \frac{dv_{Cp2}}{dt} &= \frac{i_{Ls} - i_{Lp} - i_{R2} - i_{Cp1} - i_{R1}}{C_{p2}} \end{aligned} \tag{8-11}$$

As discussed previously, the path of the current leaving the transformer secondary windings changes during the positive and negative half-cycles of the parallel capacitor voltage, due to the effect of the rectifiers allowing current to conduct only in a single direction. During the positive half-cycle interval,

D_1 is forward biased and permits the rectifier current i_R to supply the load R_{L1}. During the negative half-cycle the top rectifier is reverse-biased and D_2 supports power transfer to load R_{L2}.

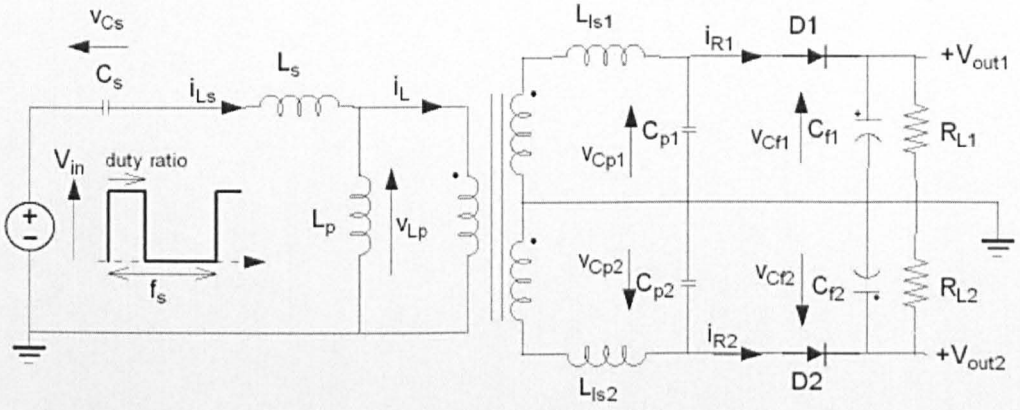

Figure 8.4 Simplified circuit diagram of the dual-load SPRC including output leakage inductances.

If the output filter capacitors are assumed to be sufficiently large so as to maintain a constant voltage on both outputs, over a switching period, their contribution to the dynamics is given by:

$$\begin{aligned}\frac{dv_{cf1}}{dt} &= \frac{i_{R1}}{C_{f1}} - \frac{v_{cf1}}{C_{f1}R_{L1}} \\ \frac{dv_{cf2}}{dt} &= \frac{i_{R2}}{C_{f2}} - \frac{v_{cf2}}{C_{f2}R_{L2}}\end{aligned} \tag{8-12}$$

As discussed, during interval $t_1 \rightarrow t_2$ (see Fig. 8.2(b)) the parallel resonant capacitor voltage is clamped to output voltage, v_{cf1} during the positive half-cycle, and conversely, to $-v_{cf2}$ during the negative half-cycle, due to the action of the rectifiers. By noting that there will be negligible current flowing through C_p during these periods, the rectifier input voltage is dependent on the direction of the current leaving the resonant tank inductances, i.e. $i_L = i_{Ls} - i_{Lp}$. The relevant coupling terms are therefore obtained by equating voltages at either side of the rectifier [H14], for each respective half-cycle, as follows:

$$\begin{aligned}v_{Cp1} &= \text{sgn}(i_L)(V_{out1} + v_{diode}) = \text{sgn}(i_L)(v_{cf1} + v_{diode}) \\ v_{Cp2} &= \text{sgn}(i_L)(V_{out2} + v_{diode}) = \text{sgn}(i_L)(v_{cf2} + v_{diode})\end{aligned} \tag{8-13}$$

Assuming a constant rectifier on-state voltage, (8-13) now reduces to:

$$\begin{aligned}\frac{dv_{Cp1}}{dt} &= \text{sgn}(i_L)\frac{dv_{cf1}}{dt} \\ \frac{dv_{Cp2}}{dt} &= \text{sgn}(i_L)\frac{dv_{cf2}}{dt}\end{aligned} \tag{8-14}$$

The use of the model is demonstrated by example. Consider the rectifier current, i_{R2}, is zero during the positive half-cycle of the parallel capacitor voltage. Equations (8-14) and (8-12) can be substituted into (8-11) and solved for the rectifier current i_{R1},

$$\frac{i_L - i_{R1} - i_{Cp2} - i_{R2}}{C_{p1}} = \mathrm{sgn}(i_L)\left(\frac{i_{R1}}{C_{f1}} - \frac{v_{cf1}}{C_{f1}R_{L1}}\right)$$

$$i_{R1}\left(\frac{\mathrm{sgn}(i_L)C_{p1} + C_{f1}}{C_{p1}C_{f1}}\right) = \frac{i_L - i_{Cp2} - i_{R2}}{C_{p1}} + \frac{\mathrm{sgn}(i_L)v_{cf1}}{C_{f1}R_{L1}} \tag{8-15}$$

$$i_{R1} = \frac{C_{p1}C_{f1}}{\mathrm{sgn}(i_L)C_{p1} + C_{f1}}\left(\frac{i_L - i_{Cp2} - i_{R2}}{C_{p1}} + \frac{\mathrm{sgn}(i_L)v_{cf1}}{C_{f1}R_{L1}}\right)$$

This leads to the following coupling equations describing the rectifier currents within each half of a switching cycle:

$$i_{R1} = \begin{cases} \dfrac{C_{p1}C_{f1}}{\mathrm{sgn}(i_L)C_{p1} + C_{f1}}\left(\dfrac{i_L - i_{Cp2} - i_{R2}}{C_{p1}} + \dfrac{\mathrm{sgn}(i_L)v_{cf1}}{C_{f1}R_{L1}}\right) & \text{for } v_{Cp1} = V_{out1} + v_{diode} \\ 0 & \text{for } v_{Cp1} < V_{out1} + v_{diode} \end{cases}$$

$$i_{R2} = \begin{cases} \dfrac{C_{p2}C_{f2}}{\mathrm{sgn}(i_L)C_{p2} + C_{f2}}\left(\dfrac{i_L - i_{Cp1} - i_{R1}}{C_{p2}} + \dfrac{\mathrm{sgn}(i_L)v_{cf2}}{C_{f2}R_{L2}}\right) & \text{for } v_{Cp2} = V_{out2} + v_{diode} \\ 0 & \text{for } v_{Cp2} < V_{out2} + v_{diode} \end{cases} \tag{8-16}$$

Figure 8.5 shows typical current waveforms at the output side of the centre-tap transformer, when operating subject to both symmetric and asymmetric input voltage excitation, and assuming the effect of transformer output leakage inductances are negligibly small i.e. L_s, C_s, L_p and C_p dominate behaviour—i_{sec1} and i_{sec2} are the currents leaving the output windings of the transformer. This then, means that the voltage across L_p is assumed to be a reflection of the voltages across C_{p1} and C_{p2}, and the state vector for the parallel inductor current in the fast sub-system (see Equation (8-11)) simplifies to $v_{Lp} = v_{Cp}$. It can be seen that C_{p1} and C_{p2} charging/discharging currents are similar, implying that current flowing from the primary side of the transformer is equally shared between them during modes M2 and M4 (when D1 and D2 are reverse-biased). Notable, in this case, is that the shunt connection of the parallel resonant capacitors can also be used to conveniently include the effects of the transformer output stray capacitances or output rectifier diode junction capacitances.

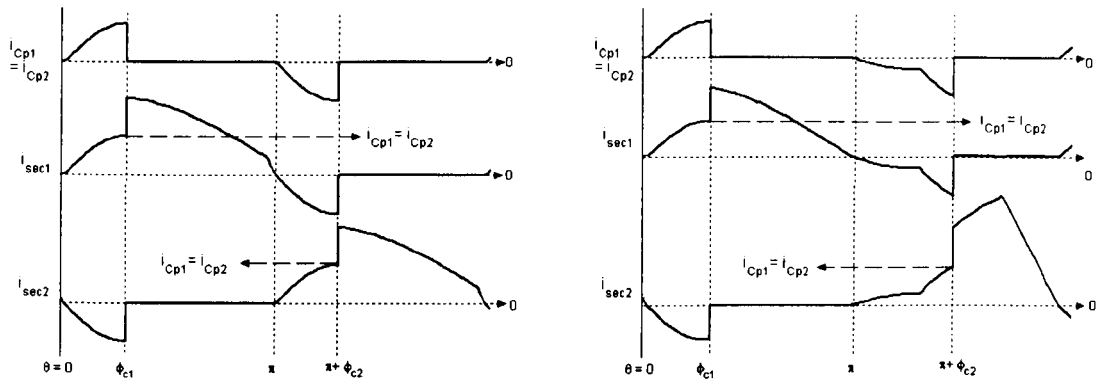

(a) (b)

Figure 8.5 Typical current waveforms from the resonant tank into rectifier when excited by (a) balanced input voltage (50% duty), and (b) asymmetrical input voltage (30% duty).

The state variable equations for the parallel resonant capacitor voltage (8-11) can be simplified to:

$$\begin{aligned} \frac{dv_{Cp1}}{dt} &= \frac{i_{Ls} - i_{Lp} - i_R}{2C_{p1}} \\ \frac{dv_{Cp2}}{dt} &= \frac{i_{Ls} - i_{Lp} - i_R}{2C_{p2}} \end{aligned} \tag{8-17}$$

The complete state-variable model of the dual-load converter (excluding the effects of output leakage inductances) is given by:

$$\dot{\mathbf{x}} = \begin{bmatrix} 0^{3\times3} & \mathbf{A}_1 & 0^{2\times3} \\ \mathbf{A}_2 & 0^{2\times2} & 0^{2\times2} \\ 0^{2\times3} & 0^{2\times2} & \mathbf{A}_3 \end{bmatrix} \mathbf{x} + \mathbf{B} \tag{8-18}$$

where

$$\mathbf{x} = \begin{bmatrix} v_{Cp1} & v_{Cp2} & v_{Cs} & i_{Lp} & i_{Ls} & v_{Cf1} & v_{Cf2} \end{bmatrix}^T$$

$$\mathbf{A}_1 = \begin{bmatrix} -\frac{1}{2C_{p1}} & \frac{1}{2C_{p1}} \\ -\frac{1}{2C_{p2}} & \frac{1}{2C_{p2}} \\ 0 & \frac{1}{C_s} \end{bmatrix}, \quad \mathbf{A}_2 = \begin{bmatrix} \frac{1}{L_p} & 0 & 0 \\ -\frac{1}{L_s} & 0 & -\frac{1}{L_s} \end{bmatrix}, \quad \mathbf{A}_3 = \begin{bmatrix} -\frac{1}{C_f R_{L1}} & 0 \\ 0 & -\frac{1}{C_{f2} R_{L2}} \end{bmatrix} \tag{8-19}$$

$$\mathbf{B} = \begin{bmatrix} -\frac{i_R}{2C_{p1}} & -\frac{i_R}{2C_{p2}} & 0^{1\times2} & \frac{V_{in}}{L_s} & \frac{i_{R1}}{C_{f1}} & \frac{i_{R2}}{C_{f2}} \end{bmatrix}^T$$

The model is now used to investigate the behaviour of the dual-load converter when subject to asymmetrical input excitation, with balanced output loads. The converter is supplied from a 30V DC-link. Model parameters for the simulations are given in Table 8.1. A resulting plot of the steady-state output voltage characteristics, V_{out1} and V_{out2}, as a function of switching frequency and duty-cycle ratio, is given in Fig. 8.6 (the secondaries of the transformer have identical turns ratios, and the parallel resonant capacitances are the same).

Table 8.1 Converter model parameters

Parameters	**Values**
Characteristic impedance	2.5
Resonant frequency, f_o (kHz)	130
Resonant capacitance ratio, C_n	0.03
Resonant inductance ratio, L_n	0.01
Series load quality factor, Q_{op1}	6

From Fig. 8.6, it is evident that for operation above resonance, the sum of the output voltages applied to the loads increases as the operating frequency tends to the effective resonant frequency, for fixed values of duty ratio. Furthermore, for 50% duty ratio, giving symmetric square-wave excitation of the tank, the converter delivers identical voltages to both high- and low-side outputs, for fixed operating frequencies, as expected.

For a given operating frequency, a decrease in the duty ratio, from 50%, is seen to deliver more energy from the resonant tank to energize output V_{out1}, thereby yielding a correspondingly higher output voltage, and power. Conversely, increasing the duty ratio beyond 50% is seen to deliver more power to the secondary winding to support a higher V_{out2}. From this characteristic, it is clear that, for balanced loads, the voltage and power distribution to each output can be independently influenced by suitable choice of duty ratio and switching frequency.

For completeness, Fig. 8.7 compares the difference between possible output voltages, from which it can be seen that the slope of the curve is greater for lower values of switching frequency. This implies that when a large difference between the output voltages is required, the converter should be operated close to resonance, leading to high efficiency operation, and zero voltage switching. However, this also means that the tank components are subjected to higher electrical stresses.

Figure 8.8(a) shows the relative voltage distributions as a function of the ratio of the input voltage duty, and load quality factor, Q_{op1}. It can be seen that the slope of the characteristic is relatively independent of the quality factor, for high Q_{op1}, although the attainable difference between the output voltages is seen to be greater for low values of load quality factor. Hence, operation with low Q_{op1} should be chosen to facilitate large voltage differences, as opposed to the use of high Q_{op1} to facilitate sinusoidal tank currents and voltages. Moreover, low Q_{op1} conditions implies that the output voltage vs. frequency behaviour of the converter has a 'flatter' characteristic, and a greater range of switching frequencies is required to regulate the output voltage when the converter is subjected to variations in DC-link voltage or load, thereby requiring greater controller effort and bandwidth for tracking control. A trade off is therefore required in the selection of the key converter parameters.

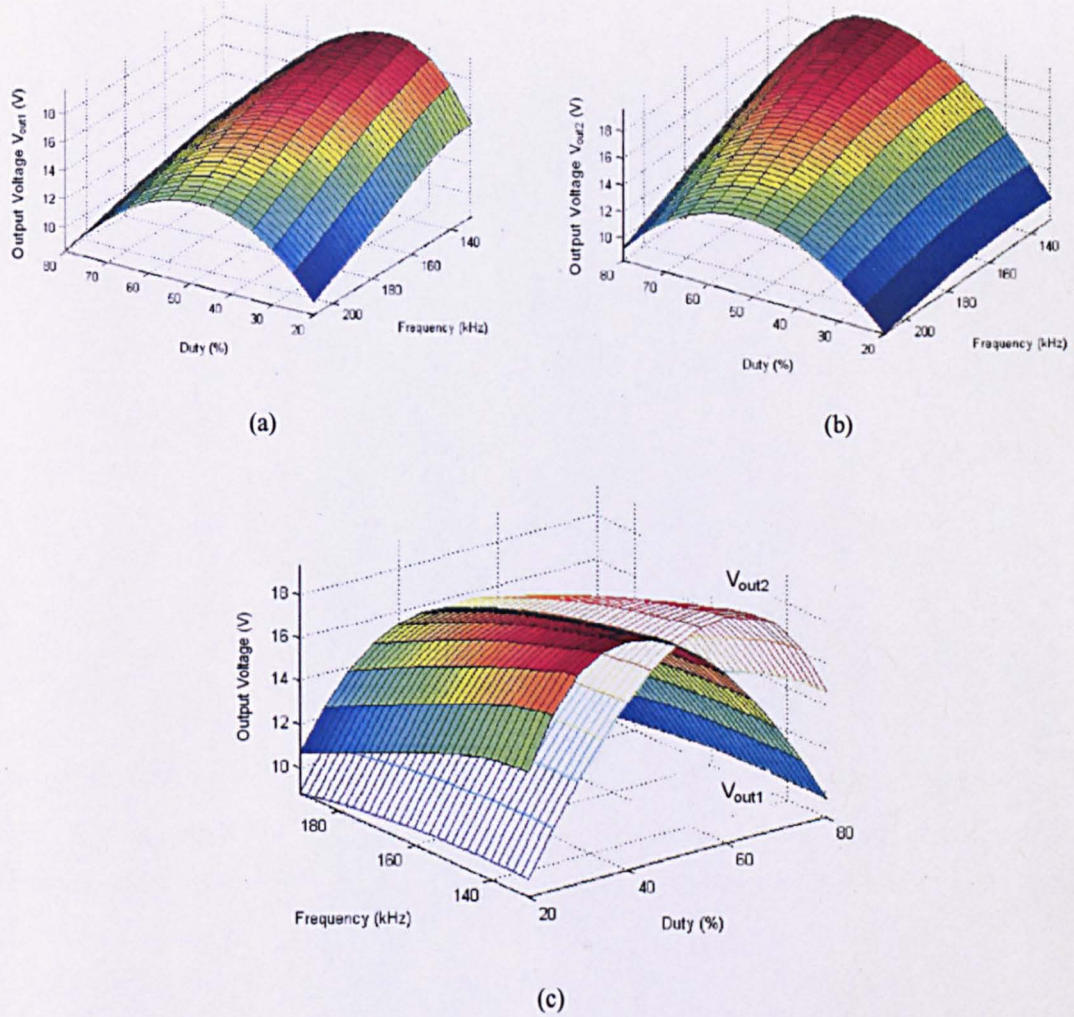

Figure 8.6 Output voltage distribution vs. switching frequency and duty ratio: (a) Output Voltage $+V_{out1}$, (b) Output Voltage $+V_{out2}$ and (c) Simulated voltage distribution.

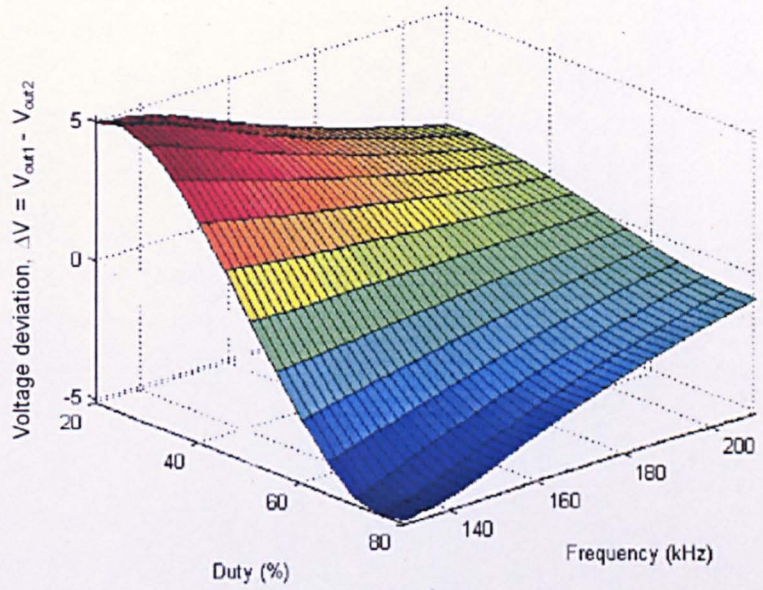

(a)

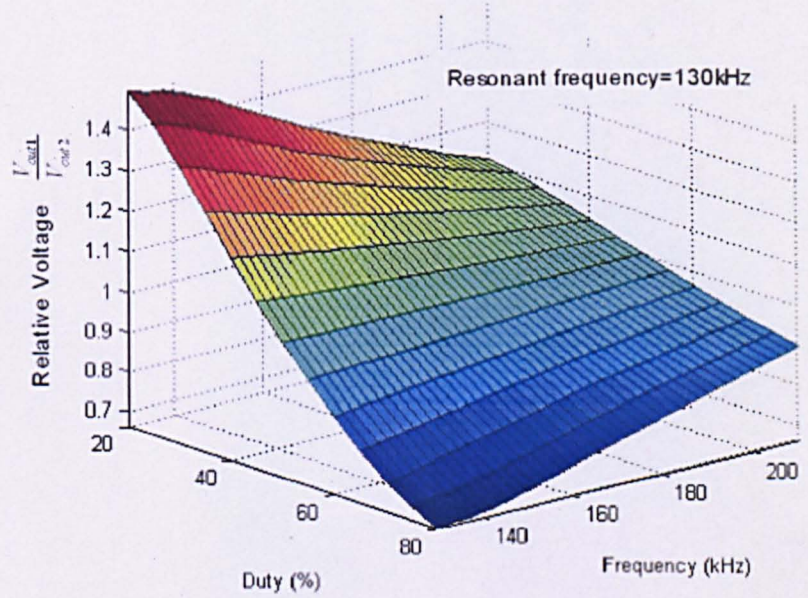

(b)

Figure 8.7 Asymmetrical output voltage distribution: (a) Output voltages deviation and (b) relative voltage distribution.

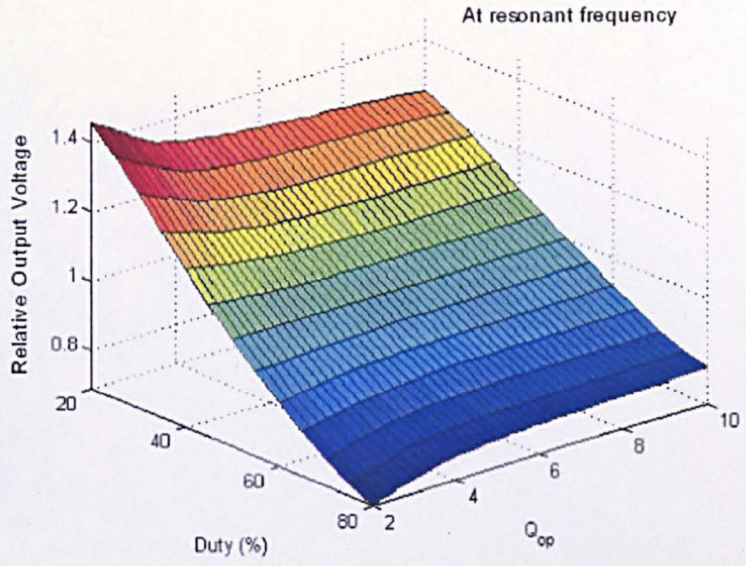

(a)

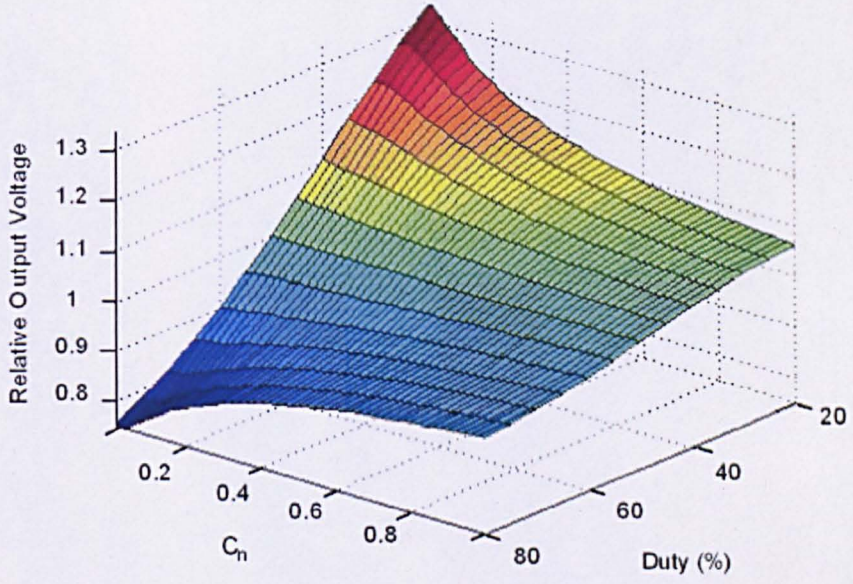

(b)

Figure 8.8 Dual output converter characteristics as a function of (a) duty ratio and Q_{op1} as design parameters and, (b) duty ratio and resonant capacitance ratio C_n as design parameters.

It is instructive to show the impact of converter parameters on the attainable voltage distribution. Figure 8.8(b) therefore shows an example of the resulting voltage distribution, as a function of duty ratio, as the resonant capacitance ratio C_n is varied. It can be seen, in particular, that the slope of the characteristic is greater for low ratios of resonant capacitance. Hence, it is instructive to choose a low value for C_n ratio during the design phase. However, a choice of low parallel capacitance means the input-output voltage characteristic exhibits a reduced resonant peak, and consequently, the voltage boosting capability of the converter is limited. Furthermore, the input-output voltage conversion ratio, at the effective resonant frequency of the tank, is consequently lower, and the resulting converter therefore appears more suitable for step-down DC-DC applications.

Figures 8.6 to 8.8 have established that a chosen distribution of output voltages (with balanced loads) can be maintained using a combination of switching frequency and duty ratio control, so long as the maximum deliverable voltage, and input voltage vs. input current phase angle, are not exceeded. For the particular converter example considered, Table 8.2 lists example operating conditions for providing various output voltage distributions, with the DC-link fixed at v_{DC}=30V.

Table 8.2 Example output voltage distributions.

f_s= 145 kHz, *duty cycle ratio*=20%						
V_{out1} (V)	V_{out2} (V)	i_{Ls} (A)	v_{Cs} (V)	$\Delta\beta_{in}$ (°)	ϕ_{c1} (°)	ϕ_{c2} (°)
15V@20W	10V@10W	7.15	8	0	53.8	51.3
f_s= 145 kHz, *duty cycle ratio*=80%						
V_{out1} (V)	V_{out2} (V)	i_{Ls} (A)	v_{Cs} (V)	$\Delta\beta_{in}$ (°)	ϕ_{c1} (°)	ϕ_{c2} (°)
10V@10W	15V@20W	4.84	25.6	64.5	51.4	53.9
f_s= 205 kHz, *duty cycle ratio*=50%						
V_{out1} (V)	V_{out2} (V)	i_{Ls} (A)	v_{Cs} (V)	$\Delta\beta_{in}$ (°)	ϕ_{c1} (°)	ϕ_{c2} (°)
15V@25W	15V@25W	5.69	16.99	47	59	59

Under nominal operation the converter is designed to be excited with a square-wave input voltage at f_s=210 kHz. Figure 8.9 therefore shows the required operating point, as a function of frequency and duty cycle, on a contour plot. Assuming both outputs can be independently regulated, if the demand on the low-side output is varied from +15V to +10V, but the demand on high-side output remained unchanged at +15V, then a compensator is required to reduce the duty-ratio to provide an asymmetrical output voltage distribution until the measured low-side output voltage is equivalent to the demand. However, a variation in the input signal duty-ratio to regulate the low-side output will also affect the high-side output voltage, due to cross-regulation. Consequently, a corresponding change in excitation

frequency, is also necessary. To compensate for a reduction in the high-side output voltage, as the duty-ratio is decreased, the compensator must also decrease the switching frequency towards the effective resonant frequency. However, due to cross-regulation, this change in switching frequency will have an impact on the low-side output voltage, which will require an appropriate change in duty ratio, once again. An appropriate compensator must therefore find a stable operating point by controlling both the switching frequency and duty-ratio, to provide both demanded output voltages. In particular, for the case considered, when operating at f_s=145 kHz, with duty-ratio of 20%, Fig. 8.9(a) shows the example converter delivers the demanded +15V to the high side output, and +10V to the low-side output.

Conversely, with an 80% input signal duty-ratio, the opposite voltage distribution is obtained, as shown in Fig. 8.9(b), by virtue of employing identical turns ratios on the secondary sides of the transformer.

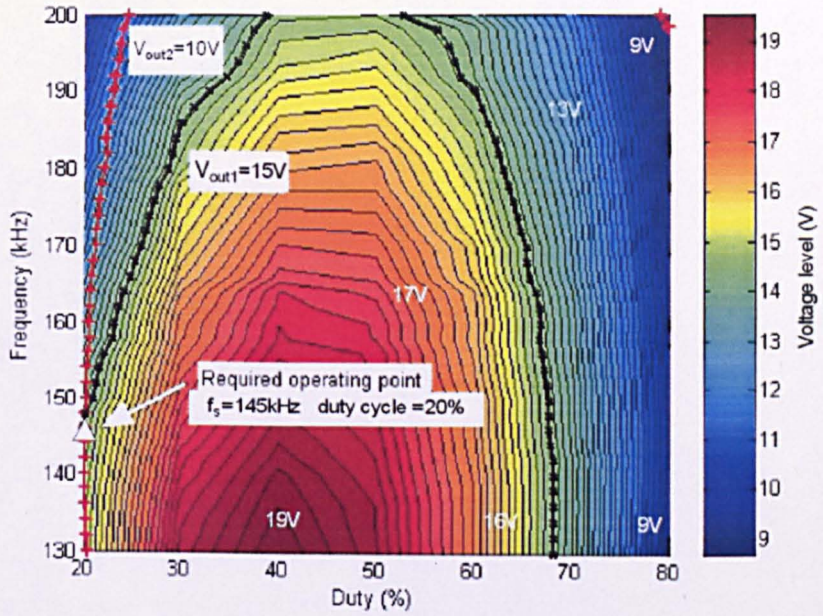

(a)

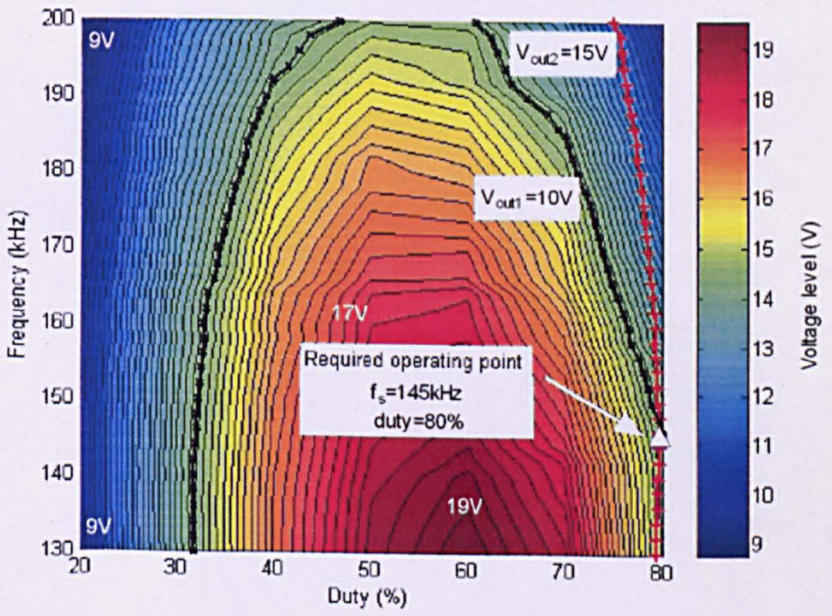

(b)

Figure 8.9 Simulated operating point for asymmetric input voltage excitation: (a) V_{out1}=15V, V_{out2}=10V and (b) V_{out1}=10V, V_{out2}=15V.

Theoretically, a controlled variation in the output voltages, as shown in Fig. 8.9, can be obtained by operating the converter around a designated point in the region of high gradient on the frequency characteristic. However, high efficiency soft-switching operation cannot be sustained if the converter is operated at resonance, to obtain the maximum output voltage difference.

Figure 8.10 shows an example input voltage vs. input current, phase difference, $\Delta\beta_{in}$, for the example converter, plotted against the normalised switching frequency $\omega_n = \omega_s/\omega_o$ and input voltage duty-ratio. At frequencies less than the tank resonant frequency, the input impedance of the tank network Z_{in} is dominated by the tank capacitance. Hence, the input switch current fundamental component leads the input voltage, and the resonant tank presents an effective capacitive load. This provides Zero Current Switching (ZCS) for $\Delta\beta_{in} < 0$. When the resonant converter is operated above resonance, Zero Voltage Switching (ZVS) occurs, and the resonant tank presents an effective inductive load to the half-bridge switches, and the switch current lags the switch voltage.

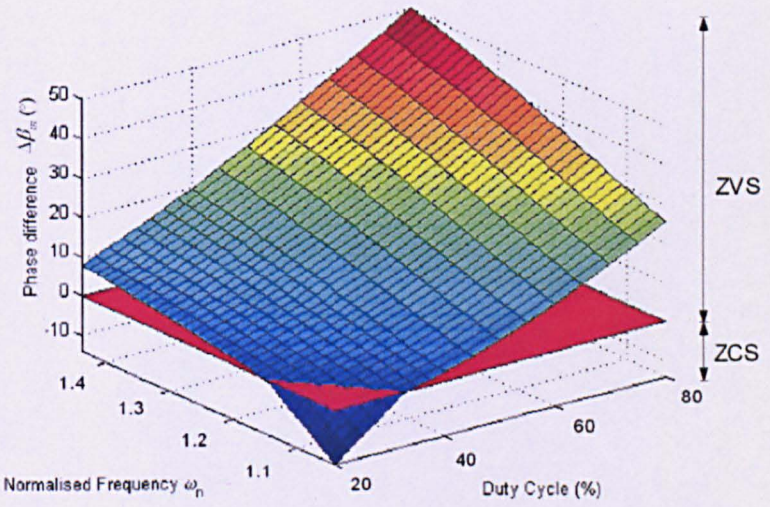

Figure 8.10 Phase difference $\Delta\beta_{in}$ versus the normalised switching frequency and duty ratio.

At the effective resonant frequency, under asymmetric square-wave input voltage excitation, the input voltage lags the first harmonic of the input current, $\Delta\beta_{in} < 0$ when the duty cycle falls below 50%—see Fig. 8.11. The condition for inductive mode conduction, under asymmetric conditions, is therefore expressed as,

$$\Delta\beta_{in} = \beta_{in} - \phi_{vi(1)} \geq 0 \qquad (8\text{-}20)$$

where $\Delta\beta_{in}$ is the phase angle between the actual square input voltage and fundamental of the input current; β_{in} is the phase lag between the first harmonic of the input voltage and current; and $\phi_{vi(1)}$ is the phase of the fundamental frequency component of the input voltage, $v_{i(1)}$. (Noting that β_{in}=0 at resonance, and β_{in}>0 above resonance, implies that the first harmonic of the input voltage leads the first harmonic of the current).

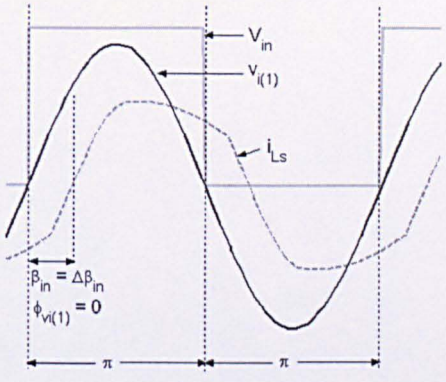

(a)

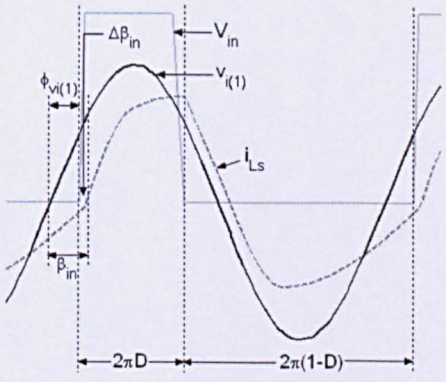

(b)

Figure 8.11 Waveforms of input voltage V_{in}, resonant circuit fundamental input voltage $v_{i(1)}$, and series inductor current i_{Ls} at (a) D=0.5 ($\Delta\beta_{in} = \beta_{in}$) and b) D=0.3 ($\Delta\beta_{in} < \beta_{in}$)

For asymmetrical operation of the converter, the duty-cycles of SW1 and SW2 are denoted, respectively, D and 1-D, where D is the ratio of the turn-on period with respect to the switching period. Asymmetric switching therefore provides an asymmetrical voltage source V_{in} to excite the tank, of amplitude v_{DC}:

$$V_{in} = \begin{cases} v_{DC} & \theta = 0 \ldots 2\pi D \\ 0 & \theta = 2\pi D \ldots 2\pi \end{cases} \tag{8-21}$$

Assuming that only the fundamental component excites the resonant tank, and applying relationship $\tan^{-1}(\cos(\theta)/\sin(\theta)) = \pi/2 + \theta$, the first harmonic of the resulting input voltage, $v_{in(1)}$, and its phase angle, $\phi_{vi(1)}$ are given by:

$$v_{i(1)} = \frac{2v_{DC}}{\pi}\sqrt{1-\cos(2\pi D)} \times \sin\left(\omega t + \phi_{vi(1)}\right)$$
$$\phi_{vi(1)} = \frac{\pi}{2} - \pi D \tag{8-22}$$

The condition for inductive switching can now be re-written as $\beta_{in} \geq \pi(0.5 - D)$, which is obtained by increasing the switching frequency to give an increase in $\Delta\beta_{in}$. However, this will induce higher circulating currents that increases conduction losses and contributes to thermal problems. Increasing the switching frequency also compromises the ability of the converter to deliver wide voltage differences between the high- and low-side outputs. The converter should, therefore, be ideally operated at the minimum switching frequency, above resonance, that can achieve ZVS. The minimum frequency allowed is called the critical frequency, f_{crit}. To preserve ZVS as D is decreased, the required critical frequency moves away from resonant frequency, as illustrated in the example of Fig. 8.12

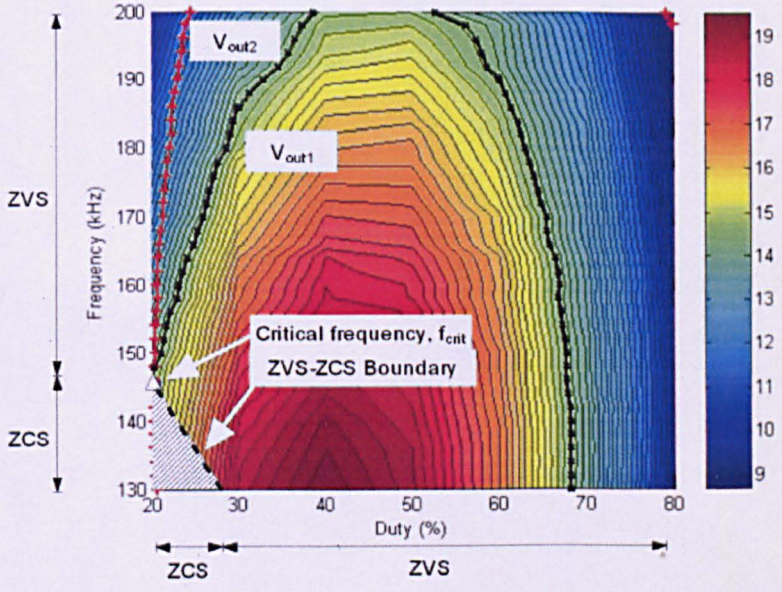

Figure 8.12 Boundary condition and critical frequency to preserve ZVS.

A study of the magnitude of the series resonant tank inductor current, i_{Ls}, and the series tank capacitor voltage, v_{Cs}, along with the phase-lag between the input voltage and current, $\Delta\beta_{in}$, and the output rectifier diode non-conduction angles (ϕ_{c1} and ϕ_{c2}) for both polarities of the parallel capacitor voltage, can be further used to identify possible operating regions for delivering asymmetrical voltage distributions, whilst maintaining inductive mode conduction, Fig. 8.13. It can be seen from Fig. 8.13 that an asymmetrical output voltage distribution can be achieved by noting the value that the parallel capacitor voltage is clamped.

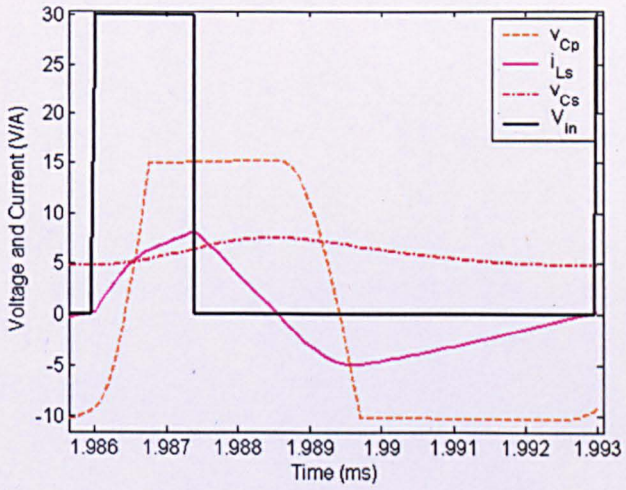

(a)

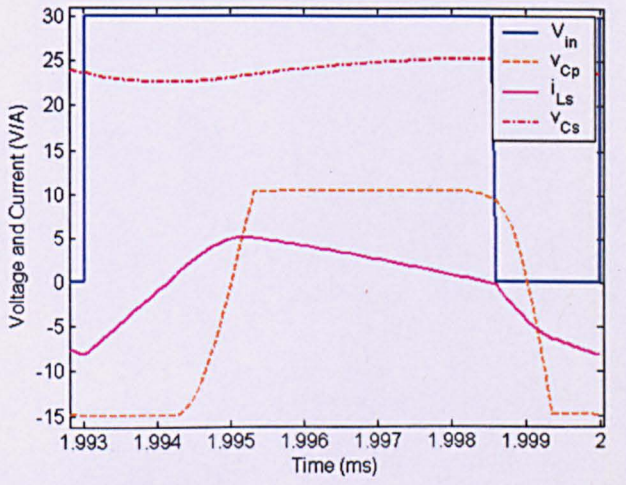

(b)

Figure 8.13 Simulated input voltage vs. current for various voltage combinations: (a) V_{out1}=+15V, V_{out2}=+10V and (b) V_{out1}=+10V, V_{out2}=+15V.

Other important design considerations are also shown Fig. 8.14, where, from Fig. 8.14(a) it can be seen that the input current leads the actual input voltage waveform by a greater phase-angle, at resonance, for high load quality factor conditions. Therefore, more energy is lost through circulating currents at light loads if the converter is ZCS. When ZVS under light load conditions, increased conduction losses also occur when compared to heavy load conditions, due to higher values of $\Delta\beta_{in}$. A design trade-off therefore exists between accepting high circulating currents under either ZVS or ZCS conditions, or high input switch currents.

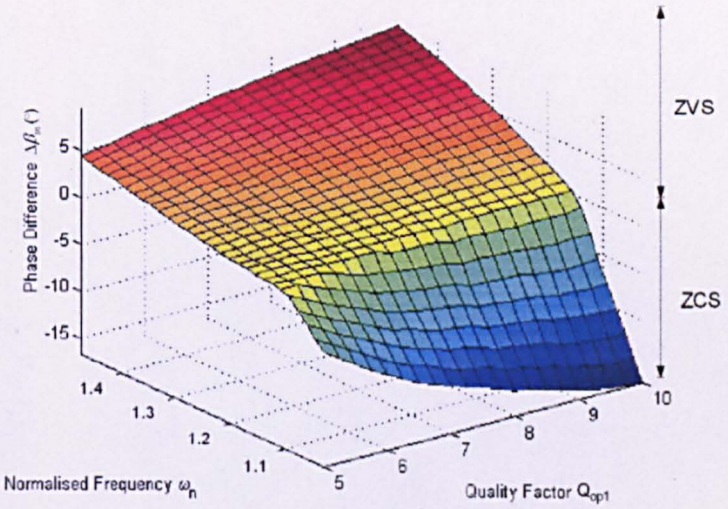

(a)

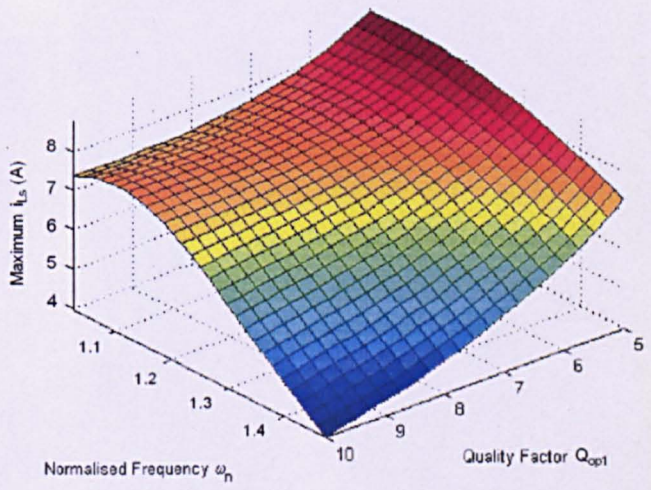

(b)

Figure 8.14 Resonant tank input characteristic at 20% duty cycle: (a) Input phase angle and (b) Maximum i_{Ls}.

8.4.1. Including the Effects of Output Leakage Inductances

Although resonant converters are generally designed to operate at relatively high frequencies, using ferrite materials often capable of operating in 200-500 kHz range and implying that low transformer leakage inductances can be obtained, designers need to be aware of the impact of even low levels of leakage inductance on converter performance. This is particularly true for converters with multiple outputs.

Here then, an enhanced state-variable model encompassing the dynamics contributed by leakage inductance, is derived. Incorporating such effects is shown to significantly complicate the analysis, particularly when determining the state of the parallel resonant inductor current, i_{Lp}, for the dual output topology, since the voltage seen across L_p cannot be assumed to be directly related to v_{Cp}, as a result of the voltages across the leakage inductances, L_{ls1} and L_{ls2}—the model must therefore be augmented with v_{Lp} to allow a solution for i_{Lp}. The resulting model is used to predict the behaviour of the converter, with comparisons of measurements from a prototype converter being used to validate the proposed analysis methodology.

As in the previous case, the converter is separated into fast- and slow-subsystems. Figure 8.15 shows a model of the resonant converter's 'fast' sub-system. A comment on the use of Fundamental Mode Approximation (FMA) based component models, is necessary at this stage. A multi-state voltage sink consists of an equivalent FMA model comprising of a large capacitance in parallel with a load resistance. Whilst the rectifier is omitted in the state-variable representation, its influence on the fast-subsystem is accommodated through the addition of current sources, as shown in Fig. 8.15.

This additional step is justifiable by noting that the interaction between the fast- and slow-subsystems is solely based on coupling equations consisting of the characteristics of the rectifier output currents i_{R1} and i_{R2}. The slow-subsystem describes the behaviour of the high- and low-side rectifier outputs and the capacitive output-filters and loads—v_{Cp1} and v_{Cp2} are considered to be the inputs to the high- and low-side output sub-systems, respectively.

The dynamics of the fast sub-system therefore consists of a set of state-variables whose value at time $t = t_0$, together with the input for all $t > t_0$, completely determines the behaviour of the system for any time $t > t_0$. The choice of states-variables is not unique—two sets are variables are employed here. One is based on the provisional selection of capacitor voltages and inductor currents, for state variables, as used in Chapter 2. This has the advantage of employing states that have a physical

meaning, but can often lead to problems when deriving models for complex piecewise linear systems, as is the case here, since the formulation of appropriate coupling equations can be difficult.

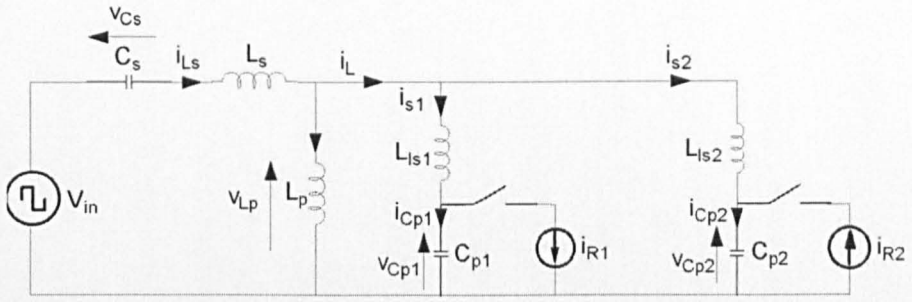

Figure 8.15 State-variable representation of the fast-subsystem.

An alternative selection, also used herein, is based the *control canonical state-space realization*. This is very attractive for this application since it allows the impact of parasitic elements to be readily included in the formulation of a dynamic model, albeit at the expense of losing some of the physical significance of the state variables. The reader is directed to Appendix B where details of the *control canonical state-space realisation* is discussed in detail, and applied to model an example 2nd-order CL resonant converter.

As previously discussed, the inclusion of transformer output inductances necessitates the augmentation of the 'fast' subsystem model with an extra state, v_{Lp}, to subsequently allow a solution for i_{Lp} (8-11). The equivalent model in Fig. 8.15 is analyzed by considering the voltage and current sources independently.

Investigating the impact of the sole voltage source V_{in} by open-circuiting the independent current sources i_{R1} and i_{R2}, the transfer function describing the relationship between parallel resonant inductor voltage v_{Lp_vi}, and voltage source, V_{in}, in the Laplace domain, is given by,

$$G(s) = \frac{b_0 s^{n-1} + \ldots + b_{n-2} s + b_{n-1}}{s^n + a_1 s^{n-1} + \ldots a_{n-1} s + a_n}$$

$$G_{vi}(s) = \frac{v_{Lp\_vi}}{V_{in}} = \frac{\frac{b_{10}}{a_{10}} s^6 + \frac{b_{11}}{a_{10}} s^4 + \frac{b_{12}}{a_{10}} s^2}{s^6 + \frac{a_{11}}{a_{10}} s^4 + \frac{a_{12}}{a_{10}} s^2 + \frac{a_{13}}{a_{10}}} \qquad \text{(8-23a)}$$

where

$$
\begin{aligned}
b_{10} &= L_p L_{ls1} L_{ls2} \\
b_{11} &= \frac{L_p L_{ls1}}{C_{p2}} + \frac{L_p L_{ls2}}{C_{p1}} \\
b_{12} &= \frac{L_p}{C_{p1} C_{p2}} \\
a_{10} &= L_p L_{ls1} L_{ls2} + L_s L_p L_{ls2} + L_s L_p L_{ls1} + L_s L_p L_{ls2} \\
a_{11} &= \frac{L_s L_{ls1}}{C_{p2}} + \frac{L_s L_{ls1}}{C_{p1}} + \frac{L_s L_p}{C_{p2}} + \frac{L_s L_p}{C_{p1}} + \frac{L_{ls1} L_{ls2}}{C_s} + \frac{L_p L_{ls2}}{C_s} + \frac{L_p L_{ls1}}{C_s} + \frac{L_p L_{ls1}}{C_{p2}} + \frac{L_p L_{ls2}}{C_{p1}} \\
a_{12} &= \frac{L_s}{C_{p1} C_{p2}} + \frac{L_{ls1}}{C_s C_{p2}} + \frac{L_{ls1}}{C_s C_{p1}} + \frac{L_p}{C_s C_{p2}} + \frac{L_p}{C_s C_{p1}} + \frac{L_p}{C_{p1} C_{p2}} \\
a_{13} &= \frac{1}{C_s C_{p1} C_{p2}}
\end{aligned}
\tag{8-23b}
$$

Transforming (8-23) into the time-domain results in a single-input/single-output (SISO) fast subsystem excited by a single voltage source, described by an ordinary differential equation:

$$
\begin{aligned}
&a_{10} \frac{d^6 v_{Lp\_vi}}{dt^6} + a_{11} \frac{d^4 v_{Lp\_vi}}{dt^4} + a_{12} \frac{d^2 v_{Lp\_vi}}{dt^2} + a_{13} v_{Lp\_vi} \\
&= b_{10} \frac{d^6 V_{in}}{dt^6} + b_{11} \frac{d^4 V_{in}}{dt^4} + b_{12} \frac{d^2 V_{in}}{dt^2}
\end{aligned}
\tag{8-24}
$$

A state-space realisation is obtained by converting the prototype input-output differential equation description into the relevant canonical/companion form, through equating coefficients of the dynamics (A_c) and output matrices (C_c), as follows,

$$
\dot{x}_1 = A_{c1} x_1 + B_{c1} u_1 \qquad y_1 = C_{c1} x_1 + D_{c1} u_1 \tag{8-25}
$$

where

$$
A_{c1} = \begin{bmatrix}
0 & 1 & 0 & 0 & 0 & 0 \\
0 & 0 & 1 & 0 & 0 & 0 \\
0 & 0 & 0 & 1 & 0 & 0 \\
0 & 0 & 0 & 0 & 1 & 0 \\
0 & 0 & 0 & 0 & 0 & 1 \\
-\frac{a_{13}}{a_{10}} & 0 & -\frac{a_{12}}{a_{10}} & 0 & -\frac{a_{11}}{a_{10}} & 0
\end{bmatrix}
\qquad
B_{c1} = \begin{bmatrix} 0^{1\times 5} \\ 1 \end{bmatrix}
$$

$$
C_{c1} = \begin{bmatrix}
-\frac{b_{10}}{a_{10}} \times \frac{a_{13}}{a_{10}} & 0 & -\frac{b_{10}}{a_{10}} \times \frac{a_{12}}{a_{10}} + \frac{b_{11}}{a_{10}} & 0 & -\frac{b_{10}}{a_{10}} \times \frac{a_{11}}{a_{10}} + \frac{b_{12}}{a_{10}} & 0
\end{bmatrix}
\qquad D_{c1} = [1]
$$

[Note: Only the final result is presented—the reader is directed to Appendix B for details of the derivation]. The procedure can be repeated to obtain the relationship between the fast-system dynamics as a result of excitation by the high-side rectifier output current source i_{R1}—the input voltage source and rectifier current, i_{R2}, being substituted with a short-circuit and an open-circuit, respectively.

Through inspection, the resulting Laplace transfer function for the input-output relationship, is given by (8-26) (full derivation details given in Appendix B),

$$G(s) = \frac{b_0 s^{n-1} + \ldots + b_{n-2} s + b_{n-1}}{s^n + a_1 s^{n-1} + \ldots a_{n-1} s + a_n} \tag{8-26}$$

$$G_{iR1}(s) = \frac{v_{Lp\_iR1}}{V_{in}} = \frac{\frac{b_{20}}{a_{20}} s^5 + \frac{b_{21}}{a_{20}} s^3 + \frac{b_{22}}{a_{20}} s}{s^6 + \frac{a_{21}}{a_{20}} s^4 + \frac{a_{22}}{a_{20}} s^2 + \frac{a_{23}}{a_{10}}}$$

where

$$b_{20} = L_s L_p L_{ls2} \quad b_{21} = \frac{L_p L_{ls2}}{C_s} + \frac{L_s L_p}{C_{p2}} \quad b_{22} = \frac{L_s}{C_s C_{p2}}$$

$$a_{20} = L_s L_p L_{ls1} C_{p1} + L_p L_{ls1} L_{ls2} C_{p1} + L_s L_{ls1} L_{ls2} C_{p1} + L_s L_p L_{ls2} C_{p1}$$

$$a_{21} = L_s L_p + L_p L_{ls2} + L_s L_{ls2} + \frac{L_p L_{ls1} C_{p1}}{C_s} + \frac{L_p L_{ls1} C_{p1}}{C_{p2}} + \frac{L_s L_{ls1} C_{p1}}{C_{p2}} + \frac{L_{ls2} L_{ls1} C_{p1}}{C_s} + \frac{L_p L_{ls2} C_{p1}}{C_s} + \frac{L_s L_p C_{p1}}{C_s}$$

$$a_{22} = \frac{L_p}{C_s} + \frac{L_p}{C_{p2}} + \frac{L_s}{C_{p1}} + \frac{L_{ls2}}{C_s} + \frac{L_p C_{p1}}{C_s C_{p2}} + \frac{L_p C_{p1}}{C_s C_{p2}}$$

$$a_{23} = \frac{1}{C_s C_{p2}}$$

Again, (8-26) can be transformed into an ordinary input-output differential equation form, and, after some mathematical manipulation and simplification, into a controllable canonical state-space realisation, as follows:

$$\dot{x}_2 = A_{c2} x_2 + B_{c2} u_2$$

$$y_2 = C_{c2} x_2 + D_{c2} u_2 \tag{8-27a}$$

where

$$A_{c2}=\begin{bmatrix} 0 & 1 & 0 & 0 & 0 & 0 \\ 0 & 0 & 1 & 0 & 0 & 0 \\ 0 & 0 & 0 & 1 & 0 & 0 \\ 0 & 0 & 0 & 0 & 1 & 0 \\ 0 & 0 & 0 & 0 & 0 & 1 \\ -\frac{a_{23}}{a_{20}} & 0 & -\frac{a_{22}}{a_{20}} & 0 & -\frac{a_{21}}{a_{20}} & 0 \end{bmatrix} \qquad B_{c2}=\begin{bmatrix} 0^{1\times 5} \\ 1 \end{bmatrix}$$

$$C_{c2}=\begin{bmatrix} \frac{b_{22}}{a_{20}} & 0 & \frac{b_{21}}{a_{20}} & 0 & \frac{b_{20}}{a_{20}} & 0 \end{bmatrix} \qquad D_{c2}=[0] \tag{8-27b}$$

Finally, the same procedure is used to obtain the state-space realisation resulting from excitation by the low-side rectifier current, i_{R2}. Inspection of the equivalent model in Fig. 8.15 shows that the resulting canonical formulation for the parallel inductor voltage, as a result of low-side rectifier current, v_{Lp_iR2} is identical to that of (8-26), with the respective input, so the derivation process is not repeated for brevity. The resulting controllable canonical state-space realisation is given in (8-28).

$$\dot{x}_3 = A_{c3}x_3 + B_{c3}u_3 \qquad y_3 = C_{c3}x_3 + D_{c3}u_3 \tag{8-28}$$

A state for the parallel resonant inductor voltage, v_{Lp}, is obtained from the summation of resultant voltages from the three models given in (8-25, 8-27 and 8-28), with inspection of the polarity and direction of flow for the high- and low-side output rectifier currents, giving: -

$$v_{Lp} = C_{c1}x_1 - D_{c1}V_{in} - C_{c2}x_2 - D_{c2}i_{R1} + C_{c3}x_3 + D_{c3}i_{R2} \tag{8-29}$$

The primary advantage of employing a canonical transformation is that ordinary differential equations are readily converted through simple analytical substitution, thereby permitting derivation of the output state that may often be difficult to otherwise obtain. However, this simplicity is at the expense of not providing an intuitive physical meaning to all the states.

By including the effects of transformer output leakage inductance, problems can be encountered whilst solving for the state of the parallel resonant capacitor voltage (8-10) due to numerical problems when calculating the matrix inversion, for simulation purposes (eg. when using the state variable models in the MATLAB®/SIMULINK environment). Moreover, the equation for v_{Cp} incurs an 'algebraic loop'. In an attempt to alleviate such problems, the canonical realisation previously used can be conveniently applied to describe high-side parallel resonant capacitor current, i_{Cp1}. By so doing, the parallel

capacitor voltage can be found from the capacitor current. Only the augmented state for the high-side capacitor current is needed to break the troublesome 'algebraic loop' in the state-variable model.

Consequently, with reference to the fast sub-system equivalent model in Fig. 8.15, the capacitor current i_{Cp1} is portrayed as the net current through the high-side parallel resonant capacitor C_{p1} when subject to excitation by V_{in}, i_{R1} and i_{R2}:

$$
\begin{aligned}
a_{40}\frac{d^6 i_{Cp\_vi}}{dt^6}+a_{41}\frac{d^4 i_{Cp\_vi}}{dt^4}+a_{42}\frac{d^2 i_{Cp\_vi}}{dt^2}+a_{43} i_{Cp\_vi} &= b_{40}\frac{d^4 V_{in}}{dt^4}+b_{41}\frac{d^2 V_{in}}{dt^2}\\
a_{50}\frac{d^6 i_{Cp\_iR1}}{dt^6}+a_{51}\frac{d^4 i_{Cp\_iR1}}{dt^4}+a_{52}\frac{d^2 i_{Cp\_iR1}}{dt^2}+a_{53} i_{Cp\_iR1} &= b_{50}\frac{d^5 i_{R1}}{dt^5}+b_{51}\frac{d^3 i_{R1}}{dt^3}+b_{52}\frac{di_{R1}}{dt}\\
a_{60}\frac{d^6 i_{Cp\_iR2}}{dt^6}+a_{61}\frac{d^4 i_{Cp\_iR2}}{dt^4}+a_{62}\frac{d^2 i_{Cp\_iR2}}{dt^2}+a_{63} i_{Cp\_iR2} &= b_{60}\frac{d^3 i_{R1}}{dt^3}+b_{61}\frac{di_{R1}}{dt}
\end{aligned}
\qquad (8\text{-}30)
$$

Full details of the derivation are given in Appendix B.

As before, the ordinary differential equation in (8-30) is used to obtain the controllable canonical state-space representation, with the dynamic state and output matrices given by,

$$
\begin{aligned}
\dot{\mathrm{x}}_4 &= \mathrm{A}_{c4}\mathrm{x}_4+\mathrm{B}_{c4}u_4 \qquad & y_4 &= \mathrm{C}_{c4}\mathrm{x}_4+\mathrm{D}_{c4}u_4\\
\dot{\mathrm{x}}_5 &= \mathrm{A}_{c5}\mathrm{x}_5+\mathrm{B}_{c5}u_5 \qquad & y_5 &= \mathrm{C}_{c5}\mathrm{x}_5+\mathrm{D}_{c5}u_5\\
\dot{\mathrm{x}}_6 &= \mathrm{A}_{c6}\mathrm{x}_6+\mathrm{B}_{c6}u_6 \qquad & y_6 &= \mathrm{C}_{c6}\mathrm{x}_6+\mathrm{D}_{c6}u_6
\end{aligned}
\qquad (8\text{-}31)
$$

The net current through the parallel resonant capacitor, i_{Cp1}, is determined from (taking care of polarity):

$$
\begin{aligned}
i_{Cp1} &= \mathrm{C}_{c4}\mathrm{x}_4+\mathrm{D}_{c4}V_{in}-\mathrm{C}_{c5}\mathrm{x}_5-\mathrm{D}_{c5}i_{R1}+\mathrm{C}_{c6}\mathrm{x}_6+\mathrm{D}_{c6}i_{R2}\\
\frac{dv_{Cp1}}{dt} &= \frac{i_{Cp1}}{C_{p1}}\\
\frac{dv_{Cp2}}{dt} &= \frac{i_{Ls}-i_{Lp}-i_{R2}-i_{Cp1}-i_{R2}}{C_{p2}}
\end{aligned}
\qquad (8\text{-}32)
$$

Substituting the output state from (8-29) and (8-32) are into (8-10), and, together with the coupling equations in (8-15), can lead to a steady state solution for the resulting state-space model. The fast- and slow-subsystem models can also be combined and used for implementation in simulation environments eg. MATLAB®/SIMULINK—see Fig. 8.16. However, by using (8-29) and (8-32), 12 new states are

introduced despite the order of the resonant converter system being only 6, implying that the 12 states are not unique and, are dependant of one another.

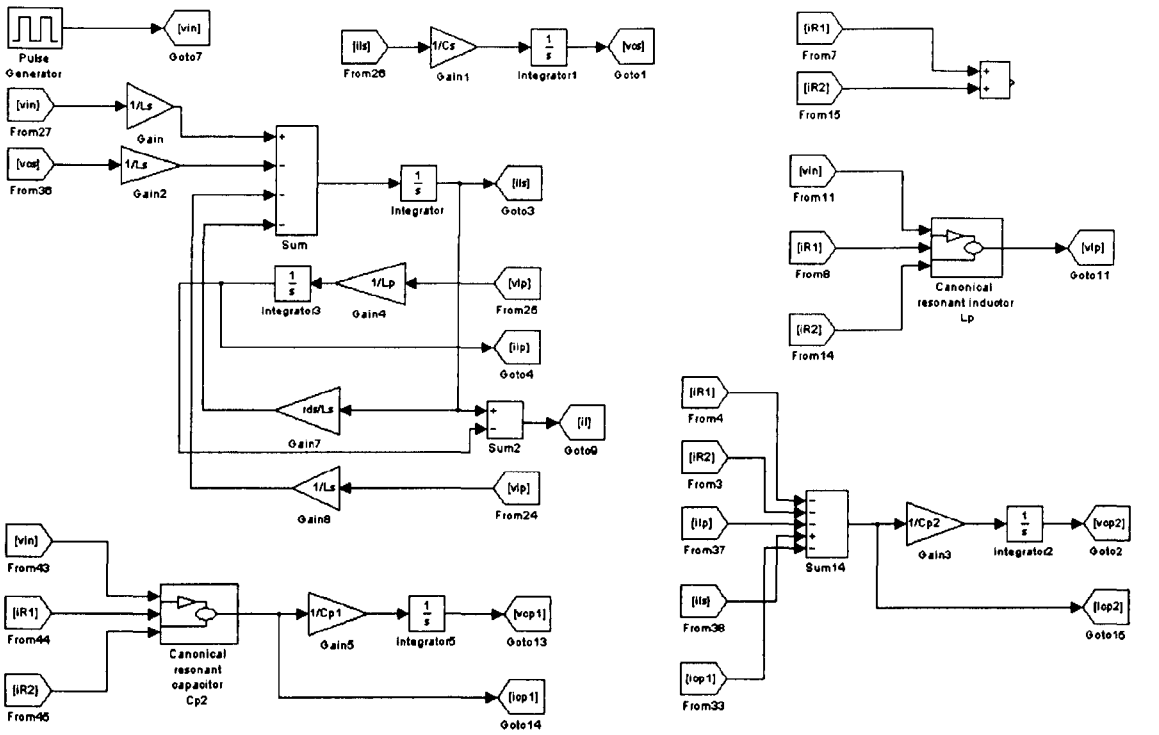

(a)

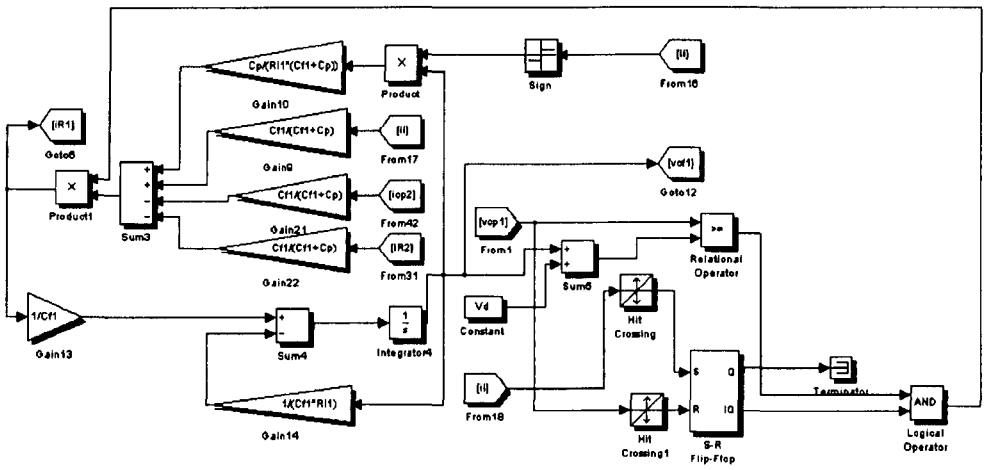

(b)

Figure 8.16 SIMULINK model for dual-load 4th-order SPRC (a) fast-subsystem and (b) slow-subsystem—high side rectifier.

Although simulation using the control canonical form can be undertaken, it incurs longer simulation time, as the model now contains redundant state variables, with detriment to the application of the state-variable model as an interactive design tool. Alternatively, this limitation can be abated to some degree, by formulating the augmented state space equation for v_{Lp}, due to each input in the *observable canonical* form. Modelling of the dual-load resonant converter using observable canonical state-space realisation is not included here for brevity. Therefore, the reader is directed to Appendix B where details of the observable canonical state-space realisation are discussed, and it is employed to model the equivalent circuit in Fig. 8.15. The subsequent state of parallel resonant inductor voltage, v_{Lp} has identical order to that of the resonant tank fast subsystem.

Having derived augmented state-variable models that include the effects of leakage inductance, they are now used to predict the steady-state output characteristics from a prototype dual-load converter. From a describing function analysis of the capacitive-output 4th-order resonant converter, discussed in Chapter 6, parameters and components for the converter can be designed. For the dual-output application, the target is to optimise the performance for two asymmetrically distributed output voltages. From the analysis given in Section 8.4, the optimal operating point of the converter is when the switching frequency is close to the resonant frequency, dictated by L_s, L_p, C_s and C_p, whilst employing a duty ratio of around 20%. This leads to a voltage gain of the high-side output being greater than that of the low-side output.

Table 8.3 Prototype 4th-order dual-output resonant converter specification and component values

Parameter	Value
DC link input voltage, v_{DC} (V)	10
Series resonant inductances, L_s (μH)	0.85
Series resonant capacitances, C_s (μF)	1.5
High-side Parallel resonant capacitances, C_{p1} (μF)	0.116
Low-side Parallel resonant capacitances, C_{p2} (μF)	0.116
Load resistance, R_L (Ω)	4
Filter capacitance, C_f (μF)	100
Magnetising inductance, L_m (μH)	109
Transformer primary leakage inductance, L_{lp} (μH)	0.7
Transformer output leakage inductance, L_{ls} (μH)	0.1

In the proposed design, a half-bridge converter is used and the transformer turns ratios are chosen to be unity. To determine the resonant tank components, many trade-off issues are involved, as has been

discussed in Chapter 6. With this in mind, an experimental converter with a step-down capability has been commissioned with the measured component values given in Table 8.3. A ferrite 3F3 suitable for high frequency applications is used for the transformer core and resonant inductor. Leakage inductances are dependent on winding arrangement; therefore the secondaries are bifilar wound close to the core and beneath the primary to reduce secondary leakage.

The parallel resonant inductor is designed to be on the transformer primary side, such that L_p utilises the magnetising inductance, L_m, of the transformer. The effective series inductance comprises of the series inductor, L_s, and the primary leakage inductance, L_{lp}, and is measured to be 1.55μH. The transformer output networks have two identical inductances and the assignment of the polarity of the rectifier current is realised through winding orientation.

A comparison of output voltage obtained from the state-variable model (8-11, 8-29 and 8-32), simulated to steady state, with results from SPICE simulation results, is given in Fig. 8.17, from which clear discrepancies are clearly evident. In particular, there is a difference in resonant frequency, and the characteristic curve becomes narrower—a feature that is attributable to the presence of non-zero transformer secondary leakage inductances. By incorporating the effects of leakage into the state-variable model (8-11, 8-29 and 8-32), the predicted output voltages of the converter are modified to those shown in Fig. 8.18, which again include SPICE simulation results, along with measurements from the prototype converter, for comparison purposes. An improved correlation between the theoretical predictions and the experimental data, is clearly evident.

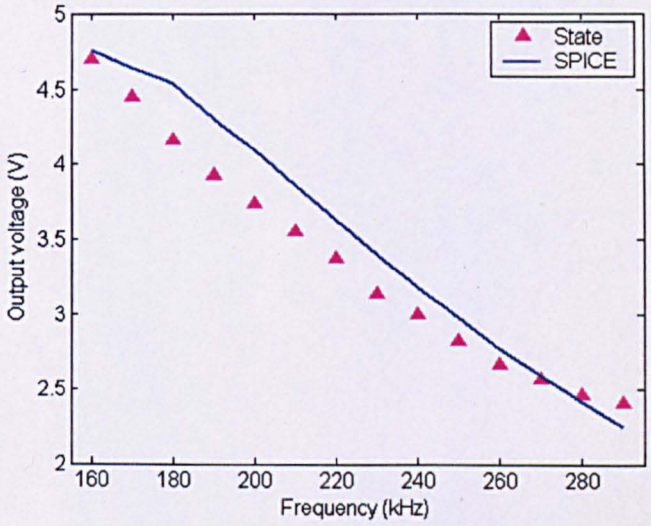

Figure 8.17 Output voltages vs. switching frequency.

A comparison of the estimated and measured control characteristics, when duty ratio control is employed, has also been obtained for various, fixed, operating frequencies viz. f_s=150 kHz, 170 kHz. The results are shown in Figs. 8.19 and 8.20, from where it can be seen that the proposed state variable model provides sufficient accuracy for design and analysis purposes, with a maximum error of 10%. The minimum duty ratio at f_s=150 kHz is selected to be 25% to prevent the converter from entering capacitive conduction mode. Furthermore, observation from Fig. 8.19 and 8.20 shows that the relative output voltage V_{out1}/V_{out2} when the input voltage duty ratio is reduced to 30%, is 1.375 at 150 kHz (closer to resonant frequency), compared to 1.297 at 170 kHz (further away from resonant frequency), thereby confirming the initial performance estimation of Fig. 8.7.

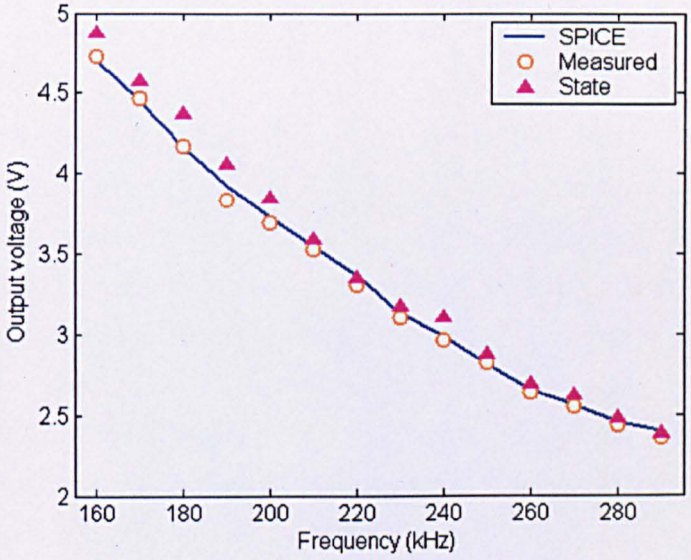

Figure 8.18 Comparison of output voltages.

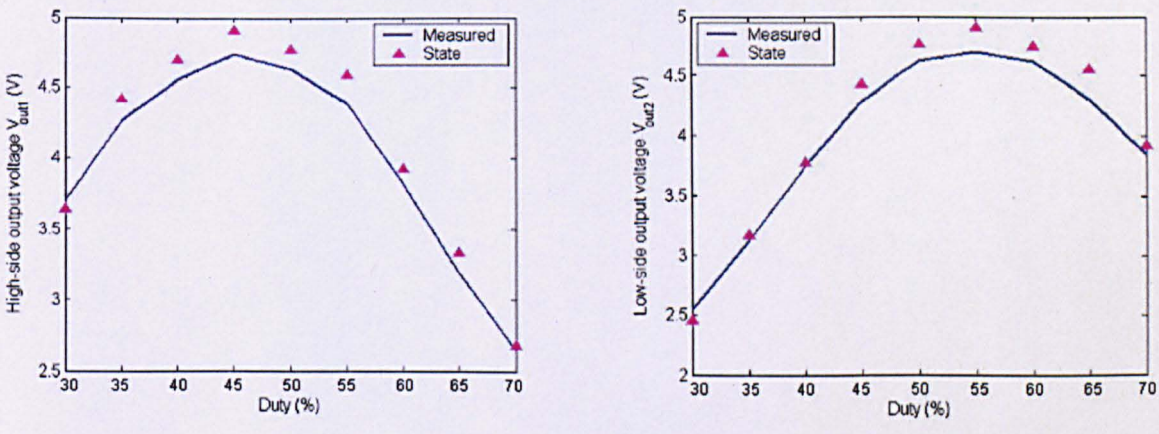

(a) (b)

Figure 8.19 Control characteristic curves for f_s=150 kHz (a) High-side output and (b) Low-side output.

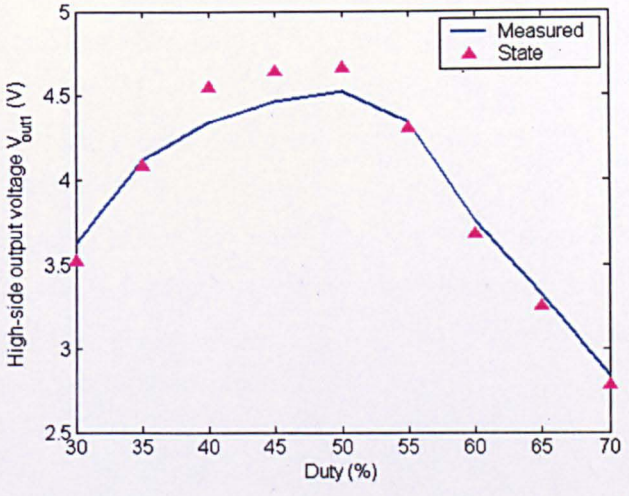

(a)

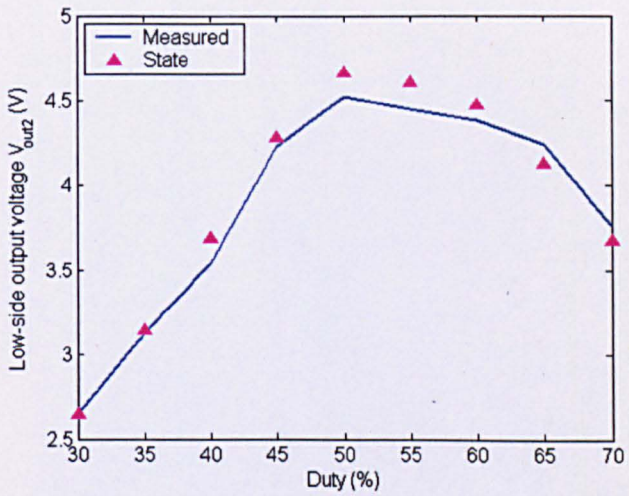

(b)

Figure 8.20 Control characteristic curves for f_s=170 kHz (a) High-side output and (b) Low-side output.

Typically, the open-loop output voltage magnitude characteristic of the converter is highly nonlinear above the resonant frequency, but can be linearised over a limited operating frequency range for controller design purposes. This can be seen from Fig. 8.21, which shows the magnitude characteristic for one of the converter outputs over a constrained frequency range. A similar approximation can also be used when a combination of f_s and duty-ratio control are applied. However, in either case, the remaining output is unregulated, or requires secondary-side post regulation to obtain the desired output.

Furthermore, Fig. 8.22 shows the output voltage V_{out1} against varying switching frequency, f_s. It can be seen that, under asymmetrical input voltage excitation (duty ratio control), a higher output voltage, and power, can be transferred to one individual output (V_{out1} in this case) compared to the magnitude of output voltage obtained with a 50% duty. Therefore, if the duty ratio is to be shifted at each switching frequency, along the control characteristic curve, a voltage boosting effect can be obtained, which is most significant at, or about, the effective resonant frequency. As the switching frequency moves away from resonance, voltage boosting performance deteriorates, and a greater separation between the output voltages cannot be maintained.

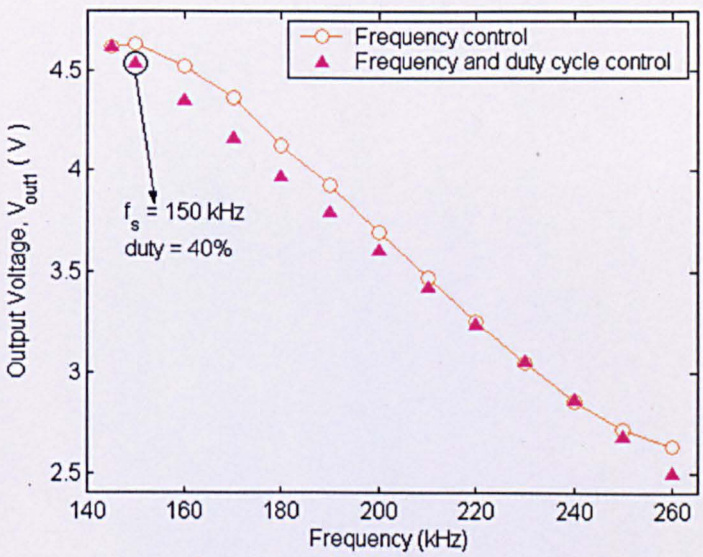

Figure 8.21 Linear regulation of output voltage V_{out1}.

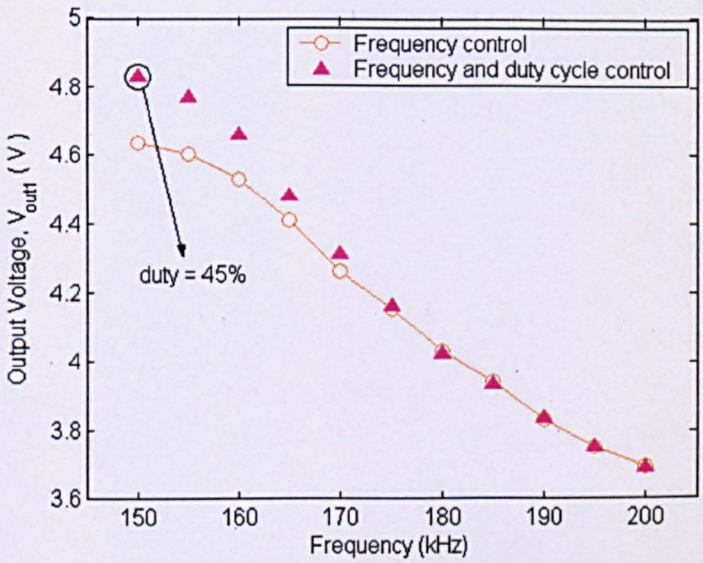

Figure 8.22 Voltage boosting of output V_{out1}.

8.5. Closed-loop Control and Experimental Realisation

A digital controller is proposed to regulate the output voltage when subjected to load and input voltage disturbances. Resonant converters are traditionally controlled using one of two methodologies a) constant frequency operation with pulse-width modulation (PWM) [H11], or b) square-wave, variable-frequency control [H9, H10]. Control using PWM is often preferred since optimization of the output filter for a ripple voltage at the output can be achieved at constant frequency. Conversely, for operation over a wide load range, voltage regulation of the output becomes problematic, particularly for low loads, where the PWM duty has a minimum on-state value, and frequency control may then be preferred.

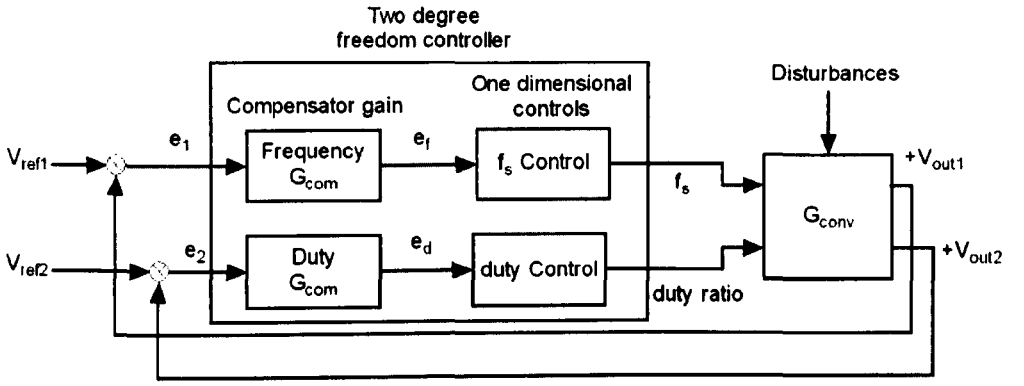

Figure 8.23 Closed-loop control of the dual-load resonant converter.

Results of the possible output voltage distributions available from the dual-output converter, Figs. 8.7 and 8.13, have demonstrated the dependence of the output voltages on both the duty-ratio and switching frequency. The objective, for control purposes, is to force the converter outputs to the set points in the presence of line voltage and load disturbances.

Figure 8.23 shows the structure for the proposed controller, employing two decoupled feedback loops for independent control of frequency and duty-ratio. Voltage feedback modulation is employed to avoid the need for relatively expensive current sensors, and the control structures are based on linear Proportional and Integral (PI) schemes, as a proof of principle. For design purposes, the output voltage vs. switching frequency and duty-ratio characteristics of the converter, are approximated to be linear over the frequency range of interest.

Although various methodologies could be considered for the design of the PI gains, the controller parameters have been selected empirically for robust tracking of the reference. In this case, effective

bandwidths for the decoupled SISO controllers: K_{p_f}=10, K_{i_f}=30, K_{p_d}=2 and K_{i_d}=10 have been chosen for good transient response and disturbance rejection. Notably, the digital compensator is tuned to respond quickly to variations of V_{out1}, whilst the controller reacting to variations of V_{out2}, acts relatively slowly—thereby effectively decoupling the interaction of the control loops. The switching frequency is restricted to values above the effective resonant frequency to maintain high efficiency operation.

A block diagram of the digitally-controlled converter is shown in Fig. 8.24, and comprises of a PIC18F452-based interface—an 8-bit fixed-point microcontroller that is optimized for low-cost, and integrates 10-bit analogue-digital converters with high sampling rates. The control outputs from the PIC microcontroller are the effective turn-ON and turn-OFF times of the power switches, which are latched into registers on a SPARTAN-2 FPGA. The FPGA is used to derive signals for switching of the power devices. Here, only the final controller design is presented—the reader is directed to Appendix C for in-depth information on implementation of the controller.

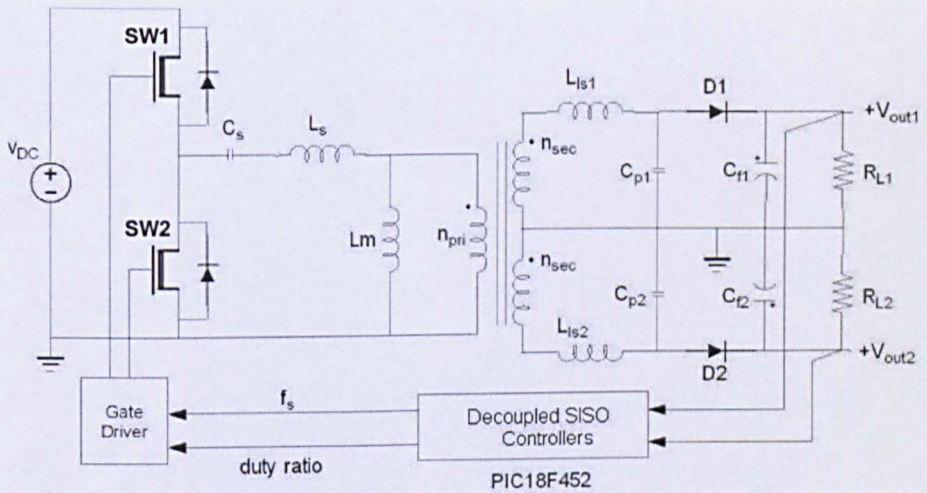

Figure 8.24 Schematic diagram of converter supplying +5V and +3.3V with controller.

The prototype converter (see Table 8.3 for parameters) should provide regulated +5V and +3.3V outputs from a DC-link input voltage in range 15V to 20V. The realisation of the converter along with control circuitry is shown in Fig. 8.25.

Investigations have been undertaken using an experimental setup that allows load changes within the range 3Ω to 6Ω, to be applied. Figure 8.26 shows the resulting steady-state error between the reference voltages, V_{ref1} and V_{ref2} and the resulting measured output voltages of the converter, over the specified range of DC-link input voltages (15V to 20V) with a 5Ω load.

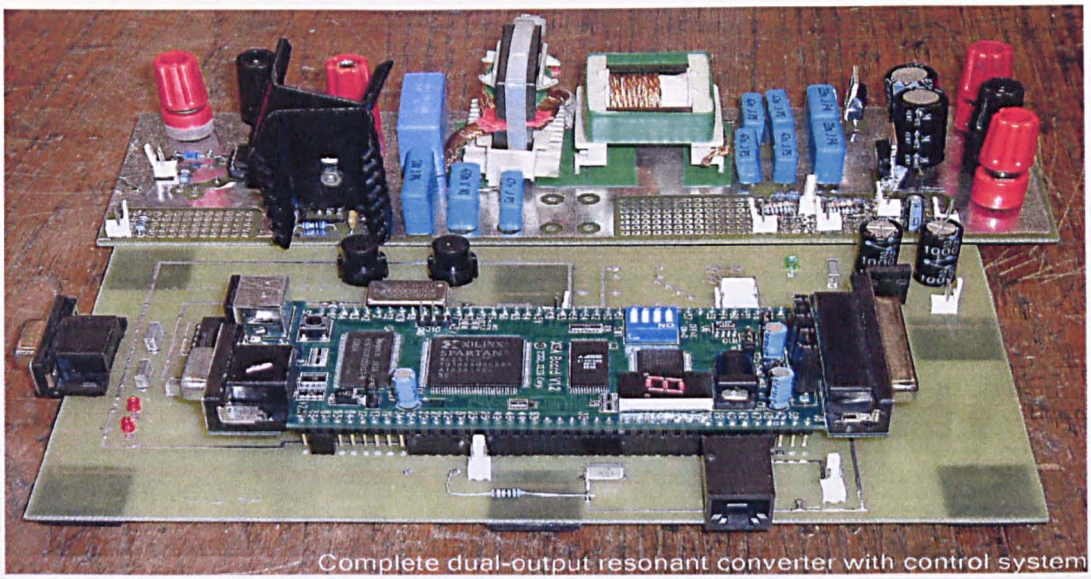

Figure 8.25 Practical realisation of digitally controlled 4th-order dual outputs resonant converter.

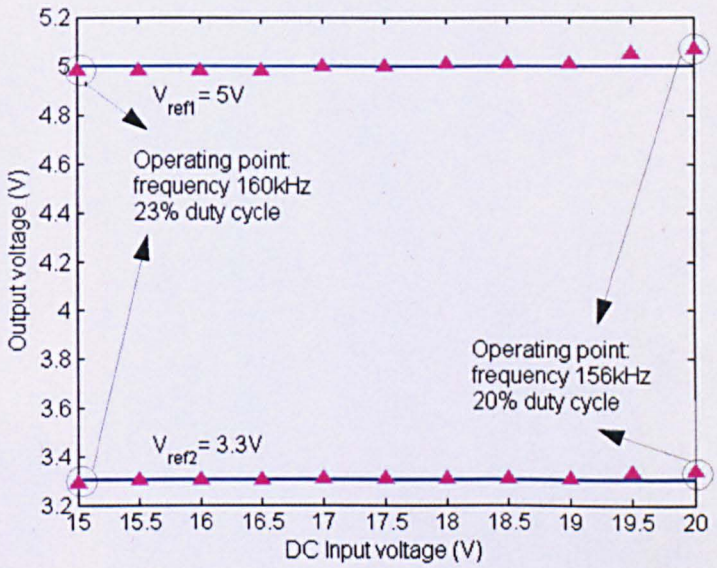

Figure 8.26 Output voltage regulation when subject to variations in input voltage.

It can be seen that the maximum regulation error for both outputs is <5%. For completeness, Fig. 8.27 shows example voltage- and current- waveforms when operating the converter with an input voltage of 15V, with a balanced transformer secondary, and an optimised output load resistance of R_L=4Ω. Moreover, Fig. 8.28 shows measured waveforms when the converter provides the asymmetrical output voltage distribution of +5V and +3.3V. As can be seen, from Fig. 8.28(a), for the balanced output loading case, controlled asymmetrical voltage distributions are achieved whilst maintaining Zero

Voltage Switching operation of the switching devices. Furthermore, decreasing the duty-ratio effectively facilitates a higher voltage to the output associated with the positive cycle of parallel capacitor voltage.

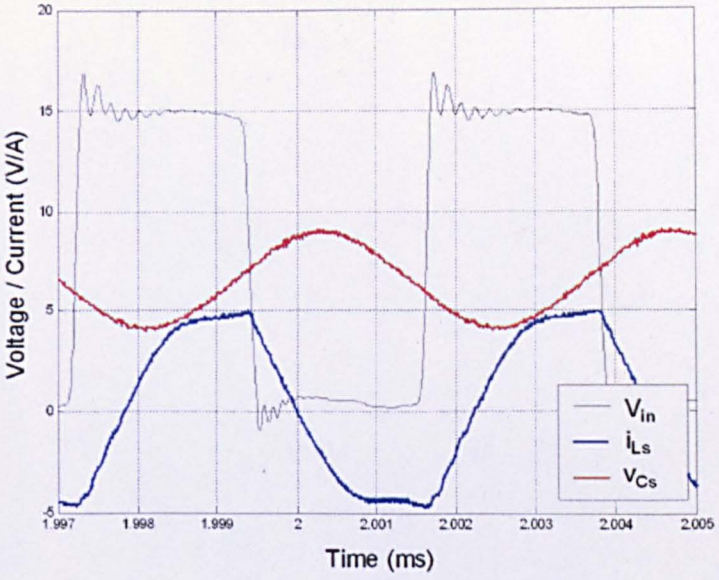

(a)

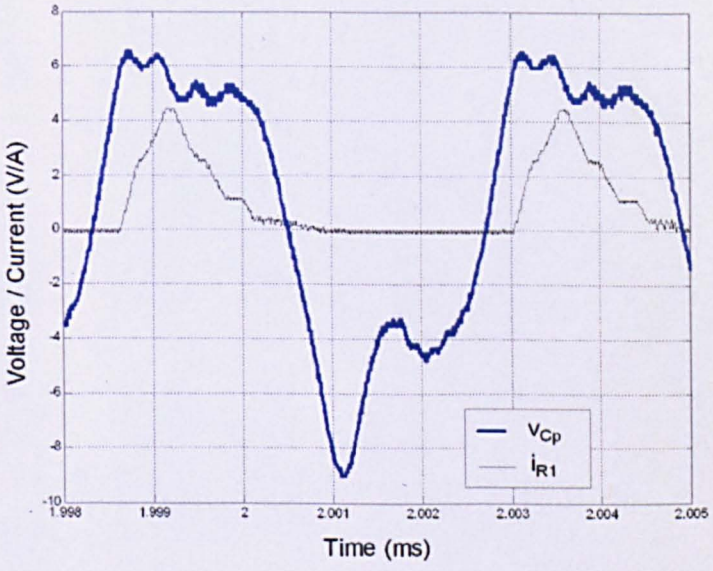

(b)

Figure 8.27 Measured waveforms: (a) input voltage and input current and series capacitor voltage and (b) parallel resonant capacitor voltage and rectifier input current.

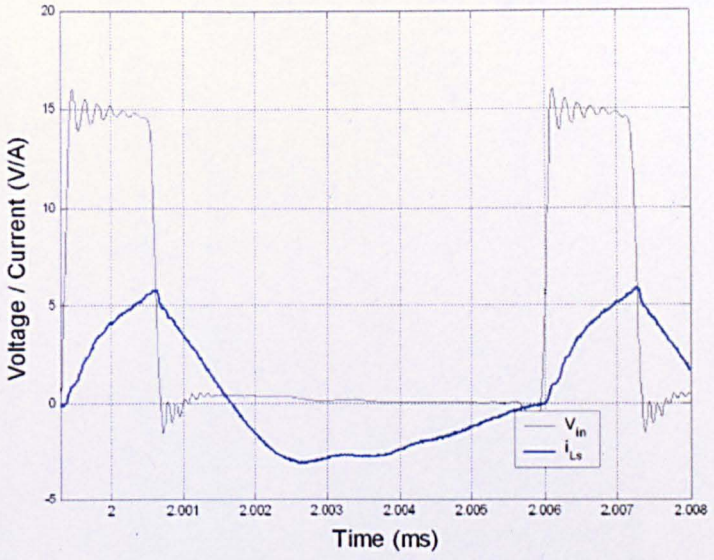

(a)

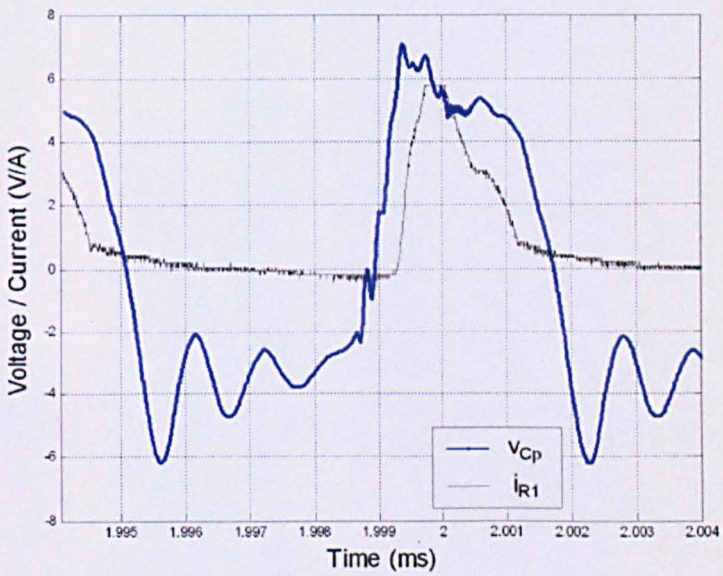

(b)

Figure 8.28 Measured waveforms at V_{out1}=+5V and V_{out2}=+3.3V: (a) input voltage and input current and (b) parallel resonant capacitor voltage and rectifier input current.

Figure 8.29 shows the resulting steady-state percentage regulation error between each output reference voltage, V_{ref1} and V_{ref2}, and the resulting measured output voltages, over the specified range of load resistances. Observation of the results shows that the design of the converter is optimised for 4Ω output resistance. When the output resistance is reduced, the input-to-output voltage conversion ratio decreases, and the measured output voltages are less than their respective reference values, and the percentage error is therefore negative. When subject to lighter load conditions, the regulation error increases on both outputs with the highest error being observed when R_{L1}= 6Ω. Again, this agrees with our investigations in Section 8.4, where greater output voltage distributions are only attainable at low load quality factor.

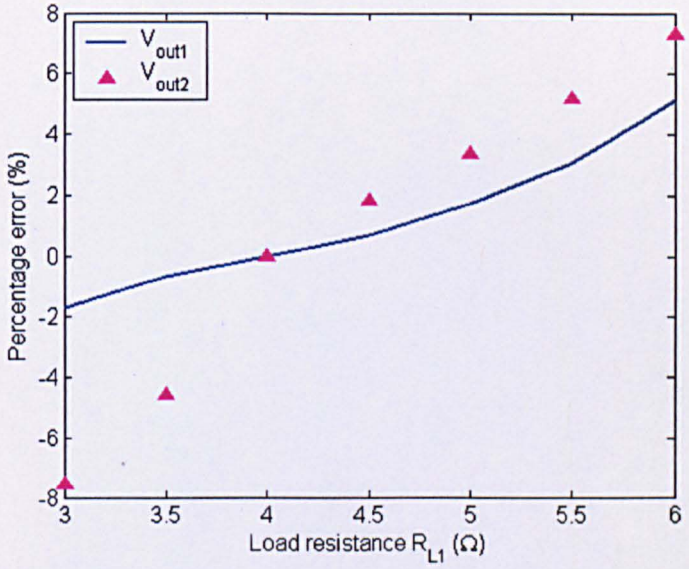

Figure 8.29 Regulation errors when subject to variations in load resistance.

Figure 8.30 shows example voltage- and current-waveforms from the state-variable model derived in Section 8.4, simulated to steady-state with parameters corresponding to those of the converter measurements in Figs. 8.27 and 8.28 (see Table 8.3 for converter's parameters). A comparison of the results shows that the model provides extremely good predictions of behaviour (notably, however, the frequency required to achieve the +5V and +3.3V output distribution, using the simulation model, is 160 kHz, compared to 155 kHz for the measured results).

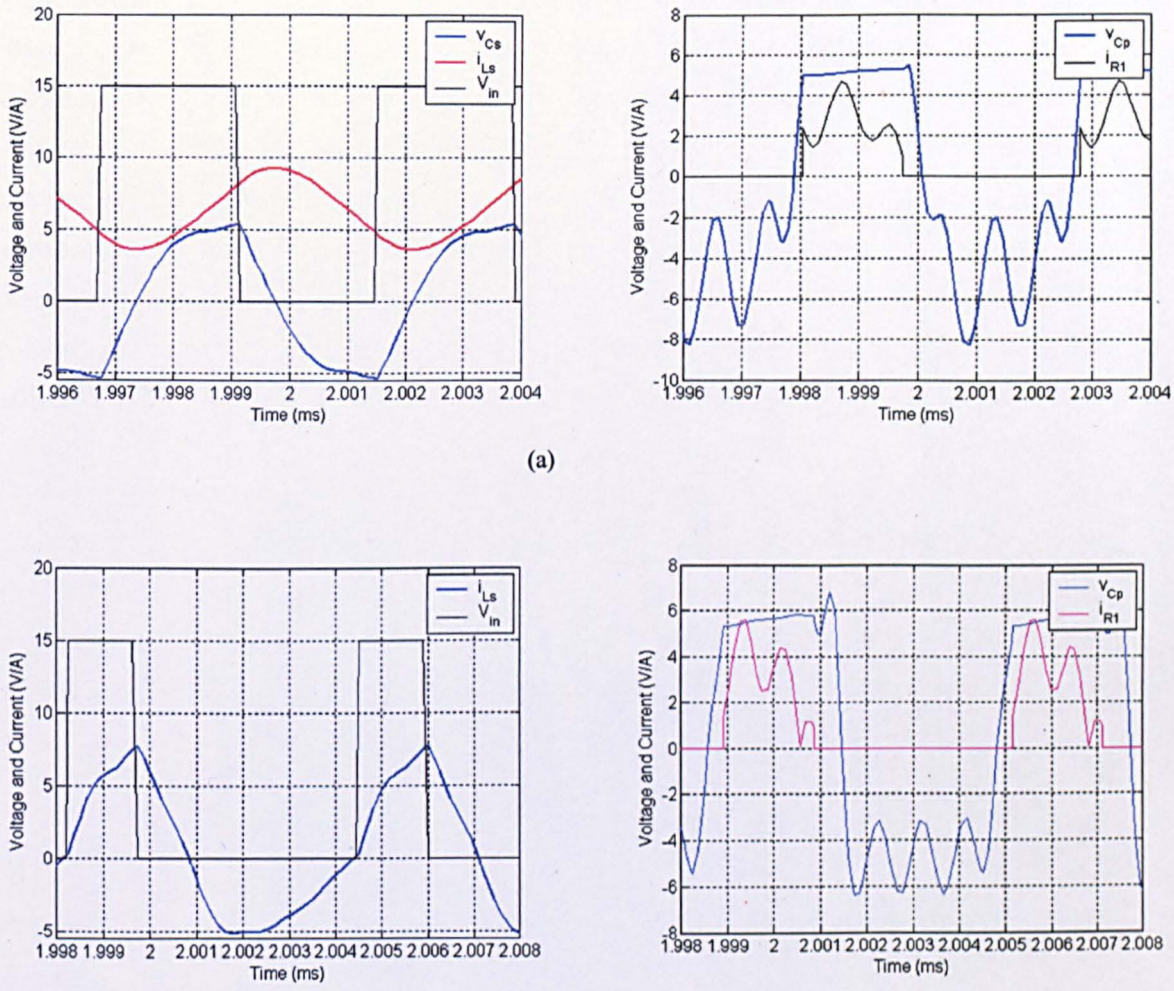

Figure 8.30 Steady state waveforms from the simulation model of the converter with balanced outputs with (a) symmetrical and (b) asymmetrical duty ratios.

To further demonstrate the versatility of the closed-loop dual-output converter, the compensator is designed to operate over a wider range of output voltage distributions, as shown in Fig. 8.31, whilst fixing the output voltage across load R_{L1} to 5V. Both outputs are frequency and duty ratio regulated while maintaining the stabilized output voltage on V_{out1} at 5V. It can be seen that the output voltage on the second output varies almost linearly with increasing frequency.

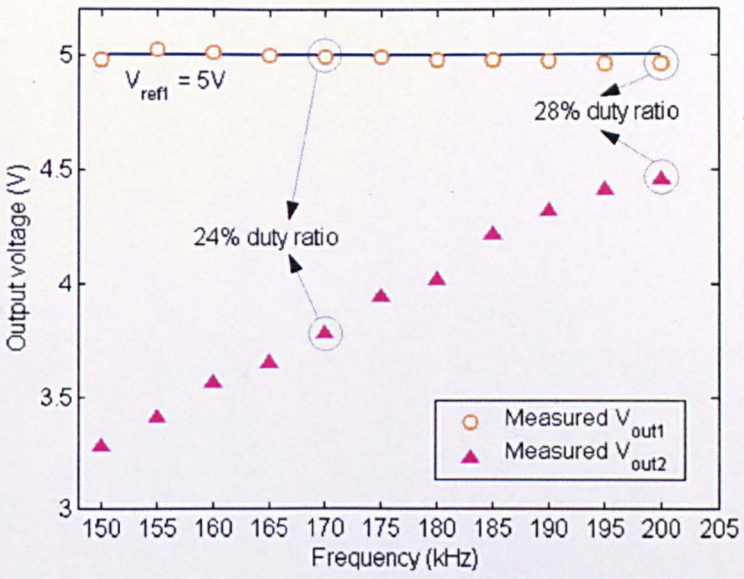

Figure 8.31 Output voltage distributions at constant load and constant $+V_{out1}$.

Figure 8.32 shows the response of the converter resulting from transient start-up conditions, for a range of applied input voltages and output voltage distributions. It can be seen that the converter voltages converge rapidly to the reference values, with an initial overshoot of ~10%. The overshoot is attributable to initial saturation of the integral action of the controller. Nevertheless, the response of the controller is deemed satisfactory in each case.

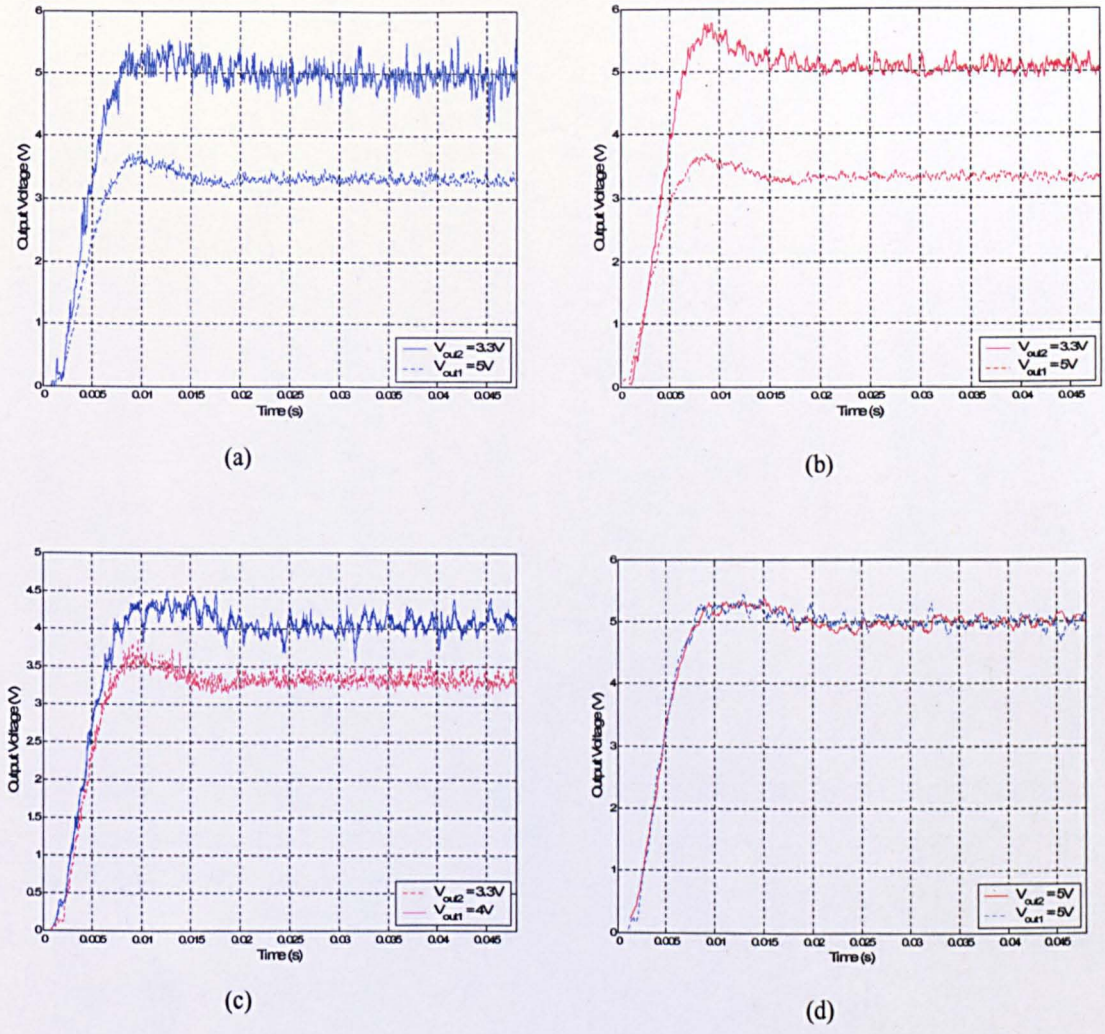

Figure 8.32 Start-up transient response for various combinations of output voltage distributions and DC-link input voltages (a) v_{DC}=15V, V_{out1}=5V, V_{out2}=3.3V; (b) v_{DC}=20V, V_{out1}=5V, V_{out2}=3.3V; (c) v_{DC}=12V, V_{out1}=4V, V_{out2}=3.3V; (d) v_{DC}=12V, V_{out1}=5V, V_{out2}=5V.

8.6. Summary

The characteristics of the dual-load, 4th-order LCLC voltage-output resonant converter, have been explored. Two state-variable models have been derived, with the latter incorporating the effects of transformer leakage inductance to improve prediction accuracy.

It has been demonstrated that the two outputs of the converter can be independently regulated to provide asymmetrical output voltage distributions. A comparison of measurements from a prototype converter, capable of delivering 5V and 3.3V suitable for a standard electronic supply, with those from a derived state-variable model, and SPICE simulations, shows that the model provides accurate

predictions of output voltage under steady state conditions. Moreover, a basic control scheme is shown to allow reliable regulation of both outputs under transient start-up conditions.

References

[H1] C. Ji and K. M. Smedley, "Cross Regulation in Flyback Converters: Analytic Model", in *IEEE Power Electronics Specialists Conference Rec.*, 1999, pp. 920-925.

[H2] Q. Chen, F. C. Lee and M. M. Jovanovic, "Dynamic characteristics of multiple-output buck-type converters with weighted voltage control", in *IEEE International Telecommunications Energy Conference Proc.*, 1994, pp. 435-442.

[H3] Q. Chen, M. M. Jovanovic and F. C. Lee, "Small-signal modeling and analysis of current-mode control for multiple-output forward converters", in *IEEE Power Electronics Specialists Conference Rec.*, 1994, pp. 1026-1033.

[H4] Q. Chen, F. C. Lee and M. M. Jovanovic, "Analysis and design of weighted voltage-mode control for a multiple-output forward converter", in *IEEE Applied Power Electronics Conference Proc.*, 1993, pp. 449-455.

[H5] Q. Chen, F. C. Lee and M. M. Jovanovic, "Small-signal analysis and design of weighted voltage-mode control for a multiple-output forward converter", in *IEEE Power Electronics Specialists Conference Rec.*, 1993, pp. 749-756.

[H6] L. Balogh, *Design Review: 140W, Multiple output high density DC/DC converters*, Texas: Texas Instruments Incorporated, 2001.

[H7] J. P. Agrawal, "Determination of Cross Regulation in Multi output Resonant Converters", *IEEE Trans. on Aerospace and Electronic Systems*, 36, pp.760-772, 2000.

[H8] J.P. Agrawal and I. Batarseh, "Improving the Dynamic Modeling and Static Cross Regulation in Multi-Output Resonant Converters", in *IEEE Applied Power Electronics Conference Proc.*, 1993, pp. 65-70.

[H9] I. Batarseh, R. Liu, C. Q. Lee, A. K. Upadhyay, "150 Watts and 140 kHz multi-output LCC-type parallel resonant converter", in *IEEE Applied Power Electronics Conference and Exposition Proc.*, 1989, pp. 221 -230.

[H10] I. Batarseh and C. Q. Lee, "Multi-Output LLCC-type Parallel Resonant Converter", in *IEEE Industrial Electronics Society Conference Proc.*, 1990, pp. 850-856.

[H11] I. Batarseh and K. Siri, "LLC-type series resonant converter with PWM control", *IEE Proc. Circuits, Devices and Systems*, 2, pp. 73-81, 1994.

[H12] R. Elfrich and T. Duerbaum, "A New Load Resonant Dual-Output Converter", in *IEEE Power Electronics Specialists Conference Rec.*, 2002, pp. 1319-1324.

[H13] Y. Ang, C. M. Bingham, M. P. Foster, D. A. Stone and D. Howe, "Design Orientated Analysis of 4th-Order LCLC Converters with Capacitive Output Filter", *IEE Proc. Electric Power Applications*, **152**, pp. 310-322, 2005.

[H14] Y. Ang, M. P. Foster, C. M. Bingham, D. A. Stone, H. I. Sewell and D. Howe, "Analysis of 4th-order LCLC Resonant Power Converters", *IEE Proc. Electric Power Applications*, **151**, pp. 169-181, 2004.

CHAPTER 9

Conclusions and Future Work

9.1. Conclusions

The thesis has developed novel techniques to facilitate rapid design and analysis of the behavioral characteristics of 4th-order LCLC resonant converters. Both frequency- and time-domain techniques have been explored, and their application demonstrated on candidate converter applications viz. a novel electrode-less fluorescent lamp electronic ballast, and a dual-output resonant power supply.

The derivation and verification of frequency domain models for the steady-state analysis of current-output LCLC converters, has been presented. An input-output transfer function, for which classical ac-analysis can be applied to analyse the frequency response of the converter, is derived, as a function of standard normalised parameters i.e. C_n, L_n, λ_r , ω_{op1} and Q_{op1}. A comparative study using results from SPICE simulations is used to demonstrate the accuracy of the model to predict the converter's output voltage characteristic, and, crucially, to estimate peak voltage and current stresses on the resonant components and switching devices. It must noted that the transient stress is higher than the estimated steady state value, and could potentially be destructive to resonant tank capacitors. Therefore, a designer should be aware of the limitation of cyclic prediction, and take extra precaution when dealing with voltage stress. Time-domain state-variable modelling could be used to assess the transient voltage stress and to select appropriate component rating, after a desired converter design is finalised. FMA based analysis is known to be applicable for light load operating conditions, above the resonant frequency. However, the behaviour of the current-output converter, under heavy load conditions, has also been considered, and boundary conditions between Continuous Conduction Mode (CCM) and Discontinuous Continuous Mode (DCM), analytically determined.

Features associated with multi-resonance behaviour, for the two resonant peaks identified for 4th-order converters, have been explored, and operation of the resonant converter around the secondary resonant peak, is advised, in order to faciltate a reduction in switching losses and operation at improved power factor. Closer examination of the voltage and current transfer functions shows that only two ratios of resonant tank elements (C_n and L_n) are needed for design purposes, even though four tank elements are

ultimately employed in realisation of an LCLC converter. Component values for the four tank elements are readily obtained from the presented design procedure. In addition to designing a current-output LCLC converter, the underlying design equations are also useful for analying and designing converters encompassing a single resonant frequency—specifically, the LCC series-parallel resonant converter and the LLC parallel resonant converter.

The capacitor–loaded 4th-order resonant power converter is normally employed to overcome the requirement for a bulky and lossy filter inductor at the supply output, thereby further improving the power density. A key feature of such converters, however, is the discontinuous resonant capacitor voltage (v_{Cp}), that greatly complicates the analysis. A methodology based on a set of describing functions that model the complex interaction between the parallel capacitor and rectifier/output-filter, are therefore developed. In particular, in addition to the classical single-resistor FMA approximation of the rectifier/output filter, an extended equivalent circuit for the LCLC voltage-output converter, is derived, that incorporates an additional capacitance in series with a resistor to account for the coupling/decoupling effects that arise from the rectifier conduction/non-conduction periods. Predictions of output voltage against a range of switching frequencies, for various load conditions, are compared with measurements on a prototype converter, and with results from SPICE simulations, with excellent agreement been shown throughout.

Although, the voltage-output LCLC converter has demonstrable advantages over the current-output variant, it is notable from the presented analysis, that the effective resonant point of the overall circuit varies with load quality factor. This can be a disadvantage from a control perspective since a wider range of switching frequencies is required to regulate the output, particularly if the converter is operated over an extended load range. Additionally, the converter incurs high-ripple currents at the output filter capacitance, rendering the converter less suited to low-voltage, high-current applications.

The proposed analysis methodologies, which are demonstrated to provide prediction accuracy comparable to that of SPICE, are eminently suitable for routine use during the design of high-order LCLC converters, due to the resulting low computational overhead. The presented describing functions have therefore also been employed to facilitate the derivation of 4-design synthesis methodologies, each satisfying different user-defined design constraints. Conditions under which each methodology might be employed, and the qualities they subsequently impart to a converter design, are also discussed.

As previously noted, large-signal simulation studies are a powerful supplement to conventional frequency domain design methodologies, to establish transient behavioural characteristics and sensitivities prior to finalising circuit designs. State-variable models of 4^{th}-order resonant converters are therefore developed as an alternative tool, to SPICE and SABER simulation packages, for both current- and voltage-output converters. The exclusion of an inductor (L_f) in the output filter network is shown to complicate circuit operation, analysis and simulation of the voltage-output converter.

Prototype converters have been commissioned to investigate the accuracy of the resulting models—their accuracy being proven to be commensurate with SPICE models, albeit requiring lower execution times. Compared to previously reported large signal models for resonant circuit evaluation, the model developed in the present work has the following merits:

1. *Wide range of validity* – The model is valid for simulation of both voltage- and current-output converters, over a wide range of power levels.
2. *Realistic* – Circuit physical phenomena including ESR can be included in the model and the effects reliably simulated.
3. *Self-consistent* – The model takes arbitrary input parameters such as input voltage, frequency, capacitance and inductance values.
4. *Rapid Simulation* – The model is proven to have at least 10× faster execution speed compared to SPICE.

Although the developed large-signal state-variable models are demonstrated to provide very accurate transient time-domain solutions, they remain computational expensive, which is often a key impediment the use of such techniques in a rapid interactive design environment.

A methodology based on cyclic-mode analysis, and its subsequence averaging technique, to facilitate rapid steady-state analysis, is therefore developed, for both converter variants, and the resulting virtues demonstrated by comparing predictions with experimental measurements. From the underlying state-variable modelling principles, dynamic matrices for each operating mode, are derived, and analytical formulae employed to estimate the mode duties for operation in both CCM and DCM. The subsequent peak electrical stresses are also estimated using extensions to the cyclic-analysis methods. The accuracy of the proposed analysis methodologies has also been demonstrated by comparisons with practical measurements, SPICE simulations and the results from non-linear state variable models, and

are shown to require significantly less computation overhead at the expense of only obtaining steady-state solutions.

For cyclic analysis purpose, although the describing functions technique presented in Chapter 6 provides convenient mechanism for estimating the switching transition times, the sinusoidal waveform assumptions, along with neglecting the effect of the parallel resonant inductor current, i_{Lp}, can lead to inaccurate estimation of the rectifier non-conduction angle, which subsequently introduces significant errors on the cyclically predicted converter output voltage. A new method has therefore been proposed that relies on localised searches, and a refined iteration procedure for estimating the required mode duties. The method is shown to provide accurate duty estimates over a wide operating range, and also for converters that provide low output voltages, when the effect of the rectifier on-state voltage (v_{diode}), is significant.

Various synthesis techniques have been developed to provide a platform for realization of LCLC converters for candidate industrial applications. Specifically, an LCLC resonant ballast, operating at 2.63MHz, is considered, that is shown to facilitate capacitive discharge and appropriate filtering for EMI, with near-resonance switching at high load quality factor promoting high efficiency operation. The design utilizes the desirable characteristic of the 4th-order resonant topology, having a fixed resonant point, to operate the fluorescent tube at its nominal power rating, and provide a high ignition voltage at a pre-defined frequency. An approximation of the value of internal capacitance c_{tap} formed by the proximity of the copper tape, and fluorescent tube gas, is given, from which the required ignition voltage is calculated.

Finally, the development and characterisation of dual-load, 4th-order LCLC voltage-output resonant converters, have been explored. Two state-variable realisation techniques are investigated, with one incorporating the effects of transformer leakage inductance to improve prediction accuracy. It has been demonstrated that the two outputs of the converter can be independently regulated to provide asymmetrical output voltage distributions. A comparison of measurements from a prototype converter, capable of delivering 5V and 3.3V suitable for standard electronic supply, with those from a derived state-variable model, and SPICE simulations, shows that the model provides accurate predictions of output voltage under steady state conditions. Moreover, a digital control scheme is realised to allow good transient responses from both outputs under start-up conditions, and steady-state regulation.

9.2. Future Work

The author acknowledges that whilst the work presented in this thesis provides a comprehensive account of modelling and design methodologies for LCLC converters, there remains significant scope for future investigations.

To achieve high power density, low profile magnetic design for inductors and transformers, is critical. Integrated magnetics should therefore be considered. The most common problem of integrated magnetic structure is that they are not readily manufactured in low quantities with consistent properties. However, using the 4^{th}-order LCLC resonant converter topology, all the tank and transformer magnetics can be integrated into a single component, thereby making it more suitable for high product volume manufacture. An integrated magnetic design should also make the final structure of the converter easier to manufacture and mechanically more stable. Compared with designs using discrete components, a significant reduction on footprint can also be expected. Furthermore, the resonant capacitor could also be integrated into the magnetic structure using planar techniques. Such integration will provide additional benefits, including further reducing the volume and cost for passive components, less interconnection and better electrical performance.

Knowledge of the small signal characteristics of LCLC converters is essential for the optimal design of closed-loop feedback systems, to provide regulation of the converter output voltage when subjected to line voltage and output load variations, and have yet to be fully explored.

There is an emerging necessity for systems, such as those that are microprocessor based, for supply technologies that provide multiple outputs of values lower than 5V, for instance, in the 1.8-3.3V range, and perhaps lower in future, as a consequence of increased integration of logic into single monolithic substrates. In such cases, the rectifier stage can constitute the greatest source of power loss, since even Schottky diodes have a relatively large voltage drop at high current ratings. To circumvent such problems, and facilitate high efficiency operation, MOSFETs with low on-state resistance should be considered for synchronous rectification, to replace the diodes.

Although simulation using the control canonical form can be undertaken when analysing the dual output resonant converter, it incurs longer simulation time, as the model contains redundant state variables, with detriment to the application of the state-variable model as an interactive design tool. In order to abate this limitation, the augmented state space equation for v_{Lp}, due to each input should be

formulated in the observable canonical form. The application of this technique for the analysis and simulation of various complex resonant converters should be investigated in future research.

APPENDIX A

Describing Function Formulae for the Analysis of Voltage-Output Resonant Converters

Derivation of the output voltage from the voltage-output 4th-order resonant converter:

$$V_{out} = \frac{\hat{i}_{in} R_L}{\pi} \times (1 + \cos(\phi_c))$$

$$V_{out} = \frac{2R_L\left(\hat{i}_{in} - 2\pi(V_{out} + 2v_{diode})f_s C_p\right)}{\pi}$$

$$V_{out} = \frac{2R_L \hat{i}_{in}}{\pi} - \frac{4\pi R_L V_{out} f_s C_p}{\pi} - \frac{8\pi R_L v_{diode} f_s C_p}{\pi} \qquad \text{(A-1)}$$

$$V_{out}\left(1 + 4R_L f_s C_p\right) = \frac{2R_L\left(\hat{i}_{in} - 4\pi f_s C_p v_{diode}\right)}{\pi}$$

$$V_{out} = \frac{2R_L\left(\hat{i}_{in} - 4\pi f_s C_p v_{diode}\right)}{\pi\left(1 + 4R_L f_s C_p\right)}$$

The fundamental of the voltage across parallel capacitor C_p obtained by summing the contributions of voltage-charging/voltage-clamping components:

$$\begin{aligned}
v_{Cp(1)} &= v_{Cp_charge(1)} + v_{Cp_clamp(1)} \\
&= \frac{\hat{i}_{in}}{\pi^2 f_s C_p}\left[j e^{-j\phi_c} - \frac{\phi_c}{2} - j\frac{e^{-j2\phi_c}}{4} - j\frac{3}{4}\right] + \frac{\hat{i}_{in}}{\pi^2 f_s C_p}\left[- j e^{-j\phi_c}(1 - \cos(\phi_c))\right] \\
&= \frac{\hat{i}_{in}}{\pi^2 f_s C_p}\left[-\frac{\phi_c}{2} - j\frac{e^{-j2\phi_c}}{4} - j\frac{3}{4} + j e^{-j\phi_c}\left(\frac{e^{j\phi_c} + e^{-j\phi_c}}{2}\right)\right] \\
&= \frac{\hat{i}_{in}}{\pi^2 f_s C_p}\left[-\frac{\phi_c}{2} + j\frac{e^{-j2\phi_c}}{4} - j\frac{1}{4}\right] \qquad \text{(A-2)} \\
&= \frac{\hat{i}_{in}}{4\pi^2 f_s C_p}\left[-2\phi_c + j e^{-j2\phi_c} - j\right] \\
&= \frac{\hat{i}_{in}}{4\pi^2 f_s C_p}\left[-2\phi_c + j(\cos(2\phi_c) - j\sin(2\phi_c)) - j\right] \\
&= \frac{\hat{i}_{in}}{4\pi^2 f_s C_p}\left[\sin(2\phi_c) - 2\phi_c + j(\cos(2\phi_c) - 1)\right]
\end{aligned}$$

Input impedance, Z_{in} of the RTFMA equivalent circuit:

$$
\begin{aligned}
Z_{in} &= j\omega_s L_s + \frac{1}{j\omega_s C_s} + \frac{1}{\left(-\omega_s{}^2 L_p C_e + \left(j\omega_s C_e \Re_e + 1\right) \Big/ \left(j\omega_s L_p - \omega_s{}^2 L_p C_e \Re_e\right)\right)} \\
&= \frac{-\dfrac{\omega_s{}^2 L_s C_e}{j\omega_s C_e \Re_e + 1} + \dfrac{L_s}{L_p} + \dfrac{C_e}{C_s\left(j\omega_s C_e \Re_e + 1\right)} - \dfrac{1}{\omega_s{}^2 C_s L_p} + 1}{\left(\left(-\omega_s{}^2 L_p C_e + j\omega_s C_e \Re_e + 1\right) \Big/ \left(j\omega_s L_p - \omega_s{}^2 L_p C_e \Re_e\right)\right)} \\
&= \frac{-\dfrac{2\pi\omega_s{}^2 L_s C_p \Big/ \left(2\phi_c - \sin(2\phi_c)\right)}{j\left(\left(1-\cos(\phi_c)\right) \Big/ \left(2\phi_c - \sin(2\phi_c)\right)\right) + 1} + \dfrac{L_s}{L_p} + \dfrac{2\pi C_p \Big/ \left(2\phi_c - \sin(2\phi_c)\right)}{C_s\left(j\left(\left(1-\cos(\phi_c)\right) \Big/ \left(2\phi_c - \sin(2\phi_c)\right)\right) + 1\right)} - \dfrac{1}{\omega_s{}^2 C_s L_p} + 1}{\left(\left(\dfrac{-2\pi\omega_s{}^2 L_p C_p}{2\phi_c - \sin(2\phi_c)} + j\left(\left(1-\cos(\phi_c)\right) \Big/ \left(2\phi_c - \sin(2\phi_c)\right)\right) + 1\right) \Big/ \left(j\omega_s L_p - \omega_s L_p\left(\left(1-\cos(\phi_c)\right) \Big/ \left(2\phi_c - \sin(2\phi_c)\right)\right)\right)\right)} \\
&= \frac{-\left(\dfrac{2\pi C_n \Big/ \left(2\phi_c - \sin(2\phi_c)\right)}{j\left(\left(1-\cos(\phi_c)\right) \Big/ \left(2\phi_c - \sin(2\phi_c)\right)\right) + 1}\right)\left(\dfrac{\omega_s{}^2}{\omega_{op1}{}^2}\right) + L_n + \dfrac{2\pi C_n \Big/ \left(2\phi_c - \sin(2\phi_c)\right)}{\left(j\left(\left(1-\cos(\phi_c)\right) \Big/ \left(2\phi_c - \sin(2\phi_c)\right)\right) + 1\right)} - L_n\left(\dfrac{\omega_{op1}{}^2}{\omega_s{}^2}\right) + 1}{\left(\left(\dfrac{-2\pi C_n}{\left(2\phi_c - \sin(2\phi_c)\right)L_n}\left(\dfrac{\omega_s{}^2}{\omega_{op1}{}^2}\right) + j\left(\left(1-\cos(\phi_c)\right) \Big/ \left(2\phi_c - \sin(2\phi_c)\right)\right) + 1\right) \Big/ \dfrac{R_L\omega_s}{Q_{op1}L_n\omega_{op1}}\left(j - \left(\left(1-\cos(\phi_c)\right) \Big/ \left(2\phi_c - \sin(2\phi_c)\right)\right)\right)\right)} \\
&= \frac{\dfrac{R_L\omega_s}{Q_{op1}L_n\omega_{op1}}\left[\begin{array}{l} -\left(2\pi C_n \Big/ \left(2\phi_c - \sin(2\phi_c)\right)\right)\left(\dfrac{\omega_s{}^2}{\omega_{op1}{}^2}\right) + jL_n\left(\left(1-\cos(\phi_c)\right) \Big/ \left(2\phi_c - \sin(2\phi_c)\right)\right) + L_n + \left(2\pi C_n \Big/ \left(2\phi_c - \sin(2\phi_c)\right)\right) \\ \quad - jL_n\left(\dfrac{\omega_{op1}{}^2}{\omega_s{}^2}\right)\left(\left(1-\cos(\phi_c)\right) \Big/ \left(2\phi_c - \sin(2\phi_c)\right)\right) - L_n\left(\dfrac{\omega_{op1}{}^2}{\omega_s{}^2}\right)\cdots \end{array}\right]}{\left(\dfrac{2j\pi C_n}{\left(2\phi_c - \sin(2\phi_c)\right)L_n}\left(\dfrac{\omega_s{}^2}{\omega_{op1}{}^2}\right) - j + \left(\left(1-\cos(\phi_c)\right) \Big/ \left(2\phi_c - \sin(2\phi_c)\right)\right)\right)} \\
&= \frac{\dfrac{R_L\omega_n}{Q_{op1}L_n}\left[\begin{array}{l} -C_n\omega_n{}^2\left(\dfrac{2\pi}{2\phi_c - \sin(2\phi_c)}\right) + L_n\left(1 - \dfrac{1}{\omega_n{}^2}\right) + C_n\left(\dfrac{2\pi}{2\phi_c - \sin(2\phi_c)}\right) + 1 \\ \quad + j\left[\dfrac{1-\cos(2\phi_c)}{2\phi_c - \sin(2\phi_c)} \cdot \left(L_n - L_n\left(\dfrac{1}{\omega_n{}^2}\right) - 1\right)\right] \end{array}\right]}{\dfrac{1-\cos(2\phi_c)}{2\phi_c - \sin(2\phi_c)} + j\left(\dfrac{2\pi\omega_n{}^2 C_n}{L_n\left(2\phi_c - \sin(2\phi_c)\right)} - 1\right)}
\end{aligned}
\tag{A-3}
$$

APPENDIX B

State Variable Modelling of Dual-load Converter

B.1. State-Space Modelling of a 2nd-Order Resonant Converter in Canonical Form

To demonstrate the application of the controllable canonical state-space realisation for modelling resonant converters, a basic 2nd-order LC parallel resonant converter, is initially considered.

The dynamic characteristics of the converter can be conveniently separated into fast- and slow-linear subsystems related by coupling equations. For the resonant topology considered, the fast subsystem comprises of the power switches and resonant tank components, whilst the slow subsystem is made up of the load and output filter. The coupling equation relating the two represents the non-linear behaviour of the rectifier. Fig. B.1 illustrates the use of partitioning on a 2nd-order CL parallel resonant converter. For the fast subsystem, the half bridge switches are replaced by an equivalent voltage source, V_{in}. Although rectifier is omitted, its influence on the fast subsystem is accounted for through the rectifier current, i_R. The slow subsystem represents the output filter/load, and the output voltage from the rectifier, v_f, is seen at the input to this sub-system.

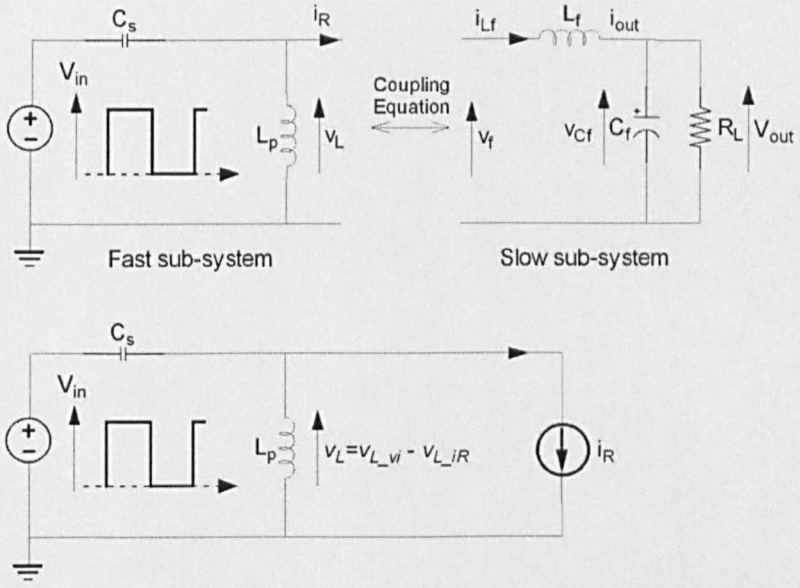

Figure B.1 State-variable representation of a 2nd-order CL resonant converter.

The differential equations describing the slow subsystem (L_f-C_f output filter and load R_L) are,

$$\dot{v}_{Cf} = \frac{i_{Lf}}{C_f} - \frac{v_{Cf}}{C_f R_L}$$
$$\dot{i}_{Lf} = \frac{v_f - v_{Cf}}{L_f} \tag{B-1}$$

Considering the voltage across the input and output of the rectifier, a coupling equation governing the action of the rectifier, can be derived.

$$v_f = |v_L| - 2v_{diode}$$
$$i_R = i_{Lf}\,\mathrm{sgn}(v_L) \tag{B-2}$$

In essence, the fast and slow subsystems can be represented by differential equations involving state variables and system inputs. The selection of state-variables is not a unique process. Various sets can be used. Some states are easier to derive, and others easier to work with, whilst some states may have physical significance. In Chapter 2, the resonant tank reactive components are described by state-variables that govern their actions. For instance, the voltage across the inductor L is governed by the rate of change of current through it; similarly for capacitor C, the current going through the capacitor is directly proportional to the rate of change of voltage across it. These rates of change become the state-variables, and when combined are used to describe the fast subsystem of the converter.

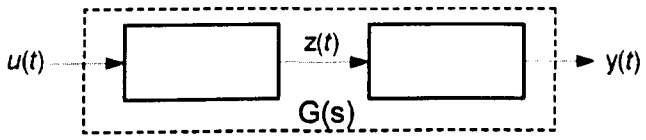

Figure B.2 Conceptual split of the SISO system into two blocks.

Conventional representation of single-input single-output (SISO) systems is given in terms of input-output differential equations and transfer function i.e.

$$y^n + a_1 y^{n-1} + \ldots a_{n-1}\dot{y} + a_n y = b_0 u^{n-1} + \ldots + b_{n-2}\dot{u} + b_{n-1}u \tag{B-3}$$

where

$$y^n = d^n y / dt^n$$
$$\mathrm{G(s)} = \frac{b_0 \mathrm{s}^{n-1} + \ldots + b_{n-2}\mathrm{s} + b_{n-1}}{\mathrm{s}^n + a_1 \mathrm{s}^{n-1} + \ldots a_{n-1}\mathrm{s} + a_n}$$

with input, $u(t)$ and output, $y(t)$.

Neglecting the dependency on time, t, for clarity, the continuous-time dynamic systems in (B-3) can be represented in state-space notation by considering the equation, which represents a third-order system:

$$\begin{aligned}&\frac{d^3y}{dt^3}+a_1\frac{d^2y}{dt^2}+a_2\frac{dy}{dt}+a_3y\\&=b_0\frac{d^2u}{dt^2}+b_1\frac{du}{dt}+b_2u\end{aligned} \tag{B-4}$$

By introducing an intermediate variable $z(t)$ such that the system, G(s) is conceptually split into two blocks, as illustrated in Fig. B.2, the intermediate variable $z(t)$ now becomes the input to the second block, to produce the output $y(t)$. Hence,

$$\begin{aligned}&\frac{d^3z}{dt^3}+a_1\frac{d^2z}{dt^2}+a_2\frac{dz}{dt}+a_3z=u\\&b_0\frac{d^2z}{dt^2}+b_1\frac{dz}{dt}+b_2z=y\end{aligned} \tag{B-5}$$

Applying inspection, the three first-order differential equations-state variables describing the third-order system can be conveniently written as,

$$\begin{aligned}&x_1=z\\&\dot{x}_1=x_2=\dot{z}\\&\dot{x}_2=x_3=\ddot{z}\end{aligned} \tag{B-6}$$

Differentiating x_3 yields,

$$\begin{aligned}&\frac{d^3z}{dt^3}+a_1\frac{d^2z}{dt^2}+a_2\frac{dz}{dt}+a_3z=u\\&\dot{x}_3=\dddot{z}=u-a_1x_3-a_2x_2-a_3x_1\end{aligned} \tag{B-7}$$

From (B-6) and (B-7), the state-space control canonical form, is given by a set of first-order differential equations–state equation and a set of single valued algebraic output equations–output equation.

$$\dot{\mathrm{x}}=\mathrm{A}_c\mathrm{x}+\mathrm{B}_cu \qquad y=\mathrm{C}_c\,\mathrm{x}+\mathrm{D}_cu \tag{B-8}$$

$$\mathrm{A}_c=\begin{bmatrix}0&1&0\\0&0&1\\-a_3&-a_2&-a_1\end{bmatrix}\quad \mathrm{B}_c=\begin{bmatrix}0\\0\\1\end{bmatrix}\quad \mathrm{C}_c=\begin{bmatrix}b_2&b_1&b_0\end{bmatrix}\quad \mathrm{D}_c=[0]$$

The first set of equations describes the dynamics of the system, and the second describes the measurements from the system. The advantage of the canonical form state-space realisation, in this case, is that it allows ordinary linear differential equations to be transformed into control canonical form by simple substitution of the differential equation coefficients into the dynamic state matrix, A_c and output matrix C_c.

The conversion can be performed by inspection of the input-output differential equations, ignoring the network theory relating inductor current and capacitor voltage. Despite this, the states of the companion form are not physically meaningful. From the perspective considered here, the internal states are not particularly important, as they are purely a matter of how we select the appropriate output variables required by the non-linear coupling equation.

The fast subsystem of the 2[nd]-order CL resonant converter now consists of the input voltage source, V_{in}, and rectifier current source, i_R. The input voltage source represents the periodic excitation of magnitude DC link input voltage at input signal frequency and duty cycle; the rectifier current couples the 'fast' subsystem to the 'slow' sub-system representing the output-filter and load. Considering each source independently, a set of input-output state-space differential equations, associated with fast sub-system, is given by (B-9).

$$G_{vi}(s) = \frac{v_{L\_vi}}{V_{in}} = \frac{s^2}{s^2 + 1/L_pC_s}$$

$$\frac{d^2 v_{L\_vi}}{dt^2} + \frac{v_{L\_vi}}{L_pC_s} = \frac{d^2 V_{in}}{dt^2} \qquad \text{(B-9)}$$

$$G_{iR}(s) = \frac{v_{L\_iR}}{i_R} = \frac{s/C_s}{s^2 + 1/L_pC_s}$$

$$\frac{d^2 v_{L\_iR}}{dt^2} + \frac{v_{L\_iR}}{L_pC_s} = \frac{1}{C_s}\frac{di_R}{dt}$$

The controllable canonical state-space form is obtained by introducing an intermediate variable $z(t)$ and, substituting (B-9) into (B6-B8):

$$\dot{x}_1 = \begin{bmatrix} 0 & -\frac{1}{L_pC_s} \\ 1 & 0 \end{bmatrix} x_1 + \begin{bmatrix} V_{in} \\ 0 \end{bmatrix} \qquad \dot{x}_2 = \begin{bmatrix} 0 & -\frac{1}{L_pC_s} \\ 1 & 0 \end{bmatrix} x_2 + \begin{bmatrix} i_R \\ 0 \end{bmatrix} \qquad \text{(B-10)}$$

Similarly, the output equation is given by,

$$v_{L\_vi} = \begin{bmatrix} 0 & -\dfrac{1}{L_p C_s} \end{bmatrix} \mathrm{x}_1 + V_{in} \qquad v_{L\_iR} = \begin{bmatrix} \dfrac{1}{C_s} & 0 \end{bmatrix} \mathrm{x}_2$$

$$v_L = v_{L\_vi} + v_{L\_iR} \tag{B-11}$$

Note, that in this particular realization of the system state has no direct physical value, and cannot be identified in Figure B1. The complete state-variable model with coupling equations, are therefore given in (B-12), and can be readily used in a MATLAB/SIMULINK environment to simulate the dynamics of the 2[nd]-order CL resonant converter.

$$\begin{bmatrix} \dot{\mathrm{x}}_1 \\ \dot{\mathrm{x}}_2 \end{bmatrix} = \begin{bmatrix} \mathrm{A}_c & 0 \\ 0 & \mathrm{A}_c \end{bmatrix} \begin{bmatrix} \mathrm{x}_1 \\ \mathrm{x}_2 \end{bmatrix} + \begin{bmatrix} V_{in} \\ 0 \\ i_R \\ 0 \end{bmatrix}$$

$$\mathrm{A}_c = \begin{bmatrix} 0 & -\dfrac{1}{L_p C_s} \\ 1 & 0 \end{bmatrix}$$

$$\begin{bmatrix} \dot{i}_{Lf} \\ \dot{v}_{Cf} \end{bmatrix} = \begin{bmatrix} 0 & -\dfrac{1}{L_f} \\ \dfrac{1}{C_f} & -\dfrac{1}{C_f R_L} \end{bmatrix} \begin{bmatrix} i_{Lf} \\ v_{Cf} \end{bmatrix} + \begin{bmatrix} \dfrac{v_f}{L_f} \\ 0 \end{bmatrix}$$

$$v_L = \begin{bmatrix} 0 & -\dfrac{1}{L_p C_s} \end{bmatrix} \mathrm{x}_1 + V_{in} + \begin{bmatrix} \dfrac{1}{C_s} & 0 \end{bmatrix} \mathrm{x}_2$$

$$v_f = |v_L| - 2v_{diode}$$

$$i_R = i_{Lf}\,\mathrm{sgn}(v_L) \tag{B-12}$$

B.2. Controllable Canonical State-Space Derivation of Augmented Parallel Inductor Voltage

Applying superposition theory, all the independent sources, except one, are removed—the fast sub-system is therefore given in Fig. 8.15, and can be inspected under the excitation of one source at a time. Removing the output rectifier current sources in parallel with resonant capacitors, C_{p1} and C_{p2}, the transfer function describing the relationship between voltage across parallel resonant inductor v_{Lp} and input voltage, V_{in}, can be found, as follows:

$$v_{Lp\_vi}(s)$$

$$= V_{in} \times \frac{\left(\dfrac{s^3 L_p L_{ls1} L_{ls2} + s\left(\dfrac{L_p L_{ls1}}{C_{p2}} + \dfrac{L_p L_{ls2}}{C_{p1}} \right) + \dfrac{L_p}{sC_{p1}C_{p2}}}{s^2\left(L_{ls1}L_{ls2} + L_p L_{ls2} + L_p L_{ls1} \right) + \left(\dfrac{L_{ls1}}{C_{p2}} + \dfrac{L_{ls2}}{C_{p1}} + \dfrac{L_p}{C_{p2}} + \dfrac{L_p}{C_{p1}} \right) + \dfrac{1}{s^2 C_{p1}C_{p2}}} \right)}{\left(sL_s + \dfrac{1}{sC_s} + \dfrac{s^3 L_p L_{ls1} L_{ls2} + s\left(\dfrac{L_p L_{ls1}}{C_{p2}} + \dfrac{L_p L_{ls2}}{C_{p1}} \right) + \dfrac{L_p}{sC_{p1}C_{p2}}}{s^2\left(L_{ls1}L_{ls2} + L_p L_{ls2} + L_p L_{ls1} \right) + \left(\dfrac{L_{ls1}}{C_{p2}} + \dfrac{L_{ls2}}{C_{p1}} + \dfrac{L_p}{C_{p2}} + \dfrac{L_p}{C_{p1}} \right) + \dfrac{1}{s^2 C_{p1}C_{p2}}} \right)}$$

$$= V_{in} \times \frac{s^6 L_p L_{ls1} L_{ls2} + s^4\left(\dfrac{L_p L_{ls1}}{C_{p2}} + \dfrac{L_p L_{ls2}}{C_{p1}} \right) + \dfrac{s^2 L_p}{C_{p1}C_{p2}}}{\left(\begin{array}{c} s^6\left(L_p L_{ls1} L_{ls2} + L_s L_p L_{ls2} + L_s L_p L_{ls1} + L_s L_p L_{ls2} \right) \\ + s^4\left(\dfrac{L_s L_{ls1}}{C_{p2}} + \dfrac{L_s L_{ls1}}{C_{p1}} + \dfrac{L_s L_p}{C_{p2}} + \dfrac{L_s L_p}{C_{p1}} + \dfrac{L_{ls1} L_{ls2}}{C_s} + \dfrac{L_p L_{ls2}}{C_s} + \dfrac{L_p L_{ls1}}{C_s} + \dfrac{L_p L_{ls1}}{C_{p2}} + \dfrac{L_p L_{ls2}}{C_{p1}} \right) \\ + s^2\left(\dfrac{L_s}{C_{p1}C_{p2}} + \dfrac{L_{ls1}}{C_s C_{p2}} + \dfrac{L_{ls1}}{C_s C_{p1}} + \dfrac{L_p}{C_s C_{p2}} + \dfrac{L_p}{C_s C_{p1}} + \dfrac{L_p}{C_{p1}C_{p2}} \right) + \dfrac{1}{C_s C_{p1} C_{p2}} \end{array} \right)} \tag{B-13}$$

Similarly, for the case when the circuit is excited by the 'high-side' output rectifier current source, i_{R1}, the input voltage source and 'low-side' rectifier current source i_{R2} is substituted with a 'short-circuit' and an 'open-state', respectively. The relevant Laplace domain transfer function for the input-output relationship, is given then by,

$$v_{Lp\_iR1}(s)$$

$$= i_{R1} \times \frac{s^3 L_s L_p L_{ls2} + s\left(\frac{L_p L_{ls2}}{C_s} + \frac{L_s L_p}{C_{p2}}\right) + \frac{L_s}{sC_s C_{p2}}}{s^2\left(L_s L_p + L_p L_{ls2} + L_s L_{ls2}\right) + \left(\frac{L_p}{C_s} + \frac{L_p}{C_{p2}} + \frac{L_s}{C_{p2}} + \frac{L_{ls2}}{C_s}\right) + \frac{1}{s^2 C_s C_{p2}}} \Bigg/ \left(1 + s^2 L_{ls1} C_{p1} + \frac{s^4 L_s L_p L_{ls2} C_{p1} + s^2\left(\frac{L_p L_{ls2} C_{p1}}{C_s} + \frac{L_s L_p C_{p1}}{C_{p2}}\right) + \frac{L_s C_{p1}}{C_s C_{p2}}}{s^2\left(L_s L_p + L_p L_{ls2} + L_s L_{ls2}\right) + \left(\frac{L_p}{C_s} + \frac{L_p}{C_{p2}} + \frac{L_s}{C_{p2}} + \frac{L_{ls2}}{C_s}\right) + \frac{1}{s^2 C_s C_{p2}}}\right)$$

$$= \frac{s^5 L_s L_p L_{ls2} + s^3\left(\frac{L_p L_{ls2}}{C_s} + \frac{L_s L_p}{C_{p2}}\right) + \frac{sL_s}{C_s C_{p2}}}{\left(\begin{array}{l} s^6\left(L_s L_p L_{ls1} C_{p1} + L_p L_{ls1} L_{ls2} C_{p1} + L_s L_{ls1} L_{ls2} C_{p1} + L_s L_p L_{ls2} C_{p1}\right) \\ + s^4\left(L_s L_p + L_p L_{ls2} + L_s L_{ls2} + \frac{L_p L_{ls1} C_{p1}}{C_s} + \frac{L_p L_{ls1} C_{p1}}{C_{p2}} + \frac{L_s L_{ls1} C_{p1}}{C_{p2}} + \frac{L_{ls2} L_{ls1} C_{p1}}{C_s} + \frac{L_p L_{ls2} C_{p1}}{C_s} + \frac{L_s L_p C_{p1}}{C_s}\right) \\ s^2\left(\frac{L_p}{C_s} + \frac{L_p}{C_{p2}} + \frac{L_s}{C_{p1}} + \frac{L_{ls2}}{C_s} + \frac{L_p C_{p1}}{C_s C_{p2}} + \frac{L_p C_{p1}}{C_s C_{p2}}\right) + \frac{1}{C_s C_{p2}} \end{array}\right)} \quad \text{(B-14)}$$

Employing superposition, therefore, the transfer function describing the relationship between the current flowing through parallel resonant capacitor, C_{p1}, and all independent sources V_{in}, i_{R1} and i_{R2} is given by,

$$i_{Cp\_vi}(s) = V_{in} \times \frac{s^4 L_p L_{ls2} + \frac{s^2 L_p}{C_{p2}}}{\left(\begin{array}{c} s^6\left(L_p L_{ls1} L_{ls2} + L_s L_p L_{ls2} + L_s L_p L_{ls1} + L_s L_p L_{ls2}\right) \\ + s^4\left(\frac{L_s L_{ls1}}{C_{p2}} + \frac{L_s L_{ls1}}{C_{p1}} + \frac{L_s L_p}{C_{p2}} + \frac{L_s L_p}{C_{p1}} + \frac{L_{ls1} L_{ls2}}{C_s} + \frac{L_p L_{ls2}}{C_s} + \frac{L_p L_{ls1}}{C_s} + \frac{L_p L_{ls1}}{C_{p2}} + \frac{L_p L_{ls2}}{C_{p1}} \right) \\ + s^2\left(\frac{L_s}{C_{p1} C_{p2}} + \frac{L_{ls1}}{C_s C_{p2}} + \frac{L_{ls1}}{C_s C_{p1}} + \frac{L_p}{C_s C_{p2}} + \frac{L_p}{C_s C_{p1}} + \frac{L_p}{C_{p1} C_{p2}} \right) + \frac{1}{C_s C_{p1} C_{p2}} \end{array} \right)}$$

$$i_{Cp\_iR1}(s) = i_{R1} \times \frac{\left(\begin{array}{c} s^5 L_s L_p L_{ls2} + L_s L_p L_{ls1} + L_p L_{ls1} L_{ls2} + L_s L_{ls1} L_{ls2} \\ s^3\left(\frac{L_p L_{ls2}}{C_s} + \frac{L_s L_p}{C_{p2}} + \frac{L_s L_{ls1}}{C_{p2}} + \frac{L_{ls1} L_{ls2}}{C_s} + \frac{L_p L_{ls1}}{C_s} \frac{L_p L_{ls1}}{C_{p2}} \right) + s\left(\frac{L_p}{C_s C_{p2}} + \frac{L_{ls1}}{C_s C_{p2}} \right) \end{array} \right)}{\left(\begin{array}{c} s^6\left(L_s L_p L_{ls1} C_{p1} + L_p L_{ls1} L_{ls2} C_{p1} + L_s L_{ls1} L_{ls2} C_{p1} + L_s L_p L_{ls2} C_{p1}\right) \\ + s^4\left(L_s L_p + L_p L_{ls2} + L_s L_{ls2} + \frac{L_p L_{ls1} C_{p1}}{C_s} + \frac{L_p L_{ls1} C_{p1}}{C_{p2}} + \frac{L_s L_{ls1} C_{p1}}{C_{p2}} + \frac{L_{ls2} L_{ls1} C_{p1}}{C_s} + \frac{L_p L_{ls2} C_{p1}}{C_s} + \frac{L_s L_p C_{p1}}{C_s} \right) \\ s^2\left(\frac{L_p}{C_s} + \frac{L_p}{C_{p2}} + \frac{L_s}{C_{p1}} + \frac{L_{ls2}}{C_s} + \frac{L_p C_{p1}}{C_s C_{p2}} + \frac{L_p C_{p1}}{C_s C_{p2}} \right) + \frac{1}{C_s C_{p2}} \end{array} \right)}$$

$$i_{Cp\_iR2}(s) = i_{R2} \times \frac{s^3 L_s L_p + \frac{s L_p}{C_s C_{p1}}}{\left(\begin{array}{c} s^6\left(L_s L_p L_{ls1} C_{p1} + L_p L_{ls1} L_{ls2} C_{p1} + L_s L_{ls1} L_{ls2} C_{p1} + L_s L_p L_{ls2} C_{p1}\right) \\ + s^4\left(L_s L_p + L_p L_{ls2} + L_s L_{ls2} + \frac{L_p L_{ls1} C_{p1}}{C_s} + \frac{L_p L_{ls1} C_{p1}}{C_{p2}} + \frac{L_s L_{ls1} C_{p1}}{C_{p2}} + \frac{L_{ls2} L_{ls1} C_{p1}}{C_s} + \frac{L_p L_{ls2} C_{p1}}{C_s} + \frac{L_s L_p C_{p1}}{C_s} \right) \\ s^2\left(\frac{L_p}{C_s} + \frac{L_p}{C_{p2}} + \frac{L_s}{C_{p1}} + \frac{L_{ls2}}{C_s} + \frac{L_p C_{p1}}{C_s C_{p2}} + \frac{L_p C_{p1}}{C_s C_{p2}} \right) + \frac{1}{C_s C_{p2}} \end{array} \right)}$$

(B-15)

A state-space canonical realisation of the classical transfer function can be achieved by first converting the prototype Laplace domain description into the relevant input-output differential form, as shown in (B-16), (B-17) and (B-18).

$$a_{40}\frac{d^6 i_{Cp\_vi}}{dt^6}+a_{41}\frac{d^4 i_{Cp\_vi}}{dt^4}+a_{42}\frac{d^2 i_{Cp\_vi}}{dt^2}+a_{43} i_{Cp\_vi}=b_{40}\frac{d^4 V_{in}}{dt^4}+b_{41}\frac{d^2 V_{in}}{dt^2}$$

$$a_{40}=L_pL_{ls1}L_{ls2}+L_sL_pL_{ls2}+L_sL_pL_{ls1}+L_sL_pL_{ls2}$$

$$a_{41}=\frac{L_sL_{ls1}}{C_{p2}}+\frac{L_sL_{ls1}}{C_{p1}}+\frac{L_sL_p}{C_{p2}}+\frac{L_sL_p}{C_{p1}}+\frac{L_{ls1}L_{ls2}}{C_s}+\frac{L_pL_{ls2}}{C_s}+\frac{L_pL_{ls1}}{C_s}+\frac{L_pL_{ls1}}{C_{p2}}+\frac{L_pL_{ls2}}{C_{p1}}$$

$$a_{42}=\frac{L_s}{C_{p1}C_{p2}}+\frac{L_{ls1}}{C_sC_{p2}}+\frac{L_{ls1}}{C_sC_{p1}}+\frac{L_p}{C_sC_{p2}}+\frac{L_p}{C_sC_{p1}}+\frac{L_p}{C_{p1}C_{p2}} \qquad \text{(B-16)}$$

$$a_{43}=\frac{1}{C_sC_{p1}C_{p2}}$$

$$b_{40}=L_pL_{ls2}$$

$$b_{41}=\frac{L_p}{C_{p2}}$$

$$a_{50}\frac{d^6 i_{Cp\_iR1}}{dt^6}+a_{51}\frac{d^4 i_{Cp\_iR1}}{dt^4}+a_{52}\frac{d^2 i_{Cp\_iR1}}{dt^2}+a_{53} i_{Cp\_iR1}=b_{50}\frac{d^5 i_{R1}}{dt^5}+b_{51}\frac{d^3 i_{R1}}{dt^3}+b_{52}\frac{di_{R1}}{dt}$$

$$a_{50}=a_{40}\quad a_{51}=a_{41}\quad a_{52}=a_{42}\quad a_{53}=a_{43}$$

$$b_{50}=L_sL_pL_{ls2}+L_sL_pL_{ls1}+L_pL_{ls1}L_{ls2}+L_sL_{ls1}L_{ls2} \qquad \text{(B-17)}$$

$$b_{51}=\frac{L_pL_{ls2}}{C_s}+\frac{L_sL_p}{C_{p2}}+\frac{L_sL_{ls1}}{C_{p2}}+\frac{L_{ls1}L_{ls2}}{C_s}+\frac{L_pL_{ls1}}{C_s}\frac{L_pL_{ls1}}{C_{p2}}$$

$$b_{52}=\frac{L_p}{C_sC_{p2}}+\frac{L_{ls1}}{C_sC_{p2}}$$

$$a_{60}\frac{d^6 i_{Cp\_iR2}}{dt^6}+a_{61}\frac{d^4 i_{Cp\_iR2}}{dt^4}+a_{62}\frac{d^2 i_{Cp\_iR2}}{dt^2}+a_{63} i_{Cp\_iR2}=b_{60}\frac{d^3 i_{R1}}{dt^3}+b_{61}\frac{di_{R1}}{dt}$$

$$a_{60}=a_{40}\quad a_{61}=a_{41}\quad a_{62}=a_{42}\quad a_{63}=a_{43}$$

$$b_{60}=\frac{L_sL_p}{C_{p1}} \qquad \text{(B-18)}$$

$$b_{61}=\frac{L_p}{C_sC_{p1}}$$

Similarly, the ordinary differential equations (B-16) to (B-18) can be used to obtain the controllable canonical state-space representation through substitution of relevant equation coefficients into the dynamic state, A_c and output matrices C_c.

$$\dot{x}_4 = A_{c4}x_4 + B_{c4}u_4 \qquad y_4 = C_{c4}x_4 + D_{c4}u_4$$

$$A_{c4} = \begin{bmatrix} 0 & 1 & 0 & 0 & 0 & 0 \\ 0 & 0 & 1 & 0 & 0 & 0 \\ 0 & 0 & 0 & 1 & 0 & 0 \\ 0 & 0 & 0 & 0 & 1 & 0 \\ 0 & 0 & 0 & 0 & 0 & 1 \\ -\frac{a_{43}}{a_{40}} & 0 & -\frac{a_{42}}{a_{40}} & 0 & -\frac{a_{41}}{a_{40}} & 0 \end{bmatrix} \qquad B_{c4} = \begin{bmatrix} 0^{1\times 5} \\ 1 \end{bmatrix} \qquad \text{(B-19)}$$

$$C_{c4} = \begin{bmatrix} 0 & \frac{b_{41}}{a_{40}} & 0 & \frac{b_{40}}{a_{40}} & 0 & 0 \end{bmatrix} \qquad D_{c4} = [0]$$

$$\dot{x}_5 = A_{c5}x_5 + B_{c5}u_5 \qquad y_5 = C_{c5}x_5 + D_{c5}u_5$$

$$A_{c4} = A_{c5} \qquad B_{c5} = \begin{bmatrix} 0^{1\times 5} \\ 1 \end{bmatrix} \qquad \text{(B-19)}$$

$$C_{c4} = \begin{bmatrix} \frac{b_{52}}{a_{50}} & 0 & \frac{b_{51}}{a_{50}} & 0 & \frac{b_{50}}{a_{50}} & 0 \end{bmatrix} \qquad D_{c5} = [0]$$

$$\dot{x}_6 = A_{c6}x_6 + B_{c6}u_6 \qquad y_6 = C_{c6}x_6 + D_{c6}u_6$$

$$A_{c6} = A_{c6} \qquad B_{c6} = \begin{bmatrix} 0^{1\times 5} \\ 1 \end{bmatrix} \qquad \text{(B-21)}$$

$$C_{c6} = \begin{bmatrix} \frac{b_{61}}{a_{60}} & 0 & \frac{b_{60}}{a_{60}} & 0 & 0 & 0 \end{bmatrix} \qquad D_{c6} = [0]$$

B.3. Observable Canonical State-Space Derivation

Although simulation using the control canonical form can be undertaken, it will be more time consuming, since the model contains redundant state variables. Alternatively, this problem can be circumvented by formulating the augmented state space equation for v_{Lp} in the observable canonical form. The relevant formulae —(8-25) and (8-27) in chapter 8 is thereby modified to address the issue.

The state-space observable canonical form is given by,

$$\dot{\mathrm{x}} = \mathrm{A}_o \mathrm{x} + \mathrm{B}_o u \qquad y = \mathrm{C}_o \mathrm{x} + \mathrm{D}_o u \tag{B-22}$$

where the system matrices have the special structure,

$$\mathrm{A}_c = \begin{bmatrix} 0 & 0 & \cdots & 0 & -a_{n-1} \\ 1 & 0 & \cdots & 0 & -a_{n-2} \\ \cdots & \cdots & \cdots & \cdots & \cdots \\ 0 & 0 & \cdots & 0 & -a_1 \\ 0 & 0 & \cdots & 1 & -a_0 \end{bmatrix} \quad \mathrm{B}_c = \begin{bmatrix} b_{n-1} \\ b_{n-2} \\ \cdots \\ b_1 \\ b_0 \end{bmatrix} \quad \mathrm{C}_c = \begin{bmatrix} 0 & 0 & \cdots & 0 & 1 \end{bmatrix} \tag{B-23}$$

The transformation to observer canonical form illustrated for the equivalent circuit in Fig. 8.15. From (8-23) and (8-26), the state-space equations for the parallel resonant inductor voltage, v_{Lp} due to voltage source, V_{in} and current sources, i_{R1} and i_{R2} in the observable canonical form are given by,

$$\begin{aligned} \dot{\mathrm{x}}_1 &= \mathrm{A}_o \mathrm{x}_1 + \mathrm{B}_{o1} V_{in} \\ y_1 &= v_{Lp\_vi} = \mathrm{C}_o \mathrm{x}_1 + \mathrm{D}_{o1} V_{in} \end{aligned} \tag{B-24}$$

$$\begin{aligned} \dot{\mathrm{x}}_2 &= \mathrm{A}_o \mathrm{x}_2 + \mathrm{B}_{o2} i_{R2} \\ y_2 &= v_{Lp\_iR1} = \mathrm{C}_o \mathrm{x}_2 + \mathrm{D}_{o2} i_{R2} \end{aligned} \tag{B-25}$$

$$\begin{aligned} \dot{\mathrm{x}}_3 &= \mathrm{A}_o \mathrm{x}_3 + \mathrm{B}_{o2} i_{R2} \\ y_3 &= v_{Lp\_iR2} = \mathrm{C}_o \mathrm{x}_3 + \mathrm{D}_{o3} i_{R2} \end{aligned} \tag{B-26}$$

where

$$\mathrm{A}_o = \left[\begin{array}{ccccc:c} 0 & 0 & 0 & 0 & 0 & -\frac{a_{13}}{a_{10}} \\ 1 & 0 & 0 & 0 & 0 & 0 \\ 0 & 1 & 0 & 0 & 0 & -\frac{a_{12}}{a_{10}} \\ 0 & 0 & 1 & 0 & 0 & 0 \\ 0 & 0 & 0 & 1 & 0 & -\frac{a_{11}}{a_{10}} \\ 0 & 0 & 0 & 0 & 1 & 0 \end{array}\right] \quad ; \quad \mathrm{B}_{c1} = \begin{bmatrix} -\frac{b_{10}}{a_{10}} \times \frac{a_{13}}{a_{10}} \\ 0 \\ -\frac{b_{10}}{a_{10}} \times \frac{a_{12}}{a_{10}} + \frac{b_{11}}{a_{10}} \\ 0 \\ -\frac{b_{10}}{a_{10}} \times \frac{a_{11}}{a_{10}} + \frac{b_{12}}{a_{10}} \\ 0 \end{bmatrix} \quad ; \quad \mathrm{B}_{c2} = \begin{bmatrix} \frac{b_{22}}{a_{10}} \\ 0 \\ \frac{b_{21}}{a_{10}} \\ 0 \\ \frac{b_{20}}{a_{10}} \\ 0 \end{bmatrix} \quad ; \quad \mathrm{B}_{c3} = -\mathrm{B}_{c2}$$

$$\mathrm{C}_o = \begin{bmatrix} 0^{5\times 1} & 1 \end{bmatrix} \quad ; \quad \mathrm{D}_{c1} = [1] \quad ; \quad \mathrm{D}_{c2} = \mathrm{D}_{c3} = [0]$$

Adding (B-24), (B-25) and (B-24) yields,

$$\dot{x}_1 + \dot{x}_2 + \dot{x}_3 = A_o(x_1 + x_2 + x_3) + \begin{bmatrix} B_{o1} & B_{o2} & B_{o3} \end{bmatrix} \begin{bmatrix} V_{in} \\ i_{R1} \\ i_{R2} \end{bmatrix}$$
$$y_1 + y_3 + y_3 = v_{Lp\_vi} + v_{Lp\_iR1} + v_{Lp\_iR2} = C_o(x_1 + x_2 + x_3) + \begin{bmatrix} D_{o1} & 0 & 0 \end{bmatrix} \begin{bmatrix} V_{in} \\ i_{R1} \\ i_{R2} \end{bmatrix} \quad \text{(B-27)}$$

By defining,

$$x = x_1 + x_2 + x_3$$
$$y = y_1 + y_3 + y_3 = v_{Lp} \quad \text{(B-28)}$$

The observable canonical state-space equation in (B-27) simplifies to,

$$\dot{x} = A_o(x_1 + x_2 + x_3) + \begin{bmatrix} B_{o1} & B_{o2} & B_{o3} \end{bmatrix} \begin{bmatrix} V_{in} \\ i_{R1} \\ i_{R2} \end{bmatrix}$$
$$y = v_{Lp} = C_o(x_1 + x_2 + x_3) + \begin{bmatrix} D_{o1} & 0 & 0 \end{bmatrix} \begin{bmatrix} V_{in} \\ i_{R1} \\ i_{R2} \end{bmatrix} \quad \text{(B-29)}$$

It is obvious that the subsequent parallel resonant inductor voltage, v_{Lp} has identical order to that of the resonant tank fast subsystem, thereby ensuring the uniqueness of the solution for the state-variable model in (8-11), (8-16) and (8-17).

APPENDIX C

Implementation of Digital Controller

Figure C.1 shows the circuit diagram of a digital controller for closed-loop control of the dual-load 4th-order converter. A PIC18F452 is used to calculate required turn-on and turn off times, that are then latched into an FPGA register. Effectively, a simple PI control algorithm, for closed loop feedback control of the two outputs, is implemented on the PIC microprocessor. The flow chart for the PIC 'C' digital controller is given in Fig. C.2.

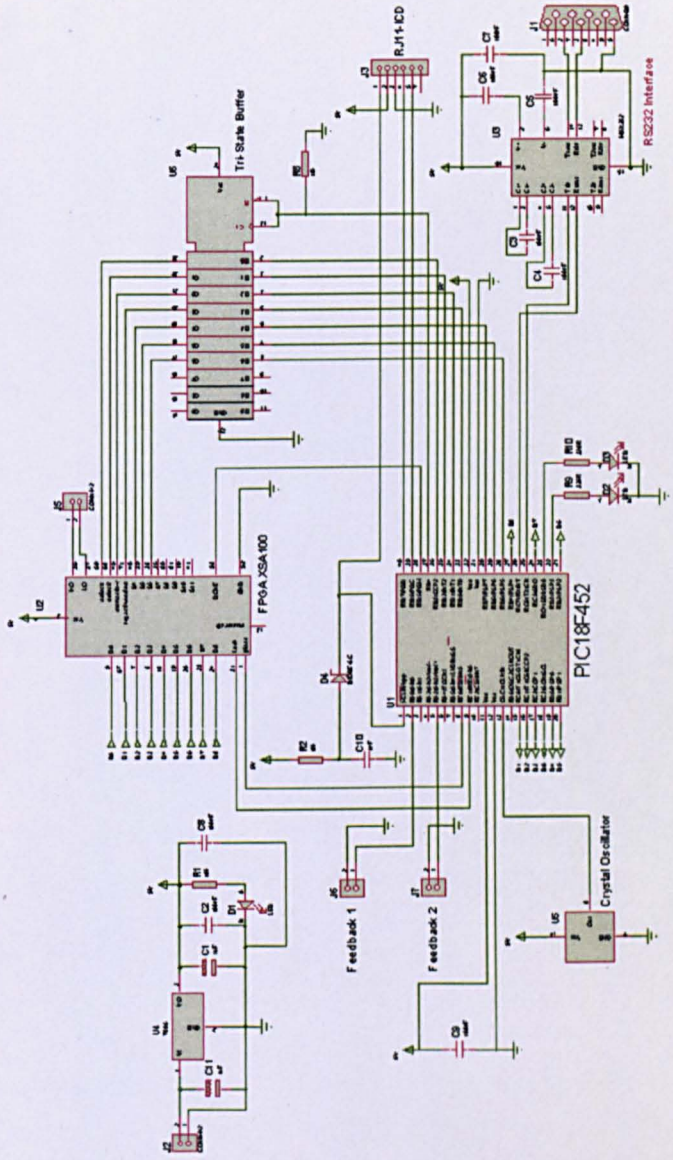

Figure C.1 Schematic diagram of digital controller.

The high- and low-side gate drive control signals are generated by the FPGA using logic circuits, with input data from the PIC. These digital logic circuits are implemented on the FPGA XSA 100—a schematic is given in Fig. C.3. The digital control circuit is constructed from two main components, the data latches that store the calculated times from PIC and, the combination logic that produces the high and low side control signals. The pair of data latches, shown in Fig. C.3(b), store the t_{on} and t_{off} times. The times are simultaneously transferred to the combination logic block in Fig. C.4(a).

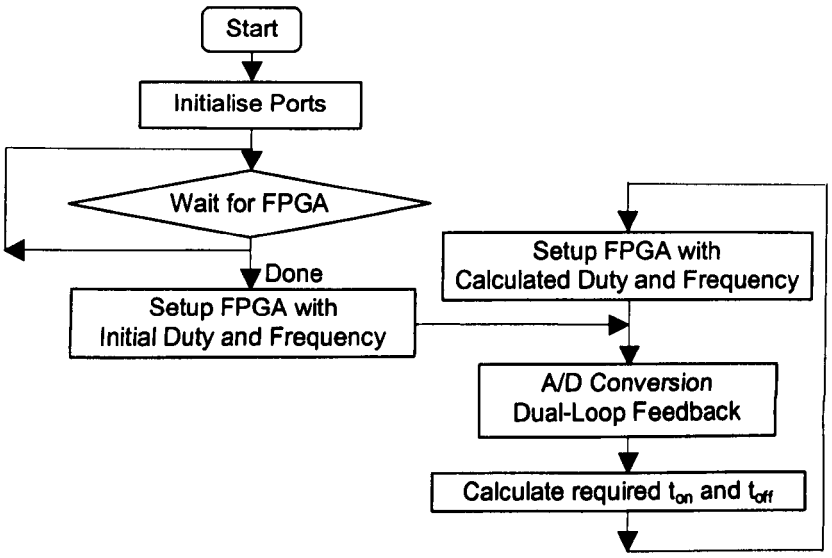

Figure C.2 Flow chart for PIC 'C' digital control.

Table C.1 Control and data line between the PIC and FPGA.

FPGA Inputs		**Functions**
9 bit data bus		Contains the 9 bit binary values for t_{on} and t_{off}.
2 bit address	- select1 and select2	Selects which latch to be enabled.
4 control bit	- startactlow	Disables FPGA output until initial times are stored in the latches. An active low input to start counter and enable output.
	- latch	Latches data onto enabled register.
	- pload	Loads stored data onto current register pair.
	- clearall	Clear all latches.
High and Low Side		Output control signal for high and low side gate drive.
Done Pine		Goes high when FPGA finishes being configured.

The combination logic block comprises of 9-bit counters, comparators and a state machine, producing the control signals. The comparators are used to compare the number from the PIC with the count of each counter. In the event when the count is equal to the number, this increments the 2-bit counter in the state-machine, see Fig. C.4(b), to output the control signal. This then resets the current counter and enables the next, hence, effectively, only one counter is active at a time. The overall control and data interface between the PIC and FPGA, are given in Table C.1.

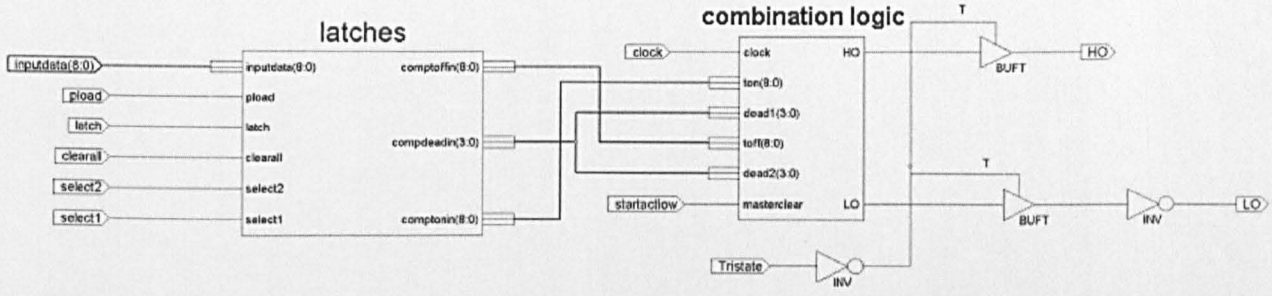

(a)

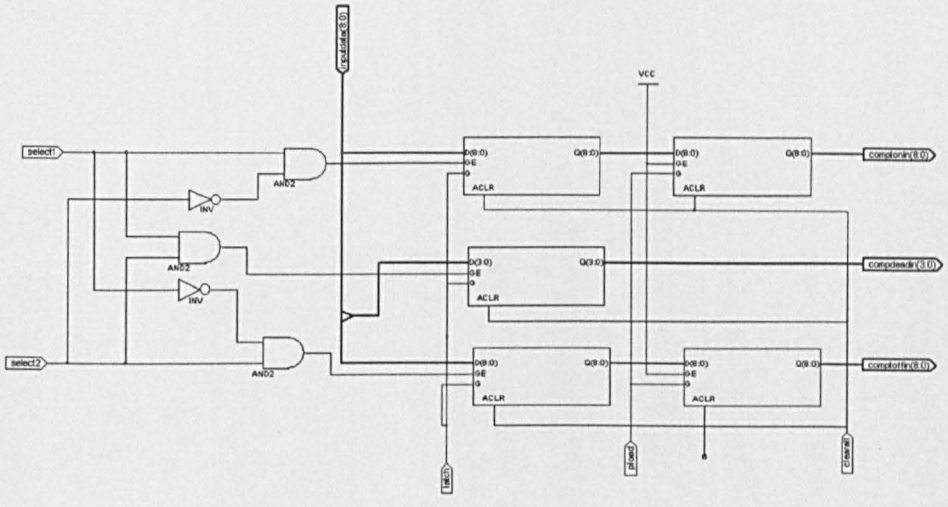

(b)

Figure C.3 XILINX FPGA XSA100 schematics: (a) Top level digital logic circuit schematic and (b) date latches.

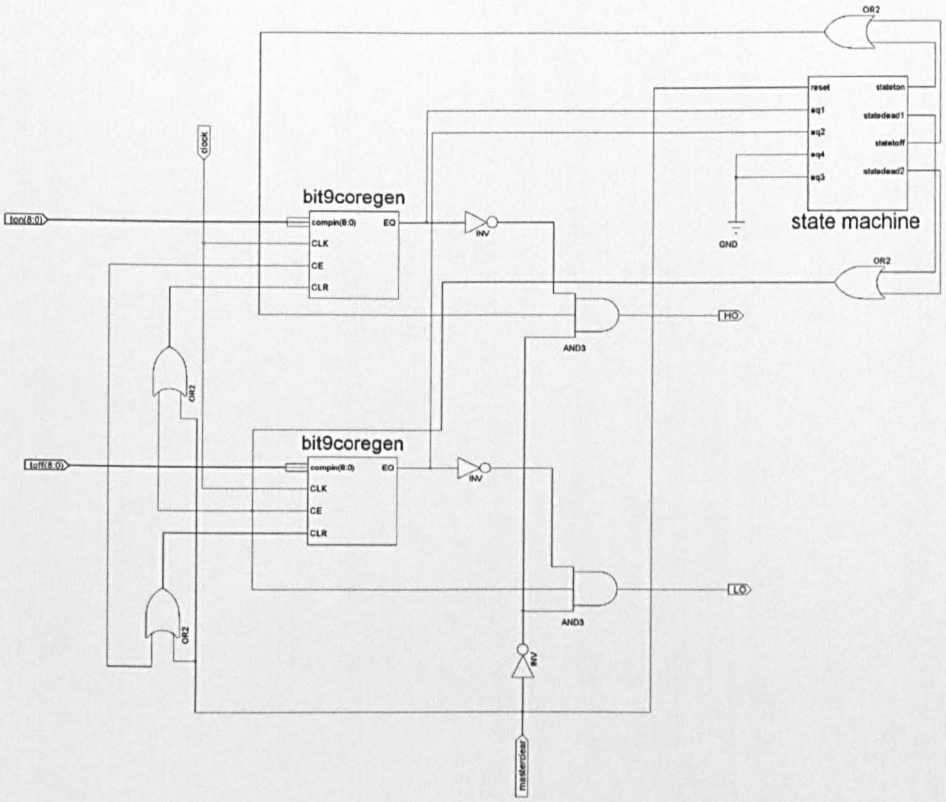

(a)

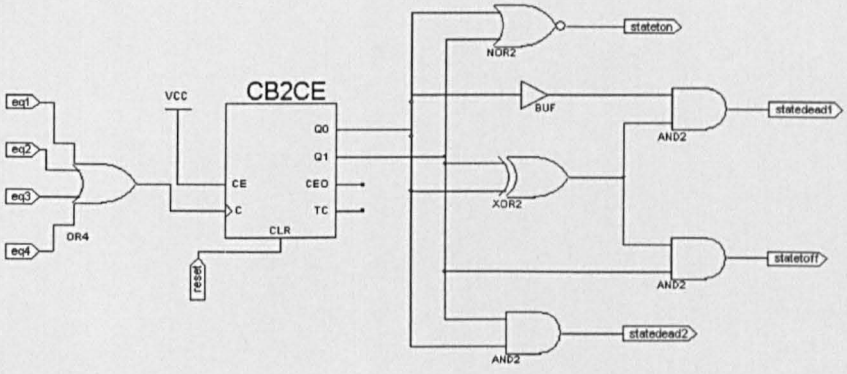

(b)

Figure C.4 XILINX FPGA schematics: (a) Combination logic and (b) State machine.

PIC18F452 'C' code for digital controller as followed:

```
#include <p18f452.h>
#include <adc.h>                                        /* for analogue to digital conversion */
#include <stdlib.h>
#include <math.h>

        #define tonset                  50                      /* Initial on time */
        #define kp_duty                 2                       /* Proportional gain */
        #define ki_duty                 10                      /* Integral gain*/
        #define kp_freq                 10
        #define ki_freq                 30
        #define deadtime                2                       /* dead time = dead time * 50ns */
        #define initial_count           100
        #define demand1                 1023*5/25
        #define demand2                 1023*3.3/5
        #define accum_max               2000000000              /* accumulator integrator */
        #define accum_min               -2000000000

        #define max_freq                66              /* 1/maximum frequency = max_freq * 50ns */
        #define min_freq                134             /* 1/minimum frequency = min_freq * 50ns*/

        #define negativeselect          PORTBbits.RB0
        #define startactlow             PORTBbits.RB1
        #define select2                 PORTBbits.RB2
        #define select1                 PORTBbits.RB3
        #define bufferenable            PORTBbits.RB4
        #define done                    PORTBbits.RB5
        #define latch                   PORTEbits.RE1
        #define pload                   PORTEbits.RE0
        #define clearall                PORTDbits.RD5
        #define LED1                    PORTDbits.RD3
        #define LED2                    PORTCbits.RC4
        #define pushbutton2             PORTAbits.RA6
        #define pushbutton              PORTEbits.RE2

//global variables go here
        unsigned int tonnum, toffnum;
        int feedback1, data, dataton, error1, P1, ei1, esum1;           /* 16 bit store for A to D result */
        int feedback2, error2, P2, ei2, esum2,count;
        long int accum1=0, accum2=0;
        unsigned long int temp_accum=0;

//functions go here ************************************************************
void present (void)
{
        char    data_array [9],index,x;                                 /* used in for loop */
        unsigned int            bitno,temp;
        bitno  = 256;
        index = 1;                                                      /*index for results array */

for (x = 1; x < 10; x++)                        /* test each bit if 1 or zero then stores in array */
        {
                temp = data & bitno;            /*masks all other bits except bitno=2^bit*/
                temp = temp - bitno;            /*result.. if bit is 1 then - bitno gives 0..Else 0 */
                if (temp == 0)
                        data_array[index] = 1;
                else
                        data_array[index] = 0;

                bitno = bitno>>1; /*256.. 128..64..32..16..8..4..2..1 */
                index++;
        }

        PORTDbits.RD4 = data_array[1];          /*d8*//* use index to put data to correct bit */
        PORTCbits.RC5 = data_array[2];                                                  /*d7*/
        PORTDbits.RD2 = data_array[3];                                                  /*d6*/
        PORTDbits.RD1 = data_array[4];                                                  /*d5*/
        PORTDbits.RD0 = data_array[5];                                                  /*d4*/
        PORTCbits.RC2 = data_array[6];                                                  /*d3*/
        PORTCbits.RC1 = data_array[7];                                                  /*d2*/
        PORTCbits.RC0 = data_array[8];                                                  /*d1*/

        if (data_array[9] == 1)
                PORTCbits.RC3 = 0;
        else
                PORTCbits.RC3 = 1;
}

void latchdata (void)
```

```
{
        latch = 0;
        latch = 1;
        latch = 0;
}

void tonselect (void)
{
        select1 = 1;
        select2 = 0;
        present ();
        latchdata ();
        select1 = 0;
}

void toffselect (void)
{
        select1 = 0;
        select2  = 1;
        present ();
        latchdata ();
        select2 = 0;
}

void tdeadselect (void)
{
        select1 = 1;
        select2 = 1;
        present ();
        latchdata ();
        select1 = 0;
        select2 = 0;
}

void loadcurrent (void)
{
        pload = 0;
        pload = 1;
        pload = 0;
}

void wait (void)
{
        char count1;
        count1 = 255;
        do
        count1--;
        while (count1 != 0);
}

void analogue_freq (void)                    /* analogue to digital conversion for feedback 1 */
{
OpenADC (ADC_FOSC_64 &                       /* opens and configures A to D.. all analogue */
        ADC_RIGHT_JUST    &
        ADC_1ANA_0REF,
        ADC_CH0           &
        ADC_INT_OFF);

        SetChanADC (ADC_CH0);                                /* selects channel */
        Delay10TCYx(6);
        ConvertADC ();                                       /* starts a to d conversion */
        while ( BusyADC() );                                 /* waits to finish */
        feedback1 = ReadADC();
        CloseADC ();
}

void analogue_duty (void)                    /* analogue to digital conversion for feedback 2 */
{
OpenADC (ADC_FOSC_64 &                       /* opens and configures A to D all analogue */
        ADC_RIGHT_JUST &
        ADC_8ANA_0REF,
        ADC_CH1  &
        ADC_INT_OFF);
        SetChanADC (ADC_CH1);                                /* selects channel */
        Delay10TCYx(6);
        ConvertADC ();                                       /* starts a to d conversion */
        while ( BusyADC() );                                 /* waits to finish*/
        feedback2 = ReadADC();
        CloseADC ();
}
```

```
void intial (void)
{
        data = tonset - deadtime;
        tonnum = data;
        dataton = data;                                          /* store tons.. used to alter duty
and calc toff */
        tonselect ();

        data = initial_count - dataton  - deadtime - deadtime;   /* calc toff from T - toff */
        toffnum = data;
        toffselect ();
        loadcurrent ();
}

void intial_deadtime (void)
{
        data = deadtime;
        tdeadselect ();
}

void controller_freq (void)
{
        error1 = demand1 - feedback1;
        P1 = error1 * kp_freq;                                   /* proportional controller */

        accum1 = accum1 + (ki_freq * error1);                  //accumulator for Integral Controller

        if (accum1 > accum_max)                                  // prevent accumulators overflow
                accum1 = accum_max;
        if (accum1 < accum_min)
                accum1 = accum_min;

        if (accum1 < 0)                                          //signed to unsigned variable
                temp_accum = -accum1;
        else
                temp_accum = accum1;

        temp_accum >> 16;                                      // shift unsigned variable by ki_freq

        if (accum1 < 0)                                          // convert back to signed
                ei1 = -temp_accum;
        else
        ei1 = temp_accum;

        esum1 = P1+ ei1;                                       //total error = Proportional + Integral error

        count = esum1;

        if (count > min_freq)
                count = min_freq;
        if (count < max_freq)
                count = max_freq;
}


void controller_duty (void)
{
        error2 = demand2 - feedback2;

        P2 = error2 * kp_duty;                                   //proportional controller

        accum2 = accum2 + (ki_duty * error2);                    //accumulator      for      Integral
Controller

        if (accum2 > accum_max)                                  // prevent accumulator overflow
                accum2 = accum_max;
        if (accum2 < accum_min)
                accum2 = accum_min;

        if (accum2 < 0)                                          //signed to unsigned variable
                temp_accum = -accum2;
        else
                temp_accum = accum2;

        temp_accum >> 16;                                        // shift unsigned variable by ki

        if (accum2 < 0)                                          // convert back to signed
                ei2 = -temp_accum;
        else
                ei2 = temp_accum;
```

```
        esum2 = P2+ ei2;

        dataton = esum2;                                        // on time = total error

        if (dataton > count)                                    // test to keep duty within range!
                dataton = count;
        if (dataton < 0)
                dataton = 0;

        data = dataton - deadtime;

        tonselect ();

        data = count - dataton  - deadtime - deadtime ;
        toffselect ();

        loadcurrent ();
 }

void main (void)
{
// main function variable go here
        int LEDFLASH=0;
        char duty_cont=0;

//setup ports
        PORTB =  0x10;                                          /*Initial value of RB4 to be 1 */
        TRISB = 0x20;                                           /*PORTB as outputs RB5 as input b'00100000'*/
        PORTD = 0;
        TRISD = 0;
        PORTC = 0;
        TRISC = 0;
        PORTE = 0;
        TRISE = 0;                                              /* PORT C D E as outputs... PORTA as INPUTS*/

        PORTA = 0xff;
        TRISA = 0xff;

READY:
        do                                                      /* disables buffer unit FPGA configured */
        {
        bufferenable = 1;
        }
        while (done == 0);

        startactlow = 1;                                        /* disable output */
        bufferenable = 0;                                       /* enable buffer */
        LED1 = 1 ;                                              /*light LED..FPGA configured. PIC operating*/

        intial_deadtime ();                                     //gets dead time
        intial ();                                              //sets initial duty cycle

while (1)
        {
        startactlow = 0;                                        // enables output

        if (done == 0)                                          // TEST to check FPGA still configured and ON

                {
                LED1 = 0;                               //FPGA no longer programmed..
                goto     READY ;
                }

      analogue_freq ();
        analogue_duty ();                                       // performs A to D conversion
        controller_freq ();                                     //calc. duty from atod.
        controller_duty ();


        if (LEDFLASH == 600)                                    //flashes LED
        {
        LED2 = 1^LED2;
        LEDFLASH=0;
        }

        LEDFLASH++;
                }                                               /* end of while loop */
}                                                               /* end of main function */
```